UNIVERSITY OF CAPE TOWN
IYUNIVESITHI YASEKAPA • UNIVERSITEIT VAN KAAPSTAD

Multiscale modelling of sutures in a high-performing biological protective structure: The turtle shell

by

Supervisor:
Prof. B.D. Reddy

Author:
Benjamin Alheit

Co-Supervisor:
Prof. Swantje Bargmann

Thesis Presented for the Degree of
Doctor of Philosophy
In the Department of Mechanical Engineering
University of Cape Town
April 2022

cerecam
Centre for Research in Computational and Applied Mechanics

Declaration

I, **Benjamin Alheit**, hereby declare that the work on which this thesis is based is my original work (except where acknowledgements indicate otherwise) and that neither the whole work nor any part of it has been, is being, or is to be submitted for another degree in this or any other university. I authorise the University to reproduce for the purpose of research either the whole or any portion of the contents in any manner whatsoever.

Portions of this work have been published with the prior knowledge and approval of the supervisors. The published portions are as follows:

1. Content from Chapter 7 has been published in the following article: B. Alheit, S. Bargmann, and B. D. Reddy. "Computationally modelling the mechanical behaviour of turtle shell sutures — A natural interlocking structure". *Journal of the Mechanical Behavior of Biomedical Materials* 110 (2020), p. 103973;

2. Content from Chapter 8 has been published in the following article: B. Alheit, S. Bargmann, and B. D. Reddy. "Dynamic mechanical behaviour of suture interfaces as inspiration for architectured hierarchical interlocking composites". *Journal of the Mechanics and Physics of Solids* 157 (2021), p. 104620;

3. Content from Chapter 9 is presented in the following article, which is in press at the time of writing this: B Alheit, S Bargmann, and B. Reddy. "How suture networks improve the protective function of natural structures: A multiscale investigation". *Acta Biomaterialia* (2022);

4. Content from Chapters 7–9 was presented at the following conference: The 25th International Congress of Theoretical and Applied Mechanics: B. Alheit, S. Bargmann, and B. D. Reddy. "Computational modelling of the mechanical behaviour of turtle shells". *25th International Congress of Theoretical and Applied Mechanics.* 2021.

Signature: Signed by candidate Date: 6 April 2022

Abstract

Many natural protective structures, such as alligator armour, turtle shells, and the skulls of many animals including humans, contain networks of sutures; those are, soft tissue that bonds adjacent stiff plates typically made of bone. Such protective structures ought to withstand large loads associated with predator attacks. Considering the ubiquity of suture networks in natural protective structures and the optimization process of evolution, it is reasonable to hypothesize that sutures improve the mechanical behaviour of protective structures during predator attacks. However, the effect of sutures in such loading scenarios is not well understood. This is addressed by using computational models of turtle shells, where special attention is paid to the influence of the network of sutures. Additionally, the structure-function relationship is elucidated using parametric studies varying the suture geometry. Computational experiments are carried out at the suture scale to investigate its mechanical behaviour and at the shell scale to elucidate the effect that sutures have on the shell. Among other insights, it is shown that: the compliance of the shell during small deformations can be increased by increasing the height of the interlocking bone protrusions and suture thickness; the bone plates interlock for sufficiently large deformations of sutures with sufficiently long protrusions; suture geometry can be used to tailor stress-wave propagation; and the presence of sutures can reduce the maximum strain energy density, a key indicator for a material failure, during a predator attack by 31 times. The work presented paves the way for the inclusion of sutures in biomimetic protective structures such as helmets and body armour. Computational solid mechanics aspects include multiscale modelling, model order reduction, and finite strain constitutive modelling aspects, such as viscoelasticity, hyperelasticity, and anisotropy.

Acknowledgements

Thanks are owed to numerous people without whom the completion of this thesis and degree would not have been possible:

- Professor Daya Reddy, my supervisor, for offering his guidance and wisdom throughout my doctoral studies and, especially, for his thorough reviewing of this thesis;
- Professor Swantje Bargmann, my co-supervisor, for providing thorough reviews of publications resulting from this work;
- Natalie Bent, for exceptional management of all the administrative tasks relating to my degree;
- Lindsay Goldberg, my mother, for endless support of my education and her general love and care;
- All my dear friends and family who helped in proofreading this work;
- The National Research Foundation of South Africa for funding this work;
- Perhaps most significantly, I thank all the educators, from primary school teachers to PhD supervisors, that have nobly offered their time and energy to provide me with the necessary skills to complete the work presented in this thesis.

Contents

List of Figures

List of Tables

Chapter 1

Introduction

This thesis is concerned with modelling of the effects of sutures on the performance of natural protective structures. Sutures are convoluted layers of soft tissue that join interlocking stiff (typically bone) plates, as illustrated in Figure 1.1. The stiff plates also typically have interdigitating protrusions, which give the sutures their convoluted shape and cause adjacent plates to interlock.

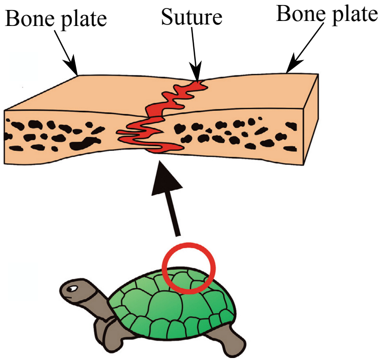

Figure 1.1: Illustration of a suture joining bone plates in a turtle shell, adapted from [5] with permission.

Sutures are found in myriad natural protective structures, such as the craniums of almost all animals [6] (including humans [7]), beaks of woodpeckers [8], shells of turtles [9], alligator armour [10], armadillo armour [11], and other structures [12, 13, 14, 15, 16]. The ubiquity of sutures in natural protective structures suggests evolutionary convergence, which, in turn, suggests that the inclusion of suture networks optimizes the functioning of protective structures. Hence, sutures may be a good candidate for biomimetic design of engineered protective structures. However, these observations raise two questions:

1. Do sutures improve the protective function of the structures in which they reside? It is possible that their ubiquity is owed to the improvement of another function, such as

locomotion, mastication, or growth;

2. If sutures do improve protective function, thus making them a good candidate for biomimetic design, what is a suitable way to model the effect of sutures on the structures in which they reside?

This thesis aims to address these two questions.

The structure of the remainder of the introduction is as follows. Section 1.1 provides more detail on the motivation for this work, introducing in greater depth the concepts of convergent evolution and biomimetic design, and how these concepts apply to sutures in protective structures. Then, Section 1.2 sets out research questions and objectives that follow from the motivation for the investigation. It also presents an outline of the method by which these questions are addressed. Finally, Section 1.3 presents the structure of the remainder of the thesis.

1.1 Motivation for investigation: convergent evolution and biomimetic design

Here, an argument is presented for the relevance of studying the influence of sutures on the mechanical behaviour, and hence, performance, of the protective structures in which they reside.

1.1.1 Convergent evolution

Convergent evolution is a process whereby disparate species evolve to obtain similar structures that perform similar functions. Some examples include:

- Wings for flying which are found in birds, bats, and insects;
- Fins for swimming which are found in fish, dolphins, and whales; even penguin wings have evolved to be fin-like;
- Sutures which are found in craniums, turtle shells, alligator armour, etc.

Convergent evolution differs from the original description of evolution famously theorised by Charles Darwin [17], where animals of the same species, when placed in different environments, evolve to obtain different traits that are better suited for survival in their new environment. This form of evolution was later termed divergent evolution [18].

For the purpose of biomimetic design, which is described in the following subsection, one would like to find biological structures that are optimized for a particular function. Convergent evolution is particularly convenient in this case because evolution is widely accepted to optimize structures. Furthermore, convergent evolution is easy to identify – one can simply observe whether similar structures are found in various species that require similar functions.

1.1.2 Biomimetics

Biomimetics is a process in which the design of structures or artefacts for a given function is guided by, and seeks to replicate, a structure in nature that performs the desired function. This approach has had great success, as evolution tends to optimize natural structures for their particular function. Some famous examples of biomimetic designs include:

- Aeroplanes which were originally inspired by birds [19];
- Velcro which was inspired by burrs and the way in which they become attached to animal hair or fur [20];
- The shape of several Japanese trains which was inspired by the shape of the heads of kingfishers [21].

While biomimetics has dramatically increased in popularity in recent decades, it is certainly not a new concept. Indeed, examples of biomimetic design date back to as early as the 15th century, where Leonardo da Vinci designed flying machines inspired by the wings of bats [22, 23].

Due to the evolutionary convergence[1] of sutures in natural protective structures it is reasonable to expect that sutures improve the mechanical performance of protective structures. Hence, sutures may be a suitable candidate for biomimetic design of engineered protective structures. However, evolutionary convergence alone is not sufficient proof that sutures improve the mechanical performance of protective structures during high loading events. The ubiquity of sutures may be owed to some other function; for example, authors have hypothesised that the function of sutures in turtle shells is to allow them to locomote with greater ease [9], while others submit that cranial sutures play a mechanical role during mastication [24]. It is also well known that sutures allow for growth of the bone structures in which they reside [25]. Hence, further investigation is required to assess the appropriateness of including

---

[1] To be clear, the meaning of "evolutionary convergence" is as presented in Section 1.1.1. Here, the presence of the word "convergence" is not to be conflated with any mathematical procedure or solution algorithm.

sutures in engineered structures. To this end, suitable research questions and objectives are posed in the subsection that follows.

1.2 Research questions and approach

This thesis aims to answer two research questions:

1. Do sutures improve the protective performance of the structures in which they reside?
2. If the answer to the above question is the affirmative, what are the mechanisms by which this occurs?

In addition to answering these research questions, there are several objectives of this thesis.

1.2.1 Objectives

The objectives of this thesis are as follows:

1. To develop a framework for modelling the influence of sutures on the mechanical behaviour of structures in which they reside that could be used to aid the design of engineered structures that include sutures;
2. To determine the structure–function relationship of sutures.

1.2.2 Method of investigation

The objectives are addressed by modelling the behaviour of suture–containing structures in various scenarios as initial boundary value problems within a continuum mechanics framework. Computational tools, such as the Finite Element Method (FEM), are used to find approximate solutions to the initial boundary value problems. In particular, models of turtle shells are constructed. This is motivated by the fact that turtle shells are already widely regarded as high performing protective structures. Additionally, computational models require the input of various material parameters and, as the results of numerous physical experiments on turtle shells are available in the literature, these parameters can readily be determined.

1.3 Structure of thesis

The structure of the remainder of this thesis is as follows. A review of the literature on the mechanical behaviour of turtle shells and sutures is presented in Chapter 2. Then, Chapters 3–6 present the necessary theoretical background for development of the mathematical models; the topics are continuum mechanics, constitutive modelling, numerical methods, and multiscale modelling, respectively. Chapters 7–9 present the results and discussion of simulations of sutures in turtle shells, starting with quasistatic simulations at the suture scale, followed by dynamic simulations at the suture scale, and finally presenting dynamic multiscale simulations. Finally, conclusions and possibilities for further work are presented in Chapter 10.

Chapter 2

Review of the mechanical behaviour of turtle shells and sutures

This chapter presents a review of the relevant literature on turtle shells and sutures. The chapter begins by describing the structure of turtle shell in Section 2.1. Then, a review of the literature on the mechanical behaviour of turtles is presented in Section 2.2. Finally, in Section 2.3, a review of the modelling of sutures is presented, that is, soft collagenous tissue which binds adjacent bone plates.

2.1 The structure of a turtle shell

The turtle shell is a biocomposite structure, that is, a structure consisting of several biological materials. These include bone, soft collagenous tissue, and hard keratinous tissue. The base of the turtle shell is its skeleton, which is displayed in Figure 2.1. The dorsal hemisphere of the shell, termed the ‘carapace’, consists of a spinal column which is aligned with the anterior axis (Figure 2.1 (a)). Several ribs protrude from the spinal column in the lateral direction. In a living turtle, each rib is separated by a suture which consists of soft collagenous tissue, as displayed in Figure 2.2. In the skeleton shown in Figure 2.1 the soft suture material has degraded, so that the spaces which would be occupied by the sutures appear as a network of cracks throughout the carapace. In addition to the sutures which bind adjacent ribs, the ribs interlock due to interdigitating bony protrusions shown in the suture region (Figure 2.1 (b)).

In a living turtle, the skeleton is covered by a skin of soft collagenous tissue, which is in turn covered by a layer of hard keratinous tissue (Figure 2.2).

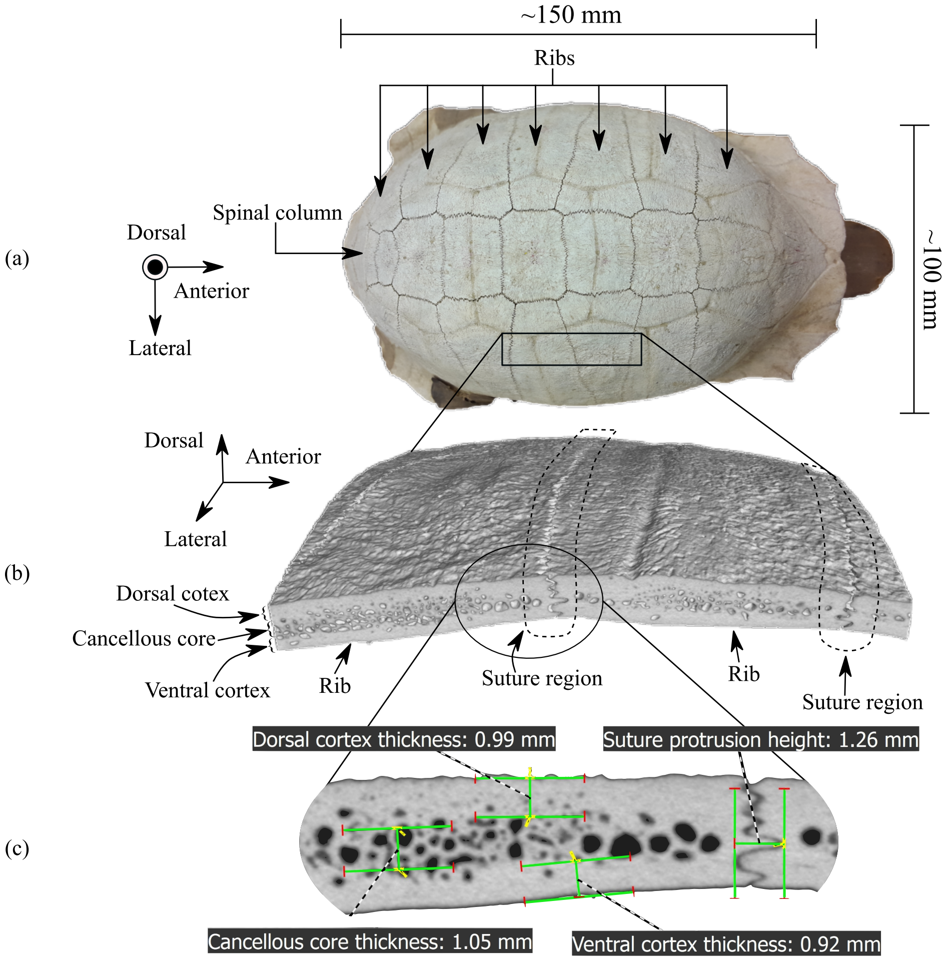

Figure 2.1: A dehydrated angulate tortoise (land turtle) skeleton shown at three levels of magnification: (a) at the length scale of the entire shell, (b) at the scale of the width of a rib, and (c) at the scale of the thickness of a rib.

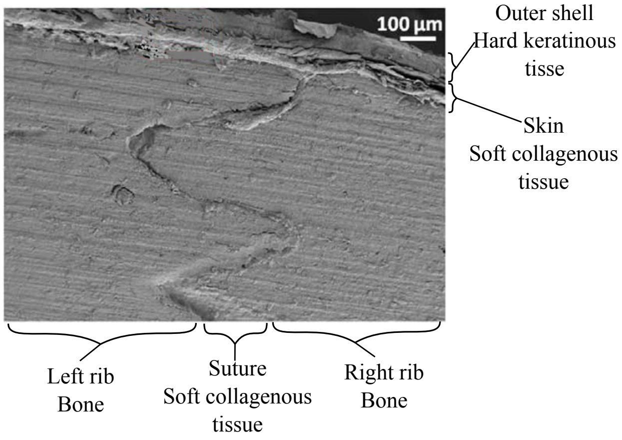

Figure 2.2: Cross-section through a turtle suture (adapted from [26] with permission).

2.1.1 Sutures

The sutures are comprised of a soft collagenous tissue. Collagenous materials are hierarchical, that is, they contain a recognizable structure at multiple length scales, as illustrated in Figure 2.3. At the smallest length scale of approximately 1 nm, collagen consists of amino acids [28].

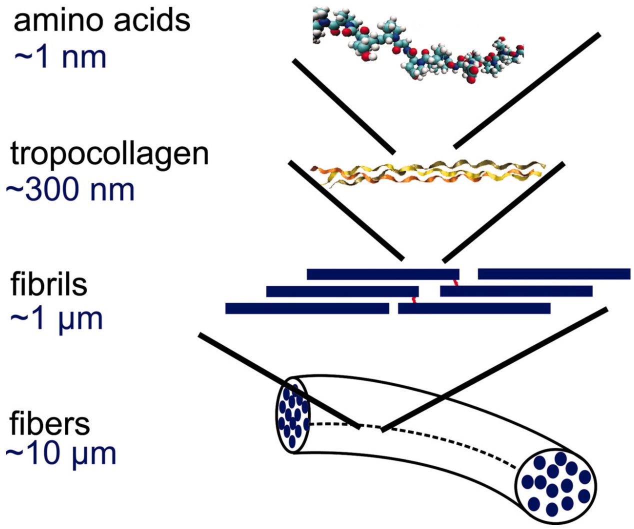

Figure 2.3: Hierarchical structure of soft collagenous tissue (adapted from [27] with permission).

The amino acids are bonded together to make up tropocollagen molecules. Tropocollagen molecules self-assemble into a helical shape and wrap together in sets of three to forming a triple helix. The triple helices self-arrange, regularly staggering their end positions, to form fibrils. Adjacent triple helices also display varying degrees of cross-linking; that is, covalent bonds shared between two different triple helices. Finally, the fibrils are arranged into fibres, which are suspended in a hydrated ground substance.

The fibrous nature of collagenous tissues gives rise to anisotropic mechanical behaviour at the continuum scale, provided that the fibres are aligned. In the sutures of a turtle shell, the alignment of the fibres and shape of the suture is related to the loading that the suture most commonly incurs. Sutures that commonly experience 'compressive loading', that is, loading where the bone plate on either side is pushed together, typically have fibres that align obliquely to the surfaces of the bone plates, as shown in Figure 2.4. Additionally, the bony protrusions connected by these sutures are typically longer and narrower [9]. On the other hand, sutures that typically experience tensile loading, where the adjacent bone plates are pulled apart, generally have fibres aligned normal to the surfaces of the bones. Furthermore, these sutures typically take on a flatter shape.

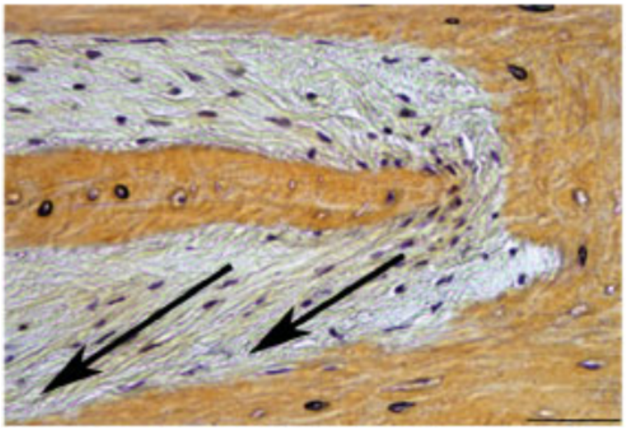

Figure 2.4: High magnification histological cross-section of a suture which commonly experiences compression (adapted from [9] with permission). Note how the collagen fibres abut the bone obliquely.

2.1.2 Bone ribs

Bone consists primarily of collagen [29]. However, in contrast to soft collagenous tissues, bone contains inorganic minerals, such as calcium phosphate. These minerals form crystals at nucleation sites along the collagen molecules, giving bone its stiffness. As with soft collagenous materials, bone can also display anisotropic mechanical behaviour due to the alignment of collagen fibres. However, if the collagen fibres are dispersed then bone may be modelled as isotropic. This is typically the case for cancellous bone.

The bone ribs of a turtle have a sandwich-like structure whereby a porous cancellous core is wrapped by dorsal and ventral dense cortical layers as shown in Figure 2.5, see also Figures 2.1 (b) and (c). The ventral cortex is divided further into two sublayers: the upper ventral and lower ventral (Figure 2.5). Both sublayers contain aligned collagen fibres. However, the fibres in the upper ventral are aligned in the lateral direction, whereas those in the lower ventral are aligned in the anterior direction [30]. In the dorsal cortex, however, the fibres are dispersed.

2.1.3 Keratinous layer

The outer keratinous layer is also a hierarchical material. At its lowest level, the material consists of beta-keratin lamellae, as shown in Figures 2.6 (b)–(c). These lamellae are stacked and arrange themselves into sections called scuta, which gives the hexagonal pattern on the outside of the turtle shell (Figure 2.6 (a)). An example of a single scute is shown on the right hand-side of Figure 2.6 (a). The lamella microstructure of the keratinous layer also gives rise to an anisotropic mechanical response.

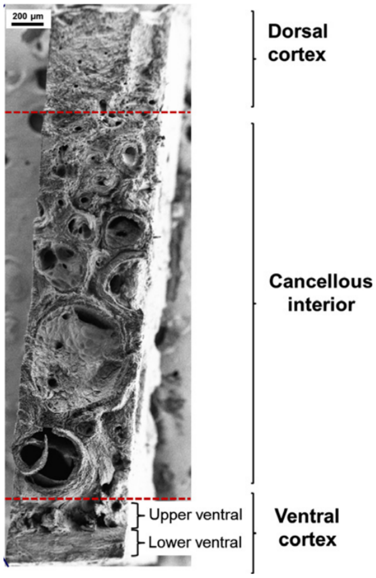

Figure 2.5: Cross-section of the rib of a juvenile red-eared slider turtle (adapted from [30] with permission).

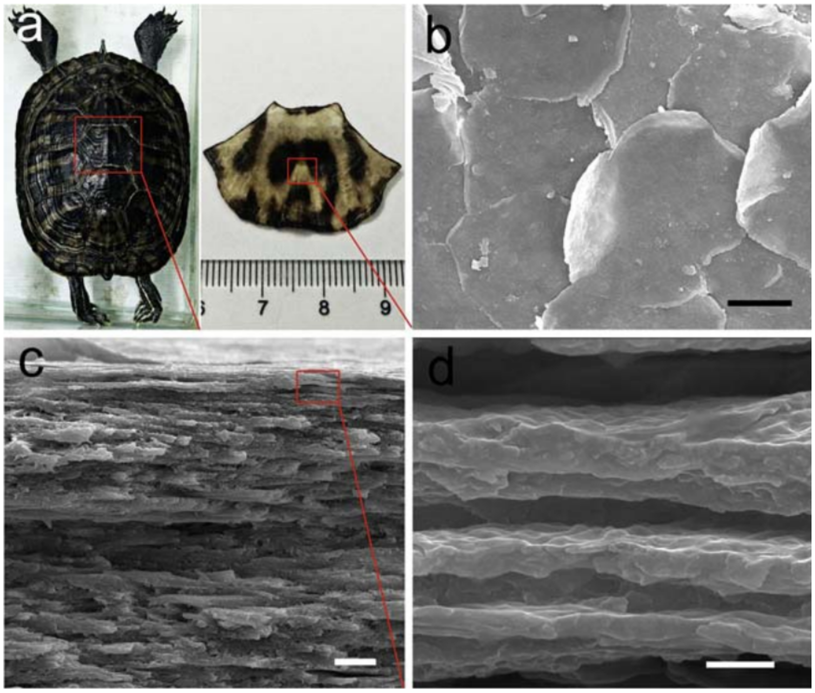

Figure 2.6: Keratin layer of a juvenile red-eared slider turtle at varying magnification levels: (a) at the scale of the entire shell; (b) at 20 microns (c) at 10 microns, and (d) at 1 micron. Length scales are indicated by the length of the horizontal line in the bottom-right corner of each subfigure. (Adapted with permission from [31].)

2.2 Review of turtle shell mechanical characterization

In the literature, the mechanical behaviour of turtle shells has been studied by means of physical experiments and computational modelling. A review of the literature for each is presented in what follows, beginning with physical experiments.

2.2.1 Physical experiments

Numerous physical experiments have been conducted on turtle shells in order to characterize their mechanical behaviour. These include nano-indentation tests [30, 32, 33], uniaxial loading tests on various portions of the shell [33, 34, 35, 31], bending tests on rib samples [36, 37], and dynamic loading experiments [26, 38, 39].

Of nano-indentation test studies, that presented in [30] is the most extensive. The authors tested several sites within the shell of an adult red-eared slider turtle, the results of which are summarized in Table 2.1. The table illustrates the isotropic behaviour of the dorsal cortex, which has approximately the same stiffness in all directions. Additionally, it shows the transversely isotropic behaviour of the upper and lower ventral cortices which are stiffer in the lateral and anterior directions, respectively; that is, in the direction of their collagen fibres. Additionally, the anisotropy of the keratinous layer is clear when hydrated. Similar values were found via nano-indentation in [33, 32]. However, in [32] values of Poisson's ratio for keratin and bone were reported in addition to stiffness as 0.4 and 0.25, respectively.

The stiffness of various portions of the shell has also been determined by uniaxial tests [33, 34, 35, 31]. In [33, 34, 35], uniaxial compression was applied to bone samples, with particular attention paid to the behaviour of the cancellous core. In the case of cancellous bone, uniaxial compression tests have an advantage over nano-indentation tests as they provide an effective stiffness of the structure instead of the local stiffness of an individual strut or column. The effective stiffness varies significantly depending on the degree of porosity, and so quoted values range from 282–804 MPa [33, 34, 35]. In [31], uniaxial tension tests were conducted on samples of the keratinous layer from a juvenile red-ear slider turtle, yielding similar results to those given in Table 2.1.

Several bending tests on rib samples have also been conducted [36, 37, 33]. In [36], load–deformation curves were presented along with images illustrating the failure mechanisms of the test samples. For example, test specimens that contained a suture in the middle experienced fracture of the bony protrusions, as presented in Figure 2.7. In [37, 33], bending tests were used to validate a material model for the cancellous region of the rib.

Table 2.1: Stiffness of various materials found in an adult red-eared slider turtle, determined by nano-indentation tests (adapted from [30] with permission).

Region	Sub-region		State	Indenting direction	E (GPa)
Rib	Cancellous interior		Dry	Spatial average	12.6
			Wet	Spatial average	6.7
	Dorsal cortex		Dry	Anterior	16.7
				Lateral	16.6
				Dorsal	16.4
			Wet	Spatial average	11.2
	Ventral cortex	Top layer	Dry	Anterior	12.3
				Lateral	18.2
				Dorsal	11.8
		Bottom layer	Dry	Anterior	17.9
				Lateral	12.7
				Dorsal	11.6
		Both layers	Wet	Parallel to fibres	13.4
				Perpendicular to fibres	5.7
Suture			Dry	Spatial average	1.6
			Wet	Spatial average	0.2
Keratin scutes			Dry	Dorsal	3.6
				Lateral	4.2
			Wet	Dorsal	1.3
				Lateral	0.7

Dynamic loading experiments have also been conducted on turtle shells [26, 38, 39]. In [26], low velocity Charpy impact tests were applied to test samples of the shell, with much attention paid to the influence of the keratin layer. It was found that the keratin layer increases the fracture energy by approximately 3 times. In [38], high strain-rate tests of the bone sandwich structure were conducted utilizing a split Hopkinson pressure bar (SHPB) test. The tests displayed significant strain-rate hardening behaviour of the bone sandwich structure. Additionally, impact tests where a ball bearing was fired at the shell were conducted. These tests showed that the keratin layer distributes the impact energy over a larger surface area, and the cancellous core provides significant energy dissipation. In [39], cyclical bending loading was applied to several specimens from a red-eared slider turtle.

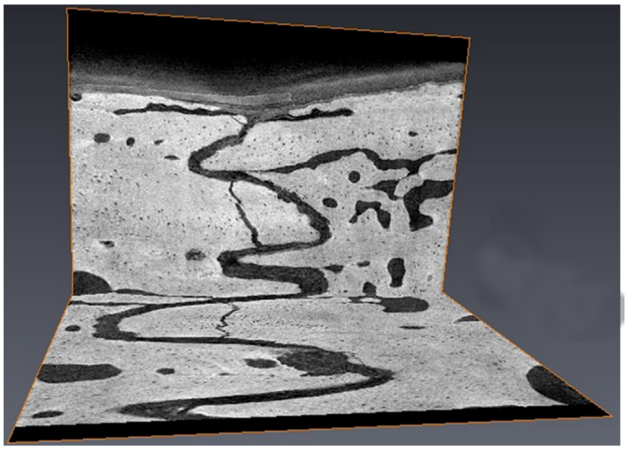

Figure 2.7: Micro-CT scan of a suture region in the centre of a three-point bending test sample after loading to failure (adapted from [36] with permission).

The tests showed that the presence of sutures increases the fatigue resistance of the shell.

2.2.2 Modelling and simulations

The mechanical behaviour of turtle shells has also been investigated by mathematical modelling and computational simulations. These include Finite Element (FE) simulations of the entire shell [40, 41], plasticity models for various regions of the shell [42, 43, 34, 35], crack propagation through the thickness of the shell [44], and homogenization simulations of the cancellous bone region [35, 32].

FE simulations of entire turtle shells have been conducted with the simplifying assumption that the shell is homogenous [40, 41]. In [41], a FE mesh was constructed from a CT scan of a red-eared slider turtle shell. Then, static compression and vibration mode analyses were conducted. The analyses showed that the structure of the shell protects the head and internal organs. This is achieved by a reduction in the deformation of the shell close to the head during compressive loading and by orientating the largest deformation regions for the most dominant vibration modes furthest from the head and vital internal organs.

In [40], the trade-off between hydrodynamic efficiency and the performance of the shell as a protective structure was investigated. The flatter, more streamlined, shells of turtles from “lotic” regions, that is, regions with fast flowing water, were found to be weaker than the rounder shells of turtles from “lentic” regions, that is, regions with still water.

Plasticity models of the shell have also been investigated for various regions [42, 43, 34, 35]. In [42, 34, 35], attention was paid to the behaviour of the cancellous bone. This typically has three distinct loading regions: linear elasticity, failure of the trabeculae, and densification, as presented in Figure 2.8. In [43], however, more attention was paid to the

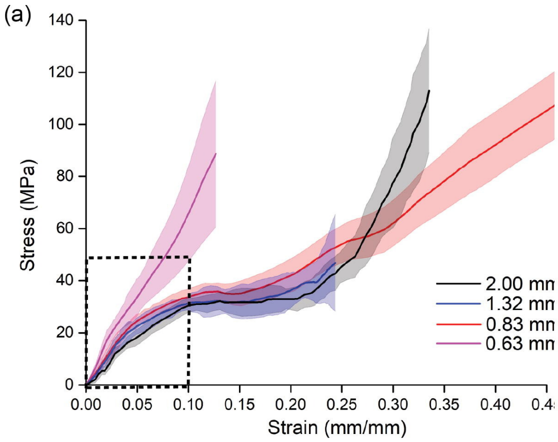

Figure 2.8: Compression tests of the cancellous bone of turtle shell for regions with different trabeculae diameter (adapted from [42] with permission). The bone displays three loading regimes: linear elasticity (for strains less than 0.05), failure of the trabeculae (for strains between 0.05 and 0.2), and densification of the failed trabeculae (for strains greater than 0.2).

plastic behaviour of the keratinous layer.

In [44], crack propagation through the thickness of the shell was modelled. In particular, the effect of the exterior keratinous and collagenous ‘bilayer’ was investigated. It was found that delamination of the bilayer significantly contributed to the energy dissipation, and hence, fracture toughness of the shell.

Finally, in [32, 35], homogenization simulations were carried out. In [32] the homogenization simulations were used to obtain an effective stiffness for the shell through its thickness, whereas, in [35], homogenization was used to validate a plasticity model for the cancellous bone region.

2.3 Modelling of suture mechanical behaviour

The behaviour of sutures has been characterized using 2D micro-mechanical models [45, 46, 47, 48, 49, 50] and by 2D FE models [51, 24, 52]. Additionally, the effect of sutures on the structures in which they reside has been modelled using FE, albeit to a lesser extent [14, 13].

The micromechanical investigations cited here assume linear material behaviour and, typically, quasistatic loading [45, 46, 47, 48, 49, 50]. In [45], the mechanical behaviour of sutures whose geometry is described by general triangular, rectangular, or trapezoidal wave forms was characterized. In particular, the anisotropy, stiffness, strength, and toughness for tensile and shear loading conditions was investigated. This was done by determining ‘approximate analytical solutions’ for 2D representative volume element (RVE) models obtained by making some simplifying assumptions. The approximate analytical solutions were verified by comparison with FE models. This work was extended in [46] for fractal suture geometries. Similar work was carried out in [53] for irregular suture geometries. However, there, FE models were used exclusively. This allowed for the modelling of the fracture process by using a cohesive model between the suture and adjacent plates as an extension to [45, 46] which only predicted the point at which failure would occur. A similar approach was taken again in [47]. However, in [47] viscoelastic mechanical behaviour and cyclical loading was considered. Finally, in [50], micromechanical models were used to characterize the behaviour of composite structures containing sutural tessellations.

Other models have focused on the effect of sutures on crack propagation [49, 52]. In [49], fracture mechanics was used to determine the conditions under which a crack would propagate through a suture or be diverted in the direction of the suture. In [52], the stress field as a crack traverses along a suture was investigated by developing analytical solutions which were validated using FE simulations.

FE models of a single sutural protrusion have also been used to gain insight into the stress field in the suture region [51, 24]. In [51], the quasistatic behaviour was investigated, and, in [24], cyclical loading and viscoelastic material behaviour was considered.

To a lesser extent, the global effect of sutures has been investigated [14, 13]. In these works, the global effect of sutures was investigated in the skulls of apes and lizards, respectively. In both contributions, all material behaviour was modelled as linear elastic and quasistatic loading was applied to simulate mastication.

Although the current body of literature on the mechanical behaviour of sutures and turtle shells contains numerous valuable contributions, there are still several topics that have not been considered:

- All the modelling of sutures mentioned above are conducted in two dimensions. However, the suture geometry in turtle shells and many other species is notably three-dimensional;

- Only linear material behaviour has been considered; however, sutures typically consist of soft collagenous material which typically displays nonlinear behaviour;

- In addition to nonlinear behaviour, the suture contains aligned collagen fibres suggesting anisotropic behaviour which has typically not been considered;

- Dynamic loading of sutures and their rate-dependent behaviour has typically been investigated under low strain-rate cyclical loading to simulate mastication; however, sutures are ubiquitous in protective structures which ought to sustain high loading rates, such as those arising from predator attacks;

- The few studies of global suture influence only consider simple flat suture geometries.

These points are addressed in this thesis by modelling the effect of sutures on the mechanical behaviour of the turtle shell using mathematical models and numerical methods, such as finite element analysis. The hyperelastic, anisotropic, and rate-dependent behaviour of the suture is modelled. Additionally, the geometric models used are three-dimensional. Investigations are conducted at multiple length-scales during low strain-rate loading, typical of locomotion, and high strain-rate loading, typical of a predator attack.

Chapter 3

Continuum mechanics

In the previous chapter, the physical structure of a turtle shell is introduced. To model the mechanics of a turtle shell – how it deforms and the internal forces it experiences when exposed to external loads – a mathematical framework is required that can quantify deformation and internal forces. The most successful framework for this purpose is continuum mechanics, in which one assumes that the material can be sufficiently described by a continuum instead of a large set of discrete particles (atoms). The continuum approach has a long and successful history of modelling solids and fluids under various loading conditions.

This chapter presents kinematics, the mathematical description of how bodies move and deform. Next, the concept of stress, a measure of the internal forces that a body is experiencing, is presented. Balance laws are then presented, which set out axioms for conservation of quantities such as mass and linear and angular momentum. Finally, the laws of thermodynamics are presented, which are pertinent for the construction of the constitutive models presented in the following chapter. However, the mathematical notation and conventions used in this thesis are first clarified.

3.1 Mathematical notation and conventions

The mathematical notation used in this thesis is outlined briefly here. See Appendix A for a more detailed presentation.

3.1.1 Notation for vectors and tensors

Vectors are denoted by boldface lower-case letters, for example $\boldsymbol{y}$, with the exception of position in the reference configuration (see section 3.2.1) which is denoted by $\boldsymbol{X}$. The components of a vector with respect to a given basis are denoted by omitting the boldface and including the component index in the subscript, for example y_i for component i. Basis vectors are denoted by $\boldsymbol{e}_i$ and an orthonormal basis is used throughout this thesis. The standard tensor product is denoted by $\otimes$; that is,

$$[\boldsymbol{a} \otimes \boldsymbol{b}]\, \boldsymbol{c} = \boldsymbol{a}\, [\boldsymbol{b} \cdot \boldsymbol{c}] \ , \tag{3.1}$$

where $\cdot$ is the dot product. The tensor product is used to create a basis for higher-order tensors using the basis vectors, for example, $\boldsymbol{e}_i \otimes \boldsymbol{e}_j$ is a basis for second-order tensors. Apart from $\boldsymbol{X}$, boldface capital letters denote second-order tensors, $\boldsymbol{B}$ for example. Similarly to vectors, the components of second-order tensors with respected to a given basis are denoted by omitting the boldface and including the indices in the subscript, for example B_{ij}. Blackboard-bold is used to denote fourth-order tensors, for example $\mathbb{C}$. The components of a fourth-order tensor are denoted by including indices in the subscript, for example $\mathbb{C}_{ijkl}$. Additionally, the standard Einsteinian summation convention is adopted for repeated indices.

Two special tensors are used in this thesis: the second-order identity tensor $\boldsymbol{I}$ and the third-order permutation tensor $\boldsymbol{\epsilon}$. The components of the identity tensor are given by the Kronecker delta, that is,

$$\delta_{ij} := \begin{cases} 1 & i = j, \\ 0 & i \neq j, \end{cases} \tag{3.2}$$

and the components of the permutation tensor are given by

$$\epsilon_{ijk} := \begin{cases} +1 & \text{if } (i,j,k) = (1,2,3),\ (3,1,2), (2,3,1)\,, \\ -1 & \text{if } (i,j,k) = (3,2,1),\ (1,3,2), (2,1,3)\,, \\ 0 & \text{if } i = j, j = k, i = k\,. \end{cases} \tag{3.3}$$

3.1.2 Notation for linear algebra operations

The dot product and inner product are denoted by $\boldsymbol{a} \cdot \boldsymbol{b}$ and $\boldsymbol{A} : \boldsymbol{B}$, respectively. The trace, determinant, and Euclidean norm of a tensor are denoted by $\mathrm{tr}\boldsymbol{A}$, $\det \boldsymbol{A}$, and $||\boldsymbol{A}||$, respectively. The cross product of two vectors is denoted by $\boldsymbol{a} \times \boldsymbol{b}$. In what follows, the symmetric tensor product $\odot$ is frequently used; that is,

$$\boldsymbol{A} \odot \boldsymbol{B} = \frac{1}{2} \left[A_{ik}B_{jl} + A_{jk}B_{il}\right] \boldsymbol{e}_i \otimes \boldsymbol{e}_j \otimes \boldsymbol{e}_k \otimes \boldsymbol{e}_l \,. \tag{3.4}$$

3.1.3 Tensor calculus

Partial derivatives with respect to vectors and tensors are defined as follows:

$$\begin{aligned}\frac{\partial a}{\partial \boldsymbol{b}} &:= \frac{\partial a}{\partial b_i}\boldsymbol{e}_i\,, & \frac{\partial \boldsymbol{a}}{\partial \boldsymbol{b}} &:= \frac{\partial a_i}{\partial b_j}\boldsymbol{e}_i \otimes \boldsymbol{e}_j\,,\\ \frac{\partial a}{\partial \boldsymbol{B}} &:= \frac{\partial a}{\partial B_{ij}}\boldsymbol{e}_i \otimes \boldsymbol{e}_j\,, & \frac{\partial \boldsymbol{A}}{\partial \boldsymbol{B}} &:= \frac{\partial A_{ij}}{\partial B_{kl}}\boldsymbol{e}_i \otimes \boldsymbol{e}_j \otimes \boldsymbol{e}_k \otimes \boldsymbol{e}_l\,.\end{aligned} \tag{3.5}$$

Partial derivatives with respect to time are denoted by $\dot{\bullet}$. The partial derivatives of tensors and vectors with respect to time in a Cartesian basis are given, respectively, by

$$\dot{\boldsymbol{A}} := \dot{A}_{ij}\boldsymbol{e}_i \otimes \boldsymbol{e}_j\,, \qquad \dot{\boldsymbol{u}} := \dot{u}_i\boldsymbol{e}_i\,. \tag{3.6}$$

The derivative of a vector with respect to position $\boldsymbol{X}$ is denoted by

$$\mathrm{Grad}\,\boldsymbol{v} := \frac{\partial \boldsymbol{v}}{\partial \boldsymbol{X}}\,. \tag{3.7}$$

The divergence of vectors and tensors in Cartesian coordinates are given, respectively, by

$$\mathrm{Div}\,\boldsymbol{a} := \frac{\partial a_i}{\partial X_i}\,, \qquad \mathrm{Div}\,\boldsymbol{A} := \frac{\partial A_{ij}}{\partial X_j}\boldsymbol{e}_i\,. \tag{3.8}$$

According to Green's theorem, for a region $\Omega_0 \subset \mathbb{R}^3$ which is bounded by the surface Γ_0 with the outward facing unit normal $\boldsymbol{n}_0$ the following holds:

$$\int_{\Omega_0} \boldsymbol{w} \cdot \mathrm{Div}\,\boldsymbol{A}\,\mathrm{d}\Omega_0 = \int_{\Gamma_0} \boldsymbol{w} \cdot \boldsymbol{A}\boldsymbol{n}_0\,\mathrm{d}\Gamma_0 - \int_{\Omega_0} \mathrm{Grad}\,(\boldsymbol{w}) : \boldsymbol{A}\,\mathrm{d}\Omega_0\,. \tag{3.9}$$

3.1.4 Convention for parentheses

For clarity, a convention is adopted whereby rounded parentheses denote arguments of a function and square parentheses denote a coefficient; that is,

$$f\,(x) \tag{3.10}$$

indicates that f is a function of x, whereas

$$f[x] \tag{3.11}$$

denotes f multiplied by x.

3.2 Kinematics

Kinematics is the mathematics of motion. Hence, it provides a framework to quantify the deformation, rotation, and translation of bodies.

3.2.1 The motion

A 3-dimensional body is described in its undeformed configuration[1] at time $t_0 = 0$ by the region $\Omega_0 \subset \mathbb{R}^3$ as illustrated in Figure 3.1. The region is bounded by the surface Γ_0 with an outward unit normal of $\boldsymbol{n}_0$. Each point in the undeformed configuration, $\boldsymbol{X} \in \Omega_0$, is uniquely mapped to a point in the deformed configuration[2], $\boldsymbol{x} \in \Omega \subset \mathbb{R}^3$, at time t by the motion φ; that is,

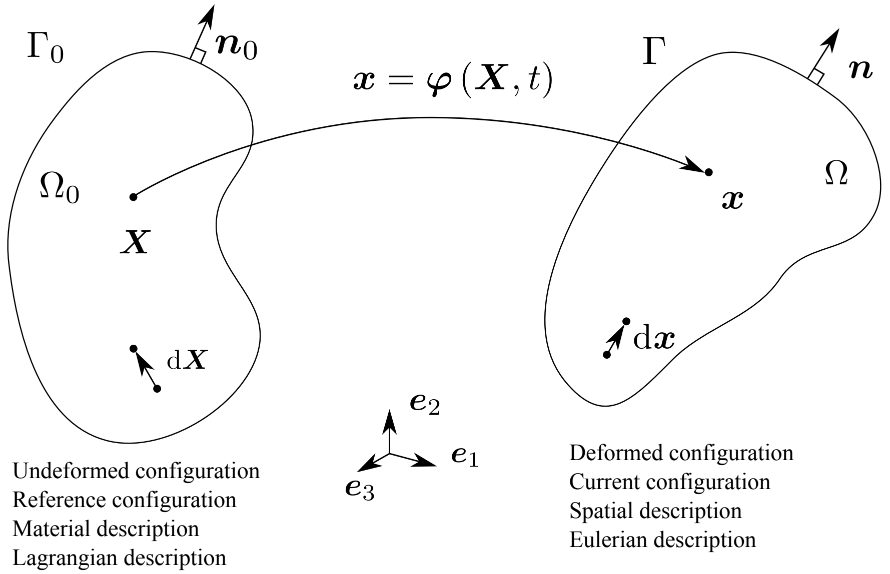

Figure 3.1: Illustration of an arbitrary 3-dimensional body experiencing some motion.

$$\boldsymbol{x} = \varphi(\boldsymbol{X}, t) \ . \tag{3.12}$$

Since the mapping is unique, it is also invertible; that is,

$$\boldsymbol{X} = \varphi^{-1}(\boldsymbol{x}, t) \ . \tag{3.13}$$

The deformed configuration is bounded by the surface Γ with normal $\boldsymbol{n}$. The displacement $\boldsymbol{u}$ is defined as the difference between the current and reference configuration positions; that is,

$$\boldsymbol{u}(\boldsymbol{X}, t) := \boldsymbol{x} - \boldsymbol{X} \ . \tag{3.14}$$

To quantify the deformation, one considers how an infinitesimal line element in the reference configuration $\mathrm{d}\boldsymbol{X}$ is transformed into its current configuration counterpart $\mathrm{d}\boldsymbol{x}$. This is given by

$$\mathrm{d}\boldsymbol{x} = \frac{\partial \varphi}{\partial \boldsymbol{X}} \mathrm{d}\boldsymbol{X} \ . \tag{3.15}$$

---

[1] Also commonly referred to as the reference configuration, material description or Lagrangian description.

[2] Also commonly referred to as the current configuration, spatial description or Eulerian description.

Hence it is useful to define the deformation gradient $\boldsymbol{F}$ as

$$\boldsymbol{F} := \frac{\partial \varphi}{\partial \boldsymbol{X}} = \frac{\partial \boldsymbol{x}}{\partial \boldsymbol{X}}\,, \qquad \mathrm{d}\boldsymbol{x} = \boldsymbol{F}\mathrm{d}\boldsymbol{X}\,. \tag{3.16}$$

Due to the invertibility of φ, the inverse of the deformation gradient exists and is given by

$$\boldsymbol{F}^{-1} = \frac{\partial \varphi^{-1}}{\partial \boldsymbol{x}} = \frac{\partial \boldsymbol{X}}{\partial \boldsymbol{x}}\,, \qquad \mathrm{d}\boldsymbol{X} = \boldsymbol{F}^{-1}\mathrm{d}\boldsymbol{x}\,. \tag{3.17}$$

In what follows, the gradient of quantities in the reference and current configuration is frequently utilised. Hence, the reference and current configuration gradient operators are defined, respectively, as

$$\mathrm{Grad}\bullet := \frac{\partial \bullet}{\partial \boldsymbol{X}}\,, \qquad \mathrm{grad}\bullet := \frac{\partial \bullet}{\partial \boldsymbol{x}}\,. \tag{3.18}$$

Using the definition of the displacement and the deformation gradient, equations (3.14) and (3.16), respectively, one can obtain the following expression for the deformation gradient:

$$\boldsymbol{F} = \boldsymbol{I} + \mathrm{Grad}\boldsymbol{u}\,. \tag{3.19}$$

Using the chain rule one can obtain a useful identity which relates the reference and current configuration gradient operators; that is,

$$\mathrm{Grad}\bullet = \frac{\partial \bullet}{\partial \boldsymbol{X}} = \frac{\partial \bullet}{\partial \boldsymbol{x}}\frac{\partial \boldsymbol{x}}{\partial \boldsymbol{X}} = \mathrm{grad}\,(\bullet)\,\boldsymbol{F}\,. \tag{3.20}$$

The divergence operator is also frequently used. This is defined in the reference and current configuration, respectively, for vectors as

$$\mathrm{Div}\,\bullet := \frac{\partial \bullet_i}{\partial X_i}\,, \qquad \mathrm{div}\,\bullet := \frac{\partial \bullet_i}{\partial x_i}\,, \tag{3.21}$$

and second-order tensors as

$$\mathrm{Div}\,\bullet = \frac{\partial \bullet_{ij}}{\partial X_j}\boldsymbol{e}_i\,, \qquad \mathrm{div}\,\bullet = \frac{\partial \bullet_{ij}}{\partial x_j}\boldsymbol{e}_i\,. \tag{3.22}$$

Using these definitions, Green's theorem, stated in equation (3.9), may be rephrased in the current configuration as

$$\int_\Omega \boldsymbol{w} \cdot \mathrm{div}\,\boldsymbol{A}\,\mathrm{d}\Omega = \int_\Gamma \boldsymbol{w} \cdot \boldsymbol{A}\boldsymbol{n}\,\mathrm{d}\Gamma - \int_\Omega \mathrm{grad}\;(\boldsymbol{w}) : \boldsymbol{A}\,\mathrm{d}\Omega\,. \tag{3.23}$$

3.2.2 Deformation quantities

To obtain a mathematical description of deformation, one considers how the length of a line element in the reference configuration is related to its image in the current configuration; that is,

$$||\mathrm{d}\boldsymbol{x}||^2 = \mathrm{d}\boldsymbol{x}^T\mathrm{d}\boldsymbol{x} = \mathrm{d}\boldsymbol{X}^T\boldsymbol{F}^T\boldsymbol{F}\mathrm{d}\boldsymbol{X}\,. \tag{3.24}$$

Hence, the right Cauchy-Green tensor $\boldsymbol{C}$ is defined as

$$\boldsymbol{C} := \boldsymbol{F}^T\boldsymbol{F}\,, \qquad ||\mathrm{d}\boldsymbol{x}||^2 = \mathrm{d}\boldsymbol{X}\cdot\boldsymbol{C}\mathrm{d}\boldsymbol{X}\,. \tag{3.25}$$

Similarly, relating the reference configuration length to the current motivates the definition of the left Cauchy-Green tensor $\boldsymbol{B}$; that is,

$$||\mathrm{d}\boldsymbol{X}||^2 = \mathrm{d}\boldsymbol{X}^T\mathrm{d}\boldsymbol{X} = \mathrm{d}\boldsymbol{x}^T\boldsymbol{F}^{-T}\boldsymbol{F}^{-1}\mathrm{d}\boldsymbol{x} = \mathrm{d}\boldsymbol{x}^T\boldsymbol{B}^{-1}\mathrm{d}\boldsymbol{x}\,, \qquad \boldsymbol{B} := \boldsymbol{F}\boldsymbol{F}^T\,. \tag{3.26}$$

Clearly, both the left and right Cauchy-Green tensors are symmetric. By considering the difference in length between the reference and current configuration line elements, one obtains

$$\frac{1}{2}\left[\mathrm{d}\boldsymbol{x}\cdot\mathrm{d}\boldsymbol{x} - \mathrm{d}\boldsymbol{X}\cdot\mathrm{d}\boldsymbol{X}\right] = \mathrm{d}\boldsymbol{X}\cdot\frac{1}{2}\left[\boldsymbol{C}-\boldsymbol{I}\right]\mathrm{d}\boldsymbol{X}\,. \tag{3.27}$$

This motivates the definition of the Green-Lagrange strain $\boldsymbol{E}$ as a measure of deformation; that is,

$$\boldsymbol{E} := \frac{1}{2}\left[\boldsymbol{C}-\boldsymbol{I}\right]\,, \tag{3.28}$$

which is also symmetric. Using the expression for the deformation gradient in equation (3.19), an alternative expression for $\boldsymbol{E}$ can be obtained; that is,

$$\boldsymbol{E} = \frac{1}{2}\left[\mathrm{Grad}\boldsymbol{u} + \mathrm{Grad}\boldsymbol{u}^T + \mathrm{Grad}\boldsymbol{u}^T\mathrm{Grad}\boldsymbol{u}\right]\,. \tag{3.29}$$

For small deformations, $||\mathrm{Grad}\boldsymbol{u}^T\mathrm{Grad}\boldsymbol{u}|| << ||\mathrm{Grad}\boldsymbol{u}||$, the Green-Lagrange strain can be approximated by the linear strain $\boldsymbol{\varepsilon}$; that is,

$$\boldsymbol{E} \approx \boldsymbol{\varepsilon} := \frac{1}{2}\left[\mathrm{Grad}\boldsymbol{u} + \mathrm{Grad}\boldsymbol{u}^T\right]\,. \tag{3.30}$$

3.2.3 Volume change

Consider an infinitesimally small parallelepiped in the reference configuration described by the edge vectors $\mathrm{d}\boldsymbol{X}_i$ $i = 1, 2, 3$, which are defined as

$$(\text{no sum}) \qquad \mathrm{d}\boldsymbol{X}_i = \boldsymbol{e}_i\mathrm{d}X_i\,. \tag{3.31}$$

The volume of the parallelepiped is given by

$$\mathrm{d}\Omega_0 = \mathrm{d}\boldsymbol{X}_1 \cdot \mathrm{d}\boldsymbol{X}_2 \times \mathrm{d}\boldsymbol{X}_3 = \mathrm{d}X_1 \mathrm{d}X_2 \mathrm{d}X_3 \,. \tag{3.32}$$

In the current configuration, each edge vector is described by

$$(\text{no sum}) \qquad \mathrm{d}\boldsymbol{x}_i = \boldsymbol{F}\mathrm{d}\boldsymbol{X}_i = \frac{\partial \boldsymbol{x}}{\partial X_i}\mathrm{d}X_i \,. \tag{3.33}$$

Then, the volume of the parallelepiped in the current configuration is given by

$$\mathrm{d}\Omega = \mathrm{d}\boldsymbol{x}_1 \cdot \mathrm{d}\boldsymbol{x}_2 \times \mathrm{d}\boldsymbol{x}_3 = \frac{\partial x_i}{\partial X_1}\mathrm{d}X_1 \frac{\partial x_j}{\partial X_2}\mathrm{d}X_2 \frac{\partial x_k}{\partial X_3}\mathrm{d}X_3 \epsilon_{ijk} = F_{i1}F_{j2}F_{k3}\epsilon_{ijk}\mathrm{d}X_1\mathrm{d}X_2\mathrm{d}X_3 \,. \tag{3.34}$$

Noting that the determinant of the deformation gradient is given by

$$\det \boldsymbol{F} = F_{i1}F_{j2}F_{k3}\epsilon_{ijk} \,, \tag{3.35}$$

motivates the definition of the volumetric Jacobian J (Jacobian, for short) as

$$J := \det \boldsymbol{F} \tag{3.36}$$

so that

$$\mathrm{d}\Omega = J \mathrm{d}\Omega_0 \,. \tag{3.37}$$

For a motion to be physically consistent, every infinitesimal volume in a body must be positive in both the reference and current configuration. Thus, it is required that

$$J > 0 \,. \tag{3.38}$$

3.2.4 Isochoric-volumetric decomposition

When dealing with bodies that are modelled as incompressible or nearly so (see Sections 4.1.2 and 4.1.3, respectively), it is convenient to decompose the motion into two parts: an isochoric and a volumetric part. Since the isochoric deformation gradient $\bar{\boldsymbol{F}}$ is volume preserving, it has a determinant of 1; that is,

$$\det \bar{\boldsymbol{F}} = 1 \,. \tag{3.39}$$

This is achieved by defining the isochoric deformation gradient as

$$\bar{\boldsymbol{F}} := J^{-1/3}\boldsymbol{F} \,. \tag{3.40}$$

The volumetric deformation gradient $\boldsymbol{F}_{vol}$ must make up the remainder of the deformation so that

$$\boldsymbol{F} = \boldsymbol{F}_{vol}\bar{\boldsymbol{F}} \,. \tag{3.41}$$

Hence, the volumetric deformation gradient is given by

$$\boldsymbol{F}_{vol} = \boldsymbol{F}\bar{\boldsymbol{F}}^{-1} = J^{1/3}\boldsymbol{I}\,, \tag{3.42}$$

and captures the entirety of the Jacobian; that is,

$$\det \boldsymbol{F}_{vol} = J\,. \tag{3.43}$$

It is useful to define an isochoric right and left Cauchy-Green tensor, respectively, as

$$\bar{\boldsymbol{C}} := \bar{\boldsymbol{F}}^T\bar{\boldsymbol{F}}\,, \qquad \bar{\boldsymbol{B}} := \bar{\boldsymbol{F}}\bar{\boldsymbol{F}}^T\,. \tag{3.44}$$

In what follows, $\bar{\bullet}$ denotes quantities that result from the isochoric part of the deformation and $\bullet_{vol}$ denotes quantities that result from the volumetric part of the deformation.

3.2.5 Rate of deformation

To determine useful descriptions of the rate of deformation, one begins with the rate of displacement $\boldsymbol{v}$, referred to as velocity; that is,

$$\boldsymbol{v}\left(\boldsymbol{x},\, t\right) = \dot{\boldsymbol{u}}\,. \tag{3.45}$$

The velocity gradient is defined as the current configuration gradient of the velocity; that is,

$$\boldsymbol{L} := \operatorname{grad}\boldsymbol{v}\,. \tag{3.46}$$

By using the identity in equation (3.20) one can obtain

$$\boldsymbol{L} = \operatorname{Grad}\left(\boldsymbol{v}\right)\boldsymbol{F}^{-1}\,. \tag{3.47}$$

Furthermore, the rate of the deformation gradient is given by

$$\dot{\boldsymbol{F}} = \frac{\partial}{\partial t}\left[\boldsymbol{I} + \mathrm{Grad}\boldsymbol{u}\right] = \mathrm{Grad}\boldsymbol{v}\,, \tag{3.48}$$

and so the velocity gradient can also be calculated using

$$\boldsymbol{L} = \dot{\boldsymbol{F}}\boldsymbol{F}^{-1}\,. \tag{3.49}$$

The symmetric and antisymmetric parts of the velocity gradient are referred to as the rate of deformation $\boldsymbol{D}$ and spin $\boldsymbol{W}$ tensors, respectively; that is,

$$\boldsymbol{D} = \frac{1}{2}\left[\boldsymbol{L} + \boldsymbol{L}^T\right]\,, \qquad \boldsymbol{W} = \frac{1}{2}\left[\boldsymbol{L} - \boldsymbol{L}^T\right]\,, \qquad \boldsymbol{L} = \boldsymbol{D} + \boldsymbol{W}\,. \tag{3.50}$$

The rate of the Green-Lagrange strain is given by

$$\dot{\boldsymbol{E}} = \frac{1}{2}\frac{\partial}{\partial t}\left[\boldsymbol{F}^T\boldsymbol{F} - \boldsymbol{I}\right] = \frac{1}{2}\left[\dot{\boldsymbol{F}}^T\boldsymbol{F} + \boldsymbol{F}^T\dot{\boldsymbol{F}}\right]. \tag{3.51}$$

Hence, using equation (3.49) and (3.50) one can obtain the relation between the rate of the Green-Lagrange strain and the rate of deformation tensor; that is,

$$\dot{\boldsymbol{E}} = \boldsymbol{F}^T\boldsymbol{D}\boldsymbol{F}. \tag{3.52}$$

It is useful to have an expression for $\dot{\boldsymbol{F}}^{-1}$ in terms of $\boldsymbol{L}$. This is obtained by taking the time-derivative of the deformation gradient multiplied by its inverse; that is,

$$\dot{\boldsymbol{I}} = \boldsymbol{0} = \frac{\partial}{\partial t}\left[\boldsymbol{F}\boldsymbol{F}^{-1}\right] = \dot{\boldsymbol{F}}\boldsymbol{F}^{-1} + \boldsymbol{F}\dot{\boldsymbol{F}}^{-1}. \tag{3.53}$$

By rearranging one obtains

$$\dot{\boldsymbol{F}}^{-1} = -\boldsymbol{F}^{-1}\dot{\boldsymbol{F}}\boldsymbol{F}^{-1} = -\boldsymbol{F}^{-1}\boldsymbol{L}. \tag{3.54}$$

3.3 Stress

The deformation of a body results in the generation of internal forces. The state of these internal forces is described through the stress tensor; that is, a tensor which maps a given normal direction to an internal traction.

3.3.1 Stress quantities

The Cauchy Stress

Consider a body in the current configuration split into two parts as shown in Figure 3.2. On

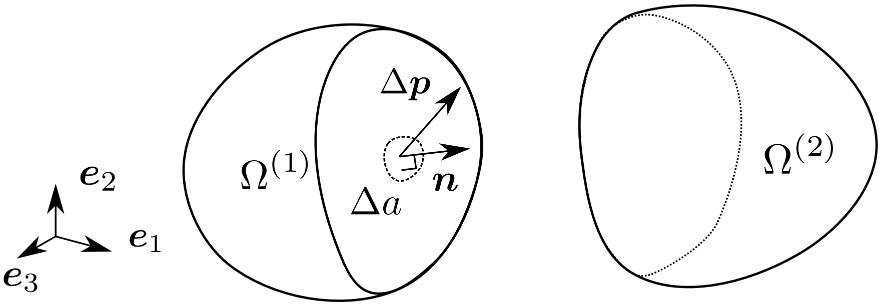

Figure 3.2: Schematic diagram of a body split into two, displaying the internal forces of the body.

the internal surface of $\Omega^{(1)}$ a force, $\Delta\boldsymbol{p}$, acts on a small area of the surface Δa. The current traction, $\boldsymbol{t}$, is defined as the force acting on a surface per unit infinitesimal area; that is,

$$\boldsymbol{t}(\boldsymbol{n}) := \lim_{\Delta a \to 0} \frac{1}{\Delta a} \Delta \boldsymbol{p}. \tag{3.55}$$

Naturally, this traction is dependent on the orientation of the cross-section of the body. This orientation can be described by the normal vector of the surface, $\boldsymbol{n}$. Cauchy's theorem states that there exists a second-order tensor, $\boldsymbol{\sigma}$, that relates the chosen normal vector to the current traction, that is,

$$\boldsymbol{t} = \boldsymbol{\sigma}\boldsymbol{n}, \tag{3.56}$$

where $\boldsymbol{\sigma}$ is the Cauchy stress. The Cauchy stress is also known as the true stress.

The first Piola-Kirchhoff stress

Now, consider a reference traction, $\boldsymbol{t}_0$, that is defined using the same force as the current traction, but is defined per unit infinitesimal area in the reference configuration Δa_0; that is,

$$\boldsymbol{t}_0(\boldsymbol{n}_0) := \lim_{\Delta a_0 \to 0} \frac{1}{\Delta a_0} \Delta \boldsymbol{p}, \tag{3.57}$$

where $\boldsymbol{n}_0$ is the reference configuration counterpart of $\boldsymbol{n}$. The first Piola-Kirchhoff stress, $\boldsymbol{P}$, is a second order tensor defined such that

$$\boldsymbol{t}_0 = \boldsymbol{P}\boldsymbol{n}_0. \tag{3.58}$$

Note that the current and reference tractions are related by

$$\boldsymbol{t}_0(\boldsymbol{n}_0)\mathrm{d}a_0 = \boldsymbol{t}(\boldsymbol{n})\mathrm{d}a. \tag{3.59}$$

This relationship can be used to relate $\boldsymbol{P}$ and $\boldsymbol{\sigma}$ according to

$$\boldsymbol{P}\boldsymbol{n}_0\mathrm{d}a_0 = \boldsymbol{\sigma}\boldsymbol{n}\mathrm{d}a. \tag{3.60}$$

Nanson's formula relates an infinitesimal area in the current configuration to its reference configuration counterpart by

$$J\boldsymbol{F}^{-T}\boldsymbol{n}_0\mathrm{d}a_0 = \boldsymbol{n}\mathrm{d}a. \tag{3.61}$$

Substitution of this relationship into (3.60) gives

$$\boldsymbol{P}\boldsymbol{n}_0\mathrm{d}a_0 = J\boldsymbol{\sigma}\boldsymbol{F}^{-T}\boldsymbol{n}_0\mathrm{d}a_0. \tag{3.62}$$

This expression must hold for all $\boldsymbol{n}_0$. Hence, $\boldsymbol{\sigma}$ is related to $\boldsymbol{P}$ by

$$\boldsymbol{\sigma} = J^{-1}\boldsymbol{P}\boldsymbol{F}^{T}. \tag{3.63}$$

The Second Piola-Kirchhoff Stress

Another traction term $\hat{\boldsymbol{t}}_0(\boldsymbol{n}_0)$ can be created by pulling back the force and dividing by the reference area; that is,

$$\hat{\boldsymbol{t}}_0(\boldsymbol{n}_0) := \lim_{\Delta a_0 \to 0} \frac{1}{\Delta a_0} \boldsymbol{F}^{-1} \Delta \boldsymbol{p}. \tag{3.64}$$

The second Piola-Kirchhoff stress, $\boldsymbol{S}$, is then defined such that

$$\hat{\boldsymbol{t}}_0 = \boldsymbol{S}\boldsymbol{n}_0. \tag{3.65}$$

Note that $\hat{\boldsymbol{t}}_0(\boldsymbol{n}_0)$ is related to $\boldsymbol{t}_0(\boldsymbol{n}_0)$ by

$$\hat{\boldsymbol{t}}_0(\boldsymbol{n}_0) = \boldsymbol{F}^{-1}\boldsymbol{t}_0(\boldsymbol{n}_0). \tag{3.66}$$

Hence, by applying similar arguments to the ones relating $\boldsymbol{\sigma}$ to $\boldsymbol{P}$, it can be shown that

$$\boldsymbol{P} = \boldsymbol{F}\boldsymbol{S}. \tag{3.67}$$

The second Piola-Kirchhoff stress does not have an obvious physical interpretation. However, it is work conjugate to the commonly used strain measure $\dot{\boldsymbol{E}}$ (see section 3.6) and it is a useful quantity for defining rate-dependent material behaviour as it is *a priori* objective, which is shown in the following subsection.

The Kirchhoff Stress

Another commonly used stress measure is the Kirchhoff stress, which is defined as

$$\boldsymbol{\tau} := J\boldsymbol{\sigma}. \tag{3.68}$$

Hence, the Kirchhoff stress scales the Cauchy stress by the volume change. The Kirchhoff stress is work conjugate to the rate of deformation tensor $\boldsymbol{D}$ (see section 3.6). Finally, note that the stress measures introduced here are related to each other by

$$\boldsymbol{\sigma} = J^{-1}\boldsymbol{\tau} = J^{-1}\boldsymbol{F}\boldsymbol{S}\boldsymbol{F}^T = J^{-1}\boldsymbol{P}\boldsymbol{F}^T. \tag{3.69}$$

3.3.2 Stress objectivity

One of the axioms considered when constructing constitutive relations is material objectivity; that is, a constitutive relation should be unaffected by the choice of observer or reference frame. The effect of a different choice of reference frame may be equivalently represented by a rigid body motion that takes $\boldsymbol{x}$ to a position in a different reference frame $\tilde{\boldsymbol{x}}$ according to the transformation [54]

$$\tilde{\boldsymbol{x}}\,(t) = \boldsymbol{c}\,(t) + \boldsymbol{Q}\,(t)\,\boldsymbol{x}\,, \tag{3.70}$$

where $\boldsymbol{c}$ represents translation and $\boldsymbol{Q}$ represents rotation; that is,

$$\boldsymbol{Q}^T = \boldsymbol{Q}^{-1}\,, \qquad \det \boldsymbol{Q} = +1\,. \tag{3.71}$$

Here, $\tilde{\bullet}$ denotes a quantity represented in a different reference frame. The deformation gradient after rigid body motion is applied is given by

$$\tilde{\boldsymbol{F}} = \boldsymbol{Q}\boldsymbol{F}\,. \tag{3.72}$$

Additionally, the current configuration traction and a normal after rigid body motion has been applied are given, respectively, by

$$\tilde{\boldsymbol{t}} = \boldsymbol{Q}\boldsymbol{t}\,, \qquad \tilde{\boldsymbol{n}} = \boldsymbol{Q}\boldsymbol{n}\,. \tag{3.73}$$

Since the Cauchy stress is given by $\boldsymbol{\sigma} = \boldsymbol{t} \otimes \boldsymbol{n}$, one obtains the constraint

$$\tilde{\boldsymbol{\sigma}} = [\boldsymbol{Q}\boldsymbol{t}] \otimes [\boldsymbol{Q}\boldsymbol{n}] = \boldsymbol{Q}\,[\boldsymbol{t} \otimes \boldsymbol{n}]\,\boldsymbol{Q}^T = \boldsymbol{Q}\boldsymbol{\sigma}\boldsymbol{Q}^T\,. \tag{3.74}$$

Hence, constitutive laws must satisfy the constraint

$$\boldsymbol{\sigma}\left(\boldsymbol{Q}\boldsymbol{F}\right) = \boldsymbol{Q}\boldsymbol{\sigma}\left(\boldsymbol{F}\right)\boldsymbol{Q}^T\,. \tag{3.75}$$

For this reason, second-order tensors that satisfy

$$\tilde{\bullet} = \boldsymbol{Q} \bullet \boldsymbol{Q}^T \tag{3.76}$$

are termed “objective” and tensors that satisfy

$$\tilde{\bullet} = \bullet \tag{3.77}$$

are “*a priori* objective”. Note that the second Piola-Kirchhoff stress is *a priori* objective,

$$\tilde{\boldsymbol{S}} = J^{-1}\tilde{\boldsymbol{F}}^{-1}\tilde{\boldsymbol{\sigma}}\tilde{\boldsymbol{F}}^{-T} = J^{-1}\tilde{\boldsymbol{F}}^{-1}\boldsymbol{Q}\boldsymbol{\sigma}\boldsymbol{Q}^T\tilde{\boldsymbol{F}}^{-T} = J^{-1}\boldsymbol{F}^{-1}\boldsymbol{\sigma}\boldsymbol{F}^{-T} = \boldsymbol{S}\,. \tag{3.78}$$

Rate-dependent materials are often better suited for implementation in rate form (see Section 3.3.3). However, in creating rate forms of constitutive laws, it is imperative to first determine objective stress rates. Since the second Piola-Kirchhoff stress is *a priori* objective, its rate is also objective; that is,

$$\dot{\tilde{\boldsymbol{S}}} = \dot{\boldsymbol{S}}\,. \tag{3.79}$$

However, although the Cauchy stress is objective, it is not *a priori* objective, and so its rate is not objective; that is,

$$\dot{\tilde{\boldsymbol{\sigma}}} = \dot{\boldsymbol{Q}}\boldsymbol{\sigma}\boldsymbol{Q}^T + \boldsymbol{Q}\dot{\boldsymbol{\sigma}}\boldsymbol{Q}^T + \boldsymbol{Q}\boldsymbol{\sigma}\dot{\boldsymbol{Q}}^T\,. \tag{3.80}$$

An objective rate of the Kirchhoff stress can be obtained by applying a push-forward operation to the rate of the second Piola-Kirchhoff stress as follows:

$$\begin{aligned}\boldsymbol{F}\dot{\boldsymbol{S}}\boldsymbol{F}^T &= \boldsymbol{F}\frac{\partial}{\partial t}\left[\boldsymbol{F}^{-1}\boldsymbol{\tau}\boldsymbol{F}^{-T}\right]\boldsymbol{F}^T \\ &= \boldsymbol{F}\left[\boldsymbol{F}^{-1}\dot{\boldsymbol{\tau}}\boldsymbol{F}^{-T} + \dot{\boldsymbol{F}}^{-1}\boldsymbol{\tau}\boldsymbol{F}^{-T} + \boldsymbol{F}^{-1}\boldsymbol{\tau}\dot{\boldsymbol{F}}^{-T}\right]\boldsymbol{F}^T \\ &= \boldsymbol{F}\left[\boldsymbol{F}^{-1}\dot{\boldsymbol{\tau}}\boldsymbol{F}^{-T} - \boldsymbol{F}^{-1}\boldsymbol{L}\boldsymbol{\tau}\boldsymbol{F}^{-T} - \boldsymbol{F}^{-1}\boldsymbol{\tau}\boldsymbol{L}^T\boldsymbol{F}^{-T}\right]\boldsymbol{F}^T \\ &= \dot{\boldsymbol{\tau}} - \boldsymbol{L}\boldsymbol{\tau} - \boldsymbol{\tau}\boldsymbol{L}^T\,.\end{aligned} \tag{3.81}$$

This motivates the definition of the Lie derivative of the Kirchhoff stress; that is,

$$\mathcal{L}\left(\boldsymbol{\tau}\right) := \dot{\boldsymbol{\tau}} - \boldsymbol{L}\boldsymbol{\tau} - \boldsymbol{\tau}\boldsymbol{L}^T\,. \tag{3.82}$$

The objectivity of this stress rate can be verified as follows:

$$\mathcal{L}\left(\tilde{\boldsymbol{\tau}}\right) = \tilde{\boldsymbol{F}}\dot{\tilde{\boldsymbol{S}}}\tilde{\boldsymbol{F}}^T = \boldsymbol{Q}\boldsymbol{F}\dot{\boldsymbol{S}}\boldsymbol{F}^T\boldsymbol{Q}^T = \boldsymbol{Q}\mathcal{L}\left(\boldsymbol{\tau}\right)\boldsymbol{Q}^T\,. \tag{3.83}$$

Hence, the stress rate is objective by analogy with equation (3.77). Another frequently used objective stress rate is the Jaumann rate of the Kirchhoff stress; that is,

$$\boldsymbol{\tau}^{\nabla} = \dot{\boldsymbol{\tau}} + \boldsymbol{\tau}\boldsymbol{W} - \boldsymbol{W}\boldsymbol{\tau}\,. \tag{3.84}$$

This stress rate is of importance when implementing constitutive models in Abaqus as presented in the following subsection.

3.3.3 Rate form and stress tangents

For many materials, particularly path- and rate-dependent ones, it may be convenient to represent the constitutive relation by relating the strain rate to the stress rate; that is,

$$\dot{\boldsymbol{S}} = \mathbb{C}\dot{\boldsymbol{E}}\,, \qquad \mathbb{C} := \frac{\partial \boldsymbol{S}}{\partial \boldsymbol{E}}\,. \tag{3.85}$$

Here, $\mathbb{C}$ is termed the reference configuration constitutive tensor[3]. Constitutive tensors are also crucial for determining the stiffness matrix when using the Finite Element Method (FEM) and so they are of interest even for path-independent materials. It is most convenient to begin with the reference configuration stress and strain rates $\dot{\boldsymbol{S}}$ and $\dot{\boldsymbol{E}}$, respectively, as they are *a priori* objective and work conjugate (see Section 3.6).

---

[3] Also commonly referred to as the stress tangent, stiffness or, in the case of pure elasticity, the elasticity tensor.

To determine useful current configuration constitutive tensors, the relation between the Lie derivative of the Kirchhoff stress and the rate of the second Piola-Kirchhoff stress is developed as follows:

$$\mathcal{L}(\boldsymbol{\tau}) = \boldsymbol{F}\dot{\boldsymbol{S}}\boldsymbol{F}^T = \boldsymbol{F}\left[\mathbb{C}\dot{\boldsymbol{E}}\right]\boldsymbol{F}^T = \boldsymbol{F}\left[\mathbb{C}\left[\boldsymbol{F}^T\boldsymbol{D}\boldsymbol{F}\right]\right]\boldsymbol{F}^T\,. \tag{3.86}$$

In index notation, the term on the right-hand side is

$$F_{iI}\left[\mathbb{C}_{IJKL}F_{kK}D_{kl}F_{lL}\right]F_{jJ} = \mathbb{C}_{IJKL}F_{iI}F_{jJ}F_{kK}F_{lL}D_{kl}\,. \tag{3.87}$$

Hence, the Lie constitutive tensor is defined as

$$\mathbbm{c}_{ijkl} := \mathbb{C}_{IJKL}F_{iI}F_{jJ}F_{kK}F_{lL}\,. \tag{3.88}$$

It is then apparent that the Lie rate of the Kirchhoff stress is related to the rate of deformation tensor by

$$\mathcal{L}(\boldsymbol{\tau}) = \dot{\boldsymbol{\tau}} - \boldsymbol{L}\boldsymbol{\tau} - \boldsymbol{\tau}\boldsymbol{L}^T = \mathbbm{c}\boldsymbol{D}\,. \tag{3.89}$$

To obtain a similar constitutive tensor for the Jaumann rate of the Kirchhoff stress, note first that

$$\boldsymbol{\tau}^{\nabla} = \mathcal{L}(\boldsymbol{\tau}) + \boldsymbol{D}\boldsymbol{\tau} + \boldsymbol{\tau}\boldsymbol{D} = \mathcal{L}(\boldsymbol{\tau}) + \left[\boldsymbol{I}\odot\boldsymbol{\tau} + \boldsymbol{\tau}\odot\boldsymbol{I}\right]\boldsymbol{D}\,. \tag{3.90}$$

Hence, the Jaumann constitutive tensor is defined as

$$\mathbbm{c}^{\nabla} := \mathbbm{c} + \boldsymbol{I}\odot\boldsymbol{\tau} + \boldsymbol{\tau}\odot\boldsymbol{I}\,, \tag{3.91}$$

and so the Jaumann rate of the Kirchhoff stress is related to the rate of deformation tensor by

$$\boldsymbol{\tau}^{\nabla} = \dot{\boldsymbol{\tau}} - \boldsymbol{W}\boldsymbol{\tau} - \boldsymbol{\tau}\boldsymbol{W}^T = \mathbbm{c}^{\nabla}\boldsymbol{D}\,. \tag{3.92}$$

When writing a user material subroutine (UMAT) for the finite element analysis software ABAQUS, the user is required to provide the constitutive tensor

$$\mathbbm{c}_{\text{ABAQUS}} = J^{-1}\mathbbm{c}^{\nabla}\,, \tag{3.93}$$

as well as the Cauchy stress.

3.4 Balance laws

Balance laws set out axiomatic assumptions about the basis of mechanical response. These laws result in a set of equations which are required to model the mechanical behaviour of continua. See [55, 56, 57, 54] for a more detailed discussion on the balance laws.

3.4.1 Balance of mass

The law of balance of mass states that the mass of a body at any point in time m is equal to the initial mass m_0. This allows for derivation of the pointwise balance of mass equation [55, 56, 57, 54]; that is,

$$\dot{\rho} + \mathrm{div}(\rho \boldsymbol{v}) = 0\,. \tag{3.94}$$

3.4.2 Balance of linear momentum

The balance of linear momentum states that the rate of change of momentum of a body is equal to the sum of the external forces acting on that body. This results in the pointwise balance of linear momentum equation [55, 56, 57, 54]; that is,

$$\rho \dot{\boldsymbol{v}} = \mathrm{div}\boldsymbol{\sigma} + \boldsymbol{g}\,. \tag{3.95}$$

3.4.3 Balance of angular momentum

The balance of angular momentum states that the rate of change of angular momentum of a body is equal to the sum of moments acting on that body. This results in the symmetry of the Cauchy stress [55, 56, 57, 54]; that is,

$$\boldsymbol{\sigma} = \boldsymbol{\sigma}^T\,. \tag{3.96}$$

As a result, the Kirchhoff and second Piola-Kirchhoff stresses are also symmetric; that is,

$$\boldsymbol{\tau}^T = \boldsymbol{\tau}\,, \qquad \boldsymbol{S}^T = \boldsymbol{S}\,. \tag{3.97}$$

However, the first Piola-Kirchhoff stress is not symmetric:

$$\boldsymbol{P}^T = \boldsymbol{S}\boldsymbol{F}^T \neq \boldsymbol{F}\boldsymbol{S} = \boldsymbol{P}\,. \tag{3.98}$$

3.5 Thermodynamic laws

Thermodynamic laws create constraints on the construction of constitutive models. These are presented here. See [55, 56, 57, 54] for a more detailed discussion on the laws of thermodynamics.

3.5.1 First law of thermodynamics: balance of energy

The first law of thermodynamics, the balance of energy, states that the rate of change of energy contained in a body is equal to the sum of the mechanical power due to external loads and the heat supply. The pointwise balance of energy under isothermal conditions is then given by [55, 56, 57, 54]

$$\dot{u} = \boldsymbol{\sigma} : \boldsymbol{D} \, . \tag{3.99}$$

Here, u is the internal energy per unit volume in the current configuration. This can be converted to the internal energy per unit reference configuration volume U by using the Jacobian; that is,

$$\dot{U} = J\boldsymbol{\sigma} : \boldsymbol{D} = \boldsymbol{\tau} : \boldsymbol{D} \, . \tag{3.100}$$

Then $\boldsymbol{\tau}$ and $\boldsymbol{D}$ are referred to as a work conjugate pair (see Section 3.6 for more on this). The internal energy is given by

$$U = T\eta + \Psi \, , \tag{3.101}$$

where T is temperature, η is entropy, and Ψ is the Helmholtz free energy per unit reference configuration volume.

3.5.2 Second law of thermodynamics: entropy inequality principle

The second law of thermodynamics states that the total production of entropy in a body is never negative. By considering that heat flows from high temperatures to low temperatures and by using equation (3.101) and the first law of thermodynamics (equation (3.100)), one may obtain a stronger form of the entropy inequality principal, that is, the Clausius-Duhem inequality [55, 56, 57, 54]. For isothermal problems, the Clausius-Duhem inequality reduces to

$$D_{\text{int}} = \boldsymbol{\tau} : \boldsymbol{D} - \dot{\Psi} \geq 0 \, . \tag{3.102}$$

Here, D_{int} is the rate of dissipation per unit reference configuration volume.

3.6 Work conjugacy

Specific stress power is given by [55, 56, 57, 54]

$$\dot{W}_{\text{int}} = J\boldsymbol{\sigma} : \boldsymbol{D} = \boldsymbol{\tau} : \boldsymbol{D} \, . \tag{3.103}$$

One then uses the terminology that the stress quantity $\boldsymbol{\tau}$ is work conjugate to the kinematic quantity $\boldsymbol{D}$, or that these quantities are work conjugate pairs. To identify a work conjugate pair using reference configuration quantities, equation (3.103) is developed as follows:

$$\begin{aligned}\dot{W}_{\text{int}} &= \boldsymbol{\tau} : \boldsymbol{D} \\ &= \boldsymbol{F}\boldsymbol{S}\boldsymbol{F}^T : \boldsymbol{D} \\ &= F_{iI}S_{IJ}F_{jJ}D_{ij} \\ &= S_{IJ}F_{iI}D_{ij}F_{jJ} \\ &= \boldsymbol{S} : \boldsymbol{F}^T\boldsymbol{D}\boldsymbol{F} \\ &= \boldsymbol{S} : \dot{\boldsymbol{E}}\,.\end{aligned} \tag{3.104}$$

Hence, $\boldsymbol{S}$ is work conjugate to $\dot{\boldsymbol{E}}$. Recalling that $\dot{\boldsymbol{E}} = \dfrac{1}{2}\dot{\boldsymbol{C}}$, one can obtain

$$\dot{W}_{\text{int}} = \boldsymbol{S} : \dot{\boldsymbol{E}} = \frac{1}{2}\boldsymbol{S} : \dot{\boldsymbol{C}}\,, \tag{3.105}$$

which proves useful when constructing hyperelastic material models (see Section 4.1). Additionally, by using equation (3.104), equation (3.102) can be altered to its reference configuration counterpart; that is,

$$D_{\text{int}} = \boldsymbol{S} : \dot{\boldsymbol{E}} - \dot{\Psi} \geq 0\,. \tag{3.106}$$

Chapter 4

Constitutive models

The equations resulting from the balance laws are not sufficient to determine all unknown quantities. This is physically intuitive, as the behaviour of a body depends on the materials of which it is composed. Hence, constitutive models describing material behaviour are introduced to complete the set of equations necessary to determine all unknown quantities. In this thesis, constitutive laws that govern the stress of solids at uniform and constant temperatures are presented.

To determine reasonable constitutive equations, there are several principles which one asserts axiomatically based on physical observations. These include:

- Material objectivity – the constitutive equations must be unaffected by the choice of observer or reference frame;
- Determinism – the material state may depend on the history of the material's state but not the future;
- Local action – processes in the direct neighbourhood of a material point have a stronger influence at that point than more distant ones;
- Admissibility – the constitutive equations must not contradict the thermodynamic laws.

Hence, one postulates that the Helmholtz free energy function per unit reference configuration volume and the second Piola-Kirchhoff stress are dependent on the right Cauchy-Green tensor and a set of history variables $\boldsymbol{\zeta} = \{\boldsymbol{\zeta}_1, \dots, \boldsymbol{\zeta}_n\}$; that is,

$$\Psi = \Psi\left(\boldsymbol{C}, \boldsymbol{\zeta}\right) , \tag{4.1}$$

$$\boldsymbol{S} = \boldsymbol{S}\left(\boldsymbol{C}, \boldsymbol{\zeta}\right) . \tag{4.2}$$

Here, material objectivity has been achieved as $\boldsymbol{C}$ is objective. Determinism is satisfied *a priori* as the history variables depend on only the history of that material point. Local action is also satisfied *a priori* as the relations are pointwise. Admissibility has not yet been satisfied. To do so, consider the time-derivative of the free energy function; that is,

$$\dot{\Psi} = 2\frac{\partial \Psi}{\partial \boldsymbol{C}} : \dot{\boldsymbol{E}} + \frac{\partial \Psi}{\partial \boldsymbol{\zeta}_i} : \dot{\boldsymbol{\zeta}}_i \,. \tag{4.3}$$

Substitution of equation (4.3) into equation (3.106), the Clausius-Duhem inequality, gives

$$D_{\text{int}} = \left[\boldsymbol{S} - 2\frac{\partial \Psi}{\partial \boldsymbol{C}}\right] : \dot{\boldsymbol{E}} - \frac{\partial \Psi}{\partial \boldsymbol{\zeta}_i} : \dot{\boldsymbol{\zeta}}_i \geq 0 \,. \tag{4.4}$$

According to the Coleman-Noll procedure [58], for inequality (4.4) to hold for arbitrary $\dot{\boldsymbol{E}}$ the coefficient of $\dot{\boldsymbol{E}}$ must be zero. Hence, it is apparent that equations (4.1) and (4.2) are not independent, they are related by

$$\boldsymbol{S} = \frac{\partial \Psi}{\partial \boldsymbol{E}} = 2\frac{\partial \Psi}{\partial \boldsymbol{C}} \,, \tag{4.5}$$

and so by postulating the free energy function the stress is postulated as a result. The Coleman-Noll procedure has a further result; that is,

$$D_{\text{int}} = -\frac{\partial \Psi}{\partial \boldsymbol{\zeta}_i} : \dot{\boldsymbol{\zeta}}_i \geq 0 \,. \tag{4.6}$$

Hence, materials that are independent of their loading history do not dissipate energy.

4.1 Hyperelastic materials

The hyperelastic materials discussed in this section are considered to be perfectly elastic; that is, they do not dissipate energy [54]. Hence, the Helmholtz free energy function Ψ is referred to as the strain energy function and is independent of the loading history. In the following section a viscoelastic extension to the material models presented here is developed, which necessitates the inclusion of history variables and, in turn, the dissipation of energy.

4.1.1 Compressible materials

Compressible materials are presented first; those are, materials which allow volume change.

Isotropy

Compressible isotropic materials are modelled by postulating a strain energy function in terms of the isotropic invariants of $\boldsymbol{C}$; that is,

$$\Psi = \Psi(I_i)\,, \qquad i = 1, 2, 3\,, \tag{4.7}$$

where the invariants are given by

$$I_1 = \mathrm{tr}(\boldsymbol{C})\,, \quad I_2 = \frac{1}{2}\left[\mathrm{tr}(\boldsymbol{C})^2 - \mathrm{tr}(\boldsymbol{C}^2)\right]\,, \quad I_3 = J^2 = \det(\boldsymbol{C})\,. \tag{4.8}$$

The stress and stiffness tensor can then be determined by differentiation of the strain energy function with respect to $\boldsymbol{C}$. However, the working is identical for the transversely isotropic material models presented in the following subsection, and so it is not shown here to avoid repetition.

Transverse isotropy and a special class of anisotropy

Transversely isotropic materials have a preferred direction that points normal to a plane of isotropy. Such materials typically have a fibrous or lamella microstructure. This is modelled by introducing a unit vector field $\boldsymbol{a}_0(\boldsymbol{X})$ aligned in the preferred direction in the reference configuration. A special class of anisotropic materials can be constructed by introducing a second unit vector field, $\boldsymbol{b}_0(\boldsymbol{X})$. This is useful for modelling materials containing two fibre bundles aligned in different directions, $\boldsymbol{a}_0$ and $\boldsymbol{b}_0$, at the same position [59].

The strain energy function is then composed of nine invariants; that is,

$$\Psi = \Psi(I_i)\,, \qquad i = 1, ..., 9\,, \tag{4.9}$$

where the invariants are given by

$$\begin{aligned}
&I_1 = \mathrm{tr}(\boldsymbol{C})\,, && I_2 = \frac{1}{2}\left[\mathrm{tr}(\boldsymbol{C})^2 - \mathrm{tr}(\boldsymbol{C}^2)\right]\,, && I_3 = J^2 = \det(\boldsymbol{C})\,,\\
&I_4 = \boldsymbol{a}_0 \cdot \boldsymbol{C}\boldsymbol{a}_0\,, && I_5 = \boldsymbol{a}_0 \cdot \boldsymbol{C}^2\boldsymbol{a}_0\,, && I_6 = \boldsymbol{b}_0 \cdot \boldsymbol{C}\boldsymbol{b}_0\,,\\
&I_7 = \boldsymbol{b}_0 \cdot \boldsymbol{C}^2\boldsymbol{b}_0\,, && I_8 = \frac{1}{2}\left[\boldsymbol{a}_0 \cdot \boldsymbol{C}\boldsymbol{b}_0 + \boldsymbol{b}_0 \cdot \boldsymbol{C}\boldsymbol{a}_0\right]\,, && I_9 = \left[\boldsymbol{a}_0 \cdot \boldsymbol{b}_0\right]^2\,.
\end{aligned} \tag{4.10}$$

Note that the first three invariants are the isotropic invariants and so the following mathematical developments apply similarly to isotropic materials. The second Piola-Kirchhoff stress is then obtained using the chain rule; that is,

$$\boldsymbol{S} = 2\frac{\partial \Psi}{\partial \boldsymbol{C}} = 2\frac{\partial \Psi}{\partial I_i}\frac{\partial I_i}{\partial \boldsymbol{C}}\,, \tag{4.11}$$

where the partial derivatives of each invariant with respect to $\boldsymbol{C}$ are given by

$$\begin{aligned}
&\frac{\partial I_1}{\partial \boldsymbol{C}} = \boldsymbol{I}\,, && \frac{\partial I_2}{\partial \boldsymbol{C}} = \boldsymbol{I}\left[\operatorname{tr}(\boldsymbol{C})\right] - \boldsymbol{C}\,, && \frac{\partial I_3}{\partial \boldsymbol{C}} = \det(\boldsymbol{C})\,\boldsymbol{C}^{-1}\,,\\
&\frac{\partial I_4}{\partial \boldsymbol{C}} = \boldsymbol{a}_0 \otimes \boldsymbol{a}_0\,, && \frac{\partial I_5}{\partial \boldsymbol{C}} = \boldsymbol{C}\boldsymbol{a}_0 \otimes \boldsymbol{a}_0 + \boldsymbol{a}_0 \otimes \boldsymbol{C}\boldsymbol{a}_0\,, && \frac{\partial I_6}{\partial \boldsymbol{C}} = \boldsymbol{b}_0 \otimes \boldsymbol{b}_0\,,\\
&\frac{\partial I_7}{\partial \boldsymbol{C}} = \boldsymbol{C}\boldsymbol{b}_0 \otimes \boldsymbol{b}_0 + \boldsymbol{b}_0 \otimes \boldsymbol{C}\boldsymbol{b}_0\,, && \frac{\partial I_8}{\partial \boldsymbol{C}} = \frac{1}{2}\left[\boldsymbol{a}_0 \otimes \boldsymbol{b}_0 + \boldsymbol{b}_0 \otimes \boldsymbol{a}_0\right]\,, && \frac{\partial I_9}{\partial \boldsymbol{C}} = \boldsymbol{0}\,.
\end{aligned} \tag{4.12}$$

The constitutive tensor is then given by

$$\mathbb{C} = 4\frac{\partial^2 \Psi}{\partial \boldsymbol{C}\partial \boldsymbol{C}} = 2\frac{\partial \boldsymbol{S}}{\partial \boldsymbol{C}} = 4\left[\frac{\partial^2 \Psi}{\partial I_m \partial I_n}\frac{\partial I_m}{\partial \boldsymbol{C}} \otimes \frac{\partial I_n}{\partial \boldsymbol{C}} + \frac{\partial \Psi}{\partial I_m}\frac{\partial^2 I_m}{\partial \boldsymbol{C}\partial \boldsymbol{C}}\right]\,, \tag{4.13}$$

where the second derivatives of the invariants are given by

$$\begin{aligned}
&\frac{\partial^2 I_2}{\partial \boldsymbol{C}^2} = \boldsymbol{I} \otimes \boldsymbol{I} - \boldsymbol{I} \odot \boldsymbol{I}\,, && \frac{\partial^2 I_3}{\partial \boldsymbol{C}^2} = \det(\boldsymbol{C})\left[\boldsymbol{C}^{-1} \otimes \boldsymbol{C}^{-1} - \boldsymbol{C}^{-1} \odot \boldsymbol{C}^{-1}\right]\,,\\
&\frac{\partial^2 I_5}{\partial \boldsymbol{C}^2} = \boldsymbol{I} \odot \boldsymbol{a}_0 \otimes \boldsymbol{a}_0 + \boldsymbol{a}_0 \otimes \boldsymbol{a}_0 \odot \boldsymbol{I}\,, && \frac{\partial^2 I_7}{\partial \boldsymbol{C}^2} = \boldsymbol{I} \odot \boldsymbol{b}_0 \otimes \boldsymbol{b}_0 + \boldsymbol{b}_0 \otimes \boldsymbol{b}_0 \odot \boldsymbol{I}\,,
\end{aligned} \tag{4.14}$$

$$\frac{\partial^2 I_p}{\partial \boldsymbol{C}^2} = \mathbb{0}\,, \quad p = 1, 4, 6, 8, 9\,. \tag{4.15}$$

If current configuration quantities are being used, the invariants can be equivalently determined by

$$\boldsymbol{a} = \boldsymbol{F}\boldsymbol{a}_0\,, \qquad \boldsymbol{b} = \boldsymbol{F}\boldsymbol{b}_0\,, \tag{4.16}$$

$$\begin{aligned}
&I_1 = \operatorname{tr}(\boldsymbol{B})\,, && I_2 = \frac{1}{2}\left[\operatorname{tr}(\boldsymbol{B})^2 - \operatorname{tr}(\boldsymbol{B}^2)\right]\,, && I_3 = J^2 = \det(\boldsymbol{B})\,,\\
&I_4 = \boldsymbol{a} \cdot \boldsymbol{a}\,, && I_5 = \boldsymbol{a} \cdot \boldsymbol{B}\boldsymbol{a}\,, && I_6 = \boldsymbol{b} \cdot \boldsymbol{b}\,,\\
&I_7 = \boldsymbol{b} \cdot \boldsymbol{B}\boldsymbol{b}\,, && I_8 = \frac{1}{2}\left[\boldsymbol{a} \cdot \boldsymbol{b} + \boldsymbol{b} \cdot \boldsymbol{a}\right]\,, && I_9 = \left[\boldsymbol{a}_0 \cdot \boldsymbol{b}_0\right]^2\,.
\end{aligned} \tag{4.17}$$

The Cauchy stress can be determined by applying a push-forward operation to the second Piola-Kirchhoff stress; that is,

$$\boldsymbol{\sigma} = J^{-1}\boldsymbol{F}\boldsymbol{S}\boldsymbol{F}^T = 2J^{-1}\frac{\partial \Psi}{\partial I_i}\boldsymbol{A}_i\,, \qquad \boldsymbol{A}_i = \boldsymbol{F}\frac{\partial I_i}{\partial \boldsymbol{C}}\boldsymbol{F}^T\,, \tag{4.18}$$

$$\begin{aligned}
&\boldsymbol{A}_1 = \boldsymbol{B}\,, && \boldsymbol{A}_2 = \operatorname{tr}(\boldsymbol{B})\,\boldsymbol{B} - \boldsymbol{B}^2\,, && \boldsymbol{A}_3 = \det(\boldsymbol{B})\,\boldsymbol{I}\,,\\
&\boldsymbol{A}_4 = \boldsymbol{a} \otimes \boldsymbol{a}\,, && \boldsymbol{A}_5 = \boldsymbol{B}\boldsymbol{a} \otimes \boldsymbol{a} + \boldsymbol{a} \otimes \boldsymbol{B}\boldsymbol{a}\,, && \boldsymbol{A}_6 = \boldsymbol{b} \otimes \boldsymbol{b}\,,\\
&\boldsymbol{A}_7 = \boldsymbol{B}\boldsymbol{b} \otimes \boldsymbol{b} + \boldsymbol{b} \otimes \boldsymbol{B}\boldsymbol{b}\,, && \boldsymbol{A}_8 = \frac{1}{2}\left[\boldsymbol{a} \otimes \boldsymbol{b} + \boldsymbol{b} \otimes \boldsymbol{a}\right]\,, && \boldsymbol{A}_9 = \boldsymbol{0}\,.
\end{aligned} \tag{4.19}$$

The Lie constitutive tensor can also be determined by applying a push-forward operation,

$$\mathbb{c}_{ijkl} = F_{iI}F_{jJ}F_{kK}F_{lL}\mathbb{C}_{IJKL}\,, \tag{4.20}$$

leading to

$$\mathbb{c} = 4\left[\frac{\partial^2\Psi}{\partial I_m \partial I_n}\boldsymbol{A}_m \otimes \boldsymbol{A}_n + \frac{\partial\Psi}{\partial I_m}\mathbb{A}_m\right], \qquad [\mathbb{A}_m]_{ijkl} = \left[\frac{\partial^2 I_m}{\partial \boldsymbol{C}\partial \boldsymbol{C}}\right]_{IJKL} F_{iI}F_{jJ}F_{kK}F_{lL}\,, \tag{4.21}$$

where the push-forward counterparts of the second derivatives of the invariants are given by

$$\begin{aligned} \mathbb{A}_2 &= \boldsymbol{B} \otimes \boldsymbol{B} - \boldsymbol{B} \odot \boldsymbol{B}\,, & \mathbb{A}_3 &= \det(\boldsymbol{B})\left[\boldsymbol{I} \otimes \boldsymbol{I} - \boldsymbol{I} \odot \boldsymbol{I}\right]\,, \\ \mathbb{A}_5\,, &= \boldsymbol{B} \odot \boldsymbol{a} \otimes \boldsymbol{a} + \boldsymbol{a} \otimes \boldsymbol{a} \odot \boldsymbol{B}\,, & \mathbb{A}_7 &= \boldsymbol{B} \odot \boldsymbol{b} \otimes \boldsymbol{b} + \boldsymbol{b} \otimes \boldsymbol{b} \odot \boldsymbol{B}\,, \end{aligned} \tag{4.22}$$

$$\mathbb{A}_p = \mathbb{0}\,, \quad p = 1, 4, 6, 8, 9\,. \tag{4.23}$$

The Jaumann constitutive tensor can then be determined using

$$\mathbb{c}^{\nabla} = \mathbb{c} + \boldsymbol{\tau} \odot \boldsymbol{I} + \boldsymbol{I} \odot \boldsymbol{\tau}\,, \tag{4.24}$$

leading to

$$\mathbb{c}^{\nabla} = 4\left[\frac{\partial^2\Psi}{\partial I_m \partial I_n}\boldsymbol{A}_m \otimes \boldsymbol{A}_n + \frac{\partial\Psi}{\partial I_m}\left[\mathbb{A}_m + \frac{1}{2}\left[\boldsymbol{A}_m \odot \boldsymbol{I} + \boldsymbol{I} \odot \boldsymbol{A}_m\right]\right]\right]\,. \tag{4.25}$$

Note that, equations (4.18) and (4.25) contain mostly kinematic terms which are independent of the material model. Hence, a subroutine can be written for implementing compressible anisotropic hyperelastic material models in ABAQUS which requires the user to input only the first and second derivatives of the strain energy function with respect to the invariants as show in Algorithm 1.

A constraint is enforced on material models that they are stress-free if no deformation is present, that is, $\boldsymbol{F} = \boldsymbol{I}$. Hence, the following must hold:

$$\begin{aligned} \boldsymbol{\sigma}\Big|_{\boldsymbol{F}=\boldsymbol{I}} =& \boldsymbol{I}\left[\frac{\partial\Psi}{\partial I_1} + 2\frac{\partial\Psi}{\partial I_2} + \frac{\partial\Psi}{\partial I_3}\right] + \boldsymbol{a}_0 \otimes \boldsymbol{a}_0\left[\frac{\partial\Psi}{\partial I_4} + 2\frac{\partial\Psi}{\partial I_5}\right] + \boldsymbol{b}_0 \otimes \boldsymbol{b}_0\left[\frac{\partial\Psi}{\partial I_6} + 2\frac{\partial\Psi}{\partial I_7}\right] \\ &+ \frac{1}{2}\left[\boldsymbol{a}_0 \otimes \boldsymbol{b}_0 + \boldsymbol{b}_0 \otimes \boldsymbol{a}_0\right]\frac{\partial\Psi}{\partial I_8} = \boldsymbol{0}\,. \end{aligned} \tag{4.26}$$

This results in the following constraint equations:

$$\left[\frac{\partial\Psi}{\partial I_1} + 2\frac{\partial\Psi}{\partial I_2} + \frac{\partial\Psi}{\partial I_3}\right]_{\boldsymbol{F}=\boldsymbol{I}} = 0\,, \tag{4.27}$$

$$\left[\frac{\partial\Psi}{\partial I_4} + 2\frac{\partial\Psi}{\partial I_5}\right]_{\boldsymbol{F}=\boldsymbol{I}} = 0\,, \tag{4.28}$$

$$\left[\frac{\partial\Psi}{\partial I_6} + 2\frac{\partial\Psi}{\partial I_7}\right]_{\boldsymbol{F}=\boldsymbol{I}} = 0\,, \tag{4.29}$$

$$\left[\frac{\partial\Psi}{\partial I_8}\right]_{\boldsymbol{F}=\boldsymbol{I}} = 0\,. \tag{4.30}$$

Algorithm 1 Procedure for determining stress and constitutive tensor required by ABAQUS for a compressible material given the derivatives of its strain energy function.

```
procedure COMPRESSIBLE_MATERIAL($\partial\Psi/\partial I$, $\partial^2\Psi/\partial I^2$, $\boldsymbol{F}$, $\boldsymbol{a}_0$, $\boldsymbol{b}_0$)
    $\boldsymbol{A}(:,:,:) = \text{CALC\_A}(\boldsymbol{F}, \boldsymbol{a}_0, \boldsymbol{b}_0)$
    $\mathbb{A}(:,:,:) = \text{CALC\_BIG\_A}(\boldsymbol{F}, \boldsymbol{a}_0, \boldsymbol{b}_0)$
    $J = \det \boldsymbol{F}$
    $\boldsymbol{\sigma} = \boldsymbol{0}$
    $\mathbb{C}_{\text{ABA}} = \mathbb{O}$
    for $m = 1, ..., 8$ do
        $\boldsymbol{\sigma} = \boldsymbol{\sigma} + 2J^{-1}\frac{\partial\Psi}{\partial I}(m)\boldsymbol{A}(m,:,:)$
        $\mathbb{C}_{\text{ABA}} = \mathbb{C}_{\text{ABA}} + 4J^{-1}\frac{\partial\Psi}{\partial I}(m)\left[\mathbb{A}(m,:,:) + \frac{1}{2}\left[\boldsymbol{A}(m,:,:)\odot\boldsymbol{I} + \boldsymbol{I}\odot\boldsymbol{A}(m,:,:)\right]\right]$
        for $n = 1, ..., 8$ do
            $\mathbb{C}_{\text{ABA}} = \mathbb{C}_{\text{ABA}} + 4J^{-1}\frac{\partial^2\Psi}{\partial I^2}(m,n)\boldsymbol{A}(m,:,:)\otimes\boldsymbol{A}(n,:,:)$
        end for
    end for
    return $\boldsymbol{\sigma}$, $\mathbb{C}_{\text{ABA}}$
end procedure
```

Note also that, when $\boldsymbol{F} = \boldsymbol{I}$ the invariants have the following values:

$$\begin{aligned} I_1 &= I_2 = 3\,, \\ I_3 &= I_4 = I_5 = I_6 = I_7 = 1\,. \end{aligned} \tag{4.31}$$

Here, I_8 has been excluded as it depends on the values of $\boldsymbol{a}_0$ and $\boldsymbol{b}_0$.

4.1.2 Incompressible materials

Many materials that incur large elastic strains are incompressible. Mathematically, this implies the constraints

$$J = 1\,, \qquad \dot{J} = 0\,. \tag{4.32}$$

The implication of this for initial boundary value problems (see Chapter 5) is that there is an additional partial differential equation, equation (4.32), that must be satisfied on the domain (in addition to balance of linear momentum). However, this also has implications for constitutive theory. According to the Coleman-Noel procedure [58], for compressible materials the second Piola-Kirchhoff stress is determined in terms of the strain energy by asserting that the following holds for arbitrary $\dot{\boldsymbol{C}}$:

$$\left[\frac{1}{2}\boldsymbol{S} - \frac{\partial \Psi}{\partial \boldsymbol{C}}\right] : \dot{\boldsymbol{C}} = 0 \,. \tag{4.33}$$

However, for incompressible materials $\dot{\boldsymbol{C}}$ is not arbitrary, it must satisfy

$$\dot{J} = \frac{\partial J}{\partial \boldsymbol{C}} : \dot{\boldsymbol{C}} = \frac{1}{2} J \boldsymbol{C}^{-1} : \dot{\boldsymbol{C}} = 0 \,. \tag{4.34}$$

Since both equations (4.33) and (4.34) must hold, one obtains the following equation:

$$\frac{1}{2}\boldsymbol{S} - \frac{\partial \Psi}{\partial \boldsymbol{C}} = \gamma \frac{1}{2} J \boldsymbol{C}^{-1} \,. \tag{4.35}$$

This can be obtained by interpreting ":" as a generalised dot product [60]. The argument is then that $\frac{1}{2}\boldsymbol{S} - \dfrac{\partial \Psi}{\partial \boldsymbol{C}}$ and $\frac{1}{2} J \boldsymbol{C}^{-1}$ are both normal to $\dot{\boldsymbol{C}}$. Hence, $\frac{1}{2}\boldsymbol{S} - \dfrac{\partial \Psi}{\partial \boldsymbol{C}}$ and $\frac{1}{2} J \boldsymbol{C}^{-1}$ are aligned but may vary in magnitude, which is resolved by the indeterminate scalar γ. Equation (4.35) can also be obtained by using γ as a Lagrange multiplier that is added to the strain energy to enforce the constraint $J - 1 = 0$ [54]. In either case, the result is that the second Piola-Kirchhoff stress is given by

$$\boldsymbol{S} = 2\frac{\partial \Psi}{\partial \boldsymbol{C}} + \gamma J \boldsymbol{C}^{-1} \,. \tag{4.36}$$

It is convenient to interpret γ as a hydrostatic pressure p; that is,

$$\gamma = p = \frac{1}{3} \operatorname{tr} \boldsymbol{\sigma} \,. \tag{4.37}$$

For this to be the case, it can be shown that the strain energy must be first order homogenous [60]; that is,

$$\Psi\left(\alpha \boldsymbol{C}\right) = \Psi\left(\boldsymbol{C}\right) \,. \tag{4.38}$$

This is achieved by making the strain energy a function of the isochoric right Cauchy-Green tensor; that is,

$$\Psi = \Psi\left(\bar{\boldsymbol{C}}\right) \,. \tag{4.39}$$

This may be rephrased so that the strain energy function Ψ is equal to an isochoric strain energy function $\bar{\Psi}$ which is invariant to volumetric deformation; that is,

$$\Psi\left(\boldsymbol{C}\right) = \bar{\Psi}\left(\boldsymbol{C}\right) = \bar{\Psi}\left(\bar{\boldsymbol{C}}\right) \,. \tag{4.40}$$

This rephrasing may seem arbitrary. However, it proves useful when introducing near-incompressible materials, which is done in the following subsection. The stress is then given by

$$\boldsymbol{S} = \bar{\boldsymbol{S}} + \boldsymbol{S}_{vol} \,, \qquad \bar{\boldsymbol{S}} = \frac{\partial \bar{\Psi}}{\partial \boldsymbol{C}} \,, \qquad \boldsymbol{S}_{vol} = p J \boldsymbol{C}^{-1} \,. \tag{4.41}$$

Isotropic materials

Incompressible isotropic materials are modelled by postulating a strain energy function in terms of the isotropic invariants of $\bar{\boldsymbol{C}}$; that is,

$$\Psi(\boldsymbol{C}) = \bar{\Psi}\left(\bar{I}_m\right) , \qquad m = 1, 2 , \tag{4.42}$$

where the isochoric invariants are given by

$$\bar{I}_1 = \operatorname{tr}(\bar{\boldsymbol{C}}) , \qquad \bar{I}_2 = \frac{1}{2}\left[\operatorname{tr}(\bar{\boldsymbol{C}})^2 - \operatorname{tr}(\bar{\boldsymbol{C}}^2)\right] . \tag{4.43}$$

The stress and constitutive tensor can be obtained by taking the relevant derivatives with respect to $\boldsymbol{C}$. However, as the working is the same for transversely isotropic materials, it is presented in the following subsection.

Transverse isotropy and a special class of anisotropy

As with compressible materials, transverse isotropy in incompressible materials is modelled by introducing the unit vector field $\boldsymbol{a}_0\left(\boldsymbol{X}\right)$. Additionally, a special class of anisotropic materials can be constructed by introducing a second unit vector field, $\boldsymbol{b}_0\left(\boldsymbol{X}\right)$ as discussed above for compressible materials (Section 4.1.1). The strain energy function is then defined by 7 isochoric invariants; that is,

$$\Psi(\boldsymbol{C}) = \bar{\Psi}\left(\bar{I}_m\right) , \qquad m = 1, 2, 4, 5, 6, 7, 8 . \tag{4.44}$$

Here, $\bar{I}_m$ are given by

$$\begin{aligned}
&\bar{I}_1 = \operatorname{tr}(\bar{\boldsymbol{C}}) , && \bar{I}_2 = \frac{1}{2}\left[\operatorname{tr}(\bar{\boldsymbol{C}})^2 - \operatorname{tr}(\bar{\boldsymbol{C}}^2)\right] , && \\
&\bar{I}_4 = \boldsymbol{a}_0 \cdot \bar{\boldsymbol{C}}\boldsymbol{a}_0 , && \bar{I}_5 = \boldsymbol{a}_0 \cdot \bar{\boldsymbol{C}}^2\boldsymbol{a}_0 , && \bar{I}_6 = \boldsymbol{b}_0 \cdot \bar{\boldsymbol{C}}\boldsymbol{b}_0 , \\
&\bar{I}_7 = \boldsymbol{b}_0 \cdot \bar{\boldsymbol{C}}^2\boldsymbol{b}_0 , && \bar{I}_8 = \frac{1}{2}\left[\boldsymbol{a}_0 \cdot \bar{\boldsymbol{C}}\boldsymbol{b}_0 + \boldsymbol{b}_0 \cdot \bar{\boldsymbol{C}}\boldsymbol{a}_0\right] . &&
\end{aligned} \tag{4.45}$$

The second Piola-Kirchhoff stress is then given by

$$\boldsymbol{S} = \bar{\boldsymbol{S}} + \boldsymbol{S}_{vol} , \qquad \bar{\boldsymbol{S}} = 2\frac{\partial\bar{\Psi}}{\partial\boldsymbol{C}} . \tag{4.46}$$

where the isochoric $\bar{\boldsymbol{S}}$ and volumetric $\boldsymbol{S}_{vol}$ stresses are given, respectively, by

$$\bar{\boldsymbol{S}} = 2\sum_{\substack{m=1\\m\neq3}}^{8} \frac{\partial\bar{\Psi}}{\partial\bar{I}_m} \det\left(\boldsymbol{C}\right)^{q_m} \left[\frac{\partial I_m}{\partial\boldsymbol{C}} + q_m I_m \boldsymbol{C}^{-1}\right] , \qquad \boldsymbol{S}_{vol} = Jp\boldsymbol{C}^{-1} . \tag{4.47}$$

Here, q_m is defined so that the standard invariants are related to the isochoric invariants by

$$\text{(no sum) } \bar{I}_m = \det(\boldsymbol{C})^{q_m} I_m, \tag{4.48}$$

which leads to

$$q_m = \begin{cases} -1/3 & m = 1, 4, 6, 8\,, \\ -2/3 & m = 2, 5\,, \\ 0 & m = 3, 9\,. \end{cases} \tag{4.49}$$

The constitutive tensor is then given by

$$\mathbb{C} = \bar{\mathbb{C}} + \mathbb{C}_{vol}\,, \qquad \bar{\mathbb{C}} = 4\frac{\partial^2 \bar{\Psi}}{\partial \boldsymbol{C}^2}\,, \qquad \mathbb{C}_{vol} = 2\frac{\partial \boldsymbol{S}_{vol}}{\partial \boldsymbol{C}}\,, \tag{4.50}$$

where the isochoric part of the constitutive tensor is given by

$$\begin{aligned} \bar{\mathbb{C}} =& 4 \sum_{\substack{m,n=1 \\ m,n\neq 3}}^{8} \frac{\partial^2 \bar{\Psi}}{\partial \bar{I}_m \partial \bar{I}_n} \det(\boldsymbol{C})^{q_m+q_n} \Bigg[\frac{\partial I_m}{\partial \boldsymbol{C}} \otimes \frac{\partial I_n}{\partial \boldsymbol{C}} + q_m I_m \boldsymbol{C}^{-1} \otimes \frac{\partial I_n}{\partial \boldsymbol{C}} + q_n I_n \frac{\partial I_m}{\partial \boldsymbol{C}} \otimes \boldsymbol{C}^{-1} \\ & \qquad + q_m q_n I_m I_n \boldsymbol{C}^{-1} \otimes \boldsymbol{C}^{-1} \Bigg] \\ & + 4 \sum_{\substack{m=1 \\ m\neq 3}}^{8} \frac{\partial \bar{\Psi}}{\partial \bar{I}_m} \det(\boldsymbol{C})^{q_m} \Bigg[\frac{\partial^2 I_m}{\partial \boldsymbol{C}^2} + q_m \left[\boldsymbol{C}^{-1} \otimes \frac{\partial I_m}{\partial \boldsymbol{C}} + \frac{\partial I_m}{\partial \boldsymbol{C}} \otimes \boldsymbol{C}^{-1} - I_m \boldsymbol{C}^{-1} \odot \boldsymbol{C}^{-1} \right] \\ & \qquad + q_m^2 I_m \boldsymbol{C}^{-1} \otimes \boldsymbol{C}^{-1} \Bigg] \end{aligned} \tag{4.51}$$

and the volumetric part of the constitutive tensor is given by

$$\mathbb{C}_{vol} = Jp \left[\boldsymbol{C}^{-1} \otimes \boldsymbol{C}^{-1} - 2\boldsymbol{C}^{-1} \odot \boldsymbol{C}^{-1} \right]. \tag{4.52}$$

If current configuration quantities are being used, then the isochoric invariants can be determined by

$$\bar{\boldsymbol{a}} = \bar{\boldsymbol{F}} \boldsymbol{a}_0\,, \qquad \bar{\boldsymbol{b}} = \bar{\boldsymbol{F}} \boldsymbol{b}_0\,, \tag{4.53}$$

$$\bar{I}_1 = \operatorname{tr}(\bar{\boldsymbol{B}})\,, \qquad \bar{I}_2 = \frac{1}{2}\left[\operatorname{tr}(\bar{\boldsymbol{B}})^2 - \operatorname{tr}(\bar{\boldsymbol{B}}^2)\right], \tag{4.54}$$

$$\bar{I}_4 = \bar{\boldsymbol{a}} \cdot \bar{\boldsymbol{a}}\,, \qquad \bar{I}_5 = \bar{\boldsymbol{a}} \cdot \bar{\boldsymbol{B}} \bar{\boldsymbol{a}}\,, \qquad \bar{I}_6 = \bar{\boldsymbol{b}} \cdot \bar{\boldsymbol{b}}\,, \tag{4.55}$$

$$\bar{I}_7 = \bar{\boldsymbol{b}} \cdot \bar{\boldsymbol{B}} \bar{\boldsymbol{b}}\,, \qquad \bar{I}_8 = \frac{1}{2}\left[\bar{\boldsymbol{a}} \cdot \bar{\boldsymbol{b}} + \bar{\boldsymbol{b}} \cdot \bar{\boldsymbol{a}}\right]. \tag{4.56}$$

The Cauchy stress can then be determined by applying a push-forward operation to the second Piola-Kirchhoff stress as follows:

$$\boldsymbol{\sigma} = \bar{\boldsymbol{\sigma}} + \boldsymbol{\sigma}_{vol}\,, \qquad \bar{\boldsymbol{\sigma}} = J^{-1} \boldsymbol{F} \bar{\boldsymbol{S}} \boldsymbol{F}^T\,, \qquad \boldsymbol{\sigma}_{vol} = J^{-1} \boldsymbol{F} \boldsymbol{S}_{vol} \boldsymbol{F}^T\,, \tag{4.57}$$

$$\bar{\boldsymbol{\sigma}} = \frac{2}{J}\sum_{\substack{m=1\\ m\neq 3}}^{8} \frac{\partial\bar{\Psi}}{\partial\bar{I}_m}\left[\bar{\boldsymbol{A}}_m + q_m\bar{I}_m\boldsymbol{I}\right]\,, \qquad \boldsymbol{\sigma}_{vol} = p\boldsymbol{I}\,. \tag{4.58}$$

Here, the isochoric counterparts $\bar{\boldsymbol{A}}_m$ of the kinematic quantities $\boldsymbol{A}_m$ are given by

$$\begin{aligned}
&\bar{\boldsymbol{A}}_1 := \bar{\boldsymbol{B}} && \bar{\boldsymbol{A}}_2 := \bar{\boldsymbol{B}}\mathrm{tr}(\bar{\boldsymbol{B}}) - \bar{\boldsymbol{B}}^2\,, && \bar{\boldsymbol{A}}_3 := \boldsymbol{0}\,,\\
&\bar{\boldsymbol{A}}_4 := \bar{\boldsymbol{a}}\otimes\bar{\boldsymbol{a}}\,, && \bar{\boldsymbol{A}}_5 := \bar{\boldsymbol{a}}\otimes\bar{\boldsymbol{B}}\bar{\boldsymbol{a}} + \bar{\boldsymbol{B}}\bar{\boldsymbol{a}}\otimes\bar{\boldsymbol{a}}\,, && \bar{\boldsymbol{A}}_6 := \bar{\boldsymbol{b}}\otimes\bar{\boldsymbol{b}}\,,\\
&\bar{\boldsymbol{A}}_7 := \bar{\boldsymbol{b}}\otimes\bar{\boldsymbol{B}}\bar{\boldsymbol{b}} + \bar{\boldsymbol{B}}\bar{\boldsymbol{b}}\otimes\bar{\boldsymbol{b}}\,, && \bar{\boldsymbol{A}}_8 := \frac{1}{2}\left[\bar{\boldsymbol{a}}\otimes\bar{\boldsymbol{b}} + \bar{\boldsymbol{b}}\otimes\bar{\boldsymbol{a}}\right]\,.
\end{aligned} \tag{4.59}$$

The isochoric and volumetric Lie constitutive tensors can both be obtained by applying the push-forward operation

$$\mathbb{c}_{ijkl} = F_{iI}F_{jJ}F_{kK}F_{lL}\mathbb{C}_{IJKL}\,, \tag{4.60}$$

leading to

$$\begin{aligned}
\bar{\mathbb{c}} = {}& 4\sum_{\substack{m,n=1\\ m,n\neq 3}}^{8} \frac{\partial^2\bar{\Psi}}{\partial\bar{I}_m\partial\bar{I}_n}\left[\bar{\boldsymbol{A}}_m\otimes\bar{\boldsymbol{A}}_n + q_m\bar{I}_m\boldsymbol{I}\otimes\bar{\boldsymbol{A}}_n + q_n\bar{I}_n\bar{\boldsymbol{A}}_m\otimes\boldsymbol{I} + q_m q_n\bar{I}_m\bar{I}_n\boldsymbol{I}\otimes\boldsymbol{I}\right]\\
&+4\sum_{\substack{m=1\\ m\neq 3}}^{8} \frac{\partial\bar{\Psi}}{\partial\bar{I}_m}\left[\bar{\mathbb{A}}_m + q_m\left[\boldsymbol{I}\otimes\bar{\boldsymbol{A}}_m + \bar{\boldsymbol{A}}_m\otimes\boldsymbol{I} - \bar{I}_m\boldsymbol{I}\odot\boldsymbol{I}\right] + q_m^2\bar{I}_m\boldsymbol{I}\otimes\boldsymbol{I}\right]\,,
\end{aligned} \tag{4.61}$$

and

$$\mathbb{c}_{vol} = Jp\left[\boldsymbol{I}\otimes\boldsymbol{I} - 2\boldsymbol{I}\odot\boldsymbol{I}\right]\,, \tag{4.62}$$

respectively. Here, the isochoric versions $\bar{\mathbb{A}}_m$ of the fourth order kinematic tensors $\mathbb{A}_m$ are given by

$$\begin{aligned}
&\bar{\mathbb{A}}_2 = \bar{\boldsymbol{B}}\otimes\bar{\boldsymbol{B}} - \bar{\boldsymbol{B}}\odot\bar{\boldsymbol{B}}\,, && \bar{\mathbb{A}}_3 = \mathbb{0}\,,\\
&\bar{\mathbb{A}}_5 = \bar{\boldsymbol{B}}\odot\bar{\boldsymbol{a}}\otimes\bar{\boldsymbol{a}} + \bar{\boldsymbol{a}}\otimes\bar{\boldsymbol{a}}\odot\bar{\boldsymbol{B}}\,, && \bar{\mathbb{A}}_7 = \bar{\boldsymbol{B}}\odot\bar{\boldsymbol{b}}\otimes\bar{\boldsymbol{b}} + \bar{\boldsymbol{b}}\otimes\bar{\boldsymbol{b}}\odot\bar{\boldsymbol{B}}\,.
\end{aligned} \tag{4.63}$$

$$\bar{\mathbb{A}}_p = \mathbb{0}\,, \quad p = 1,4,6,8,9\,. \tag{4.64}$$

The isochoric and volumetric Jaumann constitutive tensors can then be obtained, respectively, using

$$\bar{\mathbb{c}}^{\nabla} = \bar{\mathbb{c}} + \bar{\boldsymbol{\tau}}\odot\boldsymbol{I} + \boldsymbol{I}\odot\bar{\boldsymbol{\tau}}\,, \qquad \mathbb{c}_{vol}^{\nabla} = \mathbb{c}_{vol} + \boldsymbol{\tau}_{vol}\odot\boldsymbol{I} + \boldsymbol{I}\odot\boldsymbol{\tau}_{vol}\,. \tag{4.65}$$

Noting that the isochoric and volumetric Kirchhoff stress are given, respectively, by

$$\bar{\boldsymbol{\tau}} = 2\sum_{\substack{m=1\\ m\neq 3}}^{8} \frac{\partial\bar{\Psi}}{\partial\bar{I}_m}\left[\bar{\boldsymbol{A}}_m + q_m\bar{I}_m\boldsymbol{I}\right]\,, \qquad \boldsymbol{\tau}_{vol} = Jp\boldsymbol{I}\,, \tag{4.66}$$

one obtains an isochoric Jaumann constitutive tensor of

$$
\begin{aligned}
\bar{\mathbb{c}}^{\nabla} = 4 \sum_{\substack{m,n=1 \\ m,n\neq 3}}^{8} \frac{\partial^2 \bar{\Psi}}{\partial \bar{I}_m \partial \bar{I}_n} & \left[\bar{\boldsymbol{A}}_m \otimes \bar{\boldsymbol{A}}_n + q_m \bar{I}_m \boldsymbol{I} \otimes \bar{\boldsymbol{A}}_n + q_n \bar{I}_n \bar{\boldsymbol{A}}_m \otimes \boldsymbol{I} + q_m q_n \bar{I}_m \bar{I}_n \boldsymbol{I} \otimes \boldsymbol{I} \right] \\
+4 \sum_{\substack{m=1 \\ m\neq 3}}^{8} \frac{\partial \bar{\Psi}}{\partial \bar{I}_m} & \left[\bar{\mathbb{A}}_m + \frac{1}{2} \left[\bar{\boldsymbol{A}}_m \odot \boldsymbol{I} + \boldsymbol{I} \odot \bar{\boldsymbol{A}}_m \right] + q_m \left[\boldsymbol{I} \otimes \bar{\boldsymbol{A}}_m + \bar{\boldsymbol{A}}_m \otimes \boldsymbol{I} \right] + q_m^2 \bar{I}_m \boldsymbol{I} \otimes \boldsymbol{I} \right] ,
\end{aligned}
\tag{4.67}
$$

and a volumetric Jaumann constitutive tensor of

$$
\mathbb{c}_{vol}^{\nabla} = J p \boldsymbol{I} \otimes \boldsymbol{I} \, . \tag{4.68}
$$

Similarly to the case of compressible materials, the majority of the terms contained in the stress and constitutive tensor are kinematic and independent of the material model. Hence, a subroutine can be written using the pseudo-code displayed in Algorithm 2, which calculates the required quantities for implementation in ABAQUS given the relevant derivatives of the strain energy function. Note that the provision of the volumetric stress and constitutive tensors is not required, since these are independent of the material model.

Again, the stress must vanish if there is no deformation. In the case of incompressibility, the kinematic term in the stress vanishes for the first and second invariants. Hence, the following constraints are left to enforce that a model is stress-free for $\boldsymbol{F} = \boldsymbol{I}$:

$$
\begin{aligned}
\left[\frac{\partial \bar{\Psi}}{\partial \bar{I}_4} + 2 \frac{\partial \bar{\Psi}}{\partial \bar{I}_5} \right]_{\boldsymbol{F}=\boldsymbol{I}} &= 0 \, , \\
\left[\frac{\partial \bar{\Psi}}{\partial \bar{I}_6} + 2 \frac{\partial \bar{\Psi}}{\partial \bar{I}_7} \right]_{\boldsymbol{F}=\boldsymbol{I}} &= 0 \, , \\
\left[\frac{\partial \bar{\Psi}}{\partial \bar{I}_8} \right]_{\boldsymbol{F}=\boldsymbol{I}} &= 0 \, .
\end{aligned}
\tag{4.69}
$$

4.1.3 Near-incompressible materials

One can also construct near-incompressible materials models as an approximation of incompressibility. In this case, the strain energy is postulated as a superposition of an isochoric $\bar{\Psi}$ and volumetric Ψ_{vol} strain energy function; that is,

$$
\Psi = \bar{\Psi} \left(\bar{\boldsymbol{C}} \right) + \Psi_{vol} \left(J \right) \, . \tag{4.70}
$$

The volumetric strain energy depends solely on the Jacobian whereas the isochoric strain energy depends only on $\bar{\boldsymbol{C}}$. Near-incompressibility is weakly enforced via penalty by making

Algorithm 2 Procedure for determining stress and constitutive tensor required by Abaqus for an incompressible material given the derivatives of its strain energy function.

```
procedure INCOMPRESSIBLE_MATERIAL($\partial\bar{\Psi}/\partial\bar{I}$, $\partial^2\bar{\Psi}/\partial\bar{I}^2$ $\boldsymbol{F}$, $\boldsymbol{a}_0$, $\boldsymbol{b}_0$)
    $J = \det \boldsymbol{F}$
    $\bar{\boldsymbol{F}} = \boldsymbol{F} J^{-1/3}$
    $\bar{I}(:) = \text{CALC\_I}(\bar{\boldsymbol{F}}, \boldsymbol{a}_0, \boldsymbol{b}_0)$
    $\bar{\boldsymbol{A}}(:,:,:) = \text{CALC\_A}(\bar{\boldsymbol{F}}, \boldsymbol{a}_0, \boldsymbol{b}_0)$
    $\bar{\mathbb{A}}(:,:,:) = \text{CALC\_BIG\_A}(\bar{\boldsymbol{F}}, \boldsymbol{a}_0, \boldsymbol{b}_0)$
    $\boldsymbol{q} = \begin{bmatrix} -1/3 & -2/3 & 0 & -1/3 & -2/3 & -1/3 & -2/3 & -1/3 \end{bmatrix}$
    for $m = 1, ..., 8$ do
        if $m \neq 3$ then
            $\boldsymbol{\sigma} = \boldsymbol{\sigma} + 2J^{-1} \frac{\partial\bar{\Psi}}{\partial\bar{I}_m} \left[\bar{\boldsymbol{A}}_m + q_m \bar{I}_m \boldsymbol{I}\right]$
            $\mathbb{C}_{\text{ABA}} = \mathbb{C}_{\text{ABA}} + 4J^{-1} \frac{\partial\bar{\Psi}}{\partial\bar{I}_m} \left[\bar{\mathbb{A}}_m + \frac{1}{2}\left[\bar{\boldsymbol{A}}_m \odot \boldsymbol{I} + \boldsymbol{I} \odot \bar{\boldsymbol{A}}_m\right] + q_m \left[\boldsymbol{I} \otimes \bar{\boldsymbol{A}}_m + \bar{\boldsymbol{A}}_m \otimes \boldsymbol{I}\right] + q_m^2 \bar{I}_m \boldsymbol{I} \otimes \boldsymbol{I}\right]$
            for $n = 1, ..., 8$ do
                if $n \neq 3$ then
                    $\mathbb{C}_{\text{ABA}} = \mathbb{C}_{\text{ABA}} + 4J^{-1} \frac{\partial^2\bar{\Psi}}{\partial\bar{I}_m \partial\bar{I}_n} \left[\bar{\boldsymbol{A}}_m \otimes \bar{\boldsymbol{A}}_n + q_m \bar{I}_m \boldsymbol{I} \otimes \bar{\boldsymbol{A}}_n + q_n \bar{I}_n \bar{\boldsymbol{A}}_m \otimes \boldsymbol{I} + q_m q_n \bar{I}_m \bar{I}_n \boldsymbol{I} \otimes \boldsymbol{I}\right]$
                end if
            end for
        end if
    end for
    return $\boldsymbol{\sigma}$, $\mathbb{C}_{\text{ABA}}$
end procedure
```

Ψ_{vol} very sensitive to a change in J in comparison to the sensitivity of $\bar{\Psi}$ with respect to $\bar{\boldsymbol{C}}$. The stress is then given by

$$\boldsymbol{S} = 2\frac{\partial\Psi}{\partial\boldsymbol{C}} = \bar{\boldsymbol{S}} + \boldsymbol{S}_{vol}\,, \qquad \bar{\boldsymbol{S}} = 2\frac{\partial\bar{\Psi}}{\partial\boldsymbol{C}}\,, \qquad \boldsymbol{S}_{vol} = 2\frac{\partial\Psi_{vol}}{\partial\boldsymbol{C}} = J\frac{\partial\Psi_{vol}}{\partial J}\boldsymbol{C}^{-1}\,. \tag{4.71}$$

From comparison of equations (4.71) and (4.41) it is clear that the volumetric strain energy function gives rise to a pressure term; that is,

$$p = \frac{\partial\Psi_{vol}}{\partial J}\,. \tag{4.72}$$

When the isochoric invariants are used, the isochoric stress takes the same form as presented in equation (4.47). The constitutive tensor is given by

$$\mathbb{C} = \bar{\mathbb{C}} + \mathbb{C}_{vol}\,, \qquad \bar{\mathbb{C}} = 4\frac{\partial^2 \bar{\Psi}}{\partial \boldsymbol{C}^2}\,, \qquad \mathbb{C}_{vol} = 4\frac{\partial^2 \Psi_{vol}}{\partial \boldsymbol{C}^2}\,, \tag{4.73}$$

where, if the isochoric invariants are used, the isochoric part $\bar{\mathbb{C}}$ is given by equation (4.51) and the volumetric part is given by

$$\mathbb{C}_{vol} = J\left[\frac{\partial \Psi_{vol}}{\partial J} + J\frac{\partial^2 \Psi_{vol}}{\partial J^2}\right]\boldsymbol{C}^{-1}\otimes\boldsymbol{C}^{-1} - 2J\frac{\partial \Psi_{vol}}{\partial J}\boldsymbol{C}^{-1}\odot\boldsymbol{C}^{-1}\,. \tag{4.74}$$

The Cauchy stress is determined by applying a push-forward operation to obtain

$$\boldsymbol{\sigma} = \bar{\boldsymbol{\sigma}} + \boldsymbol{\sigma}_{vol}\,, \qquad \bar{\boldsymbol{\sigma}} = J^{-1}\boldsymbol{F}\bar{\boldsymbol{S}}\boldsymbol{F}^T\,, \qquad \boldsymbol{\sigma}_{vol} = J^{-1}\boldsymbol{F}\boldsymbol{S}_{vol}\boldsymbol{F}^T\,, \tag{4.75}$$

where $\bar{\boldsymbol{\sigma}}$ is given in equation (4.58) and the volumetric Cauchy stress is given by

$$\boldsymbol{\sigma}_{vol} = \frac{\partial \Psi_{vol}}{\partial J}\boldsymbol{I}\,. \tag{4.76}$$

The Lie constitutive tensor is obtained by applying the push-forward operation in equation (3.88) to equation (4.73) which gives

$$\mathbb{c} = \bar{\mathbb{c}} + \mathbb{c}_{vol}\,, \tag{4.77}$$

where $\bar{\mathbb{c}}$ is given in equation (4.61) and the volumetric part is given by

$$\mathbb{c}_{vol} = J\left[\frac{\partial \Psi_{vol}}{\partial J} + J\frac{\partial^2 \Psi_{vol}}{\partial J^2}\right]\boldsymbol{I}\otimes\boldsymbol{I} - 2J\frac{\partial \Psi_{vol}}{\partial J}\boldsymbol{I}\odot\boldsymbol{I}\,. \tag{4.78}$$

The isochoric and volumetric Jaumann constitutive tensors can then be obtained, respectively, using

$$\bar{\mathbb{c}}^{\nabla} = \bar{\mathbb{c}} + \bar{\boldsymbol{\tau}}\odot\boldsymbol{I} + \boldsymbol{I}\odot\bar{\boldsymbol{\tau}}\,, \qquad \mathbb{c}^{\nabla}_{vol} = \mathbb{c}_{vol} + \boldsymbol{\tau}_{vol}\odot\boldsymbol{I} + \boldsymbol{I}\odot\boldsymbol{\tau}_{vol}\,. \tag{4.79}$$

The isochoric and volumetric Kirchhoff stress are given, respectively, by

$$\bar{\boldsymbol{\tau}} = 2\sum_{\substack{m=1\\m\neq 3}}^{8}\frac{\partial \bar{\Psi}}{\partial \bar{I}_m}\left[\bar{\boldsymbol{A}}_m + q_m\bar{I}_m\boldsymbol{I}\right]\,, \qquad \boldsymbol{\tau}_{vol} = J\frac{\partial \Psi_{vol}}{\partial J}\boldsymbol{I}\,. \tag{4.80}$$

Hence, the volumetric Jaumann constitutive tensor is given by

$$\mathbb{c}^{\nabla}_{vol} = J\left[\frac{\partial \Psi_{vol}}{\partial J} + J\frac{\partial^2 \Psi_{vol}}{\partial J^2}\right]\boldsymbol{I}\otimes\boldsymbol{I}\,, \tag{4.81}$$

and the isochoric Jaumann constitutive tensor is given in equation (4.67). Using these equations, a UMAT can be written for ABAQUS as shown in Algorithm 3.

To enforce zero stress for $\boldsymbol{F} = \boldsymbol{I}$, near-incompressible materials have the constraint

$$\left[\frac{\partial \Psi_{vol}}{\partial J}\right]_{\boldsymbol{F}=\boldsymbol{I}} = 0\,, \tag{4.82}$$

in addition to those presented in equation (4.69).

Algorithm 3 Procedure for determining stress and constitutive tensor required by ABAQUS for a near-incompressible material given the derivatives of its strain energy function.

```
procedure NEAR_INCOMPRESSIBLE_MATERIAL($\partial\bar{\Psi}/\partial\bar{I}$, $\partial^2\bar{\Psi}/\partial\bar{I}^2$, $\partial\Psi_{vol}/\partial J$, $\partial^2\Psi_{vol}/\partial J^2$ , $\boldsymbol{F}$, $\boldsymbol{a}_0$, $\boldsymbol{b}_0$)
    $J = \det \boldsymbol{F}$
    $\bar{\boldsymbol{F}} = \boldsymbol{F} J^{-1/3}$
    $\bar{I}(:) = \text{CALC\_I}(\bar{\boldsymbol{F}}, \boldsymbol{a}_0, \boldsymbol{b}_0)$
    $\bar{\boldsymbol{A}}(:, :, :) = \text{CALC\_A}(\bar{\boldsymbol{F}}, \boldsymbol{a}_0, \boldsymbol{b}_0)$
    $\bar{\mathbb{A}}(:, :, :) = \text{CALC\_BIG\_A}(\bar{\boldsymbol{F}}, \boldsymbol{a}_0, \boldsymbol{b}_0)$
    $\boldsymbol{q} = \begin{bmatrix} -1/3 & -2/3 & 0 & -1/3 & -2/3 & -1/3 & -2/3 & -1/3 \end{bmatrix}$
    for $m = 1, ..., 8$ do
        if $m \neq 3$ then
            $\boldsymbol{\sigma} = \boldsymbol{\sigma} + 2J^{-1} \frac{\partial\bar{\Psi}}{\partial\bar{I}_m} \left[\bar{\boldsymbol{A}}_m + q_m \bar{I}_m \boldsymbol{I}\right]$
            $\mathbb{C}_{\text{ABA}} = \mathbb{C}_{\text{ABA}} + 4J^{-1} \frac{\partial\bar{\Psi}}{\partial\bar{I}_m} \left[\bar{\mathbb{A}}_m + \frac{1}{2}\left[\bar{\boldsymbol{A}}_m \odot \boldsymbol{I} + \boldsymbol{I} \odot \bar{\boldsymbol{A}}_m\right] + q_m \left[\boldsymbol{I} \otimes \bar{\boldsymbol{A}}_m + \bar{\boldsymbol{A}}_m \otimes \boldsymbol{I}\right] + q_m^2 \bar{I}_m \boldsymbol{I} \otimes \boldsymbol{I}\right]$
            for $n = 1, ..., 8$ do
                if $n \neq 3$ then
                    $\mathbb{C}_{\text{ABA}} = \mathbb{C}_{\text{ABA}} + 4J^{-1} \frac{\partial^2\bar{\Psi}}{\partial\bar{I}_m \partial\bar{I}_n} \left[\bar{\boldsymbol{A}}_m \otimes \bar{\boldsymbol{A}}_n + q_m \bar{I}_m \boldsymbol{I} \otimes \bar{\boldsymbol{A}}_n + q_n \bar{I}_n \bar{\boldsymbol{A}}_m \otimes \boldsymbol{I} + q_m q_n \bar{I}_m \bar{I}_n \boldsymbol{I} \otimes \boldsymbol{I}\right]$
                end if
            end for
        end if
    end for
    $\boldsymbol{\sigma} = \boldsymbol{\sigma} + \frac{\partial\Psi_{vol}}{\partial J} \boldsymbol{I}$
    $\mathbb{C}_{\text{ABA}} = \mathbb{C}_{\text{ABA}} + \left[\frac{\partial\Psi_{vol}}{\partial J} + J \frac{\partial^2\Psi_{vol}}{\partial J^2}\right] \boldsymbol{I} \otimes \boldsymbol{I}$
    return $\boldsymbol{\sigma}$, $\mathbb{C}_{\text{ABA}}$
end procedure
```

4.1.4 Some material models

Some material models that are used in this thesis are presented in what follows.

Neo-Hookean model

One of the simplest near-incompressible material models is the Neo-Hookean model with a strain energy function of

$$\bar{\Psi} = G\left[\bar{I}_1 - 3\right], \qquad \Psi_{vol} = \frac{1}{D}\left[J^2 + \frac{1}{J^2} - 2\right]. \tag{4.83}$$

Here, G and D are material parameters. The first derivatives of its strain energy function are given by

$$\frac{\partial\bar{\Psi}}{\partial\bar{I}_1} = G\,, \qquad \frac{\partial\Psi_{vol}}{\partial J} = \frac{2}{D}\left[J - J^{-3}\right], \tag{4.84}$$

and the second derivatives are

$$\frac{\partial^2\bar{\Psi}}{\partial\bar{I}_1^2} = 0\,, \qquad \frac{\partial^2\Psi_{vol}}{\partial J^2} = \frac{6}{D}J^{-4}\,. \tag{4.85}$$

Gasser-Ogden-Holzapfel (GOH) model

The Gasser-Ogden-Holzapfel (GOH) model was originally developed for modelling artery walls [61]. However, it has since been used to model a number of soft collagenous tissues and gained significant popularity [62, 63, 64, 65]. The model's strain energy function is given by

$$\begin{gathered}\Psi = \bar{\Psi} + \Psi_{vol}\,, \qquad \bar{\Psi} = G(\bar{I}_1 - 3) + \frac{k_1}{2k_2}\left[\exp\left(k_2\bar{E}^2\right) - 1\right], \\ \Psi_{vol} = \frac{1}{D}\left[\frac{J^2-1}{2} - \ln J\right].\end{gathered} \tag{4.86}$$

Here, $\bar{E}$ is a pseudo-invariant defined by

$$\bar{E} := \left\langle\!\left\langle \kappa\left[\bar{I}_1 - 3\right] + [1 - 3\kappa]\left[\bar{I}_4 - 1\right]\right\rangle\!\right\rangle, \qquad \langle\langle\bullet\rangle\rangle := \begin{cases}\bullet & \bullet \geq 0, \\ 0 & \bullet \leq 0\,,\end{cases} \tag{4.87}$$

and $G, k_1, k_2 \geq 0$, $D > 0$, $\kappa \in [0,\, 1/3]$ are material parameters. The first derivatives of the strain energy function are

$$\begin{gathered}\frac{\partial\bar{\Psi}}{\partial\bar{I}_1} = G + k_1\kappa\bar{E}\exp\left(k_2\bar{E}^2\right), \qquad \frac{\partial\bar{\Psi}}{\partial\bar{I}_4} = k_1\left[1 - 3\kappa\right]\bar{E}\exp\left(k_2\bar{E}^2\right), \\ \frac{\partial\Psi_{vol}}{\partial J} = \frac{1}{D}\left[J - J^{-1}\right].\end{gathered} \tag{4.88}$$

The second derivatives of the strain energy function are

$$\begin{aligned}
\frac{\partial^2\bar{\Psi}}{\partial\bar{I}_1^2} &= k_1\kappa^2\text{sign}\left(\bar{E}\right)\exp\left(k_2\bar{E}^2\right)\left[1+2k_2\bar{E}^2\right]\,,\\
\frac{\partial^2\bar{\Psi}}{\partial\bar{I}_4^2} &= k_1\left[1-3\kappa\right]^2\text{sign}\left(\bar{E}\right)\exp\left(k_2\bar{E}^2\right)\left[1+2k_2\bar{E}^2\right]\,,\\
\frac{\partial^2\bar{\Psi}}{\partial\bar{I}_1\partial\bar{I}_4} &= k_1\kappa\left[1-3\kappa\right]\text{sign}\left(\bar{E}\right)\exp\left(k_2\bar{E}^2\right)\left[1+2k_2\bar{E}^2\right]\,,\\
\frac{\partial^2\Psi_{vol}}{\partial J^2} &= \frac{1}{D}\left[1+J^{-2}\right]\,,
\end{aligned}\tag{4.89}$$

where the function sign(•) is defined by

$$\text{sign}\left(\bullet\right) := \begin{cases} +1 & \bullet > 0\,,\\ 0 & \bullet = 0\,,\\ -1 & \bullet < 0\,. \end{cases}\tag{4.90}$$

Schröder-Neff polyconvex strain energy functions

Polyconvexity of the strain energy function is a sufficient condition for the existence of a solution and stability for initial boundary value problems containing hyperelastic materials (provide that the problem is otherwise properly posed). This condition was proposed by Ball [66] as an alternative to the stronger condition of convexity of the strain energy function with respect to the Green-Lagrange strain, which would preclude the physically observed phenomenon of bifurcation. A strain energy function Ψ is polyconvex if there exists a function W, $W:\mathbb{R}^{19}\mapsto\mathbb{R}$, such that

$$\Psi(\boldsymbol{F}) = W\left(\boldsymbol{F},\,\text{Adj}\boldsymbol{F},\,\det\boldsymbol{F}\right)\,,\tag{4.91}$$

and W is convex in its arguments. Here, Adj• denotes the adjoint of •.

Schröder and Neff determined an extensive (but not exhaustive) list of anisotropic polyconvex strain energy functions [67]. To create a highly flexible material model, a number of these strain energy functions have been selected and combined here:

$$\begin{aligned}
\Psi &= \sum_{j=1}^{7}\psi_j\,, & \psi_1 &= \sum_{i=1}^{n}\kappa_{(1)i}I_1^i\,,\\
\psi_2 &= \sum_{i=1}^{n}\kappa_{(2)i}I_2^i\,, & \psi_3 &= \kappa_{(3)0}I_3^{-1}+\sum_{i=1}^{n}\kappa_{(3)i}\left[I_3+I_3^{-1}-2\right]^i\,,\\
\psi_4 &= \sum_{i=1}^{n}\kappa_{(4)i}I_4^i\,, & \psi_5 &= \sum_{i=1}^{n}\kappa_{(5)i}\left[I_5-I_4I_1+I_2\right]^i\,,
\end{aligned}$$

$$\psi_6 = \sum_{i=1}^{n} \kappa_{(6)i} I_6^i \,, \qquad \psi_7 = \sum_{i=1}^{n} \kappa_{(7)i} \left[I_7 - I_6 I_1 + I_2 \right]^i \,. \tag{4.92}$$

Here, $\kappa_{(i)j}, \kappa_{(3)0} \geq 0\,,\ i = 1, ..., 7\,,\ j = 1, ..., n$ are material parameters. To determine the stress, one must determine the partial derivatives of the strain energy function:

$$\begin{aligned}
\frac{\partial \Psi}{\partial I_1} &= \sum_{i=1}^{n} i \left[\kappa_{(1)i} I_1^{i-1} - \kappa_{(5)i} I_4 \left[I_5 - I_4 I_1 + I_2 \right]^{i-1} - \kappa_{(7)i} I_6 \left[I_7 - I_6 I_1 + I_2 \right]^{i-1} \right] \,, \\
\frac{\partial \Psi}{\partial I_2} &= \sum_{i=1}^{n} i \left[\kappa_{(2)i} I_2^{i-1} + \kappa_{(5)i} \left[I_5 - I_4 I_1 + I_2 \right]^{i-1} + \kappa_{(7)i} \left[I_7 - I_6 I_1 + I_2 \right]^{i-1} \right] \,, \\
\frac{\partial \Psi}{\partial I_3} &= -\kappa_{(3)0} I_3^{-2} + \sum_{i=1}^{n} i \kappa_{(3)i} \left[I_3 + I_3^{-1} - 2 \right]^{i-1} \left[1 - I_3^{-2} \right] \,, \\
\frac{\partial \Psi}{\partial I_4} &= \sum_{i=1}^{n} i \left[\kappa_{(4)i} I_4^{i-1} - \kappa_{(5)i} I_1 \left[I_5 - I_4 I_1 + I_2 \right]^{i-1} \right] \,, \\
\frac{\partial \Psi}{\partial I_5} &= \sum_{i=1}^{n} i \kappa_{(5)i} \left[I_5 - I_4 I_1 + I_2 \right]^{i-1} \,, \\
\frac{\partial \Psi}{\partial I_6} &= \sum_{i=1}^{n} i \left[\kappa_{(6)i} I_6^{i-1} - \kappa_{(7)i} I_1 \left[I_7 - I_6 I_1 + I_2 \right]^{i-1} \right] \,, \\
\frac{\partial \Psi}{\partial I_7} &= \sum_{i=1}^{n} i \kappa_{(7)i} \left[I_7 - I_6 I_1 + I_2 \right]^{i-1} \,.
\end{aligned} \tag{4.93}$$

For the material model to be stress-free in an undeformed state, equations (4.27)–(4.30) must be satisfied. Applying equation (4.27) reveals that $\kappa_{(3)0}$ is not independent. Rather, it is determined by the other material parameters as follows:

$$\begin{aligned}
\left[\frac{\partial \Psi}{\partial I_1} + 2 \frac{\partial \Psi}{\partial I_2} + \frac{\partial \Psi}{\partial I_3} \right]_{\boldsymbol{F}=\boldsymbol{I}} &= -\kappa_{(3)0} + \sum_{i=1}^{n} i \left[3^{i-1} \left[\kappa_{(1)i} + 2\kappa_{(2)i} \right] + \left[\kappa_{(5)i} + \kappa_{(7)i} \right] \right] = 0 \\
\Rightarrow \kappa_{(3)0} &= \sum_{i=1}^{n} i \left[3^{i-1} \left[\kappa_{(1)i} + 2\kappa_{(2)i} \right] + \left[\kappa_{(5)i} + \kappa_{(7)i} \right] \right] \,.
\end{aligned} \tag{4.94}$$

Similarly, to satisfy equation (4.28), one of the parameters out of $\kappa_{(4)i}$ and $\kappa_{(5)i}$ must be defined by the others; that is,

$$\begin{aligned}
\left[\frac{\partial \Psi}{\partial I_4} + 2 \frac{\partial \Psi}{\partial I_5} \right]_{\boldsymbol{F}=\boldsymbol{I}} &= \sum_{i=1}^{n} i \left[\kappa_{(4)i} - \kappa_{(5)i} \right] = 0 \\
\Rightarrow \kappa_{(4)1} &= \kappa_{(5)1} + \sum_{i=2}^{n} i \left[\kappa_{(5)i} - \kappa_{(4)i} \right] \,.
\end{aligned} \tag{4.95}$$

A similar requirement is needed to satisfy equation (4.29); that is,

$$\kappa_{(6)1} = \kappa_{(7)1} + \sum_{i=2}^{n} i \left[\kappa_{(7)i} - \kappa_{(6)i} \right] \,. \tag{4.96}$$

To implement this model in a UMAT, the second derivatives of the strain energy function are required. These are determined using the symbolic manipulation library `Sympy` in the programming language `Python`. Then, the FORTRAN code required for the UMAT was written using a code generating script which is written in `Python`. This avoids implementation errors as the second derivatives, which are displayed in Appendix B.1, are long and cumbersome.

4.2 Linear elasticity

Linear elasticity is typically associated with small deformations $||\mathrm{Grad}\boldsymbol{u}|| << 1$. Hence, the stress measures are equal to the first order approximation, that is,

$$\boldsymbol{\sigma} = \boldsymbol{S} = \boldsymbol{P} = \boldsymbol{\tau}\,, \tag{4.97}$$

and the linear strain is equivalent to the Green-Lagrange strain (see equation (3.30)), that is,

$$\boldsymbol{\varepsilon} = \boldsymbol{E}\,. \tag{4.98}$$

In this case, equation (4.11) reduces to Hooke's law: the strain is linearly related to the stress by a fourth-order elasticity tensor $\mathbb{C}$; that is,

$$\boldsymbol{\sigma} = \mathbb{C}\boldsymbol{\varepsilon}\,. \tag{4.99}$$

Hence, the strain energy is given by

$$\Psi = \frac{1}{2}\boldsymbol{\varepsilon} : \mathbb{C}\boldsymbol{\varepsilon}\,. \tag{4.100}$$

4.2.1 Isotropy

In the general case, $\mathbb{C}$ has 81 independent components. However, it can be shown that for isotropic small strain behaviour this reduces to 2. In this case, the stress is given by

$$\boldsymbol{\sigma} = \boldsymbol{I}\lambda\,\mathrm{tr}\boldsymbol{\varepsilon} + 2\mu\boldsymbol{\varepsilon}\,. \tag{4.101}$$

Here, λ and μ are referred to as the Lamé parameters. The Lamé parameters are related to the engineering material parameters of Young's modulus E and Poisson's ratio ν by

$$\lambda = \frac{E\nu}{[1+\nu]\,[1-2\nu]}\,, \qquad \mu = \frac{E}{2\,[1+\nu]}\,. \tag{4.102}$$

4.2.2 Transverse isotropy

For transversely isotropic small strain behaviour, the number of independent components in $\mathbb{C}$ reduces to 5 [68]. Then, the stress is related to the strain by

$$\boldsymbol{\sigma} = \boldsymbol{I}\lambda \mathrm{tr}\boldsymbol{\varepsilon} + \frac{1}{2}\mu\boldsymbol{\varepsilon} + \beta\left[\boldsymbol{M} : \boldsymbol{\varepsilon}\right]\boldsymbol{M} + \alpha\left[[\boldsymbol{M} : \boldsymbol{\varepsilon}]\boldsymbol{I} + \mathrm{tr}\boldsymbol{\varepsilon}\boldsymbol{M}\right] + 2\left[\mu_l - \mu_t\right]\left[\boldsymbol{\varepsilon}\boldsymbol{M} + \boldsymbol{M}\boldsymbol{\varepsilon}\right] , \quad (4.103)$$

where β, α, μ_l and μ_t are material parameters and $\boldsymbol{M} = \boldsymbol{a}_0 \otimes \boldsymbol{a}_0$. Equation (4.103) is represented equivalently by

$$\begin{bmatrix} \varepsilon_{11} \\ \varepsilon_{22} \\ \varepsilon_{33} \\ 2\varepsilon_{12} \\ 2\varepsilon_{13} \\ 2\varepsilon_{23} \end{bmatrix} = \underbrace{\begin{bmatrix} \frac{1}{E_t} & -\frac{\nu_t}{E_t} & -\frac{\nu_l}{E_l} & 0 & 0 & 0 \\ -\frac{\nu_t}{E_t} & \frac{1}{E_t} & -\frac{\nu_l}{E_l} & 0 & 0 & 0 \\ -\frac{\nu_l}{E_l} & -\frac{\nu_l}{E_l} & \frac{1}{E_l} & 0 & 0 & 0 \\ 0 & 0 & 0 & \frac{1}{\mu_t} & 0 & 0 \\ 0 & 0 & 0 & 0 & \frac{1}{\mu_l} & 0 \\ 0 & 0 & 0 & 0 & 0 & \frac{1}{\mu_l} \end{bmatrix}}_{\mathbb{S}} \begin{bmatrix} \sigma_{11} \\ \sigma_{22} \\ \sigma_{33} \\ \sigma_{12} \\ \sigma_{13} \\ \sigma_{23} \end{bmatrix} . \quad (4.104)$$

Here, $\bullet_l$ and $\bullet_t$ denote quantities in the longitudinal (preferred) and transverse (plane of isotropy) directions, respectively, $\mathbb{S}$ denotes the compliance tensor and μ, E, and ν denote the engineering parameters of shear modulus, Young's modulus, and Poisson's ratio, respectively. Additionally, the relation

$$\mu_t = \frac{E_t}{2[1 + \nu_t]} \quad (4.105)$$

between the transverse quantities holds.

4.3 Viscoelasticity

Viscoelasticity refers to behaviour in which the material responds to both the deformation and rate of deformation. In what follows, a simple 1D model for viscoelasticity is introduced. Then, a 3D model using a similar mathematical structure to the 1D case is developed.

4.3.1 One dimensional small strain viscoelasticity

Viscoelasticity is modelled in 1D by postulating a mechanical device that contains a viscous dashpot. In particular, a Maxwell solid is used, an example of which is presented in Figure 4.1. This is commonly referred to as the standard solid model. It consists of a spring that captures the long time-scale response of the material, which is connected in parallel with a Maxwell branch. The Maxwell branch consists of a spring and dashpot connected in series.

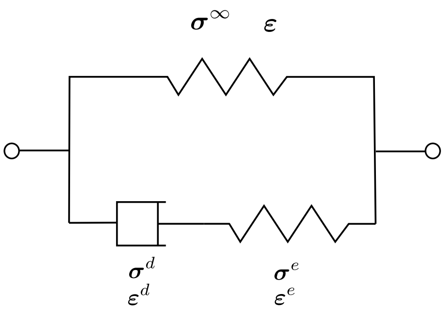

Figure 4.1: Schematic diagram of a one-dimensional mechanical device representing a Maxwell solid.

Here, σ^{∞}, σ^{d}, and σ^{e} denote the stress in the long time-scale spring, the dashpot, and the Maxwell branch spring, respectively. Additionally, ε, ε^{d}, and ε^{e} denote the strain in the long time-scale spring, the dashpot, and the Maxwell branch spring, respectively. Note also that, the strain in the long time-scale spring is equal to the strain of the device as a whole. It is asserted that each spring and dashpot has a cross-sectional area of 1. Hence, using elementary mechanics (force-balance, Newton's third law, and 1D kinematics) one obtains

$$\sigma = \sigma^{\infty} + \sigma^{v}\,, \tag{4.106}$$

$$\varepsilon = \varepsilon^{d} + \varepsilon^{e}\,, \tag{4.107}$$

$$\sigma^{v} := \sigma^{d}\left(\dot{\varepsilon}^{d}\right) = \sigma^{e}\left(\varepsilon^{e}\right)\,. \tag{4.108}$$

Here, the symbol σ^{v} is added to denote the viscous stress since $\sigma^{e} = \sigma^{d}$. Note that, from equation (4.107) one can obtain

$$\dot{\varepsilon} = \dot{\varepsilon}^{d} + \dot{\varepsilon}^{e}\,. \tag{4.109}$$

Equations (4.106)-(4.108) may be rewritten as

$$\sigma\left(\varepsilon, \varepsilon^{d}\right) = \sigma^{\infty}\left(\varepsilon\right) + \sigma^{e}\left(\varepsilon - \varepsilon^{d}\right)\,, \tag{4.110}$$

$$\sigma^{d}\left(\dot{\varepsilon}^{d}\right) = \sigma^{e}\left(\varepsilon - \varepsilon^{d}\right)\,. \tag{4.111}$$

Hence, the resulting constitutive equation (equation (4.110)) is dependent on the strain ε and the history variable ε^{d}, which is determined by satisfying the evolution equation (equation (4.111)). The constitutive relation is completely defined by choosing constitutive relations for each component in the device. Linear relations are chosen; that is,

$$\begin{aligned} \sigma^{\infty}\left(\varepsilon\right) &= E^{\infty}\varepsilon\,, \\ \sigma^{e}\left(\varepsilon^{e}\right) &= E^{e}\varepsilon^{e}\,, \\ \sigma^{d}\left(\dot{\varepsilon}^{d}\right) &= \eta\dot{\varepsilon}^{d}\,. \end{aligned} \tag{4.112}$$

Here, E^{∞}, E^{e}, and η are constant material parameters. In the mathematical development that follows, it is convenient to adopted two other viscoelastic material parameters β and τ which are defined so that $E^{e} = \beta E^{\infty}$, $\eta = \tau\beta E^{\infty}$, and

$$\begin{aligned} \sigma^{e}\left(\varepsilon^{e}\right) &= \underbrace{\beta E^{\infty}}_{E^{e}}\varepsilon^{e}\,, \\ \sigma^{d}\left(\dot{\varepsilon}^{d}\right) &= \underbrace{\tau\beta E^{\infty}}_{\eta}\dot{\varepsilon}^{d}\,. \end{aligned} \tag{4.113}$$

Here τ is the relaxation time of the Maxwell branch and β is the relative stiffness of the spring in the Maxwell branch in comparison to the long times-scale spring. With the constitutive models for each component in hand, the evolution equation (equation (4.111)) can be satisfied analytically as follows. Substitution of equations (4.109) and (4.113) into equation (4.111) gives

$$\tau\beta\underbrace{E^{\infty}\dot{\varepsilon}}_{\dot{\sigma}^{\infty}} - \tau\underbrace{\beta E^{\infty}\dot{\varepsilon}^{e}}_{\dot{\sigma}^{e}=\dot{\sigma}^{v}} = \underbrace{\sigma^{e}}_{\sigma^{v}}\,. \tag{4.114}$$

Equation (4.114) may be rewritten as

$$\beta\dot{\sigma}^{\infty} = \frac{1}{\tau}\sigma^{v} + \dot{\sigma}^{v}\,. \tag{4.115}$$

Multiplication of both sides of equation (4.115) by the integration factor $\exp(t/\tau)$ gives

$$\exp\left(\frac{t}{\tau}\right)\beta\dot{\sigma}^{\infty} = \frac{\mathrm{d}}{\mathrm{d}t}\left[\exp\left(\frac{t}{\tau}\right)\sigma^{v}\right]\,. \tag{4.116}$$

Finally, one obtains an analytical expression for the viscous stress by integrating equation (4.116) on both sides and rearranging to give

$$\sigma^{v} = \beta\int_{-\infty}^{t}\exp\left(-\frac{t-s}{\tau}\right)\dot{\sigma}^{\infty}\,\mathrm{d}s\,. \tag{4.117}$$

Substitution of equations (4.117) and (4.112) into equation (4.110) gives

$$\sigma = E^{\infty}\int_{-\infty}^{t}\left[1+\exp\left(-\frac{t-s}{\tau}\right)\right]\dot{\varepsilon}\,\mathrm{d}s\,. \tag{4.118}$$

Hence, a closed form equation for the stress is obtained by solving the evolution equation (4.111).

To determine the dissipation caused by the viscous dashpot one first constructs the strain energy function to be

$$\Psi = \underbrace{\frac{1}{2}E^{\infty}\varepsilon^{2}}_{\Psi^{\infty}} + \underbrace{\frac{1}{2}E^{e}\left[\varepsilon^{e}\right]^{2}}_{\Psi^{v}}\,. \tag{4.119}$$

Then, as per equation (4.6), taking the derivative of equation (4.119) with respect to the history variables gives

$$D_{\text{int}} = -\frac{\partial \Psi}{\partial \varepsilon^d}\dot{\varepsilon}^d = -\underbrace{\frac{\partial \Psi^e}{\partial \varepsilon^e}}_{\sigma^e=\sigma^d}\frac{\partial \varepsilon^e}{\partial \varepsilon^d}\dot{\varepsilon}^d = -\underbrace{\left[\sigma^d\right]}_{\eta\dot{\varepsilon}^d}[-1]\,\dot{\varepsilon}^d = \eta\left[\dot{\varepsilon}^d\right]^2 \geq 0\,. \tag{4.120}$$

Hence, for the dissipation to be non-negative, that is to satisfy the second law of thermodynamics, it is required that

$$\eta \geq 0\,. \tag{4.121}$$

4.3.2 Three-dimensional finite strain linear viscoelasticity

Finite strain viscoelastic framework

Using the 1D viscoelastic model as motivation (see equation (4.106)), one assumes that the second Piola-Kirchhoff stress is additively decomposed into long time-scale $\boldsymbol{S}^{\infty}$ and viscous $\boldsymbol{S}^{v}$ parts to construct a three-dimensional viscoelastic framework; that is,

$$\boldsymbol{S} = \boldsymbol{S}^{\infty} + \boldsymbol{S}^{v}\,. \tag{4.122}$$

For biological materials, one assumes that the viscous material behaviour results from interstitial fluid. Since this fluid is incompressible, one postulates that the viscous stress depends on the isochoric deformation and so $\bar{\boldsymbol{S}}^{v}$ is used to denote the viscous stress [54]. It then becomes convenient to take an isochoric $\bar{\boldsymbol{S}}^{\infty}$ and volumetric $\boldsymbol{S}^{\infty}_{vol}$ split of the long time-scale stress. Hence, the second Piola-Kirchhoff stress is written as

$$\boldsymbol{S} = \bar{\boldsymbol{S}}^{\infty} + \boldsymbol{S}^{\infty}_{vol} + \bar{\boldsymbol{S}}^{v}\,. \tag{4.123}$$

Additionally, it is assumed that the isochoric deformation gradient can be multiplicatively decomposed into an elastic $\bar{\boldsymbol{F}}^{e}$ and a viscous $\bar{\boldsymbol{F}}^{d}$ part; that is,

$$\bar{\boldsymbol{F}} = \bar{\boldsymbol{F}}^{e}\bar{\boldsymbol{F}}^{d}\,. \tag{4.124}$$

This is analogous to many finite strain elastoplasticity models where the deformation gradient is decomposed into an elastic and a plastic part [69]. Here, $\bar{\boldsymbol{F}}^{d}$ represents the map of line elements from the reference configuration to a viscous intermediate configuration $\bar{\Omega}^d$, as shown in Figure 4.2, and $\bar{\boldsymbol{F}}^{e}$ represents the map of line elements from the viscous intermediate configuration to the isochoric current configuration. It is then useful to define the following kinematic quantities:

$$\bar{\boldsymbol{C}}^{e} := \left[\bar{\boldsymbol{F}}^{e}\right]^{T}\bar{\boldsymbol{F}}^{e}\,, \qquad \bar{\boldsymbol{E}}^{e} := \frac{1}{2}\left[\bar{\boldsymbol{C}}^{e} - \boldsymbol{I}\right]\,, \qquad \bar{\boldsymbol{C}}^{d} := \left[\bar{\boldsymbol{F}}^{d}\right]^{T}\bar{\boldsymbol{F}}^{d}\,, \qquad \bar{\boldsymbol{E}}^{d} := \frac{1}{2}\left[\bar{\boldsymbol{C}}^{d} - \boldsymbol{I}\right]\,. \tag{4.125}$$

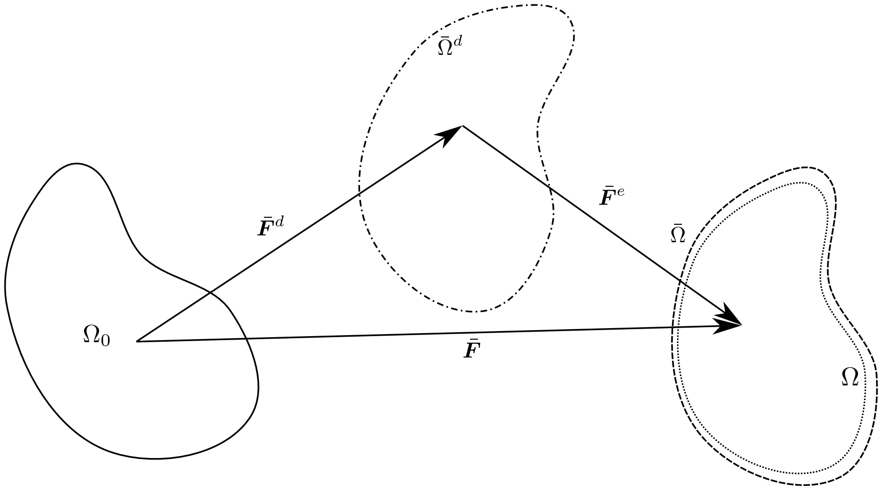

Figure 4.2: Illustration of the reference configuration (solid line), intermediate viscous configuration (dot-dashed line), isochoric configuration (dashed line), and current configuration (dotted line).

Using the 1D Maxwell model as motivation, an evolution equation is constructed by equating a viscous stress to an elastic stress (see equation (4.111)). It is natural for the viscous stress to depend on $\dot{\bar{\boldsymbol{E}}}^d$. However, $\bar{\boldsymbol{E}}^e$ in not used to define the elastic stress as $\bar{\boldsymbol{F}}^e$ is defined relative to a moving configuration and so it is not objective. To obtain an objective strain measure for the elastic stress, a pull-back operation is applied as follows:

$$\bar{\boldsymbol{E}}^e_0 := \left[\bar{\boldsymbol{F}}^d\right]^T \bar{\boldsymbol{E}}^e \bar{\boldsymbol{F}}^d = \frac{1}{2}\left[\bar{\boldsymbol{C}} - \bar{\boldsymbol{C}}^d\right] = \bar{\boldsymbol{E}} - \bar{\boldsymbol{E}}^d \,. \tag{4.126}$$

It is clear that $\bar{\boldsymbol{E}}^e_0$ is objective since both $\bar{\boldsymbol{E}}$ and $\bar{\boldsymbol{E}}^d$ are objective. Additionally, note the similarity between equation (4.126) and its small strain 1D equivalent (equation (4.107)).

A suitable finite strain viscoelastic framework is then constructed by choosing $\bar{\boldsymbol{E}}^d$ as a history variable and asserting the following constitutive and evolution equations, respectively:

$$\boldsymbol{S}\left(\boldsymbol{E},\, \bar{\boldsymbol{E}}^d\right) = \bar{\boldsymbol{S}}^\infty\left(\boldsymbol{E}\right) + \boldsymbol{S}^\infty_{vol}\left(\boldsymbol{E}\right) + \bar{\boldsymbol{S}}^e\left(\bar{\boldsymbol{E}} - \bar{\boldsymbol{E}}^d\right) \,, \tag{4.127}$$

$$\bar{\boldsymbol{S}}^v := \bar{\boldsymbol{S}}^d\left(\dot{\bar{\boldsymbol{E}}}^d\right) = \bar{\boldsymbol{S}}^e\left(\bar{\boldsymbol{E}} - \bar{\boldsymbol{E}}^d\right) \,. \tag{4.128}$$

Here, $\bar{\boldsymbol{S}}^d$ denotes the viscous ‘dashpot’ stress, $\bar{\boldsymbol{S}}^e$ denotes the elastic ‘spring’ stress, and $\bar{\boldsymbol{S}}^v = \bar{\boldsymbol{S}}^d = \bar{\boldsymbol{S}}^e$ has been used, which is motivated by the 1D model (equation (4.108)).

Finite strain linear viscoelasticity

The viscoelastic model is completed by choosing appropriate equations for $\bar{\boldsymbol{S}}^\infty$, $\boldsymbol{S}^\infty_{vol}$, $\bar{\boldsymbol{S}}^e$, and $\bar{\boldsymbol{S}}^d$. In this work, the material is assumed to be close to thermodynamic equilibrium and so $\bar{\boldsymbol{S}}^e$ and $\bar{\boldsymbol{S}}^d$ are defined relative to the long time-scale stress as follows:

$$\dot{\bar{\boldsymbol{S}}}^\infty = \bar{\mathbb{C}}^\infty \dot{\bar{\boldsymbol{E}}}^\infty \,, \tag{4.129}$$

$$\dot{\bar{\boldsymbol{S}}}^e = \beta \bar{\mathbb{C}}^\infty \dot{\bar{\boldsymbol{E}}}_0^e \,, \tag{4.130}$$

$$\bar{\boldsymbol{S}}^d = \tau \beta \bar{\mathbb{C}}^\infty \dot{\bar{\boldsymbol{E}}}^d \,. \tag{4.131}$$

The viscoelastic model that results from these constitutive choices is referred to as finite strain linear viscoelasticity [70, 54]. Substitution of equations (4.131) and (4.126) into equation (4.128) gives

$$\tau\beta \underbrace{\bar{\mathbb{C}}^\infty \dot{\bar{\boldsymbol{E}}}}_{\dot{\bar{\boldsymbol{S}}}^\infty} - \tau \underbrace{\beta \bar{\mathbb{C}}^\infty \dot{\bar{\boldsymbol{E}}}_0^e}_{\dot{\bar{\boldsymbol{S}}}^e = \dot{\bar{\boldsymbol{S}}}^v} = \bar{\boldsymbol{S}}^v \,, \tag{4.132}$$

which can be developed to obtain

$$\beta \dot{\bar{\boldsymbol{S}}}^\infty = \frac{1}{\tau} \bar{\boldsymbol{S}}^v + \dot{\bar{\boldsymbol{S}}}^v \,. \tag{4.133}$$

Equation (4.133) can then be solved by introducing an integration factor as done in equations (4.115)-(4.117) to obtain

$$\bar{\boldsymbol{S}}^v = \beta \int_0^t \exp\left(-\frac{t-s}{\tau}\right) \dot{\bar{\boldsymbol{S}}}^\infty \mathrm{d}s \,. \tag{4.134}$$

Hence, if the constitutive equations (4.130) and (4.131) are used for the viscoelastic part of the stress then the stress is given by

$$\boldsymbol{S}\left(\boldsymbol{E},\right) = \bar{\boldsymbol{S}}^\infty\left(\boldsymbol{E}\right) + \boldsymbol{S}^\infty_{vol}\left(\boldsymbol{E}\right) + \beta \int_0^t \exp\left(-\frac{t-s}{\tau}\right) \dot{\bar{\boldsymbol{S}}}^\infty \mathrm{d}s \,, \tag{4.135}$$

which is obtained by solving the evolution equation analytically.

Thermodynamic considerations

The strain energy for the viscoelastic model presented above is given by

$$\Psi = \bar{\Psi}^\infty + \Psi^\infty_{vol} + \bar{\Psi}^v \,, \tag{4.136}$$

where each term is defined so that

$$\begin{gathered} \boldsymbol{S} = \bar{\boldsymbol{S}}^\infty + \boldsymbol{S}^\infty_{vol} + \bar{\boldsymbol{S}}^v \,, \\ \bar{\boldsymbol{S}}^\infty = \frac{\partial \bar{\Psi}^\infty}{\partial \boldsymbol{E}} \,, \qquad \boldsymbol{S}^\infty_{vol} = \frac{\partial \Psi^\infty_{vol}}{\partial \boldsymbol{E}} \,, \qquad \bar{\boldsymbol{S}}^v = \frac{\partial \bar{\Psi}^v}{\partial \boldsymbol{E}} \,. \end{gathered} \tag{4.137}$$

As per equation (4.6), the dissipation is given by

$$D_{\text{int}} = -\frac{\partial \bar{\Psi}^v}{\partial \bar{\boldsymbol{E}}^d} : \dot{\bar{\boldsymbol{E}}}^d \geq 0 \,. \tag{4.138}$$

The chain rule can be used to obtain

$$D^\alpha_{\text{int}} = -\frac{\partial \bar{\Psi}^v}{\partial \bar{\boldsymbol{E}}^d} : \dot{\bar{\boldsymbol{E}}}^d = -\frac{\partial \bar{\Psi}^v}{\partial \boldsymbol{E}} : \frac{\partial \boldsymbol{E}}{\partial \boldsymbol{C}} : \frac{\partial \boldsymbol{C}}{\partial \bar{\boldsymbol{C}}} : \frac{\partial \bar{\boldsymbol{C}}}{\partial \bar{\boldsymbol{E}}_0^e} : \frac{\partial \bar{\boldsymbol{E}}_0^e}{\partial \bar{\boldsymbol{E}}^d} : \dot{\bar{\boldsymbol{E}}}^d, \tag{4.139}$$

where the partial derivatives are given by

$$\begin{aligned} \frac{\partial \boldsymbol{E}}{\partial \boldsymbol{C}} &= \frac{1}{2}\boldsymbol{I} \odot \boldsymbol{I}\,, \quad \frac{\partial \boldsymbol{C}}{\partial \bar{\boldsymbol{C}}} = \det(\boldsymbol{C})^{1/3}\boldsymbol{I} \odot \boldsymbol{I}\,, \\ \frac{\partial \bar{\boldsymbol{C}}}{\partial \bar{\boldsymbol{E}}_0^e} &= 2\boldsymbol{I} \odot \boldsymbol{I}\,, \quad \frac{\partial \bar{\boldsymbol{E}}_0^e}{\partial \bar{\boldsymbol{E}}^d} = -\boldsymbol{I} \odot \boldsymbol{I}\,. \end{aligned} \tag{4.140}$$

Substitution of the bottom right equation of (4.137) and equations (4.140) into equation (4.139) reveals that the dissipation is given by

$$D_{\text{int}}^{\alpha} = \det(\boldsymbol{C})^{1/3}\bar{\boldsymbol{S}}^v : \dot{\bar{\boldsymbol{E}}}^d \geq 0\,. \tag{4.141}$$

This holds irrespective of the choice of constitutive relations chosen for $\bar{\boldsymbol{S}}^e$ and $\bar{\boldsymbol{S}}^d$. If one chooses $\bar{\boldsymbol{S}}^d$ to be defined by equation (4.131), then the dissipation is given by

$$D_{\text{int}}^{\alpha} = \tau\beta \det(\boldsymbol{C})^{1/3}\dot{\bar{\boldsymbol{E}}}^d : \bar{\mathbb{C}}^{\infty}\dot{\bar{\boldsymbol{E}}}^d \geq 0\,. \tag{4.142}$$

Hence, it is required that $\tau\beta\bar{\mathbb{C}}$ is positive semi-definite to satisfy the Clausius-Duhem inequality.

In the following chapters, the significance of the viscous material behaviour is frequently compared with that of the long time-scale behaviour. This is done by comparing the non-equilibrium energy, that is,

$$\Phi = \int_0^t \bar{\boldsymbol{S}}^v : \dot{\boldsymbol{E}}\, ds\,, \tag{4.143}$$

with the long time-scale strain energy, that is,

$$\Psi^{\infty} = \bar{\Psi}^{\infty} + \Psi_{vol}^{\infty}\,. \tag{4.144}$$

Generalized Maxwell finite strain linear viscoelasticity

The model presented in equation (4.135) can be generalized further by postulating N_m intermediate configurations evolving independently of each other. This is analogous to having N_m Maxwell branches in parallel in the 1D case, which is termed a generalized Maxwell model. The viscous strains for each intermediate configuration, that is $\bar{\boldsymbol{E}}_1^d, ..., \bar{\boldsymbol{E}}_{N_m}^d$, are then used as the history variables. The stress is then given by

$$\boldsymbol{S}\left(\boldsymbol{E}, \bar{\boldsymbol{E}}_1^d, ..., \bar{\boldsymbol{E}}_{N_m}^d\right) = \bar{\boldsymbol{S}}^{\infty}\left(\boldsymbol{E}\right) + \boldsymbol{S}_{vol}^{\infty}\left(\boldsymbol{E}\right) + \sum_{\alpha=1}^{N_m} \bar{\boldsymbol{S}}_{\alpha}^e\left(\bar{\boldsymbol{E}} - \bar{\boldsymbol{E}}_{\alpha}^d\right)\,, \tag{4.145}$$

which must be accompanied by N_m evolution equations to define the history variables; those are,

$$\begin{aligned} \bar{\boldsymbol{S}}_1^d\left(\dot{\bar{\boldsymbol{E}}}_1^d\right) &= \bar{\boldsymbol{S}}_1^e\left(\bar{\boldsymbol{E}} - \bar{\boldsymbol{E}}_1^d\right)\,, \\ &\vdots \\ \bar{\boldsymbol{S}}_{N_m}^d\left(\dot{\bar{\boldsymbol{E}}}_{N_m}^d\right) &= \bar{\boldsymbol{S}}_{N_m}^e\left(\bar{\boldsymbol{E}} - \bar{\boldsymbol{E}}_{N_m}^d\right)\,. \end{aligned} \tag{4.146}$$

Similarly to the case of a single Maxwell branch, the following constitutive relations for the viscoelastic stresses are chosen:

$$\dot{\bar{\boldsymbol{S}}}^e_\alpha = \beta_\alpha \bar{\mathbb{C}}^\infty \left[\dot{\bar{\boldsymbol{E}}} - \dot{\bar{\boldsymbol{E}}}^d_\alpha \right] , \tag{4.147}$$

$$\text{(no sum) } \bar{\boldsymbol{S}}^d_\alpha = \tau_\alpha \beta_\alpha \bar{\mathbb{C}}^\infty \dot{\bar{\boldsymbol{E}}}^d_\alpha , \tag{4.148}$$

where τ_α and β_α are material parameters. With these constitutive relations in hand, solving each evolution equation leads to

$$\bar{\boldsymbol{S}}^v_\alpha = \beta_\alpha \int_0^t \exp\left(-\frac{t-s}{\tau_\alpha}\right) \dot{\bar{\boldsymbol{S}}}^\infty \mathrm{d}s , \tag{4.149}$$

and so the stress is given by

$$\boldsymbol{S}\left(\boldsymbol{E}\right) = \bar{\boldsymbol{S}}^\infty\left(\boldsymbol{E}\right) + \boldsymbol{S}^\infty_{vol}\left(\boldsymbol{E}\right) + \sum_{\alpha=1}^{N_m} \beta_\alpha \int_0^t \exp\left(-\frac{t-s}{\tau_\alpha}\right) \dot{\bar{\boldsymbol{S}}}^\infty \mathrm{d}s . \tag{4.150}$$

Numerical implementation

Here, a temporal discretization of equation (4.150) is presented, which is required for implementation of the model in a finite element solver such as ABAQUS. To do so, a partitioning of the time domain is first constructed as follows:

$$0 = t_0 < t_1 < ... < t_n < t_{n+1} = t . \tag{4.151}$$

The time increment Δt_{n+1} and the mid-step time $t_{n+0.5}$ are then defined, respectively, as

$$\Delta t_{n+1} := t_{n+1} - t_n , \qquad t_{n+0.5} := \frac{1}{2}\left[t_{n+1} + t_n\right] . \tag{4.152}$$

Splitting the integration in equation (4.150) up over the current time-step and all the previous time-steps gives

$$\bar{\boldsymbol{S}}^v_\alpha = \beta_\alpha \int_{t_n}^{t_{n+1}} \exp\left(-\frac{t_{n+1}-s}{\tau_\alpha}\right) \dot{\bar{\boldsymbol{S}}}^\infty \mathrm{d}s + \beta_\alpha \int_0^{t_n} \exp\left(-\frac{t_{n+1}-s}{\tau_\alpha}\right) \dot{\bar{\boldsymbol{S}}}^\infty \mathrm{d}s . \tag{4.153}$$

The integration over the current time-step can be approximated using a mid-point integration scheme, that is

$$\int_{t_n}^{t_{n+1}} \bullet\left(s\right) \mathrm{d}s \approx \int_{t_n}^{t_{n+1}} \bullet\left(t_{n+0.5}\right) \mathrm{d}s , \tag{4.154}$$

to obtain

$$\begin{aligned} \beta_\alpha \int_{t_n}^{t_{n+1}} \exp\left(-\frac{t_{n+1}-s}{\tau_\alpha}\right) \dot{\bar{\boldsymbol{S}}}^\infty \mathrm{d}s &\approx \beta_\alpha \xi_{\alpha(n+1)} \left[\bar{\boldsymbol{S}}^\infty_{n+1} - \bar{\boldsymbol{S}}^\infty_n\right] , \\ \xi_{\alpha(n+1)} &:= \exp\left(-\frac{\Delta t_{n+1}}{2\tau_\alpha}\right) , \end{aligned} \tag{4.155}$$

where $\bar{\boldsymbol{S}}^{\infty}_{n+1}$ and $\bar{\boldsymbol{S}}^{\infty}_{n}$ are the isochoric long time-scale stresses at time-step $n+1$ and n, respectively. The right-hand side term in equation (4.153) can be developed to obtain

$$\begin{aligned}
&\beta_\alpha \int_0^{t_n} \exp\left(-\frac{t_{n+1}-s}{\tau_\alpha}\right) \dot{\bar{\boldsymbol{S}}}^{\infty} \mathrm{d}s \\
&= \beta_\alpha \exp\left(-\frac{\Delta t_{n+1}}{\tau_\alpha}\right) \int_0^{t_n} \exp\left(-\frac{t_n - s}{\tau_\alpha}\right) \dot{\bar{\boldsymbol{S}}}^{\infty} \mathrm{d}s \\
&= \xi^2_{\alpha(n+1)} \bar{\boldsymbol{S}}^{v}_{\alpha(n)} \,,
\end{aligned} \tag{4.156}$$

where $\bar{\boldsymbol{S}}^{v}_{\alpha(n)}$ is the stress in the Maxwell branch for the previous time-step. Hence, the stress for the current time-step can be obtained using

$$\bar{\boldsymbol{S}}^{v}_{\alpha(n+1)} = \beta_\alpha \xi_{\alpha(n+1)} \left[\bar{\boldsymbol{S}}^{\infty}_{n+1} - \bar{\boldsymbol{S}}^{\infty}_{n}\right] + \xi^2_{\alpha(n+1)} \bar{\boldsymbol{S}}^{v}_{\alpha(n)} \,. \tag{4.157}$$

The constitutive tensor can be obtained the usual way; that is,

$$\begin{gathered}
\mathbb{C} = \bar{\mathbb{C}}^{\infty} + \mathbb{C}^{\infty}_{vol} + \bar{\mathbb{C}}^{v} \,, \quad \bar{\mathbb{C}}^{\infty} = 2\frac{\partial \bar{\boldsymbol{S}}^{\infty}}{\partial \boldsymbol{C}} \,, \quad \mathbb{C}^{\infty}_{vol} = 2\frac{\partial \boldsymbol{S}^{\infty}_{vol}}{\partial \boldsymbol{C}} \qquad \bar{\mathbb{C}}^{v} = 2\frac{\partial \bar{\boldsymbol{S}}^{v}}{\partial \boldsymbol{C}} \,, \\
\bar{\mathbb{C}}^{v} = \sum_{\alpha}^{N_m} \bar{\mathbb{C}}^{v}_{\alpha} \,, \qquad \bar{\mathbb{C}}^{v}_{\alpha} = 2\frac{\partial \bar{\boldsymbol{S}}^{v}_{\alpha(n+1)}}{\partial \boldsymbol{C}} \,.
\end{gathered} \tag{4.158}$$

From equation (4.157), it is apparent that the contribution of each Maxwell branch to the overall stiffness is

$$\bar{\mathbb{C}}^{v}_{\alpha} = 2\beta_\alpha \xi_{\alpha(n+1)} \frac{\partial \bar{\boldsymbol{S}}^{\infty}_{n+1}}{\partial \boldsymbol{C}} = \beta_\alpha \xi_{\alpha(n+1)} \bar{\mathbb{C}}^{\infty} \,. \tag{4.159}$$

Hence, the constitutive tensor is given by

$$\mathbb{C} = \left[1 + \sum_{\alpha}^{N_m} \beta_\alpha \xi_{\alpha(n+1)}\right] \bar{\mathbb{C}}^{\infty} + \mathbb{C}^{\infty}_{vol} \,. \tag{4.160}$$

To determine the Cauchy stress, a push-forward operation is applied to equation (4.157), giving

$$\boldsymbol{\sigma}^{v}_{\alpha(n+1)} = \xi_{\alpha(n+1)} \beta_\alpha \bar{\boldsymbol{\sigma}}^{\infty}_{n+1} + \underbrace{\xi_{\alpha(n+1)} \det(\boldsymbol{G})^{-1} \boldsymbol{G}^T \left[\xi_{\alpha(n+1)} \bar{\boldsymbol{\sigma}}^{v}_{\alpha(n)} - \beta_\alpha \bar{\boldsymbol{\sigma}}^{\infty}_{n}\right] \boldsymbol{G}}_{\boldsymbol{H}_\alpha} \,, \tag{4.161}$$

where the kinematic tensor $\boldsymbol{G}$ is given by

$$\boldsymbol{G} = \boldsymbol{F}^{-1}_{n} \boldsymbol{F}_{n+1} \,. \tag{4.162}$$

It is useful to define a historic stress term for the branch $\boldsymbol{H}_\alpha$ and the Maxwell network collectively $\boldsymbol{H}$, respectively, as

$$\boldsymbol{H}_\alpha := \xi_{\alpha(n+1)} \det(\boldsymbol{G})^{-1} \boldsymbol{G}^T \left[\xi_{\alpha(n+1)} \boldsymbol{\sigma}^{v}_{\alpha(n)} - \beta_\alpha \boldsymbol{\sigma}^{\infty}_{n}\right] \boldsymbol{G} \,, \qquad \boldsymbol{H} := \sum_{\alpha}^{N_m} \boldsymbol{H}_\alpha \,. \tag{4.163}$$

The Lie constitutive tensor can be determined using the push-forward operation defined in equation (3.88) to obtain

$$\mathbb{c} = \bar{\mathbb{c}}^{\infty} + \bar{\mathbb{c}}^{v} + \mathbb{c}^{\infty}_{vol}\,, \qquad \bar{\mathbb{c}}^{v} = \sum_{\alpha}^{N_m} \beta_\alpha \xi_{\alpha(n+1)} \bar{\mathbb{c}}^{\infty}\,. \tag{4.164}$$

Determining the Jaumann constitutive tensor, however, requires caution. By using equation (3.91) and separating the Kirchhoff stress into its isochoric long time-scale $\bar{\boldsymbol{\tau}}^{\infty}$, volumetric long time-scale $\boldsymbol{\tau}^{\infty}_{vol}$ and viscous $\bar{\boldsymbol{\tau}}^{v}$ stress, one obtains

$$\begin{aligned}\mathbb{c}^{\nabla} &= \bar{\mathbb{c}}^{\infty} + \bar{\mathbb{c}}^{v} + \mathbb{c}^{\infty}_{vol} + \boldsymbol{\tau} \odot \boldsymbol{I} + \boldsymbol{I} \odot \boldsymbol{\tau} \\ &= \bar{\mathbb{c}}^{\infty} + \bar{\boldsymbol{\tau}}^{\infty} \odot \boldsymbol{I} + \boldsymbol{I} \odot \bar{\boldsymbol{\tau}}^{\infty} \\ &\quad + \mathbb{c}^{\infty}_{vol} + \boldsymbol{\tau}^{\infty}_{vol} \odot \boldsymbol{I} + \boldsymbol{I} \odot \boldsymbol{\tau}^{\infty}_{vol} \\ &\quad + \bar{\mathbb{c}}^{v} + \bar{\boldsymbol{\tau}}^{v} \odot \boldsymbol{I} + \boldsymbol{I} \odot \bar{\boldsymbol{\tau}}^{v}\,.\end{aligned} \tag{4.165}$$

The second and third rows are equivalent to the isochoric $\bar{\mathbb{c}}^{\nabla\infty}$ and volumetric $\mathbb{c}^{\nabla\infty}_{vol}$ Jaumann constitutive tensors (see equation (4.79)) leaving

$$\mathbb{c}^{\nabla} = \bar{\mathbb{c}}^{\nabla\infty} + \mathbb{c}^{\nabla\infty}_{vol} + \bar{\mathbb{c}}^{v} + \bar{\boldsymbol{\tau}}^{v} \odot \boldsymbol{I} + \boldsymbol{I} \odot \bar{\boldsymbol{\tau}}^{v}\,. \tag{4.166}$$

Expanding the terms due to the Maxwell branches yields

$$\begin{aligned}\bar{\mathbb{c}}^{v} + \bar{\boldsymbol{\tau}}^{v} \odot \boldsymbol{I} + \boldsymbol{I} \odot \bar{\boldsymbol{\tau}}^{v} =& \sum_{\alpha}^{N_m} \beta_\alpha \xi_{\alpha(n+1)} \left[\bar{\mathbb{c}}^{\infty} + \bar{\boldsymbol{\tau}}^{\infty} \odot \boldsymbol{I} + \boldsymbol{I} \odot \bar{\boldsymbol{\tau}}^{\infty}\right] \\ &+ J_{n+1} \left[\boldsymbol{H} \odot \boldsymbol{I} + \boldsymbol{I} \odot \boldsymbol{H}\right]\,.\end{aligned} \tag{4.167}$$

Hence, the history terms form part of the Jaumann constitutive tensor in contrast to the Lie and reference configuration constitutive tensors. As a result, the Jaumann constitutive tensor is given by

$$\mathbb{c}^{\nabla} = \left[1 + \sum_{\alpha}^{N_m} \beta_\alpha \xi_{\alpha(n+1)}\right] \bar{\mathbb{c}}^{\nabla\infty} + \mathbb{c}^{\nabla\infty}_{vol} + J_{n+1} \left[\boldsymbol{H} \odot \boldsymbol{I} + \boldsymbol{I} \odot \boldsymbol{H}\right]\,. \tag{4.168}$$

The equations above allow one to write a UMAT capable of modelling a viscoelastic material in ABAQUS as shown in Algorithm 4. This, of course, must be implemented with a chosen long time-scale material model. If an isochoric–volumetric split of the long time-scale strain energy function has been used then the isochoric and volumetric stresses are easily available. However, this is not the case for compressible materials that do not use an isochoric volumetric split of the strain energy function. In this case, the volumetric and isochoric stresses can be obtained, respectively, using

$$\boldsymbol{\sigma}^{\infty}_{vol} = \frac{1}{3} \boldsymbol{I}\, \mathrm{tr} \boldsymbol{\sigma}^{\infty}\,, \qquad \bar{\boldsymbol{\sigma}}^{\infty} = \boldsymbol{\sigma}^{\infty} - \boldsymbol{\sigma}^{\infty}_{vol}\,. \tag{4.169}$$

Algorithm 4 Procedure for determining the stress and constitutive tensor required by Abaqus for a viscoelastic material at time-step $n+1$

```
procedure VISCOELASTIC_MATERIAL($\boldsymbol{F}_n$, $\boldsymbol{F}_{n+1}$, $\beta$, $\tau$, $N_m$, $\bar{\boldsymbol{\sigma}}_n^v$, $\bar{\boldsymbol{\sigma}}_n^\infty$, $\bar{\boldsymbol{\sigma}}_{n+1}^\infty$, $\boldsymbol{\sigma}_{vol(n+1)}^\infty$, $\bar{\mathbb{c}}^{\nabla\infty}$, $\mathbb{c}_{vol}^{\nabla\infty}$, $\Delta t$)
    $\boldsymbol{G} = \boldsymbol{F}_n^{-1}\boldsymbol{F}_{n+1}$
    $dG = 1/\det\boldsymbol{G}$
    $\boldsymbol{\sigma} = \bar{\boldsymbol{\sigma}}_{n+1}^\infty + \boldsymbol{\sigma}_{vol(n+1)}^\infty$
    $J = \det\boldsymbol{F}_{n+1}$
    $\mathbb{c}_{\text{ABA}} = J^{-1}\left[\bar{\mathbb{c}}^{\nabla\infty} + \mathbb{c}_{vol}^{\nabla\infty}\right]$
    for $\alpha = 1, .., N_m$ do
        $\xi_{\alpha(n+1)} = \exp\left(-\frac{\Delta t}{2\tau(\alpha)}\right)$
        $\boldsymbol{H}_\alpha = \xi_{\alpha(n+1)} dG \boldsymbol{G}^T \left[\xi_{\alpha(n+1)}\bar{\boldsymbol{\sigma}}_n^v(\alpha,:,:) - \beta(\alpha)\bar{\boldsymbol{\sigma}}_n^\infty\right]\boldsymbol{G}$
        $\bar{\boldsymbol{\sigma}}_{n+1}^v(\alpha,:,:) = \xi_{\alpha(n+1)}\beta(\alpha)\bar{\boldsymbol{\sigma}}_{n+1}^\infty + \boldsymbol{H}_\alpha$
        $\boldsymbol{\sigma} = \boldsymbol{\sigma} + \bar{\boldsymbol{\sigma}}_{n+1}^v(\alpha,:,:)$
        $\mathbb{c}_{\text{ABA}} = \mathbb{c}_{\text{ABA}} + J^{-1}\xi_{\alpha(n+1)}\beta(\alpha)\bar{\mathbb{c}}^{\nabla\infty} + \boldsymbol{H}_\alpha \odot \boldsymbol{I} + \boldsymbol{I} \odot \boldsymbol{H}_\alpha$
    end for
    return $\boldsymbol{\sigma}$, $\bar{\boldsymbol{\sigma}}_{n+1}^v$, $\mathbb{c}_{\text{ABA}}$
end procedure
```

To implement the model in Abaqus, one also requires the isochoric and volumetric constitutive tensors. To obtain these, one first applies a pull-back operation to the isochoric and volumetric Cauchy stresses to obtain their second Piola-Kirchhoff counterparts; those are, respectively,

$$\boldsymbol{S}_{vol}^\infty = \frac{1}{3}\boldsymbol{C}^{-1}\left[\boldsymbol{S}^\infty : \boldsymbol{C}\right], \qquad \bar{\boldsymbol{S}}^\infty = \boldsymbol{S}^\infty - \boldsymbol{S}_{vol}^\infty \,. \tag{4.170}$$

The volumetric reference configuration constitutive tensor is then given by

$$\mathbb{C}_{vol}^\infty = 2\frac{\partial \boldsymbol{S}_{vol}^\infty}{\partial \boldsymbol{C}} = \frac{1}{3}\left[\boldsymbol{C}^{-1} \otimes \left[\boldsymbol{C} : \mathbb{C}^\infty + 2\boldsymbol{S}^\infty\right] - 2\left[\boldsymbol{S}^\infty : \boldsymbol{C}\right]\boldsymbol{C}^{-1} \odot \boldsymbol{C}^{-1}\right] . \tag{4.171}$$

The isochoric constitutive tensor is then simply given by

$$\bar{\mathbb{C}}^\infty = 2\left[\frac{\partial \boldsymbol{S}^\infty}{\partial \boldsymbol{C}} - \frac{\partial \boldsymbol{S}_{vol}^\infty}{\partial \boldsymbol{C}}\right] = \mathbb{C}^\infty - \mathbb{C}_{vol}^\infty \,. \tag{4.172}$$

The volumetric Lie constitutive tensor can then be determined using the push-forward operation defined in equation (3.88), resulting in

$$\mathbb{c}_{vol}^\infty = \frac{1}{3}\left[\boldsymbol{I} \otimes \left[\boldsymbol{I} : \mathbb{c}^\infty + 2\boldsymbol{\tau}^\infty\right] - 2\operatorname{tr}\left(\boldsymbol{\tau}^\infty\right)\boldsymbol{I} \odot \boldsymbol{I}\right] . \tag{4.173}$$

Then, using equation (3.91) and (4.79), the volumetric Jaumann constitutive tensor can be determined; that is,

$$\begin{aligned}\mathbb{c}^{\nabla\infty}_{vol} &= \frac{1}{3}\left[\boldsymbol{I}\otimes\left[\boldsymbol{I}:\left[\mathbb{c}^{\nabla\infty}-\boldsymbol{\tau}^{\infty}\odot\boldsymbol{I}-\boldsymbol{I}\odot\boldsymbol{\tau}^{\infty}\right]+2\boldsymbol{\tau}^{\infty}\right]-2\mathrm{tr}\left(\boldsymbol{\tau}^{\infty}\right)\boldsymbol{I}\odot\boldsymbol{I}\right]+\boldsymbol{\tau}^{\infty}_{vol}\odot\boldsymbol{I}+\boldsymbol{I}\odot\boldsymbol{\tau}^{\infty}_{vol}\\ &= \frac{1}{3}\boldsymbol{I}\otimes\boldsymbol{I}:\mathbb{c}^{\nabla\infty}\,.\end{aligned} \tag{4.174}$$

Hence, if the Jaumann constitutive tensor is known, its volumetric part can be determined using equation (4.174) and its isochoric part can be determined using

$$\bar{\mathbb{c}}^{\nabla\infty} = \mathbb{c}^{\nabla\infty} - \mathbb{c}^{\nabla\infty}_{vol}\,. \tag{4.175}$$

4.4 Fitting material models to data

Constitutive models are constructed with a particular mathematical structure which reflects the expected material behaviour. However, the response of a model is not dependent on its mathematical structure alone; it also depends on several material parameters $\boldsymbol{c}$. Hence, one requires a means to determine the values of these parameters so that each model accurately represents the behaviour of the material it is intended to model.

This can be done by obtaining data of the stress in the material during loading applied in a physical test. Then, the optimal values of the material parameters can be obtained by fitting the stress response of the model to the data for the same loading. This requires an analytical solution for the stress response during the given loading path. One can then define an objective function representing the error between the model and the data. The optimal material parameters $\boldsymbol{c}^*$ are then determined by minimizing the objective function.

A difficulty typically arises from the fact that the test data typically does not define the entire deformation gradient. This can be resolved by determining the unknown values in the deformation gradient using some known stress values. For example, during uniaxial loading, one is provided with data defining F_{11} and σ_{11}. Additionally, if the material is isotropic or if the preferred directions are aligned or perpendicular to the loading, all off diagonal entries in $\boldsymbol{F}$ are zero, as well as all entries in $\boldsymbol{\sigma}$ apart from σ_{11}. However, F_{22} and F_{33} are unknown. This can be resolved by determining F_{22} and F_{33} such that $\sigma_{22} = \sigma_{33} = 0$.

In what follows, the procedure for obtaining these analytical solutions is outlined for four loading paths: uniaxial, biaxial, shear, and pressure loading. Additionally, four classes of materials are considered: compressible transversely isotropic, compressible isotropic, incompressible transversely isotropic, and incompressible isotropic. Then, the requirements for extending these procedures to viscoelasticity is outlined.

For all loading paths besides shear, the deformation gradient and stress, respectively, are of the form

$$\boldsymbol{F} = \mathrm{Diag}\begin{bmatrix}\lambda_1 & \lambda_2 & \lambda_3\end{bmatrix}\,, \qquad \boldsymbol{\sigma} = \mathrm{Diag}\begin{bmatrix}\sigma_1 & \sigma_2 & \sigma_3\end{bmatrix}\,. \tag{4.176}$$

The superscript $\bullet^*$ denotes values that are measured (besides for the case of the optimal material parameters $\boldsymbol{c}^*$). The number of measurements in a test is denoted by N. Hence, the objective function $\mathcal{X}$ is typically of the form

$$\mathcal{X}\left(\boldsymbol{c}\right) = \sum_{m=1}^{N} ||\boldsymbol{\sigma}\left(\boldsymbol{c}, \boldsymbol{F}_m^*\right) - \boldsymbol{\sigma}_m^*||^2 \tag{4.177}$$

4.4.1 Uniaxial loading

During uniaxial loading, stretching is applied in a single direction of a test sample and all other surfaces are traction free. It is convenient to choose a basis such that the first direction is aligned with the loading direction. Then the stretch λ_1^* and stress σ_1^* in direction 1 are measured, the stresses in directions 2 and 3 are zero,

$$\sigma_2 = \sigma_3 = 0\,, \tag{4.178}$$

and the stretches λ_2 and λ_3 are unknown. However, the stretches λ_2 and λ_3 can be determined by using equation (4.178) for given values of $\boldsymbol{c}$ and λ_1^*. The mathematical development for this differs for compressible transversely isotropic, compressible isotropic, incompressible transversely isotropic, and incompressible isotropic materials and is presented in the subsections that follow. The optimal material parameters can then be determined by solving the least squares problem

$$\boldsymbol{c}^* = \arg\min_{\boldsymbol{c}} \mathcal{X} = \sum_{m=1}^{N} \left[\sigma_1\left(\boldsymbol{c}, \lambda_{1(m)}^*\right) - \sigma_{1(m)}^*\right]^2\,. \tag{4.179}$$

Here, $\lambda_{1(m)}^*$ and $\sigma_{1(m)}^*$ are the stretch and stress, respectively, of measurement m and $\arg\min_{\bullet} \Box$ denotes the value of $\bullet$ that minimizes $\Box$.

Compressible transversely isotropic

For compressible transversely isotropy, the stretches λ_2 and λ_3 differ. The stretches can be determined by defining the residual vector

$$\boldsymbol{r}_{\mathrm{uni}} = \begin{bmatrix}\sigma_2\left(\boldsymbol{c}, \lambda_1, \lambda_2, \lambda_3\right)\\ \sigma_3\left(\boldsymbol{c}, \lambda_1, \lambda_2, \lambda_3\right)\end{bmatrix}\,, \tag{4.180}$$

and finding its root for a given value of $\boldsymbol{c}$ and λ_1. Hence, the stretches are determined by

$$\begin{bmatrix}\lambda_2\left(\boldsymbol{c}, \lambda_1\right)\\ \lambda_3\left(\boldsymbol{c}, \lambda_1\right)\end{bmatrix} = \arg\min_{\lambda_2, \lambda_3} ||\boldsymbol{r}_{\mathrm{uni}}||\,. \tag{4.181}$$

Compressible isotropic

If the material is isotropic, or has a plane of isotropy that is perpendicular to the loading direction, the problem is simplified since

$$\lambda_2 = \lambda_3 \,. \tag{4.182}$$

Hence, the unknown stretches can both be found from

$$\lambda_2 = \lambda_3 = \arg\min_{\lambda_2} \sigma_2 \left(\boldsymbol{c}, \lambda_1, \lambda_2, \lambda_2\right)^2 \,. \tag{4.183}$$

Incompressible transversely isotropic

Since incompressible materials incur no volume change, λ_3 can be determined from λ_1 and λ_2; that is,

$$J = \lambda_1 \lambda_2 \lambda_3 = 1 \,, \qquad \lambda_3 = \frac{1}{\lambda_1 \lambda_2} \,. \tag{4.184}$$

However, incompressible material add an unknown in the form of an undetermined pressure p; that is,

$$\boldsymbol{\sigma} = \mathrm{Diag}\begin{bmatrix}\bar{\sigma}_1 & \bar{\sigma}_2 & \bar{\sigma}_3\end{bmatrix} + p\boldsymbol{I} \,. \tag{4.185}$$

Using equation (4.178), it is apparent that the pressure is related to the isochoric stress by

$$p = -\bar{\sigma}_2 = -\bar{\sigma}_3 \,. \tag{4.186}$$

Hence, λ_2 is determined by defining the residual equation

$$r = \bar{\sigma}_2 - \bar{\sigma}_3 = 0 \,, \tag{4.187}$$

and finding its root for a given value of $\boldsymbol{c}$ and λ_1; that is,

$$\lambda_2 = \arg\min_{\lambda_2} \left[\bar{\sigma}_2 \left(\boldsymbol{c}, \lambda_1, \lambda_2, \frac{1}{\lambda_1 \lambda_2}\right) - \bar{\sigma}_3 \left(\boldsymbol{c}, \lambda_1, \lambda_2, \frac{1}{\lambda_1 \lambda_2}\right)\right]^2 \,. \tag{4.188}$$

Then, the value of the pressure can be determined from

$$p = -\bar{\sigma}_2 \left(\boldsymbol{c}, \lambda_1, \lambda_2, \frac{1}{\lambda_1 \lambda_2}\right) \,, \tag{4.189}$$

and finally the desired stress value can be obtained from

$$\sigma_1 = \bar{\sigma}_1 + p \,. \tag{4.190}$$

Incompressible isotropic

If the material is considered to be isotropic and incompressible then the deformation gradient is entirely defined by λ_1,

$$\lambda_2 = \lambda_3 = \frac{1}{\sqrt{\lambda_1}}\,. \tag{4.191}$$

The pressure can be determined by

$$p = -\bar{\sigma}_2 = -\bar{\sigma}_3\,, \tag{4.192}$$

and the desired stress can be obtained from

$$\sigma_1 = \bar{\sigma}_1 + p\,. \tag{4.193}$$

4.4.2 Biaxial loading

During biaxial loading, stretching is applied in two directions and the third direction is left traction free. Now, it is convenient to choose a basis so that the first and second basis vectors are each aligned with one of the loading directions. Then the stretches λ_1^* and λ_2^* as well as the stresses σ_1^* and σ_2^* are measured. In the third direction, the stretch λ_3 is unknown, and the stress is known to be zero; that is,

$$\sigma_3 = 0\,. \tag{4.194}$$

The objective function in the case of biaxial loading is

$$\mathcal{X} = \sum_{m=1}^{N} \left[\sigma_1\left(\boldsymbol{c}, \lambda_{1(m)}^*, \lambda_{2(m)}^*\right) - \sigma_{1(m)}^*\right]^2 + \left[\sigma_2\left(\boldsymbol{c}, \lambda_{1(m)}^*, \lambda_{2(m)}^*\right) - \sigma_{2(m)}^*\right]^2\,. \tag{4.195}$$

Compressible materials

For compressible materials, the stretch in the third direction can be determined for given $\boldsymbol{c}$, λ_1 and λ_2 using

$$\lambda_3 = \arg\min_{\lambda_3} \sigma_3\left(\boldsymbol{c}, \lambda_1, \lambda_2, \lambda_3\right)^2\,. \tag{4.196}$$

This holds true irrespective of whether the material is transversely isotropic or isotropic.

Incompressible materials

For incompressible materials, the stretch in the third direction is determined by the other two stretches

$$\lambda_3 = \frac{1}{\lambda_2 \lambda_3}\,. \tag{4.197}$$

However, incompressibility introduces another unknown to be solved for – pressure. Using equation (4.194), the pressure can be determined from

$$p = -\bar{\sigma}_3 \left(\boldsymbol{c}, \lambda_1, \lambda_2, \lambda_3\right) . \tag{4.198}$$

Then the stresses in the first and second direction are given, respectively, by

$$\sigma_1 = \bar{\sigma}_1 + p \,, \qquad \sigma_2 = \bar{\sigma}_2 + p \,. \tag{4.199}$$

Again, this holds true irrespective of whether the material is transversely isotropic or isotropic.

4.4.3 Pressure loading

What is termed 'pressure loading' here is not a typical physical test that one would carry out. This type of loading has been used in this thesis to elucidate the pressure response of representative volume elements (RVEs) through computational experiments, see chapter 6 for details.

The aim of pressure loading is to obtain a stress state that is equivalent to a hydrostatic pressure; that is,

$$\boldsymbol{\sigma} = p\boldsymbol{I} \,. \tag{4.200}$$

However, when using an RVE with period boundary conditions (see chapter 6) one cannot prescribe the stress state of the RVE, one can only prescribe the deformation. Hence, one stretch is chosen, λ_1, and the others, λ_2 and λ_3, are adjusted until the RVE is in a state of hydrostatic pressure. Hence, the measured values are λ_1^* and p^* and the objective function is

$$\mathcal{X} = \sum_{m=1}^{N} \left[p\left(\boldsymbol{c}, \lambda^*_{1(m)}\right) - p^*_m\right]^2 . \tag{4.201}$$

Note that this type of loading is only sensible for compressible materials.

Transversely isotropic materials

For compressible transversely isotropy, the stretches λ_2 and λ_3 differ. The stretches can be determined by defining the residual vector

$$\boldsymbol{r}_{\text{pres}} = \begin{bmatrix} \sigma_2 - \sigma_1 \\ \sigma_3 - \sigma_1 \end{bmatrix} , \tag{4.202}$$

and finding its root for a given value of $\boldsymbol{c}$ and λ_1. Hence, the stretches are determined by

$$\begin{bmatrix} \lambda_2 \left(\boldsymbol{c}, \lambda_1\right) \\ \lambda_3 \left(\boldsymbol{c}, \lambda_1\right) \end{bmatrix} = \underset{\lambda_2, \lambda_3}{\arg\min} \, ||\boldsymbol{r}_{\text{pres}}|| \,. \tag{4.203}$$

Isotropic materials

For isotropic materials, all the stretches must simply be equal; that is,

$$\lambda_1 = \lambda_2 = \lambda_3 \, . \tag{4.204}$$

4.4.4 Shear loading

Similarly to 'pressure loading', the shear loading applied in this work does not describe a typical physical test. Rather, it is used for determining the response of an RVE to simple shear. Simple shear is described by a deformation gradient of the form

$$\boldsymbol{F} = \boldsymbol{I} + \gamma \boldsymbol{e}_i \otimes \boldsymbol{e}_j \, , \qquad i \neq j \, , \tag{4.205}$$

where γ is a parameter controlling the degree of the shear and i and j control the direction in which the sample is being sheared. In this case, the entire deformation gradient is defined. The objective function for this testing scenario is

$$\mathcal{X} = \sum_{m=1}^{N} \left[\sigma_{ij} \left(\boldsymbol{c}, \boldsymbol{F}_m^* \right) - \sigma_{ij(m)}^* \right]^2 \, . \tag{4.206}$$

4.4.5 Considerations for viscoelasticity

Viscoelastic materials introduce another layer of complexity, as the stress response depends not only on the current deformation, but also on the entire deformation history. Additionally, the stress response for the class of viscoelastic materials outlined in section 4.3.2 requires the evaluation of an integral, of which the integrand differs from one problem to the next. Hence, developing a general approach for finding an analytical solution is intractable. Instead, the discretized version of stress response presented in equation (4.161) is used. Then, for each time-step $n+1$, one can determine the unknown values in the deformation gradient $\boldsymbol{F}_{n+1}$ such that the correct entries in the stress $\boldsymbol{\sigma}_{n+1}$ are zero. An example of this is shown in pseudo-code for uniaxial loading of a compressible transversely isotropic material in Algorithm 5. In the pseudo-code $\dot{\lambda}_1^*$ is the rate of stretch in the first direction, t^* is an array of times at which measurements were taken and σ_1^* is an array of measured stresses at times t^*.

4.5 Some notes on implementation

User subroutines (written in FORTRAN) for the aforementioned constitutive models were implemented in the finite element analysis software ABAQUS. ABAQUS has two solvers used in this work: standard and explicit. The standard solver is used for time-independent problems and time-dependent problems that use an implicit integration scheme. To implement a material model for the standard solver, one is required to write a UMAT that provides the Cauchy stress and the Jaumann constitutive tensor multiplied by one over the Jacobian, that is, $J^{-1}\mathbb{c}^{\nabla}$. The standard solver uses Voigt notation with the ordering

$$\boldsymbol{\sigma}_{\text{standard}} = \begin{bmatrix}\sigma_{11} & \sigma_{22} & \sigma_{33} & \sigma_{12} & \sigma_{13} & \sigma_{23}\end{bmatrix}^T . \tag{4.207}$$

The explicit solver is used for time-dependent problems that utilise an explicit time integration scheme. To implement material models for the explicit solver, one is required to write a VUMAT which requires the Cauchy stress only. The explicit solver also uses Voigt notation. However, the ordering differs to the convention for the standard solver and is given by

$$\boldsymbol{\sigma}_{\text{explicit}} = \begin{bmatrix}\sigma_{11} & \sigma_{22} & \sigma_{33} & \sigma_{23} & \sigma_{13} & \sigma_{12}\end{bmatrix}^T . \tag{4.208}$$

Fitting of material models was done in the programming language `Python` using minimization and root finding functions provided by the library `Scipy`. To avoid having to implement the aforementioned materials in both `Python` and `FORTRAN`, the command line tool `f2py` was used, which compiles `FORTRAN` subroutines and makes them available in `Python` as functions in a library.

Algorithm 5 Procedure for calculating the objective function of a viscoelastic material under uniaxial loading

```
procedure $\boldsymbol{r}_{\text{UNI}}(\boldsymbol{F}_n,\ \lambda_{1(n+1)},\ \lambda_{2(n+1)},\ \lambda_{3(n+1)},\ \beta,\ \tau,\ \boldsymbol{c},\ \bar{\boldsymbol{\sigma}}_n^{\infty},\ \bar{\boldsymbol{\sigma}}_n^{v})$
    $\boldsymbol{F}_{n+1} = \boldsymbol{I}$
    $\boldsymbol{F}_{n+1}(1,1),\ \boldsymbol{F}_{n+1}(2,2),\ \boldsymbol{F}_{n+1}(3,3) = \lambda_{1(n+1)},\ \lambda_{2(n+1)},\ \lambda_{3(n+1)}$
    $\boldsymbol{\sigma}_{n+1},\ \bar{\boldsymbol{\sigma}}_n^{\infty},\ \bar{\boldsymbol{\sigma}}_n^{v}$ =VISCO_MATERIAL$(\boldsymbol{F}_n,\ \boldsymbol{F}_{n+1},\ \beta,\ \tau,\ \boldsymbol{c},\ \bar{\boldsymbol{\sigma}}_n^{\infty},\ \bar{\boldsymbol{\sigma}}_n^{v})$
    return $\boldsymbol{\sigma}_{(n+1)}(2,2)^2 + \boldsymbol{\sigma}_{(n+1)}(3,3)^2$
end procedure
procedure VISCOELASTIC_UNIAXIAL_OBJECTIVE$(\beta,\ \tau,\ N,\ \boldsymbol{c},\ \dot{\lambda}_1^*,\ t^*,\ \sigma_1^*,\ \Delta t_{\max})$
    $\sigma_1 = \text{zeros}(N)$
    $\boldsymbol{\sigma}_n,\ \boldsymbol{\sigma}_{n+1},\ \bar{\boldsymbol{\sigma}}_n^{\infty},\ \bar{\boldsymbol{\sigma}}_n^{v} = \mathbf{0},\ \mathbf{0},\ \mathbf{0},\ \mathbf{0}$
    $\boldsymbol{F}_n = \boldsymbol{I}$
    $\boldsymbol{F}_{n+1} = \boldsymbol{I}$
    $m = 1$
    $t_{\text{measure}} = t^*(1)$
    while $t < \text{last}(t^*)$ do
        if $t + \Delta t_{\max} > t_{\text{measure}}$ then
            $\Delta t = t_{\text{measure}} - t$
        else
            $\Delta t = \Delta t_{\max}$
        end if
        $t = t + \Delta t$
        $\lambda_{1(n+1)} = \boldsymbol{F}_n(1,1) + \Delta t \dot{\lambda}_1^*$
        $\lambda_{2(n+1)}, \lambda_{3(n+1)} = \arg\min_{\lambda_{2(n+1)},\lambda_{3(n+1)}} ||\boldsymbol{r}_{\text{UNI}}(\boldsymbol{F}_n,\ \lambda_{1(n+1)},\ \lambda_{2(n+1)},\ \lambda_{3(n+1)},\ \beta,\ \tau,\ \boldsymbol{c},\ \bar{\boldsymbol{\sigma}}_n^{\infty},\ \bar{\boldsymbol{\sigma}}_n^{v})||$
        $\boldsymbol{F}_{n+1}(1,1),\ \boldsymbol{F}_{n+1}(2,2),\ \boldsymbol{F}_{n+1}(3,3) = \lambda_{1(n+1)},\ \lambda_{2(n+1)},\ \lambda_{3(n+1)}$
        $\boldsymbol{\sigma}_{n+1}, \bar{\boldsymbol{\sigma}}_n^{\infty}, \bar{\boldsymbol{\sigma}}_n^{v}$ =VISCO_MATERIAL$(\boldsymbol{F}_n,\ \boldsymbol{F}_{n+1},\ \beta,\ \tau,\ \boldsymbol{c},\ \bar{\boldsymbol{\sigma}}_n^{\infty},\ \bar{\boldsymbol{\sigma}}_n^{v})$
        if $t == t_{\text{measure}}$ then
            $\sigma_1(m) = \boldsymbol{\sigma}_{n+1}(1,1)$
            $m = m + 1$
            $t_{\text{measure}} = t^*(m)$
        end if
        $\bar{\boldsymbol{\sigma}}_n^{\infty},\ \bar{\boldsymbol{\sigma}}_n^{v},\ \boldsymbol{F}_n = \bar{\boldsymbol{\sigma}}_{n+1}^{\infty},\ \bar{\boldsymbol{\sigma}}_{n+1}^{v},\ \boldsymbol{F}_{n+1}$
    end while
    return $\text{sum}\left([\sigma_1 - \sigma_1^*]^2\right)$
end procedure
```

Chapter 5

Numerical methods

When modelling the mechanical behaviour of a structure, one defines the geometry (domain) of the body, appropriate boundary conditions, constitutive laws, and initial values such that the initial boundary value problem is properly posed. For solid mechanics problems the resulting problem, termed the 'strong form', is as follows: find the displacement field $\boldsymbol{u}(\boldsymbol{x}, t)$ that satisfies the balance of linear momentum

$$\rho\ddot{\boldsymbol{u}} = \mathrm{div}\boldsymbol{\sigma} + \boldsymbol{g} \qquad \text{for } \boldsymbol{x} \in \Omega,\, t \in [0, t_{\text{end}}]\,, \tag{5.1}$$

the boundary conditions[1]

$$\begin{aligned} u_i &= \bar{u}_i & &\text{on } \Gamma_i^D\,, & (5.2)\\ t_i &= \bar{t}_i & &\text{on } \Gamma_i^N\,, & (5.3)\\ \Gamma_i^N \cup \Gamma_i^D &= \Gamma\,, & &\Gamma_i^N \cap \Gamma_i^D = \varnothing\,, & (5.4) \end{aligned}$$

and initial conditions

$$\begin{aligned} \boldsymbol{u} &= \bar{\boldsymbol{u}}_0 & &\text{at } t = 0\,, & (5.5)\\ \dot{\boldsymbol{u}} &= \bar{\boldsymbol{v}}_0 & &\text{at } t = 0\,. & (5.6) \end{aligned}$$

Here, the Cauchy stress $\boldsymbol{\sigma}$ is defined by the gradient of the displacement field $\mathrm{Grad}(\boldsymbol{u})$ and its history in the temporal domain $[0, t]$. Hence, the solution of the strong form is

---

[1] It is conventional to stipulate a single Dirichlet portion of the boundary Γ^D and a single Neumann portion of the boundary Γ^N with the condition $\Gamma^N \cup \Gamma^D = \Gamma\,,\ \Gamma^N \cap \Gamma^D = \varnothing$. However, one may assign a Dirichlet condition to one component of the solution and a Neumann condition to a different component of the solution's gradient at the same position. Hence, a Dirichlet and Neumann boundary are defined for each component Γ_i^D and Γ_i^N, respectively. Then, the condition $\Gamma_i^N \cup \Gamma_i^D = \Gamma\,,\ \Gamma_i^N \cap \Gamma_i^D = \varnothing$ applies. However, note that in general $\Gamma_i^N \cup \Gamma_j^D \neq \Gamma\,,\ \Gamma_i^N \cap \Gamma_j^D \neq \varnothing$ for $i \neq j$.

sufficiently defined by the displacement field. Additionally, Ω is the domain in its deformed configuration as illustrated in Figure 3.1. However, finding analytical solutions to these problems is intractable for all but the most simple cases. Hence, one resorts to numerical methods to find an approximate, but sufficiently accurate, solution. In particular, the finite element method (FEM) is used to discretize the problem in space. In the case of time-dependent problems, this results in a set of semi-discrete equations; that is, discretized in space but not in time. One can then use a numerical time integration scheme to discretize the semi-discrete equations in time. In what follows, two time integration schemes are presented: central difference and Newmark method.

5.1 The finite element method for spatial discretization

The finite element method utilises a linear combination of basis functions, defined piecewise over the domain, to approximate functions within the domain [60, 71]. Hence, one can determine an approximate solution by solving for the coefficients of the basis functions. The FEM is developed using a weak form of the problem. This is presented next.

5.1.1 Weak form

To construct the weak form, one defines the residual $\boldsymbol{r}$ as

$$\boldsymbol{r} = \rho\ddot{\boldsymbol{u}} - \mathrm{div}\boldsymbol{\sigma} - \boldsymbol{g}\,. \tag{5.7}$$

To enforce a zero residual, a virtual work per unit time δW is constructed by taking the dot product of the residual with an arbitrary virtual velocity $\delta\boldsymbol{v}$, integrating over the domain, and setting this value to zero:

$$\delta W = \int_\Omega \delta\boldsymbol{v}\cdot\boldsymbol{r}\,\mathrm{d}\Omega = 0\,. \tag{5.8}$$

Although $\delta\boldsymbol{v}$ is arbitrary, it is required to satisfy the constraint $\delta v_i = 0$ on Γ_i^D. Likewise, the virtual velocity gradient, virtual rate of deformation, and virtual strain rate are defined, respectively, by

$$\delta\boldsymbol{L} := \mathrm{grad}\delta\boldsymbol{v}\,,\quad \delta\boldsymbol{D} := \frac{1}{2}\left[\delta\boldsymbol{L} + \delta\boldsymbol{L}^T\right]\,,\quad \delta\dot{\boldsymbol{E}} := \frac{1}{2}\left[\mathrm{Grad}\delta\boldsymbol{v}^T\boldsymbol{F} + \boldsymbol{F}^T\mathrm{Grad}\delta\boldsymbol{v}\right] = \boldsymbol{F}^T\delta\boldsymbol{D}\boldsymbol{F}\,. \tag{5.9}$$

By substituting equation (5.7) into equation (5.8) one obtains

$$\delta W = \int_\Omega \left[\rho\delta\boldsymbol{v}\cdot\ddot{\boldsymbol{u}} - \delta\boldsymbol{v}\cdot\mathrm{div}\boldsymbol{\sigma} - \delta\boldsymbol{v}\cdot\boldsymbol{g}\right]\mathrm{d}\Omega = 0\,. \tag{5.10}$$

The second term of the integrand in equation (5.10) can be expanded using Green's theorem to obtain

$$\int_\Omega \delta\boldsymbol{v}\cdot\operatorname{div}\boldsymbol{\sigma}\,\mathrm{d}\Omega = \int_\Gamma \delta\boldsymbol{v}\cdot\boldsymbol{t}\,\mathrm{d}\Gamma - \int_\Omega \delta\boldsymbol{D}:\boldsymbol{\sigma}\,\mathrm{d}\Omega\,, \tag{5.11}$$

where

$$\delta\boldsymbol{L}:\boldsymbol{\sigma} = \delta\boldsymbol{D}:\boldsymbol{\sigma} \tag{5.12}$$

has been used due to the symmetry of $\boldsymbol{\sigma}$. Since $\delta v_i = 0$ on Γ_i^D the first term on the right-hand side of equation (5.11) can be reduced to

$$\int_\Gamma \delta\boldsymbol{v}\cdot\boldsymbol{t}\,\mathrm{d}\Gamma = \sum_{i=1}^{3}\int_{\Gamma_i^N}\delta v_i\bar{t}_i\mathrm{d}\Gamma\,. \tag{5.13}$$

The following definition is then made for conciseness:

$$\int_{\Gamma^N}\delta\boldsymbol{v}\cdot\bar{\boldsymbol{t}}\,\mathrm{d}\Gamma := \sum_{i=1}^{3}\int_{\Gamma_i^N}\delta v_i\bar{t}_i\mathrm{d}\Gamma\,. \tag{5.14}$$

Substitution of equations (5.11), (5.13), and (5.14) into equation (5.10) yields

$$\delta W = \underbrace{\int_\Omega \rho\delta\boldsymbol{v}\cdot\ddot{\boldsymbol{u}}\,\mathrm{d}\Omega}_{\delta W_{\text{kin}}} + \underbrace{\int_\Omega \delta\boldsymbol{D}:\boldsymbol{\sigma}\,\mathrm{d}\Omega}_{\delta W_{\text{int}}} - \underbrace{\left[\int_\Omega \delta\boldsymbol{v}\cdot\boldsymbol{g}\,\mathrm{d}\Omega + \int_{\Gamma^N}\delta\boldsymbol{v}\cdot\bar{\boldsymbol{t}}\,\mathrm{d}\Gamma\right]}_{\delta W_{\text{ext}}} = 0\,, \tag{5.15}$$

where δW_{kin}, δW_{int} and δW_{ext} are referred to as the kinetic, internal, and external virtual work, respectively. Equation (5.15) can be altered so that the integrations are performed over the initial configuration, leading to

$$\delta W = \underbrace{\int_{\Omega_0} \rho_0\delta\boldsymbol{v}\cdot\ddot{\boldsymbol{u}}\,\mathrm{d}\Omega_0}_{\delta W_{\text{kin}}} + \underbrace{\int_{\Omega_0} \delta\boldsymbol{D}:\boldsymbol{\tau}\,\mathrm{d}\Omega_0}_{\delta W_{\text{int}}} - \underbrace{\left[\int_{\Omega_0} \delta\boldsymbol{v}\cdot\boldsymbol{g}_0\,\mathrm{d}\Omega_0 + \int_{\Gamma_0^N}\delta\boldsymbol{v}\cdot\bar{\boldsymbol{t}}_0\,\mathrm{d}\Gamma\right]}_{\delta W_{\text{ext}}} = 0\,, \tag{5.16}$$

where

$$\rho_0 = J\rho\,, \qquad \boldsymbol{g}_0 = J\boldsymbol{g}\,, \qquad \bar{\boldsymbol{t}}_0 = \boldsymbol{P}\boldsymbol{n}_0\,. \tag{5.17}$$

Additionally, δW_{int} can be rewritten entirely in terms of reference configuration quantities by analogy with equation (3.104), leading to

$$\delta W_{\text{int}} = \int_{\Omega_0}\delta\dot{\boldsymbol{E}}:\boldsymbol{S}\,\mathrm{d}\Omega_0\,. \tag{5.18}$$

Hence, the virtual work can be written in the reference configuration as

$$\delta W = \underbrace{\int_{\Omega_0} \rho_0\delta\boldsymbol{v}\cdot\ddot{\boldsymbol{u}}\,\mathrm{d}\Omega_0}_{\delta W_{\text{kin}}} + \underbrace{\int_{\Omega_0} \delta\dot{\boldsymbol{E}}:\boldsymbol{S}\,\mathrm{d}\Omega_0}_{\delta W_{\text{int}}} - \underbrace{\left[\int_{\Omega_0} \delta\boldsymbol{v}\cdot\boldsymbol{g}_0\,\mathrm{d}\Omega_0 + \int_{\Gamma_0^N}\delta\boldsymbol{v}\cdot\bar{\boldsymbol{t}}_0\,\mathrm{d}\Gamma\right]}_{\delta W_{\text{ext}}} = 0\,. \tag{5.19}$$

The weak form of the problem is then to find $\boldsymbol{u}$ that satisfies equations (5.15), (5.16), or (5.19) (if one of them is satisfied then the others are since they are equivalent) for all $\delta\boldsymbol{v}$ where $\delta v_i = 0$ and $u_i = \bar{u}_i$ on Γ_i^D.

Linearisation

For nonlinear problems, discretizing the weak form results in a nonlinear discrete system of equations. These are solved using the Newton-Raphson method, which requires linearisation of the virtual work. The linearisation can be applied directly to the discrete system of equations, or it can be applied to the weak form and then discretized. The later approach is used in this work, and so the linearisation of the virtual work is presented here. The linearisation of the virtual work in the direction of a change in displacement is given by

$$\mathrm{L}\left[\delta W\right]\Delta\boldsymbol{u} = \delta W + \mathrm{D}\left[\delta W\right]\Delta\boldsymbol{u}\,. \tag{5.20}$$

For problems where δW_{kin} and δW_{ext} are not dependent on the solution the directional derivative of the virtual work in the direction of $\Delta\boldsymbol{u}$ is given by

$$\mathrm{D}\left[\delta W\right]\Delta\boldsymbol{u} = \mathrm{D}\left[\delta W_{\mathrm{int}}\right]\Delta\boldsymbol{u} = \int_{\Omega_0} \boldsymbol{S} : \mathrm{D}\left[\delta\dot{\boldsymbol{E}}\right]\Delta\boldsymbol{u} + \delta\dot{\boldsymbol{E}} : \mathrm{D}\left[\boldsymbol{S}\right]\Delta\boldsymbol{u}\,\mathrm{d}\Omega_0\,. \tag{5.21}$$

To determine the directional derivative of the virtual strain rate, it is convenient to first determine the directional derivative of the deformation gradient; that is,

$$\mathrm{D}\left[\boldsymbol{F}\right]\Delta\boldsymbol{u} = \frac{d}{d\epsilon}\left[\boldsymbol{I} + \mathrm{Grad}\left(\boldsymbol{u} + \epsilon\Delta\boldsymbol{u}\right)\right]_{\epsilon=0} = \mathrm{Grad}\,\Delta\boldsymbol{u}\,. \tag{5.22}$$

Then, using equation (5.9), the directional derivative of the virtual strain rate is obtained; that is,

$$\mathrm{D}\left[\delta\dot{\boldsymbol{E}}\right]\Delta\boldsymbol{u} = \frac{1}{2}\left[\mathrm{Grad}\delta\boldsymbol{v}^T\mathrm{Grad}\Delta\boldsymbol{u} + \mathrm{Grad}\Delta\boldsymbol{u}^T\mathrm{Grad}\delta\boldsymbol{v}\right]\,. \tag{5.23}$$

Additionally, since $\boldsymbol{S}$ is symmetric, the identity

$$\boldsymbol{S} : \bullet = \boldsymbol{S} : \bullet^T \tag{5.24}$$

holds. Hence, the first entry in the integrand of equation (5.21) reduces to

$$\boldsymbol{S} : \mathrm{D}\left[\delta\dot{\boldsymbol{E}}\right]\Delta\boldsymbol{u} = \boldsymbol{S} : \left[\left(\mathrm{Grad}\delta\boldsymbol{v}\right)^T\mathrm{Grad}\Delta\boldsymbol{u}\right]\,. \tag{5.25}$$

Using the chain rule, the directional derivative of the stress can be expressed as

$$\mathrm{D}\left[\boldsymbol{S}\right]\Delta\boldsymbol{u} = \frac{\partial\boldsymbol{S}}{\partial\boldsymbol{E}}\mathrm{D}\left[\boldsymbol{E}\right]\Delta\boldsymbol{u}\,, \tag{5.26}$$

and so the constitutive tensor naturally emerges; that is,

$$\mathbb{C} = \frac{\partial\boldsymbol{S}}{\partial\boldsymbol{E}}\,. \tag{5.27}$$

Using the directional derivative of the deformation gradient (equation (5.22)) the direction derivative of the strain can be determined to be

$$\mathrm{D}\left[\boldsymbol{E}\right]\Delta\boldsymbol{u} = \frac{1}{2}\left[\mathrm{Grad}\Delta\boldsymbol{u}^T\boldsymbol{F} + \boldsymbol{F}^T\mathrm{Grad}\Delta\boldsymbol{u}\right]\,. \tag{5.28}$$

By substituting equations (5.27) and (5.28) into equation (5.26), an expression for the directional derivative of the stress is obtained:

$$\mathrm{D}\left[\boldsymbol{S}\right]\Delta\boldsymbol{u} = \frac{1}{2}\mathbb{C}\left[\mathrm{Grad}\Delta\boldsymbol{u}^T\boldsymbol{F} + \boldsymbol{F}^T\mathrm{Grad}\Delta\boldsymbol{u}\right] . \tag{5.29}$$

The directional derivative of the internal virtual work is then obtained by substituting equations (5.25) and (5.29) into equation (5.21) to give

$$\mathrm{D}\left[\delta W_{\mathrm{int}}\right]\Delta\boldsymbol{u} = \int_{\Omega_0}\boldsymbol{S} : \left[\mathrm{Grad}\delta\boldsymbol{v}^T\mathrm{Grad}\Delta\boldsymbol{u}\right] + \frac{1}{2}\delta\dot{\boldsymbol{E}} : \mathbb{C}\left[\mathrm{Grad}\Delta\boldsymbol{u}^T\boldsymbol{F} + \boldsymbol{F}^T\mathrm{Grad}\Delta\boldsymbol{u}\right] \mathrm{d}\Omega_0 . \tag{5.30}$$

The directional derivative can be converted to be in terms of current configuration quantities by using the identities

$$\begin{aligned} \mathrm{Grad}\bullet &= \mathrm{grad}\left(\bullet\right)\boldsymbol{F} , \qquad & \boldsymbol{\tau} &= \boldsymbol{F}\boldsymbol{S}\boldsymbol{F}^T , \\ \delta\dot{\boldsymbol{E}} &= \boldsymbol{F}^T\delta\boldsymbol{D}\boldsymbol{F} , \qquad & \mathbb{c}_{ijkl} &= \mathbb{C}_{IJKL}F_{iI}F_{jJ}F_{kK}F_{lL} , \end{aligned} \tag{5.31}$$

to obtain

$$\mathrm{D}\left[\delta W_{\mathrm{int}}\right]\Delta\boldsymbol{u} = \int_{\Omega_0}\boldsymbol{\tau} : \mathrm{grad}\delta\boldsymbol{v}^T\mathrm{grad}\Delta\boldsymbol{u} + \frac{1}{2}\delta\boldsymbol{D} : \mathbb{c}\left[\mathrm{grad}\Delta\boldsymbol{u}^T + \mathrm{grad}\Delta\boldsymbol{u}\right] \mathrm{d}\Omega_0 . \tag{5.32}$$

After discretizing equations (5.20) and (5.32) using finite elements, an approximate solution can be obtained using the Newton-Raphson method (see section 5.2.1).

5.1.2 Discretization: finite element form

Finding a solution to the weak form is also typically an intractable problem. However, an approximate solution to the weak form can be found as a finite linear combination of basis or shape functions. The procedure for obtaining this system of equations is outlined here.

Elements

The domain is approximated by a union of a finite number of subdomains termed elements, as illustrated in Figure 5.1. The union of these elements is referred to as a mesh. Each element is defined by several nodes and a connectivity between them. For low-order elements as shown in Figure 5.1 all nodes coincide with the vertices of the element. However, higher-order elements may have additional nodes on the edges of the element, inside the element, or on the face of the element in 3D.

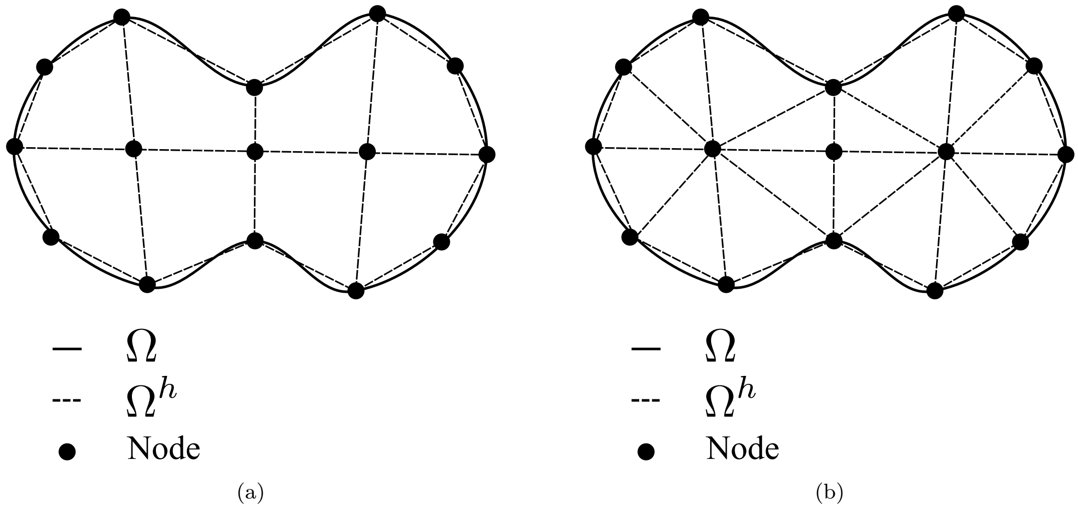

(a) (b)

Figure 5.1: Two examples of approximating a spacial domain Ω as a union of finite elements Ω^h. In (a) the domain is discretized using quadrilateral elements whereas (b) is discretized using triangular elements. This is shown in 2D for ease of illustration, however the same concepts extend to 3D. In the 3D equivalent, (a) would use hexahedra and (b) would use tetrahedra.

Shape functions

Each node in the mesh is assigned a 'shape function' N which is non-zero on the elements to which the node is attached and is zero for all other elements. These functions are used to interpolate values at each node to some point within the mesh. For instance, the displacement at some point $\boldsymbol{x}$ is approximated as the summation of the displacement at each node $\boldsymbol{u}_i$ weighted by the value of that node's shape function N_i at position $\boldsymbol{x}$; that is,

$$\boldsymbol{u} \approx \sum_{i=1}^{N_{\text{nodes}}} \boldsymbol{u}_i N_i\left(\boldsymbol{x}\right) \,, \tag{5.33}$$

where N_{nodes} is the number of nodes in the mesh. A boldface vector with a subscript $\bullet_i$ denotes the value of $\bullet$ at node i. However, the shape functions are not defined in terms of position in the current or reference domain. In fact, the shape functions are defined on a reference element. The reference element, shown for hexahedra and tetrahedra in Figures 5.2 (a) and (b), respectively, is the same for each hexahedron element and for each tetrahedron element in the mesh. Each hexahedron occupies the region $\{-1 \leq \xi_1 \leq 1,\, -1 \leq \xi_2 \leq 1,\, -1 \leq \xi_3 \leq 1\}$ whereas each tetrahedron has vertices at the points [1 0 0], [0 1 0], [0 0 1] and [0 0 0].

The shape functions satisfy the Kronecker delta property; that is,

$$N_i\left(\boldsymbol{\xi}_j\right) = \delta_{ij} \,, \tag{5.34}$$

where $\boldsymbol{\xi}_j$ is the position of node j in the reference element. For example, the shape functions

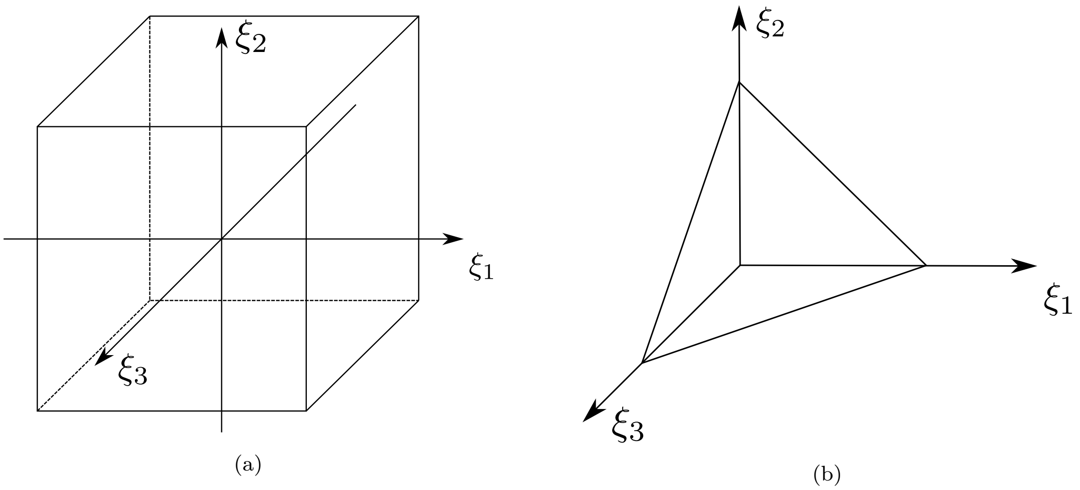

Figure 5.2: Hexahedron (a) and tetrahedron (b) elements in the reference domain. The hexahedron (a) occupies the region $\{-1 \leq \xi_1 \leq 1, -1 \leq \xi_2 \leq 1, -1 \leq \xi_3 \leq 1\}$ whereas the tetrahedron (b) has vertices at the points [1 0 0], [0 1 0], [0 0 1] and [0 0 0].

for an 8 noded trilinear hexahedron are

$$\begin{aligned}
N_1 &= \frac{1}{8}\left[\xi_1 - 1\right]\left[\xi_2 - 1\right]\left[\xi_3 - 1\right] , \quad & N_2 &= \frac{1}{8}\left[\xi_1 + 1\right]\left[\xi_2 - 1\right]\left[\xi_3 - 1\right] , \\
N_3 &= \frac{1}{8}\left[\xi_1 + 1\right]\left[\xi_2 + 1\right]\left[\xi_3 - 1\right] , \quad & N_4 &= \frac{1}{8}\left[\xi_1 - 1\right]\left[\xi_2 + 1\right]\left[\xi_3 - 1\right] , \\
N_5 &= \frac{1}{8}\left[\xi_1 - 1\right]\left[\xi_2 - 1\right]\left[\xi_3 + 1\right] , \quad & N_6 &= \frac{1}{8}\left[\xi_1 + 1\right]\left[\xi_2 - 1\right]\left[\xi_3 + 1\right] , \\
N_7 &= \frac{1}{8}\left[\xi_1 + 1\right]\left[\xi_2 + 1\right]\left[\xi_3 + 1\right] , \quad & N_8 &= \frac{1}{8}\left[\xi_1 - 1\right]\left[\xi_2 + 1\right]\left[\xi_3 + 1\right] .
\end{aligned} \tag{5.35}$$

The shape functions for a linear 4 noded tetrahedron are

$$\begin{aligned}
N_1 &= \xi_1 , \quad N_2 = \xi_2 , \\
N_3 &= \xi_3 , \quad N_4 = 1 - \xi_1 - \xi_2 - \xi_3 .
\end{aligned} \tag{5.36}$$

In equations (5.35) and (5.36) an element level enumeration of the shape functions has been used. This enumeration is mapped to the global enumeration of the nodes by an interconnectivity array, which must be defined for each mesh. The shape functions in equations (5.35) and (5.36) only hold within the element to which the node is attached, and are zero for all other elements. Moreover, for both hexahedra and tetrahedra, higher order shape functions can be constructed by adding nodes to the element.

The shape functions are used to create a map from the reference element to the current and reference configuration; that is, respectively,

$$\boldsymbol{x} = \sum_{i=1}^{N_{\text{nodes}}} \boldsymbol{x}_i N_i\left(\boldsymbol{\xi}\right) , \qquad \boldsymbol{X} = \sum_{i=1}^{N_{\text{nodes}}} \boldsymbol{X}_i N_i\left(\boldsymbol{\xi}\right) . \tag{5.37}$$

The shape functions are also used to approximate the solution and virtual velocity by interpolating their values at the nodes; that is,

$$\boldsymbol{u} \approx \boldsymbol{u}^h = \sum_{i=1}^{N_{\text{nodes}}} \boldsymbol{u}_i N_i \,, \qquad \delta\boldsymbol{v} \approx \delta\boldsymbol{v}^h = \sum_{i=1}^{N_{\text{nodes}}} \delta\boldsymbol{v}_i N_i \,. \tag{5.38}$$

Derivatives and gradients

In addition to approximating values such as the displacement and virtual velocity, one also requires a means to approximate gradients. This is done by taking the gradient of the approximation; that is,

$$\text{grad}\bullet \approx \text{grad}\bullet^h = \sum_{i=1}^{N_{\text{nodes}}} \bullet_i \otimes \text{grad}N_i \,. \tag{5.39}$$

However, this poses a difficulty in that N_i is defined on the reference element. This can be overcome by using the chain rule to obtain

$$\text{grad}N_i = \left[\frac{\partial\boldsymbol{\xi}}{\partial\boldsymbol{x}}\right]^T \frac{\partial N_i}{\partial\boldsymbol{\xi}} \,. \tag{5.40}$$

To evaluate equation (5.40), the Jacobian matrix is determined; that is,

$$\boldsymbol{J} = \frac{\partial\boldsymbol{x}}{\partial\boldsymbol{\xi}} = \sum_{i=1}^{N_{\text{nodes}}} \boldsymbol{x}_i \otimes \frac{\partial N_i}{\partial\boldsymbol{\xi}} \,. \tag{5.41}$$

Then the gradient of the shape function in the current configuration can be determined using

$$\text{grad}N_i = \boldsymbol{J}^{-T} \frac{\partial N_i}{\partial\boldsymbol{\xi}} \,. \tag{5.42}$$

Hence, the gradient of some quantity $\bullet$ is approximated by

$$\text{grad}\bullet \approx \sum_{i=1}^{N_{\text{nodes}}} \bullet_i \otimes \boldsymbol{J}^{-T} \frac{\partial N_i}{\partial\boldsymbol{\xi}} \,. \tag{5.43}$$

A similar approach is used to determine the gradient in the reference configuration. One takes the reference configuration gradient of the approximation of the desired quantity; that is,

$$\text{Grad}\bullet \approx \text{Grad}\bullet^h = \sum_{i=1}^{N_{\text{nodes}}} \bullet_i \otimes \text{Grad}N_i \,. \tag{5.44}$$

The chain rule is used to determine the reference configuration gradient of the shape functions; that is,

$$\text{Grad}N_i = \left[\frac{\partial\boldsymbol{\xi}}{\partial\boldsymbol{X}}\right]^T \frac{\partial N_i}{\partial\boldsymbol{\xi}} \,. \tag{5.45}$$

The reference configuration Jacobian matrix is then determined from

$$\boldsymbol{J}_0 = \frac{\partial \boldsymbol{X}}{\partial \boldsymbol{\xi}} = \sum_{i=1}^{N_{\text{nodes}}} \boldsymbol{X}_i \otimes \frac{\partial N_i}{\partial \boldsymbol{\xi}} \,, \tag{5.46}$$

and so the reference configuration gradient is given by

$$\text{Grad}\bullet \approx \sum_{i=1}^{N_{\text{nodes}}} \bullet_i \otimes \boldsymbol{J}_0^{-T} \frac{\partial N_i}{\partial \boldsymbol{\xi}} \,. \tag{5.47}$$

One also requires a means to approximate the deformation gradient. This can be done using the reference configuration gradient of the displacement, that is,

$$\boldsymbol{F} = \boldsymbol{I} + \text{Grad}\boldsymbol{u}^h \,, \tag{5.48}$$

or by using the reference and current Jacobian matrices; that is,

$$\boldsymbol{F} = \frac{\partial \boldsymbol{x}}{\partial \boldsymbol{X}} = \frac{\partial \boldsymbol{x}}{\partial \boldsymbol{\xi}} \frac{\partial \boldsymbol{\xi}}{\partial \boldsymbol{X}} = \boldsymbol{J} \boldsymbol{J}_0^{-1} \,. \tag{5.49}$$

Integration: Gaussian quadrature

In addition to derivatives, the weak form equations contain integrals. Hence, one requires a means to evaluate the integrals computationally. To do so, the integral is first represented as the summation of the integrals over each element; that is,

$$\int_{\Omega_0^h} g\left(\boldsymbol{X}\right) \mathrm{d}\Omega = \sum_{e=1}^{N_e} \int_{\Omega_0^e} g\left(\boldsymbol{X}\right) \mathrm{d}\Omega \,, \tag{5.50}$$

where Ω_0^h is the domain approximated by the undeformed mesh, g is a placeholder for a given integrand, Ω_0^e is the region occupied by element e in the reference configuration and N_e is the number of elements. The integral over each element is then transformed so that it is evaluated in the reference element domain as follows:

$$\int_{\Omega_0^e} g\left(\boldsymbol{X}\right) \mathrm{d}\Omega = \int_{\Omega_\square} g\left(\boldsymbol{X}\left(\boldsymbol{\xi}\right)\right) \det\left(\frac{\partial \boldsymbol{X}}{\partial \boldsymbol{\xi}}\right) \mathrm{d}\Omega_\square = \int_{\Omega_\square} g\left(\boldsymbol{X}\left(\boldsymbol{\xi}\right)\right) \det\left(\boldsymbol{J}_0\right) \mathrm{d}\Omega_\square \,, \tag{5.51}$$

where $\Omega_\square$ denotes the region of the element in the reference domain. One can then approximate the integral using Gaussian quadrature; that is,

$$\int_{\Omega_\square} g\left(\boldsymbol{X}\left(\boldsymbol{\xi}\right)\right) \det\left(\boldsymbol{J}_0\right) \mathrm{d}\Omega_\square \approx \sum_{p=1}^{n_p} g\left(\boldsymbol{X}\left(\boldsymbol{\xi}_p\right)\right) \det\left(\boldsymbol{J}_0\left(\boldsymbol{\xi}_p\right)\right) W_p \,, \tag{5.52}$$

where n_p is the number of integration points, $\boldsymbol{\xi}_p$ is the position of integration point p and W_p is the weight of integration point p. These values are given for different orders of Gaussian quadrature for hexahedral and tetrahedral elements in Tables 5.1 and 5.2, respectively.

Table 5.1: Gaussian quadrature points and weights for hexahedral elements [71]

n_p	p	ξ_1	ξ_2	ξ_3	W_p
4	1	0	$\sqrt{2/3}$	$-1/\sqrt{3}$	2
	2	0	$-\sqrt{2/3}$	$-1/\sqrt{3}$	2
	3	$\sqrt{2/3}$	0	$1/\sqrt{3}$	2
	4	$-\sqrt{2/3}$	0	$1/\sqrt{3}$	2
6	1	1	0	0	4/3
	2	-1	0	0	4/3
	3	0	1	0	4/3
	4	0	-1	0	4/3
	5	0	0	1	4/3
	6	0	0	-1	4/3

Table 5.2: Gaussian quadrature points and weights for tetrahedral elements [71]

n_p	p	ξ_1	ξ_2	ξ_3	W_p
1	1	1/4	1/4	1/4	1/6
5	1	1/4	1/4	1/4	-2/15
	2	1/6	1/6	1/6	3/40
	3	1/6	1/6	1/2	3/40
	4	1/6	1/2	1/6	3/40
	5	1/2	1/6	1/6	3/40

Discretized weak form

Here the weak form, equation (5.16), is discretized by using the finite element approximations. However, it is useful to first define a notation that allows one to represent symmetric matrices as vectors; that is, Voigt notation. The notation $\hat{\bullet}$ denotes the Voigt notation (that is, the vector) counterpart of the symmetric matrix $\bullet$. The Voigt notation of stress quantities, such as the Kirchhoff stress, is given by

$$\hat{\boldsymbol{\tau}} = \begin{bmatrix}\tau_{11} & \tau_{22} & \tau_{33} & \tau_{12} & \tau_{13} & \tau_{23}\end{bmatrix}^T , \tag{5.53}$$

whereas, for kinematic quantities, the off diagonal terms are multiplied by 2. Hence, the Voigt notation version of the rate of deformation is

$$\hat{\boldsymbol{D}} = \begin{bmatrix}D_{11} & D_{22} & D_{33} & 2D_{12} & 2D_{13} & 2D_{23}\end{bmatrix}^T . \tag{5.54}$$

Then, the inner product of the tensor quantities can be determined equivalently using the Voigt notation representation as

$$\delta \boldsymbol{D} : \boldsymbol{\tau} = \delta \hat{\boldsymbol{D}}^T \hat{\boldsymbol{\tau}} \,. \tag{5.55}$$

The symmetric gradient, that is,

$$\mathrm{grad}_\mathrm{s} \bullet = \frac{1}{2} \left[\mathrm{grad} \bullet^T + \mathrm{grad} \bullet \right] , \tag{5.56}$$

occurs several times in the weak form and its linearisation. Hence, it is useful to define a Voigt notation symmetric gradient operator for each node $\boldsymbol{B}_i$ such that

$$\hat{\boldsymbol{D}} \approx \sum_{i=1}^{N_\mathrm{nodes}} \boldsymbol{B}_i \boldsymbol{v}_i \,. \tag{5.57}$$

Note that $\hat{\boldsymbol{D}}$ is given by

$$\hat{\boldsymbol{D}} \approx \sum_{i=1}^{N_\mathrm{nodes}} \begin{bmatrix} v_1^i \dfrac{\partial N_i}{\partial x_1} \\ v_2^i \dfrac{\partial N_i}{\partial x_2} \\ v_3^i \dfrac{\partial N_i}{\partial x_3} \\ v_1^i \dfrac{\partial N_i}{\partial x_2} + v_2^i \dfrac{\partial N_i}{\partial x_1} \\ v_1^i \dfrac{\partial N_i}{\partial x_3} + v_2^i \dfrac{\partial N_i}{\partial x_1} \\ v_2^i \dfrac{\partial N_i}{\partial x_3} + v_3^i \dfrac{\partial N_i}{\partial x_2} \end{bmatrix} , \tag{5.58}$$

where v_j^i denotes the j^th component of the velocity at the i^th node. From inspection, it is apparent that $\boldsymbol{B}_i$ is given by

$$\boldsymbol{B}_i = \begin{bmatrix} \dfrac{\partial N_i}{\partial x_1} & 0 & 0 \\ 0 & \dfrac{\partial N_i}{\partial x_2} & 0 \\ 0 & 0 & \dfrac{\partial N_i}{\partial x_3} \\ \dfrac{\partial N_i}{\partial x_2} & \dfrac{\partial N_i}{\partial x_1} & 0 \\ \dfrac{\partial N_i}{\partial x_3} & 0 & \dfrac{\partial N_i}{\partial x_1} \\ 0 & \dfrac{\partial N_i}{\partial x_3} & \dfrac{\partial N_i}{\partial x_2} \end{bmatrix} . \tag{5.59}$$

Hence, the integrand of the internal virtual work can be developed as follows:

$$\delta \boldsymbol{D} : \boldsymbol{\tau} = \delta \hat{\boldsymbol{D}}^T \hat{\boldsymbol{\tau}} \approx \sum_{i=1}^{N_\mathrm{nodes}} \left[\boldsymbol{B}_i \delta \boldsymbol{v}_i \right]^T \hat{\boldsymbol{\tau}} = \sum_{i=1}^{N_\mathrm{nodes}} \delta \boldsymbol{v}_i^T \boldsymbol{B}_i^T \hat{\boldsymbol{\tau}} \,. \tag{5.60}$$

Substitution of the finite element approximations, that is, equations (5.38) and (5.60), into the weak form equation (5.16) results in

$$\begin{aligned} \delta W^h = \sum_{i=1}^{N_{\text{nodes}}} \sum_{j=1}^{N_{\text{nodes}}} \Bigg[& \int_{\Omega_0} \rho_0 N_i \delta \boldsymbol{v}_i^T \ddot{\boldsymbol{u}}_j N_j \,\mathrm{d}\Omega_0 \\ & + \int_{\Omega_0} \delta \boldsymbol{v}_i^T \boldsymbol{B}_i^T \hat{\boldsymbol{\tau}} \,\mathrm{d}\Omega_0 \\ & - \left[\int_{\Omega_0} N_i \delta \boldsymbol{v}_i^T \boldsymbol{g}_0 \,\mathrm{d}\Omega_0 + \int_{\Gamma_0^N} N_i \delta \boldsymbol{v}_i^T \bar{\boldsymbol{t}}_0 \,\mathrm{d}\Gamma \right] \Bigg] = 0\,. \end{aligned} \tag{5.61}$$

Since the virtual velocity and acceleration at each node do not depend on $\boldsymbol{X}$, one may take these values out the integrals and rearrange to obtain

$$\delta W^h = \sum_{i=1}^{N_{\text{nodes}}} \delta \boldsymbol{v}_i^T \sum_{j=1}^{N_{\text{nodes}}} \underbrace{\left[\int_{\Omega_0} \rho_0 N_i N_j \boldsymbol{I} \,\mathrm{d}\Omega_0 \ddot{\boldsymbol{u}}_j + \int_{\Omega_0} \boldsymbol{B}_i^T \hat{\boldsymbol{\tau}} \,\mathrm{d}\Omega_0 - \left(\int_{\Omega_0} N_i \boldsymbol{g}_0 \,\mathrm{d}\Omega_0 + \int_{\Gamma_0^N} N_i \bar{\boldsymbol{t}}_0 \,\mathrm{d}\Gamma \right) \right]}_{\boldsymbol{r}_i^h} = 0\,, \tag{5.62}$$

where $\boldsymbol{r}_i^h$ is the discretized residual at each node i. Since $\delta \boldsymbol{v}$ is arbitrary, equation (5.62) must hold for all $\delta \boldsymbol{v}_i$. Hence, the object is now to find the displacement of each node $\boldsymbol{u}_i\,(t)$ that satisfies

$$\boldsymbol{r}_i^h = \underbrace{\int_{\Omega_0} \rho_0 N_i N_j \boldsymbol{I} \,\mathrm{d}\Omega_0}_{\boldsymbol{M}_{ij}} \ddot{\boldsymbol{u}}_j + \underbrace{\int_{\Omega_0} \boldsymbol{B}_i^T \hat{\boldsymbol{\tau}} \,\mathrm{d}\Omega_0}_{\boldsymbol{F}_{int(i)}} - \underbrace{\left[\int_{\Omega_0} N_i \boldsymbol{g}_0 \,\mathrm{d}\Omega_0 + \int_{\Gamma_0^N} N_i \bar{\boldsymbol{t}}_0 \,\mathrm{d}\Gamma \right]}_{\boldsymbol{F}_{\text{ext}(i)}} = \boldsymbol{0}\,, \tag{5.63}$$

where $\boldsymbol{M}_{ij}$ is the mass matrix for the node pair ij and $\boldsymbol{F}_{\text{int}(i)}$ and $\boldsymbol{F}_{\text{ext}(i)}$ are the internal and external forces, respectively, at node i. In practice, this residual is determined using Gaussian quadrature as per the subsection above. Upon determining the mass matrix and internal and external force for each node, one may assemble these values into a global system of nonlinear equations; that is,

$$\boldsymbol{R} = \boldsymbol{M} \ddot{\boldsymbol{d}} + \boldsymbol{F}_{\text{int}} - \boldsymbol{F}_{\text{ext}} = \boldsymbol{0}\,, \tag{5.64}$$

where

$$\begin{gathered} \boldsymbol{R} = \begin{bmatrix} \boldsymbol{r}_1^h \\ \boldsymbol{r}_2^h \\ \vdots \\ \boldsymbol{r}_{N_{\text{nodes}}}^h \end{bmatrix}, \qquad \ddot{\boldsymbol{d}} = \begin{bmatrix} \ddot{\boldsymbol{u}}_1 \\ \ddot{\boldsymbol{u}}_2 \\ \vdots \\ \ddot{\boldsymbol{u}}_{N_{\text{nodes}}} \end{bmatrix}, \qquad \boldsymbol{F}_{\text{int}} = \begin{bmatrix} \boldsymbol{F}_{\text{int}(1)} \\ \boldsymbol{F}_{\text{int}(2)} \\ \vdots \\ \boldsymbol{F}_{\text{int}(N_{\text{nodes}})} \end{bmatrix}, \qquad \boldsymbol{F}_{\text{ext}} = \begin{bmatrix} \boldsymbol{F}_{\text{ext}(1)} \\ \boldsymbol{F}_{\text{ext}(2)} \\ \vdots \\ \boldsymbol{F}_{\text{ext}(N_{\text{nodes}})} \end{bmatrix}, \\ \boldsymbol{M} = \begin{bmatrix} \boldsymbol{M}_{11} & \boldsymbol{M}_{12} & \dots & \boldsymbol{M}_{1N\text{nodes}} \\ \boldsymbol{M}_{21} & \boldsymbol{M}_{22} & \dots & \boldsymbol{M}_{2N\text{nodes}} \\ \vdots & \ddots & \ddots & \vdots \\ \boldsymbol{M}_{N\text{nodes}1} & \boldsymbol{M}_{N\text{nodes}2} & \dots & \boldsymbol{M}_{N\text{nodes}N\text{nodes}} \end{bmatrix}. \end{gathered} \tag{5.65}$$

Discretized weak form linearisation

The linearisation of the semi-discrete problem is given by

$$\mathrm{L}\left[\delta W^h\right]\Delta\boldsymbol{u} = \delta W^h + \mathrm{D}\left[\delta W^h\right]\Delta\boldsymbol{u}\,. \tag{5.66}$$

Recall that the directional derivative of the internal virtual work given in equation (5.32) (see section 5.1.1) is

$$\mathrm{D}\left[\delta W_{\mathrm{int}}\right]\Delta\boldsymbol{u} = \int_{\Omega_0} \boldsymbol{\tau} : \mathrm{grad}\delta\boldsymbol{v}^T\mathrm{grad}\Delta\boldsymbol{u} + \delta\boldsymbol{D} : \mathbb{c}\,\mathrm{grad_s}\Delta\boldsymbol{u}\,\mathrm{d}\Omega_0\,. \tag{5.67}$$

To determine a useful expression for the discretization of the directional derivative, the following notation is temporarily adopted:

$$\frac{\partial\bullet}{\partial x_i} = \bullet_{,i}\,. \tag{5.68}$$

Then, the finite element approximations of the gradient of the virtual velocity and the increment in the solution can be expressed, respectively, as

$$\begin{aligned}\mathrm{grad}\delta\boldsymbol{v} &= \delta v_{i,j}\boldsymbol{e}_i\otimes\boldsymbol{e}_j \approx \sum_{k=1}^{N_{\mathrm{nodes}}}\delta v_i^k N_{,j}^k\boldsymbol{e}_i\otimes\boldsymbol{e}_j\,,\\ \mathrm{grad}\Delta\boldsymbol{u} &= \Delta u_{i,j}\boldsymbol{e}_i\otimes\boldsymbol{e}_j \approx \sum_{k=1}^{N_{\mathrm{nodes}}}\Delta u_i^k N_{,j}^k\boldsymbol{e}_i\otimes\boldsymbol{e}_j\,.\end{aligned} \tag{5.69}$$

Here the superscript is used to denote the node number and subscript is used to denote vector and tensor components. Using this notation, the first term in the integrand of the directional derivative (5.67) can be developed as follows:

$$\begin{aligned}\boldsymbol{\tau} : \mathrm{grad}\delta\boldsymbol{v}^T\mathrm{grad}\Delta\boldsymbol{u} &= \tau_{ij}\delta v_{k,i}\Delta u_{k,j}\\ &\approx \sum_{m=1}^{N_{\mathrm{nodes}}}\sum_{n=1}^{N_{\mathrm{nodes}}}\delta v_k^m N_{,i}^m\tau_{ij}N_{,j}^n\Delta u_k^n\\ &= \sum_{m=1}^{N_{\mathrm{nodes}}}\sum_{n=1}^{N_{\mathrm{nodes}}}\delta\boldsymbol{v}_m^T\left[\mathrm{grad}N_m\cdot\boldsymbol{\tau}\mathrm{grad}N_n\right]\boldsymbol{I}\Delta\boldsymbol{u}_n\,.\end{aligned} \tag{5.70}$$

Due to the minor symmetries of the constitutive tensor, that is,

$$\mathbb{c}_{ijkl} = \mathbb{c}_{jikl} = \mathbb{c}_{ijlk}\,, \tag{5.71}$$

one can construct a suitable Voigt notation representation as

$$\hat{\mathbb{c}} = \begin{bmatrix} \mathbb{c}_{1111} & \mathbb{c}_{1122} & \mathbb{c}_{1133} & \mathbb{c}_{1112} & \mathbb{c}_{1113} & \mathbb{c}_{1123}\\ \mathbb{c}_{2211} & \mathbb{c}_{2222} & \mathbb{c}_{2233} & \mathbb{c}_{2212} & \mathbb{c}_{2213} & \mathbb{c}_{2223}\\ \mathbb{c}_{3311} & \mathbb{c}_{3322} & \mathbb{c}_{3333} & \mathbb{c}_{3312} & \mathbb{c}_{3313} & \mathbb{c}_{3323}\\ \mathbb{c}_{1211} & \mathbb{c}_{1222} & \mathbb{c}_{1233} & \mathbb{c}_{1212} & \mathbb{c}_{1213} & \mathbb{c}_{1223}\\ \mathbb{c}_{1311} & \mathbb{c}_{1322} & \mathbb{c}_{1333} & \mathbb{c}_{1312} & \mathbb{c}_{1313} & \mathbb{c}_{1323}\\ \mathbb{c}_{2311} & \mathbb{c}_{2322} & \mathbb{c}_{2333} & \mathbb{c}_{2312} & \mathbb{c}_{2313} & \mathbb{c}_{2323} \end{bmatrix}. \tag{5.72}$$

Then, the finite element approximation of the second term in the integrand of the directional derivative (5.67) is given by

$$\delta \boldsymbol{D} : \mathbb{c}\mathrm{grad}_{\mathrm{s}} \Delta \boldsymbol{u} \approx \sum_{i=1}^{N_{\mathrm{nodes}}} \sum_{j=1}^{N_{\mathrm{nodes}}} \delta \boldsymbol{v}_i^T \boldsymbol{B}_i^T \hat{\mathbb{c}} \boldsymbol{B}_j \Delta \boldsymbol{u}_j \, . \tag{5.73}$$

Substitution of equations (5.70) and (5.73) into the directional derivative (5.67) yields the finite element approximation of the directional derivative; that is,

$$\mathrm{D}\left[\delta W_{\mathrm{int}}^h\right] \Delta \boldsymbol{u} = \sum_{i=1}^{N_{\mathrm{nodes}}} \delta \boldsymbol{v}_i^T \sum_{j=1}^{N_{\mathrm{nodes}}} \underbrace{\left[\int_{\Omega_0} \left[\mathrm{grad} N_i \cdot \boldsymbol{\tau} \mathrm{grad} N_j\right] \boldsymbol{I} + \boldsymbol{B}_i^T \hat{\mathbb{c}} \boldsymbol{B}_j \, \mathrm{d}\Omega_0\right]}_{\boldsymbol{K}_{ij}} \Delta \boldsymbol{u}_j \, , \tag{5.74}$$

where $\boldsymbol{K}_{ij}$ is the tangent stiffness matrix of the node pair ij.

5.2 Methods for solving quasistatic nonlinear problems

For many problems in solid mechanics, the loading rate is slow enough that the inertial forces are negligible. These problems are referred to as quasistatic. For quasistatic problems, the global residual reduces to

$$\boldsymbol{R}_q = \boldsymbol{F}_{\mathrm{int}} - \boldsymbol{F}_{\mathrm{ext}} = \boldsymbol{0} \, . \tag{5.75}$$

However, this does not imply that the problem is time-independent as the one or more of the involved constitutive laws may be rate- or path-dependent. Moreover, it is often beneficial to apply loads incrementally, as this improves the likelihood of convergence. Hence, even for quasistatic problems, it is useful to consider a partition of the time domain, that is,

$$0 = t_0 < t_1 < ... < t_n < t_{n+1} = t \, , \tag{5.76}$$

and define the time increment as

$$\Delta t_{n+1} = t_{n+1} - t_n \, . \tag{5.77}$$

Then, provided that the constitutive models have been converted to a suitable incremental form, equation (5.75) reduces from a potentially time-dependent problem, to a series of stationary problems; that is

$$\boldsymbol{R}_q^{n+1} = \boldsymbol{F}_{\mathrm{int}}\left(\boldsymbol{d}^{n+1}, \, \boldsymbol{d}^n\right) - \boldsymbol{F}_{\mathrm{ext}}\left(t_{n+1}\right) = \boldsymbol{0} \, , \tag{5.78}$$

where $\boldsymbol{d}^{n+1}$ is the solution at the current time step and $\boldsymbol{d}^n$ is the known solution at the previous time step. Then, one can find the solution to each stationary problem using the Newton-Raphson method.

5.2.1 Newton-Raphson method

The Newton-Raphson method determines the root of the residual at time step $n + 1$ by iteratively finding the root of the linearisation of virtual work; that is,

$$\mathrm{L}\left[\delta W^h\right]\Delta\boldsymbol{d}_{n+1} = [\delta\boldsymbol{v}]^T\left[\boldsymbol{R}_q^{n+1} + \boldsymbol{K}^{n+1}\Delta\boldsymbol{d}^{n+1}\right] = 0\,, \tag{5.79}$$

where $[\delta\boldsymbol{v}]$ denotes a global assembly of the virtual velocity at the nodes and $\boldsymbol{K}^{n+1}$ is a global assembly of the stiffness between every node pair determined from equation (5.74). Noting again that $\delta\boldsymbol{v}$ is arbitrary, setting the linearisation to zero implies that

$$\boldsymbol{R}_q^{n+1} + \boldsymbol{K}^{n+1}\Delta\boldsymbol{d}^{n+1} = \boldsymbol{0}\,, \tag{5.80}$$

and so the required change in the solution is given by

$$\Delta\boldsymbol{d}^{n+1} = -\left[\boldsymbol{K}^{n+1}\right]^{-1}\boldsymbol{R}_q^{n+1}\,. \tag{5.81}$$

Then, the solution for $\boldsymbol{d}^{n+1}$ that satisfies equation (5.75) can be found by iteratively finding the root of the linearisation; that is,

$$\boldsymbol{d}_{i+1}^{n+1} = \boldsymbol{d}_i^{n+1} - \left[\boldsymbol{K}_i^{n+1}\right]^{-1}\boldsymbol{R}_{q(i)}^{n+1}\,, \tag{5.82}$$

where $\boldsymbol{d}_{i+1}^{n+1}$ and $\boldsymbol{d}_i^{n+1}$ denote the solution after and before the current Newton-Raphson iteration, respectively, $\boldsymbol{K}_i^{n+1}$ denotes the current tangent stiffness matrix and $\boldsymbol{R}_{q(i)}^{n+1}$ denotes the current residual. After the change in the solution becomes sufficiently small, one may exit the Newton-Raphson procedure and proceed to the next time step. This is the approach taken by the ABAQUS/Standard solver when a quasistatic load step is prescribed [72].

5.3 Methods for solving nonlinear time-dependent systems of equations

For problems where inertial forces are present, one must adopt a time integration scheme. Generally speaking, these break into two categories: explicit time integration and implicit time integration. Explicit time integration schemes assert that the initial value ODEs (in our case given by equation (5.64)) holds at the start of the time step, whereas implicit schemes assert that the ODEs hold at the end of the time step. Additionally, explicit schemes are typically only conditionally stable, that is the solution remains finite as long as the time step size is below some tolerance, whereas implicit schemes are typically unconditionally stable.

5.3.1 Central difference method – explicit time integration

The central difference method approximates the acceleration at time step n as

$$\ddot{\boldsymbol{d}}^n = \frac{\boldsymbol{d}^{n+1} - 2\boldsymbol{d}^n + \boldsymbol{d}^{n-1}}{\Delta t^2} \,. \tag{5.83}$$

One can then construct an explicit time integration scheme by asserting that the residual is zero at time step n; that is

$$\boldsymbol{M}\ddot{\boldsymbol{d}}^n + \boldsymbol{F}_{\text{int}}\left(\boldsymbol{d}^n, \boldsymbol{d}^{n-1}\right) - \boldsymbol{F}_{\text{ext}}\left(t_n\right) = 0 \,. \tag{5.84}$$

Substitution of the central difference approximation, equation (5.83), into the dynamic equilibrium equation (5.84) and rearranging yields

$$\boldsymbol{d}^{n+1} = 2\boldsymbol{d}^n - \boldsymbol{d}^{n-1} + \Delta t^2 \boldsymbol{M}^{-1}\left[\boldsymbol{F}_{\text{ext}} - \boldsymbol{F}_{\text{int}}\right] \,. \tag{5.85}$$

Hence, the solution at the next time step can be approximated without the need for linearisation. Additionally, this central difference time integration scheme is often implemented with mass lumping, whereby the mass matrix is approximated by a diagonal matrix. Then, the inverse of the mass matrix is determined trivially and so little computational effort is required per time step. This is the approach taken by the Abaqus/Explicit solver [72].

The stable time increment is limited by the maximum eigenvalue in the system ω_{max} according to

$$\Delta t \leq \frac{2}{\omega_{max}} \,. \tag{5.86}$$

This can be conservatively estimated by

$$\Delta t \leq \min_e \frac{L_e}{c_d} \,, \tag{5.87}$$

where L_e is the characteristic element length of element e and c_d is the current effective dilatation wave speed of the material. Hence, the permissible time increment is typically small, which makes this method most suitable for problems with a small time domain.

5.3.2 Newmark method – implicit time integration

According to the Newmark method, the solution and velocity at the next time step is approximated, respectively, by

$$\boldsymbol{d}^{n+1} = \boldsymbol{d}^n + \Delta t\dot{\boldsymbol{d}}^n + \Delta t^2\left[\left[\frac{1}{2} - \beta\right]\ddot{\boldsymbol{d}}^n - \beta\ddot{\boldsymbol{d}}^{n+1}\right] \,, \tag{5.88}$$

$$\dot{\boldsymbol{d}}^{n+1} = \dot{\boldsymbol{d}}^n + \Delta t\left[\left[1 - \gamma\right]\ddot{\boldsymbol{d}}^n + \gamma\ddot{\boldsymbol{d}}^{n+1}\right] \,. \tag{5.89}$$

Here β and γ are user chosen parameters given by

$$\beta = \frac{1}{4}\left[1-\alpha\right]^2 , \qquad \gamma = \frac{1}{2} - \alpha \, , \qquad -\frac{1}{2} < \alpha < 0 \, . \tag{5.90}$$

One can then construct an implicit time integration scheme by asserting that the residual is zero at the next time step; that is,

$$\boldsymbol{M}\ddot{\boldsymbol{d}}^{n+1} + \boldsymbol{F}_{\text{int}} - \boldsymbol{F}_{\text{ext}} = \boldsymbol{0} \, . \tag{5.91}$$

By rearranging equation (5.91) and substitution into equation (5.88) one can construct the residual equation

$$\boldsymbol{R}_d^{n+1} = \boldsymbol{M}\left[\boldsymbol{d}^{n+1} - \boldsymbol{d}^{n} - \Delta t^2 \left[\frac{1}{2} - \beta\right] \ddot{\boldsymbol{d}}^{n}\right] + \beta \Delta t^2 \left[\boldsymbol{F}_{\text{int}}^{n+1} - \boldsymbol{F}_{\text{ext}}^{n+1}\right] = \boldsymbol{0} \, . \tag{5.92}$$

The directional derivative of the residual in the direction of a change in the solution at the time step $n+1$ is given by

$$\mathrm{D}\left[\boldsymbol{R}_d^{n+1}\right] \Delta \boldsymbol{d}^{n+1} = \left[\boldsymbol{M} + \beta \Delta t^2 \boldsymbol{K}^{n+1}\right] \Delta \boldsymbol{d}^{n+1} \, . \tag{5.93}$$

Hence, the solution at time step $n+1$ that satisfies equation (5.92) can be determined by iteratively evaluating the equation

$$\boldsymbol{d}_{i+1}^{n+1} = \boldsymbol{d}_{i}^{n+1} - \left[\boldsymbol{M} + \beta \Delta t^2 \boldsymbol{K}_i^{n+1}\right]^{-1} \boldsymbol{R}_d^{n+1} \, . \tag{5.94}$$

As with quasistatic problems, after the change in the solution becomes sufficiently small one may exit the Newton-Raphson procedure and proceed to the next time step. This is the approach taken by the ABAQUS/Standard solver when an implicit dynamic load step is prescribed [72].

Each Newmark method time step is more computationally expensive than a central difference method time step, since it requires the inversion of a (non-diagonal) matrix. However, the time increment size is not limited by stability, it is unconditionally stable in contrast to the central difference method. Hence, the Newmark method is well suited for problems with a large time domain.

Chapter 6

Multiscale modelling

It may be the case that a structure contains heterogeneities at a length scale that is significantly smaller than that of the entire structure. However, the heterogeneities significantly affect the mechanical behaviour of the structure as a whole. A naive approach to modelling the behaviour of the structure using the FEM would be to create a mesh fine enough to capture the heterogeneities. However, this will typically lead to an unmanageably large number of degrees of freedom and intractable computational requirements. This difficulty can be avoided using multiscale modelling, of which homogenization is a key component.

Homogenization is a procedure by which the mechanical behaviour of a heterogeneous material is described by an averaged response of a representative volume element (RVE) of the material. When conducting multiscale modelling, the homogenized response of the RVE is used to define the constitutive relation at the macroscale. Then, a suitably (but not excessively) fine mesh of the structure at the macroscale can be used with the constitutive relation provided by the RVE to model the behaviour of the structure as a whole.

This is pertinent in the computational experiments on the mechanical behaviour of turtle shells presented in Chapter 9. In particular, the goal is to determine the effect of a network of sutures on the mechanical behaviour of the shell as a whole. An additional goal is to elucidate the structure-property relationship by simulating the mechanical behaviour for various suture geometries. However, the geometric features of the sutures are far smaller than the length scale of the entire shell, and so a multiscale modelling approach is used to avoid the requirement of an excessively fine mesh.

6.1 Theory

At the core of homogenization theory is the Hill-Mandel principle. It asserts that the stress power at a macroscopic point must be equal to the volume average of the stress power of the associated RVE [73, 74]; that is,

$$\boldsymbol{P}_M : \dot{\boldsymbol{F}}_M = \left\langle \boldsymbol{P}_m : \dot{\boldsymbol{F}}_m \right\rangle_{\Omega_m} . \tag{6.1}$$

Here, the notation $\bullet_M$ denotes a macroscale quantity, $\bullet_m$ denotes a microscale quantity, and $\langle \bullet \rangle_\square$ denotes the average of $\bullet$ over the reference domain $\square$; that is,

$$\langle \bullet \rangle_\square = \frac{1}{V_\square} \int_\square \bullet \, \mathrm{d}\square \,, \tag{6.2}$$

where $V_\square$ is the reference configuration volume of the domain $\square$. Furthermore, the macroscopic deformation gradient and the volume average of the microscopic deformation gradient are equated; that is,

$$\boldsymbol{F}_M = \langle \boldsymbol{F}_m \rangle_{\Omega_m} . \tag{6.3}$$

It then follows that the microscopic deformation gradient is the sum of the macroscopic deformation gradient, which is constant over the RVE, and a microscopic fluctuation $\tilde{\boldsymbol{F}}_m$; that is,

$$\boldsymbol{F}_m = \boldsymbol{F}_M + \tilde{\boldsymbol{F}}_m \,. \tag{6.4}$$

Of course, to satisfy equation (6.3) the volume average of the microscopic fluctuation must be zero; that is,

$$\left\langle \tilde{\boldsymbol{F}}_m \right\rangle_{\Omega_m} = \boldsymbol{0} \,. \tag{6.5}$$

Substitution of equation (6.4) into the Hill-Mandel principle (6.1) yields

$$\boldsymbol{P}_M : \dot{\boldsymbol{F}}_M = \langle \boldsymbol{P}_m \rangle_{\Omega_m} : \dot{\boldsymbol{F}}_M + \left\langle \boldsymbol{P}_m : \dot{\tilde{\boldsymbol{F}}}_m \right\rangle_{\Omega_m} , \qquad \forall \dot{\boldsymbol{F}}_M ,\, \dot{\tilde{\boldsymbol{F}}}_m \,. \tag{6.6}$$

By considering the case where $\dot{\tilde{\boldsymbol{F}}}_m = \boldsymbol{0}$ the stress averaging relation between the microscale and macroscale is obtained; that is,

$$\boldsymbol{P}_M = \langle \boldsymbol{P}_m \rangle_{\Omega_m} , \qquad \forall \boldsymbol{F}_M \,. \tag{6.7}$$

Hence, asserting the Hill-Mandel principle and the equality of the macroscale deformation gradient to the volume average of the microscale deformation gradient, results is the macroscale first Piola-Kirchhoff stress being equal to the volume average of its microscale counterpart. Then, by substitution of equations (6.3) and (6.7) into equation (6.1) one obtains

$$\boldsymbol{P}_M : \dot{\boldsymbol{F}}_M = \langle \boldsymbol{P}_m \rangle_{\Omega_m} : \left\langle \dot{\boldsymbol{F}}_m \right\rangle_{\Omega_m} = \left\langle \boldsymbol{P}_m : \dot{\boldsymbol{F}}_m \right\rangle_{\Omega_m} , \tag{6.8}$$

which is commonly referred to as the Hill-Mandel condition. This condition is satisfied by choosing appropriate boundary conditions. Three commonly used suitable boundary conditions are:

- Linear displacement; that is,

  $$\boldsymbol{u}|_{\Gamma_m} = [\boldsymbol{F}_M - \boldsymbol{I}]\,\boldsymbol{X}\,, \tag{6.9}$$

  where Γ_m is the boundary of the RVE;

- Uniform traction; that is,

  $$\boldsymbol{t}_0|_{\Gamma_m} = \boldsymbol{P}_M\boldsymbol{n}_0\,; \tag{6.10}$$

- Periodic boundary conditions; that is,

  $$\boldsymbol{u}^+ - \boldsymbol{u}^- = [\boldsymbol{F}_M - \boldsymbol{I}]\left[\boldsymbol{X}^+ - \boldsymbol{X}^-\right]\,. \tag{6.11}$$

  Here, $\bullet^+$ and $\bullet^-$ denote corresponding values on opposite sides of the RVE.

When equipped with suitable boundary conditions, an RVE provides a constitutive relation at the macroscale; that is, it relates the macroscale deformation gradient to the macroscale stress. Periodic boundary conditions are considered to be preferable for periodic structures [75], and so, due to the periodicity of suture geometry, periodic boundary conditions are used in this work.

On a separate point, it has been shown that only the fluctuations of microscale inertia and body forces affect the resulting homogenized stress [76]. Hence, if the loading rate is orders of magnitude lower than the acoustic velocity of the materials involved, one may use the special case of equilibrium as the governing equation at the microscale in place of the linear balance of momentum.

The strong form of the two-scale boundary value problem is then as follows: find the displacement field $\boldsymbol{u}_M(\boldsymbol{x}_M, t)$ that satisfies

$$\rho\ddot{\boldsymbol{u}}_M = \mathrm{div}\boldsymbol{\sigma}_M + \boldsymbol{g} \qquad \text{for } \boldsymbol{x}_M \in \Omega_M,\ t \in [0, t_{end}]\,, \tag{6.12}$$

the boundary conditions

$$\begin{aligned} \boldsymbol{u}_M &= \bar{\boldsymbol{u}}_M && \text{on } \Gamma^D\,, && (6.13)\\ \boldsymbol{t}_M &= \bar{\boldsymbol{t}}_M && \text{on } \Gamma^N\,, && (6.14)\\ \Gamma^N \cup \Gamma^D &= \Gamma\,, && \Gamma^N \cap \Gamma^D = \varnothing\,, && (6.15) \end{aligned}$$

and initial conditions

$$\boldsymbol{u} = \bar{\boldsymbol{u}}_0 \qquad \text{at } t = 0\,, \tag{6.16}$$

$$\dot{\boldsymbol{u}} = \bar{\boldsymbol{v}}_0 \qquad \text{at } t = 0\,, \tag{6.17}$$

where $\boldsymbol{\sigma}_M$ is given by

$$\boldsymbol{\sigma}_M = \det(\boldsymbol{F}_M)^{-1} \left\langle \boldsymbol{P}_m \right\rangle_{\Omega_m} \boldsymbol{F}_M^T\,, \tag{6.18}$$

$$\boldsymbol{F}_M = \boldsymbol{I} + \mathrm{Grad}\, \boldsymbol{u}_M\,. \tag{6.19}$$

The microscale stress field $\boldsymbol{P}_m$ is obtained by finding the microscale displacement field $\boldsymbol{u}_m(\boldsymbol{x}_m, t)$ that satisfies

$$\boldsymbol{0} = \mathrm{div}\boldsymbol{\sigma}_m\,, \qquad \text{for } \boldsymbol{x}_m \in \Omega_m,\ t \in [0, t_{end}] \tag{6.20}$$

and the microscale boundary conditions

$$\boldsymbol{u}_m^+ - \boldsymbol{u}_m^- = [\boldsymbol{F}_M - \boldsymbol{I}] \left[\boldsymbol{X}_m^+ - \boldsymbol{X}_m^-\right]\,, \tag{6.21}$$

where

$$\boldsymbol{\sigma}_m = \det(\boldsymbol{F}_m)^{-1} \boldsymbol{P}_m \boldsymbol{F}_m^T\,. \tag{6.22}$$

6.2 Computational homogenization

For geometrically simple RVEs, it may be possible to obtain an analytical solution for the microscale BVP. However, this is typically not the case. Hence, one resorts to a computational approach. This section presents how ABAQUS can be used to create a constitutive relation at the macroscale for a given RVE.

6.2.1 Using Abaqus to homogenize a nonlinear RVE for finite deformations

Homogenizing an RVE using ABAQUS requires several components of code. A high-level code architecture diagram for this procedure is presented in Figure 6.1. A brief description of the architecture is provided here, and more detailed explanations are provided in the following subsections. The procedure is orchestrated by the `Python` script `execute_rve.py`. The `execute_rve.py` script must be provided with the macroscale deformation gradient $\boldsymbol{F}_M$ and a template for the RVE input file `rve_tmp.inp`. The input file template contains a description

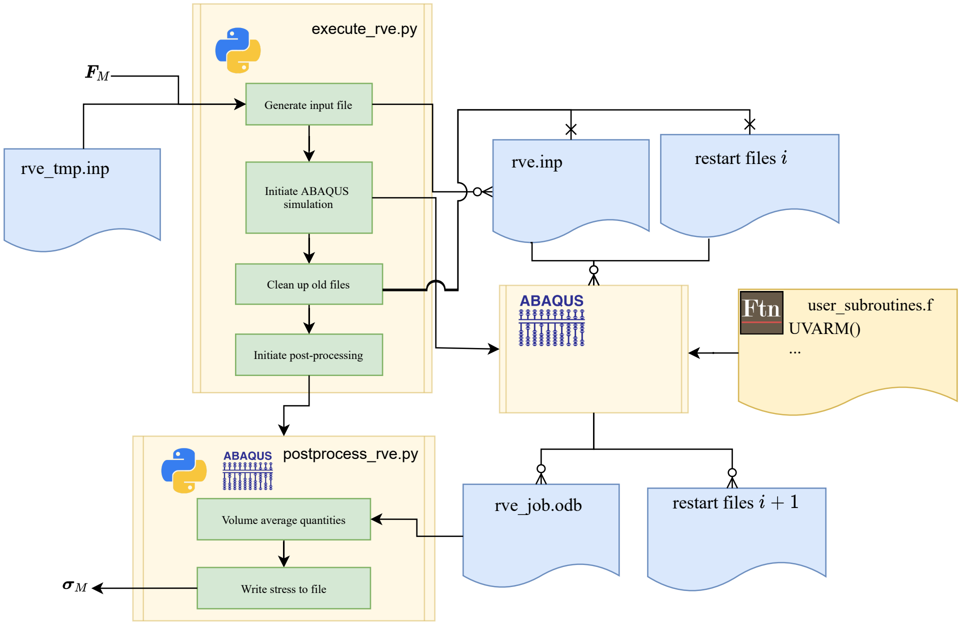

Figure 6.1: Code architecture diagram for homogenization of an RVE using Abaqus.

of the mesh and constitutive models for the materials in the RVE. Then, in `execute_rve.py`, an input file `rve.inp` is written by adding the periodic boundary conditions defined using $\boldsymbol{F}_M$ to the input file template. An Abaqus simulation is then initiated which solves the finite element problem described by the input file. The simulation may optionally be provided with restart files from a previous RVE simulation. The reason for this is explained in more detail later in this section. The simulation is also provided with a `UVARM` user subroutine. This subroutine allows for user-defined output variables at integration points. Hence, it is used to record volume weighted stress values at the integration points. Once the simulation completes, a database `rve_job.odb` of the simulation results along with several restart files is produced. The `execute_rve.py` script then removes the old input and restart files and runs another `Python` script `postprocess_rve.py`. However, this script must be run in the Abaqus kernel since it requires access to the Abaqus API to read and operate on the output database `rve_job.odb`. The `postprocess_rve.py` script sums the volume weighted stress values at each integration point (created by the `UVARM` subroutine) to complete the Gaussian quadrature of the stress over the volume of the RVE. It divides the resulting value by the volume of the RVE to create the volume averaged stress, which is then written to a file. Of course, throughout the entire procedure, one must take care to ensure the correct reference or current configuration quantities are used in the correct places. Hence, a number of push-forward and pull-back operations are applied throughout the procedure.

Input file template: applying periodic boundary conditions

The input file template is constructed by creating a model of the RVE in the ABAQUS/CAE graphical user interface (GUI). Here, one creates the geometry of the RVE, defines the material models for each region of the model and generates an appropriate finite element mesh. Carrying out these tasks is a standard requirement for every ABAQUS model, and so the details are not provided here. However, one also requires a means to apply periodic boundary conditions to the RVE, which is not a standard feature in ABAQUS. Hence, a significant amount of input is required from the user to enforce periodic boundary conditions. The procedure to do so is as follows:

- One creates a 'control node' for each $\bullet^+$ and $\bullet^-$ boundary facet pair, as illustrated in Figure 6.2. The position of each control node is not important.
- One then creates sets of boundary node pairs. Given that the dimensions of the RVE are $L_x \times L_y \times L_z$, the appropriate pair node for a node with position $\boldsymbol{x}$ on the boundary with outward facing normal $\boldsymbol{n}$ has a position of $\boldsymbol{x} - L_i \boldsymbol{n}$, where i is a place-holder for x, y or z depending on which boundary facet the node is on. An example of a node pair is labelled in 6.2 for the nodes x_1^- and x_1^+. Here, if node x_1^- has the position $[x_1 \ \ y_1 \ \ z_1]$, then node x_1^+ has the position $[x_1 + L_x \ \ y_1 \ \ z_1]$. This, of course, requires that the mesh is symmetric on the boundary.
- Multipoint constraints between the node pairs and the relevant control node are then defined with the constraint equation

  $$\boldsymbol{u}_i^+ - \boldsymbol{u}_i^- = \boldsymbol{u}_{control} \, , \tag{6.23}$$

  where $\boldsymbol{u}_i^+$ and $\boldsymbol{u}_i^-$ are the displacements of some node pair i on the positive and negative boundaries, respectively, and $\boldsymbol{u}_{control}$ is the displacement of the relevant control node.
- Periodic boundary conditions can then be prescribed by setting

  $$\boldsymbol{u}_{control} = [\boldsymbol{F}_M - \boldsymbol{I}] \left[\boldsymbol{X}^+ - \boldsymbol{X}^-\right] \tag{6.24}$$

  for each control node.
- Finally, to avoid rigid-body displacements and rotations, a direct and torsional spring is applied for each direction to one node in the mesh.

Since the mesh contains many nodes, the above procedure is automated through a macro written in `Python`.

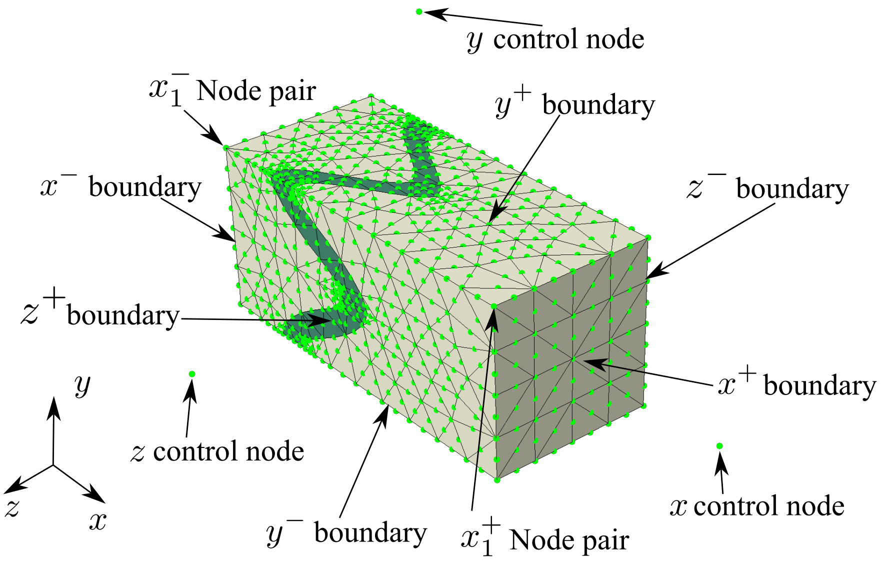

Figure 6.2: Illustration of an RVE with the relevant control nodes used to prescribe periodic boundary conditions.

Once the model has been generated, with the necessary control nodes and multipoint constraints, an input file, `rve_tmp.inp`, is generated using the Abaqus/CAE GUI. This input file is used as the input file template, that is, the loading steps are added to the input file later by string manipulation in `Python` instead of by manually adding steps and boundary conditions in the Abaqus/CAE GUI.

Averaging quantities: `UVARM` subroutine and post-processing

Determining the volume averaged stress requires integration of the stress over the domain. This is done numerically using Gaussian quadrature; that is,

$$\begin{aligned}\langle \boldsymbol{P}_m \rangle_{\Omega_m} &= \frac{1}{V_{\Omega_m}} \int_{\Omega_m} \boldsymbol{P}_m \mathrm{d}\Omega_m \\ &= \frac{1}{V_{\Omega_m}} \sum_{e=1}^{N_e} \int_{\Omega_{m(e)}} \boldsymbol{P}_m \mathrm{d}\Omega_m \\ &= \frac{1}{V_{\Omega_m}} \sum_{e=1}^{N_e} \sum_{p=1}^{n_p} \boldsymbol{P}_m \left(\boldsymbol{X}_e \left(\boldsymbol{\xi}_p \right) \right) \underbrace{\det \left(\boldsymbol{J}_{0(e)} \left(\boldsymbol{\xi}_p \right) \right) W_p}_{ivol_0} .\end{aligned} \tag{6.25}$$

Here N_e is the number of elements in the RVE mesh, $\Omega_{m(e)}$ is the domain of the e^{th} element in the reference configuration and $\boldsymbol{X}_e$ and $\boldsymbol{J}_{0(e)}$ denotes the map from the reference element to the reference domain and the reference configuration Jacobian matrix, respectively, for element e. Additionally, the term $\det\left(\boldsymbol{J}_{0(e)}\left(\boldsymbol{\xi}_p\right)\right) W_p$ is commonly referred to as the integration point volume and so the shorthand $ivol_0$ is assigned. The subscript 0 implies that it is the reference configuration volume of the integration point. In Abaqus, user-defined outputs at integration points can be defined using the `UVARM` subroutine. However, Abaqus uses current configuration quantities, such as the Cauchy stress and the current configuration integration point volume; that is,

$$ivol = \det\left(\boldsymbol{J}_{(e)}\left(\boldsymbol{\xi}_p\right)\right) W_p\,, \tag{6.26}$$

where $\boldsymbol{J}_{(e)}$ denotes the current configuration Jacobian matrix. Hence, pull-back operations are required to obtain the correct quantities. The first Piola-Kirchhoff stress can be obtained from the Cauchy stress using

$$\boldsymbol{P} = J\boldsymbol{\sigma}\boldsymbol{F}^{-T}\,. \tag{6.27}$$

To pull back the integration point volume, recall from equation (5.49) that the deformation gradient can be obtained from the reference and current configuration Jacobian matrices using

$$\boldsymbol{F} = \boldsymbol{J}\boldsymbol{J}_0^{-1}\,. \tag{6.28}$$

Taking the determinant of both sides of equation (6.28) gives

$$J = \frac{\det\left(\boldsymbol{J}\right)}{\det\left(\boldsymbol{J}_0\right)}\,. \tag{6.29}$$

Hence, the reference configuration integration point volume can be determined from its current configuration counterpart using

$$ivol_0 = ivol/J\,. \tag{6.30}$$

Using equations (6.27) and (6.30) an appropriate `UVARM` subroutine can be written.

The Gauss quadrature is then completed by summing the values for $\boldsymbol{P}_m\, ivol_0$ (see equation (6.25)) stored in the output database at each integration point. This is done using the `Python` script `postprocess_rve.py`.

Restarts

Each integration point in the macroscopic geometry follows a loading path through time. In practice, the time domain is discretized and so the loading path consists of a finite number of deformation gradients and corresponding stresses; that is, respectively,

$$\left\{\boldsymbol{F}_{M(1)},\, \boldsymbol{F}_{M(2)},\, ...,\boldsymbol{F}_{M(i)},\, ...,\, \boldsymbol{F}_{M(n)}\right\}, \qquad \left\{\boldsymbol{\sigma}_{M(1)},\, \boldsymbol{\sigma}_{M(2)},\, ...,\boldsymbol{\sigma}_{M(i)},\, ...,\, \boldsymbol{\sigma}_{M(n)}\right\}. \tag{6.31}$$

Since the constitutive model is provided by an RVE, the RVE ought to follow this same loading path. For RVEs that contain path- or rate-dependent materials this is clearly essential. For hyperelastic RVEs that are not path- or rate-dependant this is not essential, but it is preferable as the load increment required to go from the solution at step i to $i+1$ is typically less than the increment required to go from the stress-free reference state to the solution at $i+1$. Hence, convergence to the solution at $i+1$ is typically obtained sooner if the load increment is applied to the solution at step i instead of the stress-free state.

To achieve this, it is required that the RVE simulations at each step are restarted from the converged solution at the previous macroscale step. This can be done in ABAQUS by using 'restarts'. Restarts allow one to add loading steps to an ABAQUS simulation after it has concluded. Then, the simulation can be restarted from where it last concluded, and each new loading step will be processed. Hence, during the iterative Newton-Raphson procedure at the macroscale each new trial stress value is calculated by adding a load step to the RVE at the previous converged step. Then, once the macroscale Newton-Raphson procedure has converged, the restart files for the previous step are deleted and the restart files for the current step are used to initialize the solution at the subsequent step.

Verification of periodic boundary conditions and stress homogenization

To verify that the periodic boundary conditions and stress averaging are implemented correctly, the homogenization procedure is applied to a homogeneous test RVE. The test RVE, show in Figure 6.3, is a unit cube that is meshed using 10 × 10 × 10 quadratic hexahedral elements (C3D20R).

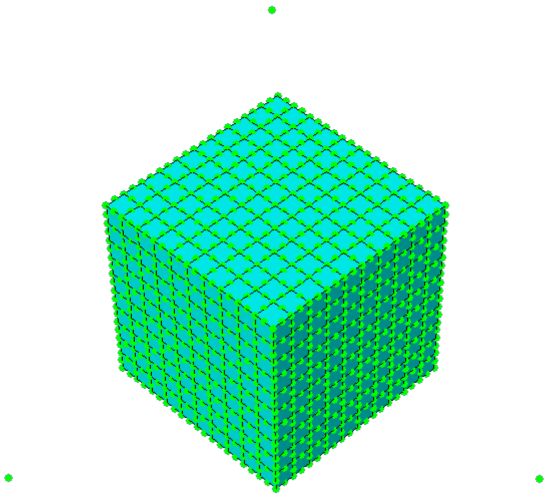

Figure 6.3: Test RVE used to verify the implementation of periodic boundary conditions and stress homogenization. The control nodes are included in the image.

The homogenous RVE is assigned a Neo-Hookean constitutive law of the form

$$\boldsymbol{\sigma}_{NH} = \frac{2C}{J}\left[\bar{\boldsymbol{B}} - \frac{1}{3}\bar{I}_1\boldsymbol{I}\right] + \frac{2}{D}\left[J-1\right]\boldsymbol{I}\,, \tag{6.32}$$

where C and D are material parameters with the values

$$C = 1\,, \qquad D = 0.1\,. \tag{6.33}$$

Since the RVE is homogenous, the homogenized stress should be equal to that of the prescribed constitutive law, so that

$$\boldsymbol{\sigma}_M = \det\left(\boldsymbol{F}_M\right)^{-1} \langle \boldsymbol{P}_m \rangle_{\Omega_m} \boldsymbol{F}_M^T = \boldsymbol{\sigma}_{NH}\,. \tag{6.34}$$

Additionally, the periodic boundary conditions should ensure that the applied macroscale deformation gradient is equal to the homogenized microscale deformation gradient; that is,

$$\boldsymbol{F}_M = \langle \boldsymbol{F}_m \rangle_{\Omega_m}\,. \tag{6.35}$$

Here, $\langle \boldsymbol{F}_m \rangle_{\Omega_m}$ can be determined using a simple extension of the `UVARM` subroutine. Hence, one can verify that the periodic boundary conditions have been implemented correctly by applying a range of macroscale deformation gradients to the RVE and verifying that the difference between the macroscale deformation gradient and the volume averaged deformation gradient is small; that is, determining if the value of

$$\frac{\left|\left|\boldsymbol{F}_M - \langle \boldsymbol{F}_m \rangle_{\Omega_m}\right|\right|}{\left|\left|\boldsymbol{F}_M\right|\right|} \tag{6.36}$$

is sufficiently small. The implementation of the stress homogenization can be verified similarly by verifying that the value of

$$\frac{\left|\left|\boldsymbol{\sigma}_{NH} - \det(\boldsymbol{F}_M)^{-1} \langle \boldsymbol{P}_m \rangle_{\Omega_m} \boldsymbol{F}_M^T\right|\right|}{\left|\left|\boldsymbol{\sigma}_{NH}\right|\right|} \tag{6.37}$$

is sufficiently small. A range of deformation gradients used to test on the RVE are created using the equation

$$\boldsymbol{F}_M = \boldsymbol{I} + \alpha \begin{bmatrix} 0.2 & 0.1 & 0.25 \\ 0.3 & -0.3 & -0.1 \\ -0.2 & 0.2 & -0.15 \end{bmatrix}, \tag{6.38}$$

where $\alpha \in [0,\, 1]$ and the matrix which is scaled by α has been chosen arbitrarily. Then, 30 linearly spaced values of α are used to create 30 deformation gradients to apply to the RVE. The resulting relative difference in the homogenized deformation gradient and stress are displayed in Figures 6.4 (a) and (b), respectively. The relative difference is less than 2×10^{-4} for both the deformation gradient and stress, that is, less than $0.02\,\%$. The presence of this small difference is attributed to round-off error in the Gaussian quadrature procedure and is deemed to be sufficiently small.

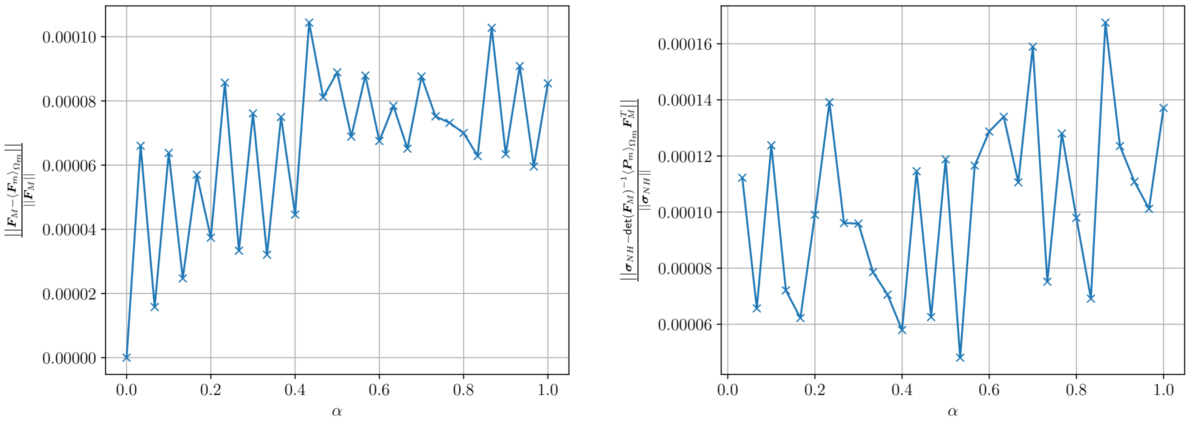

(a) (b)

Figure 6.4: Plots of relative difference for (a) the homogenized and macroscale deformation gradient and (b) the homogenized and macroscale stress.

6.2.2 Computational multiscale modelling

Concurrent multiscale modelling

During concurrent multiscale modelling, each macroscale integration point is assigned an RVE. Then a simulation at the RVE level is carried out each time the constitutive law is required at the macroscale. This results in several RVE FE simulations running concurrently with the macroscale FE simulation, hence, the term ‘concurrent multiscale modelling’. This is also commonly referred to as FE^2 [77, 78, 79].

To apply this in Abaqus one would write a `UMAT` which initiates the code architecture displayed in Figure 6.1 with the appropriate deformation gradient. Then, once the RVE simulation completes, it would read in the stress. However, the Jaumann constitutive tensor (see equation (3.91)) is also required. This can be obtained by using a differencing procedure similar to that presented in [80] which would require six more RVE simulations. Hence, seven nonlinear RVE FE simulations are required for each integration point in the macroscale geometry for each Newton-Raphson iteration. This makes concurrent homogenization both extremely memory and computationally expensive.

Several approaches have been used in the literature to resolve this issue. These include the use of large-scale parallelization, reduced order modelling, and the use of surrogate models. The large-scale parallelization approach presents two difficulties: one requires access to an extremely powerful High Performance Computing (HPC) facility, and one requires an excessive number of ‘analysis tokens’. Both of these requirements are extremely financially costly.

Reduced order modelling

Reduced order multiscale modelling was introduced in [81]. During reduced order modelling one assumes that the solution vector $\boldsymbol{d} \in \mathbb{R}^D$ can be sufficiently well approximated by a solution generated from a reduced dimension; that is,

$$\boldsymbol{d}^R(t) = \boldsymbol{\phi}_0 + \boldsymbol{\Phi}\boldsymbol{\zeta}(t)\,. \tag{6.39}$$

Here, $\boldsymbol{\phi}_0$ is a constant vector, $\boldsymbol{\zeta} \in \mathbb{R}^P$ $(P << D)$ are the degrees of freedom in the reduced dimension and $\boldsymbol{\Phi} \in \mathbb{R}^{D\times P}$ is a matrix of basis vectors $\boldsymbol{\phi}_i$; that is

$$\boldsymbol{\Phi} = \begin{bmatrix} \boldsymbol{\phi}_1 & \boldsymbol{\phi}_2 & \dots & \boldsymbol{\phi}_P \end{bmatrix}\,. \tag{6.40}$$

Given S ‘snapshots’ of the solution $\boldsymbol{d}_i$, the basis vectors can be found by minimizing

$$\sum_{i=1}^{S} \left|\left|\boldsymbol{d}_i - \boldsymbol{d}^R(t_i)\right|\right| \tag{6.41}$$

subject to the constraint

$$\boldsymbol{\phi}_i \cdot \boldsymbol{\phi}_j = \delta_{ij}\,. \tag{6.42}$$

This implies that the constant vector $\boldsymbol{\phi}_0$ is the mean of the solution snapshots

$$\boldsymbol{\phi}_0 = \bar{\boldsymbol{d}} = \frac{1}{S}\sum_{i=1}^{S}\boldsymbol{d}_i \tag{6.43}$$

and the basis vectors are given by solving the eigenvalue problem

$$\boldsymbol{Q}\boldsymbol{\phi}_i = \lambda_i\boldsymbol{\phi}_i\,, \tag{6.44}$$

where $\boldsymbol{Q}$ is the covariance matrix defined by

$$\boldsymbol{Q} = \boldsymbol{U}\boldsymbol{U}^T\,, \tag{6.45}$$

where

$$\boldsymbol{U} = \begin{bmatrix} \boldsymbol{d}_1 - \bar{\boldsymbol{d}} & \boldsymbol{d}_2 - \bar{\boldsymbol{d}} & \dots & \boldsymbol{d}_S - \bar{\boldsymbol{d}} \end{bmatrix}\,. \tag{6.46}$$

Once the basis vectors are determined, one can relate an increment in the reduced dimension solution to an increment in the solution using

$$\Delta\boldsymbol{d}^R = \boldsymbol{\Phi}\Delta\zeta\,. \tag{6.47}$$

When solving the nonlinear FE problem (see Chapter 5), one repetitively finds the solution to the linear system of equations

$$\boldsymbol{K}\Delta\boldsymbol{d} = -\boldsymbol{R}\,. \tag{6.48}$$

This requires the inversion $\boldsymbol{K} \in \mathbb{R}^{D\times D}$ which is computationally expensive for large D. The reduced order model circumvents this by substituting equation (6.47) into equation (6.48) and left multiplying by $\boldsymbol{\Phi}^T$ to obtain

$$\underbrace{\boldsymbol{\Phi}^T\boldsymbol{K}\boldsymbol{\Phi}}_{\boldsymbol{K}^R}\Delta\boldsymbol{\zeta} = -\boldsymbol{\Phi}^T\boldsymbol{R}\,. \tag{6.49}$$

Hence, $\Delta\boldsymbol{\zeta}$ can be found by inverting $\boldsymbol{K}^R \in \mathbb{R}^{P\times P}$ which is computationally cheap since $P << D$. The corresponding increment in the solution can then be found using equation (6.47).

In [81] this reduced model multiscale method was applied to the RVE level simulations. The method is attractive because many simulations are run on the RVE during concurrent multiscale modelling. This generates many solution snapshots that can be used to determine the reduced basis vectors. This approach has been further developed in subsequent works [82, 83, 84, 85]

The difficulty in applying this approach when using ABAQUS is that it requires fine control over the FE solution procedure which is difficult to attain in ABAQUS, if at all possible.

Non-concurrent multiscale modelling: surrogate models

Non-concurrent multiscale modelling consists of two steps: first, one applies several loads to the RVE and stores the resulting macroscopic stress-strain data in a database; second, one constructs a surrogate model for the RVE, that is simply a constitutive model at the macroscale, which is informed by the data. Then, when FE simulations are run at the macroscale the surrogate model is used instead of the RVE and so macroscale simulation times are similar to those where a standard constitutive model is used to relate the stress and the strain. The accuracy with which the surrogate model replicates the behaviour of the RVE is dependent on its mathematical form and the distribution of data available to inform the model. The construction of judicious surrogate models and approaches to obtaining optimal sampling of data-points is still an open problem at the time this is being written.

The first documentation of the concept of non-concurrent homogenization is in [86] and was repeated soon after in [87]. However, both of these contributions lack crucial mathematical details of how the surrogate model was constructed. Later, Temizer and Zohdi developed a non-concurrent homogenization approach for isotropic non-linear elastic RVEs in [88]. Here, they noted that the most general expression for the second Piola-Kirchhoff stress of an isotropic material is given by

$$\boldsymbol{S} = \alpha_0\boldsymbol{I} + \alpha_1\boldsymbol{E} + \alpha_2\boldsymbol{E}^2\,, \tag{6.50}$$

where α_i $i = 1, 2, 3$ are functions of the principal stretches. They then used FE shape functions to approximate α_i; that is,

$$\alpha_i = \sum_I \alpha_i^I N^I(\lambda_1, \lambda_2, \lambda_3). \tag{6.51}$$

Here, α_i^I is the value of α_i at node I and N^I is the shape function for node I. Note that the domain of this FE mesh describes a domain of principal stretches and not the usual domain in physical space. Then the value for each node α_i^I is determined by applying the principal stretches, which are the 'position' of that node, to the RVE. This approach was extended in [89] to include orthotropic materials. The approach was then developed further in [90, 91] by storing the averaged strain energy values instead of stress values to reduce the size of the database. This creates the necessity of using piecewise C^2 continuous shape functions so that the elasticity tensor, that is the second derivative of the strain energy, is non-zero. The difficulty with these approaches is that they suffer from the 'curse of dimensionality'. For isotropic three-dimensional problems, those investigated in [88], there are only three independent variables, the principal stretches. Hence, to create a grid-like database consisting of n variations in each independent variable requires n^3 microscale simulations. However, for a general three-dimensional anisotropic material there are 6 independent variables: these could be the 3 principal stretches and the angles their corresponding principal directions make with the chosen basis [89], or the 6 unique entries in the right Cauchy-Green matrix [90]. Hence, to create a grid-like database consisting of n variations in each independent variable requires n^6 microscale simulations. Even for a modest number of increments in each variable (say, 10) an excessive number of non-linear microscale simulations are required (10^6). Note that although the mathematics for a general three-dimensional approach was presented in [89, 90, 91] the computational examples provided in these contributions were conducted on two-dimensional problems, for which the number of simulations required to fill out the database is only n^3.

More recently, machine learning approaches have been used to create the surrogate model. In particular, neural networks [92, 93, 94, 95, 96, 97, 98, 99] and regression [100] have been used to construct surrogate models. A key advantage of these machine learning approaches is that there is no constraint on the deformations for which the RVE response is sampled; they do not need to define the nodes of a FE mesh, as the methods in the above paragraph do. This allows one to develop strategies to sample the RVE behaviour for an optimal set of deformations. However, a key disadvantage is that they still require a large amount of data, and they are prone to numerical instability [101]. This issue was addressed in very recent work [101]. There, the authors used a standard constitutive model with Gaussian process regression, which applies a correction to the constitutive model so that the resulting surrogate model fits the data well.

In this work, the machine learning approaches to non-concurrent homogenization are extended by using general polyconvex constitutive models which are fitted to the behaviour of the RVE in a regression sense. The constraint of polyconvexity limits the flexibility of the surrogate model. However, it ensures numerical stability of the macroscale simulation in contrast to other machine learning approaches. The approach is then extended to include visco-hyperelasticity of the RVE.

6.2.3 Non-concurrent multiscale modelling using general polyconvex strain energy functions

The surrogate model

In this approach, one assumes that the long time-scale hyperelastic behaviour of the RVE can be sufficiently described by the transversely isotropic polyconvex strain energy functions presented by Schröder and Neff [67] which are displayed in equation (4.92) and repeated here for convenience,

$$\begin{aligned}
\Psi^\infty &= \sum_{j=1}^{7} \psi_j \,, & \psi_1 &= \sum_{i=1}^{n} \kappa_{(1)i} I_1^i \,, \\
\psi_2 &= \sum_{i=1}^{n} \kappa_{(2)i} I_2^i \,, & \psi_3 &= \kappa_{(3)0} I_3^{-1} + \sum_{i=1}^{n} \kappa_{(3)i} \left[I_3 + I_3^{-1} - 2 \right]^i \,, \\
\psi_4 &= \sum_{i=1}^{n} \kappa_{(4)i} I_4^i \,, & \psi_5 &= \sum_{i=1}^{n} \kappa_{(5)i} \left[I_5 - I_4 I_1 + I_2 \right]^i \,, \\
\psi_6 &= \sum_{i=1}^{n} \kappa_{(6)i} I_6^i \,, & \psi_7 &= \sum_{i=1}^{n} \kappa_{(7)i} \left[I_7 - I_6 I_1 + I_2 \right]^i \,.
\end{aligned} \tag{6.52}$$

Here, $\kappa_{(i)j}, \kappa_{(3)0} \geq 0\,,\ i = 1, ..., 7\,,\ j = 1, ..., n$ are material parameters, $I_i\ i = 1, ..., 7$ are the invariants of the right Cauchy-Green tensor and n defines the polynomial order of the strain energy functions. For the model to be stress-free in the undeformed configuration, the constraints are enforced:

$$\begin{aligned}
\kappa_{(3)0} &= \sum_{i=1}^{n} i \left[3^{i-1} \left[\kappa_{(1)i} + 2\kappa_{(2)i} \right] + \left[\kappa_{(5)i} + \kappa_{(7)i} \right] \right] \,, \\
\kappa_{(4)1} &= \kappa_{(5)1} + \sum_{i=2}^{n} i \left[\kappa_{(5)i} - \kappa_{(4)i} \right] \,, \\
\kappa_{(6)1} &= \kappa_{(7)1} + \sum_{i=2}^{n} i \left[\kappa_{(7)i} - \kappa_{(6)i} \right] \,.
\end{aligned} \tag{6.53}$$

For more details on the model, see Section 4.1.4. Note that n can be increased to increase the flexibility of the model. The long time-scale second Piola-Kirchhoff stress is then given by

$$\boldsymbol{S}^{\infty} = 2\frac{\partial \Psi^{\infty}}{\partial \boldsymbol{C}} \,. \tag{6.54}$$

One also assumes that the overall second Piola-Kirchhoff stress response of the RVE can be sufficiently represented by a superposition of the viscous $\boldsymbol{S}^v$ and long time-scale stress $\boldsymbol{S}^{\infty}$. Hence, the surrogate model is given by

$$\boldsymbol{S}_S = \boldsymbol{S}^{\infty} + \boldsymbol{S}^v \,, \tag{6.55}$$

where the viscous stress is given by

$$\begin{aligned} \boldsymbol{S}^v &= \sum_{\alpha=1}^{N_m} \int_0^t \beta_\alpha \exp\left(-\frac{t-s}{\tau_\alpha}\right) \dot{\bar{\boldsymbol{S}}}^{\infty} \,\mathrm{d}s \\ \bar{\boldsymbol{S}}^{\infty} &= \boldsymbol{S}^{\infty} - \frac{1}{3}\left[\boldsymbol{S}^{\infty} : \boldsymbol{C}\right] \boldsymbol{C}^{-1} \,. \end{aligned} \tag{6.56}$$

Here, β_α and τ_α are material parameters. Hence, the surrogate model is completely described by equations (6.52)–(6.56). The Cauchy stress for the surrogate model can then be obtained by the usual push-forward operation; that is,

$$\boldsymbol{\sigma}_S = J^{-1} \boldsymbol{F} \boldsymbol{S}_S \boldsymbol{F}^T \tag{6.57}$$

This constitutive model is implemented in a discretized sense; that is, discretized in time cf. Section 4.3.2. Of course, the actual macroscale Cauchy stress defined by the RVE is given by

$$\boldsymbol{\sigma}_M = J^{-1} \left\langle \boldsymbol{P}_m \right\rangle_{\Omega_m} \boldsymbol{F}^T \,, \tag{6.58}$$

and the goal is for $\boldsymbol{\sigma}_S$ to closely replicate $\boldsymbol{\sigma}_M$. One assumes that $\boldsymbol{\sigma}_S$ can closely replicate $\boldsymbol{\sigma}_M$ by obtaining appropriate values for the material parameters $\boldsymbol{\kappa}$, $\boldsymbol{\beta}$, and $\boldsymbol{\tau}$. Here, $\boldsymbol{\kappa}$ denotes the set of material parameters defining the material's long time-scale behaviour, that is $\kappa_{(i)j}, \kappa_{(3)0}\,,\ i = 1, ..., 7\,,\ j = 1, ..., n$, and $\boldsymbol{\beta}$ and $\boldsymbol{\tau}$ denote the set of material parameters that define the viscous material behaviour, that is β_α and τ_α, $\alpha = 1, ..., N_m$.

Training the surrogate model using RVE data

To obtain the optimal values for the material parameters, one first constructs an objective function representing the difference between the surrogate model and constitutive behaviour provided by the RVE. This function requires data of the RVE behaviour as an input. Since the RVEs used in this work contain viscoelastic materials, the RVEs' behaviour is rate-dependent. Hence, the data is obtained by applying n_{pths} loading paths at different rates to the RVE, which consist of n_{pts} sequential macroscale deformation gradients. A suitable objective function is then given by

$$\mathcal{X} = \sum_{i}^{n_{pths}} \sum_{j}^{n_{pts}} \left|\left|\boldsymbol{\sigma}_S \left(\boldsymbol{F}_M^{ij}, \boldsymbol{\kappa}, \boldsymbol{\beta}, \boldsymbol{\tau}\right) - \boldsymbol{\sigma}_M^{ij}\right|\right|^2 , \tag{6.59}$$

where $\boldsymbol{F}_M^{ij}$ and $\boldsymbol{\sigma}_M^{ij}$ are the applied macroscopic deformation gradient and macroscopic Cauchy stress, respectively, for point j of loading path i. Of course, because the surrogate model is time dependent, $\boldsymbol{\sigma}_S$ is also dependent on history variables from the previous loading increment $j-1$. However, this has not been included explicitly in equation (6.59) for conciseness.

As for the choice of loading paths, inspiration is taken from typical physical tests that are applied to novel materials to elucidate their constitutive behaviour. These include uniaxial, shear and pressure loading [102] and so these three loading paths are used to elucidate the RVE's behaviour. Since the RVE may be anisotropic, uniaxial loading is applied in three directions and shear loading is applied in the six shear directions, that is, the six permutations obtained by choosing two of the three basis vectors $\boldsymbol{e}_1$, $\boldsymbol{e}_2$ and $\boldsymbol{e}_3$.

Recall that the analytical solutions for the stress responses under these loading paths are presented in Section 4.4 along with suitable objective functions to fit a constitutive model to the relevant data. These are repeated here briefly for convenience. For uniaxial loading in the first direction, the form of the stress response for the surrogate model and the RVE are

$$\boldsymbol{\sigma}_S = \text{Diag}\begin{bmatrix}\sigma_{S1} & 0 & 0\end{bmatrix} , \qquad \boldsymbol{\sigma}_M = \text{Diag}\begin{bmatrix}\sigma_{M1} & 0 & 0\end{bmatrix} , \tag{6.60}$$

respectively. Additionally, the deformation gradient is of the form

$$\boldsymbol{F}_M = \text{Diag}\begin{bmatrix}\lambda_1 & \lambda_2 & \lambda_3\end{bmatrix} . \tag{6.61}$$

The contribution to the objective function is then given by

$$\mathcal{X}_{uni} = \sum_{j}^{n_{pts}} \left[\sigma_{S1}\left(\lambda_1^j, \boldsymbol{\kappa}, \boldsymbol{\beta}, \boldsymbol{\tau}\right) - \sigma_{M1}^j\right]^2 . \tag{6.62}$$

When obtaining the data by applying the load path to the RVE and when fitting the surrogate model to the data one uses $\sigma_2 = \sigma_3 = 0$ to obtain the missing entries in the deformation gradient by solving the minimization problem

$$\begin{bmatrix}\lambda_2(\lambda_1)\\ \lambda_3(\lambda_1)\end{bmatrix} = \underset{\lambda_2,\lambda_3}{\arg\min} \left|\left|\begin{bmatrix}\sigma_2(\lambda_1,\lambda_2,\lambda_3)\\ \sigma_3(\lambda_1,\lambda_2,\lambda_3)\end{bmatrix}\right|\right| . \tag{6.63}$$

In the case of running tests on the RVE σ_2 and σ_3 represent the second and third diagonal entries of $\boldsymbol{\sigma}_M$ and in the case of the determining the response of the surrogate model σ_2 and

σ_3 represent the second and third diagonal entries of $\boldsymbol{\sigma}_S$. A similar procedure is applied for uniaxial loading in the second and third directions.

For shear loading in the kl direction, the deformation gradient is given by

$$\boldsymbol{F}_M = \boldsymbol{I} + \gamma \boldsymbol{e}_k \otimes \boldsymbol{e}_l \,, \tag{6.64}$$

where γ is a parameter that describes the magnitude of the loading. The contribution to the objective function is then given by

$$\mathcal{X}_{shear} = \sum_{j}^{n_{pts}} \left[\sigma_{S(kl)} \left(\boldsymbol{F}_M^j, \, \boldsymbol{\kappa}, \, \boldsymbol{\beta}, \, \boldsymbol{\tau} \right) - \sigma_{M(kl)}^j \right]^2 . \tag{6.65}$$

Here, $\sigma_{S(kl)}$ denotes entry kl in the stress produced by the surrogate model and $\sigma_{M(kl)}^j$ denotes the kl entry in the macroscale Cauchy stress at the j^{th} increment in the loading path.

For pressure loading the stress responses are of the form

$$\boldsymbol{\sigma}_S = p_S \boldsymbol{I} \,, \qquad \boldsymbol{\sigma}_M = p_M \boldsymbol{I} \,, \tag{6.66}$$

and the deformation gradient is of the form

$$\boldsymbol{F}_M = \text{Diag} \begin{bmatrix} \lambda_1 & \lambda_2 & \lambda_3 \end{bmatrix} . \tag{6.67}$$

The contribution to the objective function is then given by

$$\mathcal{X}_{pressure} = \sum_{j}^{n_{pts}} \left[p_S \left(\lambda_1^j, \, \boldsymbol{\kappa}, \, \boldsymbol{\beta}, \, \boldsymbol{\tau} \right) - p_M^j \right]^2 . \tag{6.68}$$

Here, $\sigma_1 = \sigma_2 = \sigma_3$ is used to obtain the stretches λ_2 and λ_3 by solving the minimization problem

$$\begin{bmatrix} \lambda_2 (\boldsymbol{c}, \lambda_1) \\ \lambda_3 (\boldsymbol{c}, \lambda_1) \end{bmatrix} = \underset{\lambda_2, \lambda_3}{\arg\min} \left\| \begin{bmatrix} \sigma_2 - \sigma_1 \\ \sigma_3 - \sigma_1 \end{bmatrix} \right\| . \tag{6.69}$$

It is convenient to fit the long time-scale behaviour of the surrogate model to the RVE independently to the viscous behaviour. To this end, the above loading paths are first applied to the RVE with the viscous behaviour of the RVE's materials 'turned off'. Since the viscous behaviour of the materials in the RVE is modelled using the generalised Maxwell model described in 4.3.2 this is done by setting $\beta_\alpha = 0$ for each material. Once the data is obtained, the long time-scale material parameters can be obtained by solving the minimization problem

$$\min_{\boldsymbol{\kappa}} \mathcal{X}_{uni} + \mathcal{X}_{shear} + \mathcal{X}_{pressure} \,. \tag{6.70}$$

This is done in python using the L-BFGS-B algorithm [103, 104] provided by the function `scipy.optimize.minimize()` in the `Scipy` library [105].

To elucidate the viscoelastic behaviour of the RVE, each of the above described loading paths are repeated at difference loading rates. The loading rates are informed by the relaxation times τ_α of the materials in the RVE. In particular, a set of uniaxial, shear and pressure loading paths are run for each relaxation time in the RVE. For example, if the RVE consists of n_{mats} materials each of which contains N_m relaxation times then $n_{rates} = n_{mats} \times N_m$ sets of uniaxial, shear and pressure loading paths are applied to the RVE at different loading rates. The loading rate is set to be $1/\tau_\alpha$. In the case of uniaxial and pressure loading, the loading rate is applied to the principal stretch in the direction of concern, that is $\dot{\lambda}_1 = 1/\tau_\alpha$ if uniaxial loading is being applied in the first direction, and, in the case of shear loading, the loading rate is applied to the loading parameter γ, that is $\dot{\gamma} = 1/\tau_\alpha$. The viscous material parameters are then obtained by solving the minimization problem

$$\min_{\boldsymbol{\beta}, \boldsymbol{\tau}} \sum_{i}^{n_{rates}} \mathcal{X}^i_{uni} + \mathcal{X}^i_{shear} + \mathcal{X}^i_{pressure} \, . \tag{6.71}$$

Here, $\mathcal{X}^i_\bullet$ denotes the contribution to the objective function for the i^{th} applied loading rate on the $\bullet$ loading path. It was found that the differential evolution algorithm [106] given by the function `scipy.optimize.differential_evolution()` from the `Scipy` library [105] works well for solving this minimization problem. In equation (6.71) the long time-scale material parameters $\boldsymbol{\kappa}$ are kept constant as determined by solving the minimization problem in equation (6.70).

Chapter 7

Quasistatic suture scale simulations

This chapter presents several quasistatic simulations investigating the mechanical behaviour of the suture region in a turtle shell. The model of the suture region is validated by comparing the results from a simulation with those from a physical bending test on a portion of the shell. The model is used to investigate aspects of the suture region's mechanical behaviour during a predator attack, which is modelled quasistatically here as a first approximation; Chapter 8 presents similar simulations with more realistic dynamic loading. Finally, the influence of suture geometry on the region's mechanical behaviour is investigated by means of a parametric study.

The chapter is arranged as follows. Section 7.1 presents the various material models and parameters that are used in the simulations which follow. In Section 7.2 comparisons are made between a physical three-point bending test and an equivalent simulation to validate the model. Section 7.3 presents simulations of a predator attack. Section 7.4 investigates the effect of the suture geometry on the suture region's mechanical behaviour. Finally, Section 7.5 presents some concluding remarks on the results presented in the chapter.

7.1 Material models and parameters

This section presents the relevant material models used in the simulations, along with the appropriate values for their parameters. There are three materials of interest, namely bone, keratin, and soft collagenous tissue.

7.1.1 Soft collagenous tissue

Material model

The soft collagenous tissue which is contained in both the suture and skin is modelled using an incompressible Gasser-Ogden-Holzapfel (GOH) model, which has been detailed in Section 4.1.4. The strain energy function is given again here for convenience:

$$\Psi = \bar{\Psi} = G\left[\bar{I}_1 - 3\right] + \frac{k_1}{2k_2}\left[\exp\left(k_2 \bar{E}^2\right) - 1\right] . \tag{7.1}$$

Recall that $\bar{E}$ is an invariant defined by

$$\bar{E} := \left\langle\left\langle \kappa\left[\bar{I}_1 - 3\right] + [1 - 3\kappa]\left[\bar{I}_4 - 1\right]\right\rangle\right\rangle , \qquad \langle\langle\bullet\rangle\rangle := \begin{cases} \bullet & \bullet \geq 0, \\ 0 & \bullet \leq 0\,, \end{cases} \tag{7.2}$$

and $G, k_1, k_2 \geq 0\,, \kappa \in [0,\, 1/3]$ are material parameters. Additionally, the isochoric stress, displayed again here for convenience, is given by

$$\bar{\boldsymbol{\sigma}} = 2J^{-1}\left[G\bar{\boldsymbol{B}} + k_1 \bar{E} \exp\left(k_2 \bar{E}^2\right)\left[\kappa \bar{\boldsymbol{B}} + [1 - 3\kappa]\, \bar{\boldsymbol{a}} \otimes \bar{\boldsymbol{a}}\right]\right] . \tag{7.3}$$

Determination of material parameters

There does not appear to exist test data in the literature for turtle shell sutures that would allow for determination of the material parameters in the constitutive relation. This deficiency is circumvented by scaling existing test data from rabbit skin [107] (presented in 7.1 (b)) – another soft collagenous tissue – such that the Young's modulus is 0.2 GPa, the Young's modulus of sutures in a turtle shell determined from nano-indentation tests [30]. The data is scaled by determining a scale factor,

$$\kappa_{\text{scale}} = \frac{E_{\text{turtle data}}}{E_{\text{curve data}}}, \tag{7.4}$$

where $E_{\text{turtle data}}$ is the Young's modulus reported in [30] and $E_{\text{curve data}}$ is the slope of the stress-strain data from [107] as $\lambda \rightarrow 1$. Each stress value in the data from [107] is multiplied by κ_{scale} to obtain the scaled data. This scaling approach is used throughout this thesis.

The test data in [107] are derived from two tensile tests: one in which the fibre direction is parallel to the direction of loading, and the other for which it is perpendicular. Hence, the stress response can be determined using the procedure outlined in Section 4.4.1. This results in an analytical solution for the nominal stress in the first direction N (see Section 3.3.1) of

$$N = \begin{cases} 2G\left[\lambda_1 - \lambda_1^{-2}\right] + 2k_1 \bar{E} \exp\left(k_2 \bar{E}^2\right)\left[\kappa\left[\lambda_1 - \lambda_1^{-2}\right] + [1 - 3\kappa]\, \lambda_1\right] & \beta = 0°, \\ 2[G + \kappa k_1 \bar{E} \exp\left(k_2 \bar{E}^2\right)]\left[\lambda_1 - \lambda_1^{-3}\lambda_2^{-2}\right] & \beta = 90°, \end{cases} \tag{7.5}$$

where $\beta = 0^\circ$ corresponds to parallel loading, $\beta = 90^\circ$ corresponds to perpendicular loading and the stretch λ_2 is given by

$$\lambda_2 = \arg\min_{\lambda_2} R(\lambda_2) = \Bigg[\left[G + \kappa k_1 \bar{E} \exp\left(k_2 \bar{E}^2\right)\right] \left[\lambda_2^2 - [\lambda_1 \lambda_2]^{-2}\right] \\ + k_1 \bar{E} \exp\left(k_2 \bar{E}^2\right) [1 - 3\kappa]\, \lambda_2^2 \Bigg]^2 . \tag{7.6}$$

The optimal values for the material parameters are found by using a non-linear least squares method to fit equation (7.5) to the scaled data. The resulting material parameters are displayed in Table 7.1. Additionally, the resulting stress-stretch curves determined by the analytical solution and an equivalent simulation in ABAQUS are displayed in Figure 7.1 along with the scaled data. It is evident from Figure 7.1 that the material model and parameters give a satisfactory fit to the scaled data. Furthermore, since the solution given by ABAQUS matches the analytical solution, it is evident that the implementation of the material model in ABAQUS behaves as expected.

Table 7.1: Soft collagenous tissue material parameters

G (MPa)	κ	k_1 (MPa)	k_2
53.17	0.2547	212.1	47.47

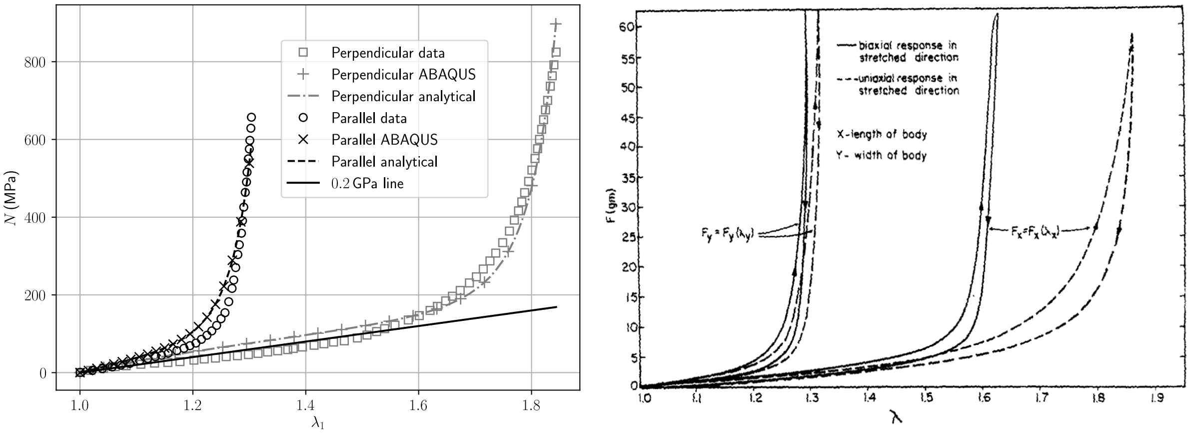

(a) (b)

Figure 7.1: Plot of, (a) scaled and (b) original, soft collagenous tissue tensile test data. The data from [107] is scaled using data from [30]. Additionally, the load curves for the fitted Gasser-Ogden-Holzapfel model given by both the analytical solution (equation (7.5)) and the solution given by an equivalent simulation in ABAQUS are displayed. The model gives a satisfactory fit to the experimental data, and the ABAQUS implementation of the model behaves as expected.

Fibre direction

Collagenous fibres in sutures tend to align themselves so that they are loaded in tension [51, 9]. The directions $\boldsymbol{n}_1$ and $\boldsymbol{n}_3$ of the maximum and minimum principal strains, respectively, are determined prior to each simulation using the procedure outlined in Appendix C.1.4. The fibre direction is then defined using

$$\boldsymbol{a}_0(\boldsymbol{X}) = \boldsymbol{n}_1(\boldsymbol{X})\cos\alpha + \boldsymbol{n}_3(\boldsymbol{X})\sin\alpha\,, \tag{7.7}$$

where α is the angle between the fibre direction and the first eigenvector in the plane, which contains both the first and third eigenvectors. Unless otherwise stated, assume that $\alpha = 0°$ so that the fibres are aligned with the direction of the maximum principal strain. Representative maximum principal strain and fibre direction vector fields for $\alpha = 0°$ are shown in Figure 7.2. It is clear that the directions of the fields match.

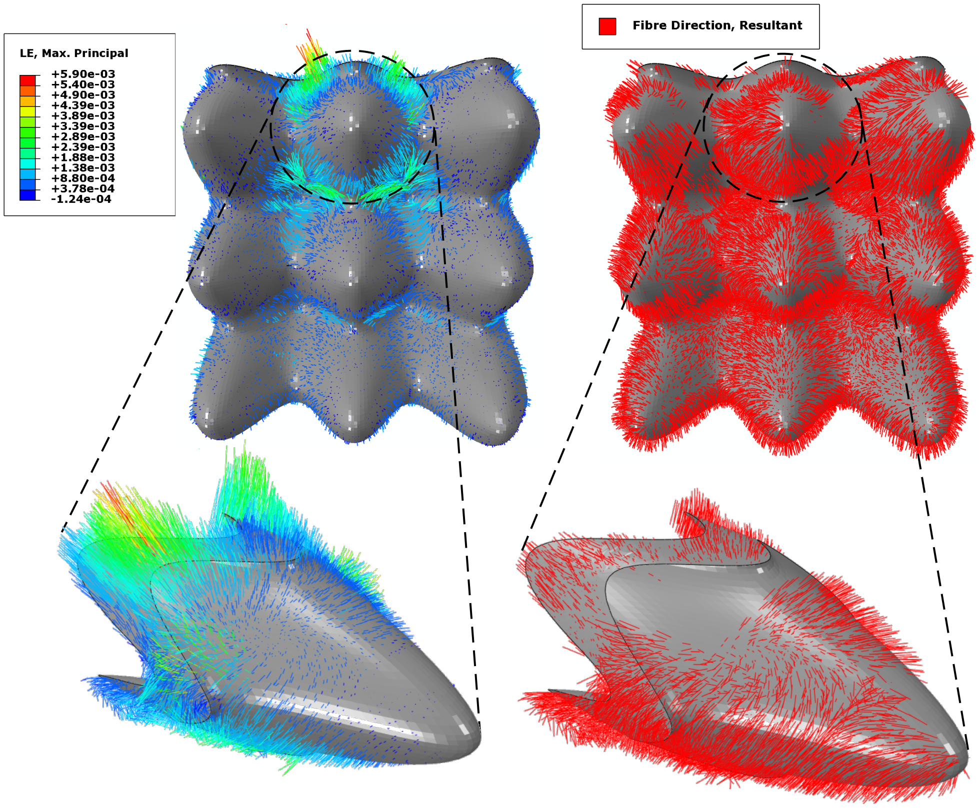

(a) (b)

Figure 7.2: Turtle shell suture: comparison of maximum principal strain direction of a setup simulation shown in (a) with the fibre directions of the subsequent simulation with $\alpha = 0°$ shown in (b). It is apparent that the directions of the vector fields match.

7.1.2 Bone

Both the cortical and cancellous bone are modelled as linear isotropic elastic materials. Hence, the stress for these materials is given by

$$\boldsymbol{\sigma} = \frac{E\nu}{[1+\nu][1-2\nu]}\mathrm{tr}(\boldsymbol{\varepsilon})\boldsymbol{I} + \frac{E}{1+\nu}\boldsymbol{\varepsilon}. \tag{7.8}$$

Here, E is Young's modulus and ν is Poisson's ratio. The cortical bone is assigned a Young's modulus of 12 GPa being the average of measurements found in numerous sites of cortical bone in the turtle shell via nano-indentation tests [30]. Additionally, a Poisson's ratio of 0.25 is used, also based on tests [32].

The effective Young's modulus of the cancellous bone is determined by averaging the results of compression tests found in the literature, yielding a value of 1 GPa [33, 35]. Again, a Poisson's ratio of 0.25 is used.

7.1.3 Keratin

The keratinous tissue is a transversely isotropic material, with its preferred direction transverse to the surface of the shell [31]. Additionally, it is feasible to model this material as linearly elastic for the range of strains considered here. The literature does not appear to contain sufficient data for the determination of the five independent material parameters for a linear transversely isotropic material. Instead, the literature only appears to contain three material parameters for turtle shell keratin: the Young's modulus in the longitudinal (preferred) direction $E_l = 1.3\,\mathrm{GPa}$; the Young's modulus in the transverse direction $E_t = 0.7\,\mathrm{GPa}$ and Poison's ratio $\nu = 0.4$ [30]. Hence, the Poisson's ratio and shear modulus are assumed to be equal in all directions as a simplification. The material model is then fully defined by the three material parameters listed above.

For verification of material stability see Appendix C.1.3.

7.2 Validation simulation: Bending test

The model is validated by comparing the results of a physical three-point bend test found in the literature [36] with an equivalent simulation. In [36] the specimen was created by cutting transversely across two ribs so that it contained a suture in the middle. It was found that the tests resulted in fractures across the extent of the bony protrusions. Hence, it is reasonable to assume that the largest stresses occurred in the protrusions and that the maximum principal stresses pointed normal to the fracture surfaces. Additionally, [36] presents an 'effective' stress-strain curve determined from force-displacement values and beam theory equations from [108]. This curve is converted back to a force-displacement curve here, as this representation is more useful for comparison with the following computational results.

Based on these results, success of the validation simulation is assessed on the following three metrics:

1. The largest stresses should occur in the protrusions;
2. The direction of the largest principal stresses in the protrusions should point in the direction normal to the fracture surfaces in [36];
3. The force-displacement curve of the simulation should resemble the converted equivalent stress-strain curve reported in [36].

7.2.1 Simulation setup

An equivalent geometry, displayed in Figure 7.3, is created to mimic the test specimen in [36]. The procedure for generating the model geometry is outlined in Appendix C.1.1. The dimensions for the geometry, which are given in Table 7.2, are taken from micro-CT scans in [36].

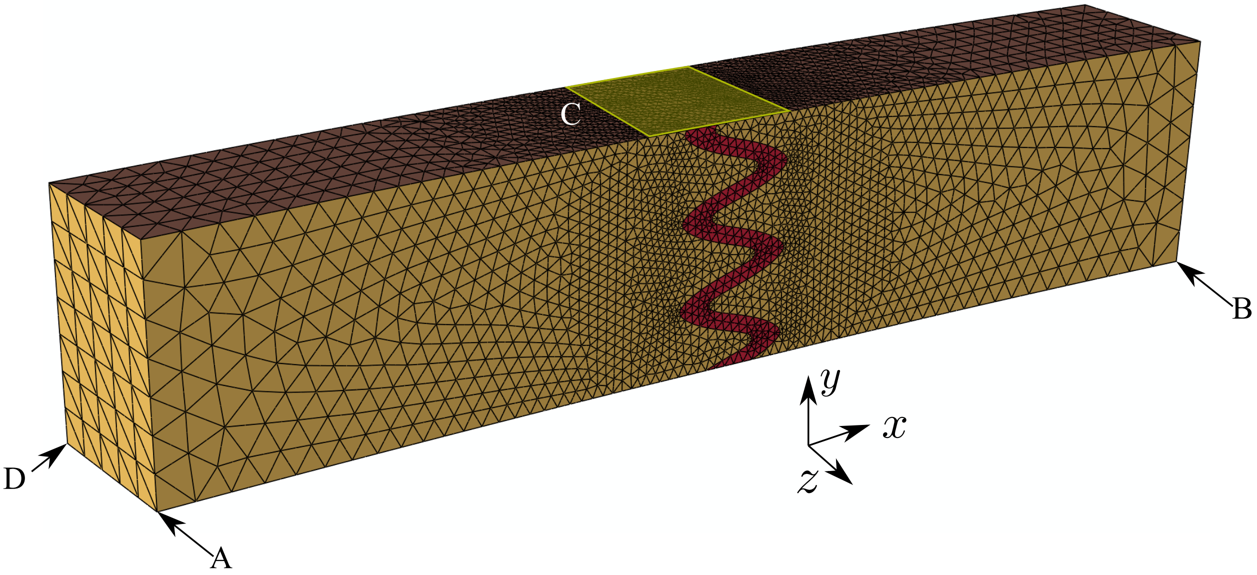

Figure 7.3: Validation model. Edge A is fixed in the x- and y-directions, edge B is fixed in the y-direction, vertex D is fixed in all directions and region C has a Dirichlet boundary condition of $u_2 = -1$mm. All other regions are traction free.

Table 7.2: Values of geometric parameters for validation simulation geometry. See Figure C.1 for interpretation of symbols

l_r (mm)	t_r (mm)	d_r (mm)	w (mm)	h (mm)	t_s (mm)	t_c (mm)	t_k (mm)
14.0	2.80	2.00	1.00	1.00	0.20	0.03	0.03

Since the specimen contains mostly cancellous bone, the bone is assigned a Young's modulus of 2 GPa as a weighted average of the cancellous and cortical bone mechanical parameters. The suture and keratin mechanical parameters are as stated in Sections 7.1.1 and 7.1.3, respectively. The boundary conditions are prescribed to mimic the loading described in [36], as displayed in Figure 7.3.

7.2.2 Numerical bending test: Results

The largest von Misses stress[1] occurs mid-way through the protrusions, mimicking the mechanical tests in [36] (Figure 7.4).

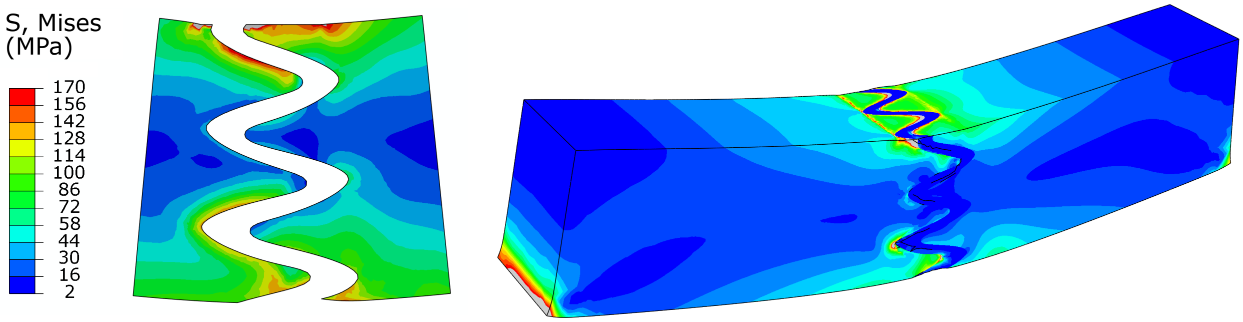

(a)

(b)

Figure 7.4: Von Mises stress contour plots from validation bend test. (a) Bony protrusions. The maximum stress occurs midway through the protrusions, which is consistent with the behaviour seen in physical tests [36]. (b) Entire model. The softness of the collagenous tissue results in low stresses within the suture.

Additionally, the maximum principal stresses in the protrusions are parallel to the protrusions' axis, that is, normal to the fracture surfaces in [36], in the lower portion of the model (Figure 7.5).

Comparison with the force-displacement curve corresponding to the mechanical test gives a reasonable match (Figure 7.6). However, the two curves deviate at a displacement of 0.1 mm as the experimental data shows a plateau in force up to approximately 0.4 mm. This plateau is characteristic of the plastic collapse of the trabecular bone (at 0.1 mm) and subsequent densification (at 0.4 mm) [37].

---

[1] The von Mises stress is defined as $\sqrt{\sigma_{ij}\sigma_{ij}}$.

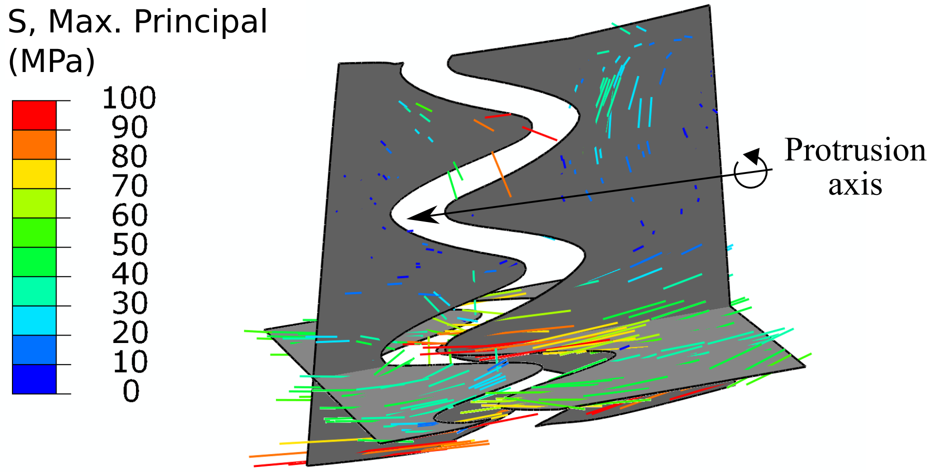

Figure 7.5: Vector plot of maximum principal stresses within the protrusions. The principal stresses in the lower portion of the model are parallel to the protrusion axis, that is, normal to fracture planes in the [36].

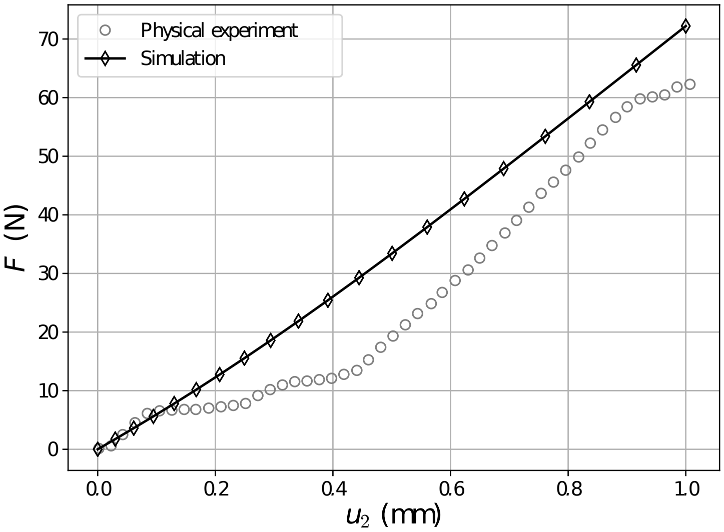

Figure 7.6: Experimental [36] and computational force-displacement plots for the bending test. The results give a reasonable match apart from the plateau at 0.1 mm and subsequent stiffening at 0.4 mm of the experimental data. This is due to the buckling and subsequent densification of the cancellous bone [37] which is not considered in the computational model.

7.2.3 Discussion

The model replicates many features of the three-point bending tests reported in [36]. The only incongruence is that the maximum principal stresses in the upper protrusions do not point in the direction of the protrusion axis. The deviation of the force-displacement curves in Figure 7.6 is likely due to plastic collapse of the cancellous bone (at 0.1 mm) and subsequent densification (at 0.4 mm), which is typical in three-point bending of turtle shell specimens [37, 34]. In the following section, however, the modelled region does not contain cancellous bone.

7.3 Simulation of a predator attack

The following section presents simulations replicating the mechanical behaviour of the suture region of the shell during a predator attack. To determine how sutures affect the mechanical behaviour of the shell, a model with a suture is compared to one without. Additionally, the effect of the fibre direction within the suture is investigated.

7.3.1 Simulation setup

The geometry is generated using the procedure outlined in Appendix C.1.1 and the values for the geometric parameters are again taken from micro-CT scans in [36]. However, the overall length, width, and depth of the geometry are adjusted so that the model is focused on the suture region. The geometry is presented in Figure 7.7 and the geometric parameters are given in Table 7.3.

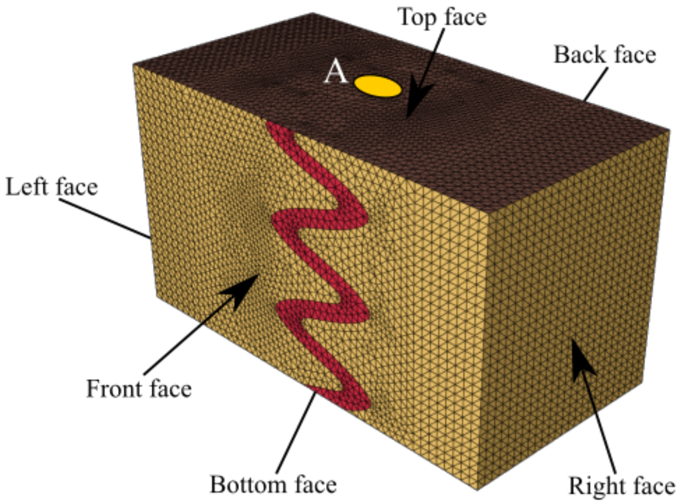

Figure 7.7: Model geometry used for the simulation of a predator attack. Region A is assigned a Dirichlet boundary condition of $u_2 = -1\,\text{mm}$. The front, back, left and right faces are assigned spring boundary conditions. All other regions are traction free.

Since the bone consists primarily of cortical bone, the mechanical parameters for cortical bone are used. Note that no region of cancellous bone is modelled in this section. The mechanical parameters for the soft tissue and keratinous tissue are as stated in Sections 7.1.1 and 7.1.3, respectively.

Table 7.3: Values of geometric parameters for predator attack simulation geometry. See Figure C.1 for interpretation of symbols

l_r (mm)	t_r (mm)	d_r (mm)	w (mm)	h (mm)	t_s (mm)	t_c (mm)	t_k (mm)
5.00	2.80	2.50	1.00	1.00	0.20	0.03	0.03

To determine the effect of the fibre direction, six simulations are run for fibre directions α ranging from $0° - 90°$ (see equation (7.7)). Comparison between the suture-containing and suture-excluding models is carried out for $\alpha = 0°$.

Boundary conditions

The boundary conditions replicate the loading that would be experienced during a predator attack *in vivo*. However, loading is modelled quasistatically as a simplification. A Dirichlet boundary condition of $u_2 = -1\,\text{mm}$ is applied in a circular region with radius of approximately 0.08 mm, illustrated as region A in Figure 7.7, to represent the tooth or claw of a predator. The position of the region is chosen to be above the suture, as it is expected to be the position that is most likely to cause injury to the turtle. The remainder of the top face and the entire bottom face are traction free.

The front, back, left and right faces in Figure 7.7 have spring boundary conditions applied to each node to account for the behaviour of the remainder of the shell, a proven method for applying boundary conditions that are representative of in vivo conditions [109]. However, the application of the spring boundary conditions is novel in this case, as the stiffness of each spring decreases with an increase in mesh density. These are defined as functions of the Young's modulus of the external material, see C.1.5 for details. The Young's modulus of the external material is set to 1 GPa for the left and right faces to represent cancellous bone, and 12 GPa for the front and back faces to represent cortical bone.

7.3.2 Results

Effect of the presence of sutures

Comparison of the suture-containing and suture-excluding models shows that sutures increase the strain energy for a given displacement, as is evident from Figure 7.8.

Furthermore, the strain energy density distributions shows that sutures cause a larger dispersion of strain energy throughout the bone portion of the geometry, as shown by Figure 7.9. However, the strain energy within the suture remains low.

Moreover, the presence of a suture decreases the maximum principal strain in the bone,

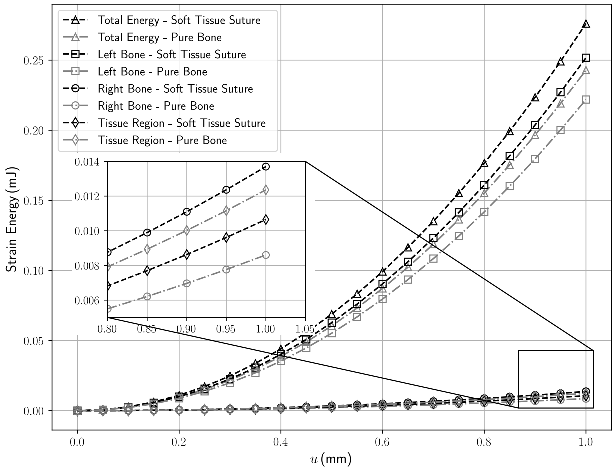

Figure 7.8: Strain energy in different regions of the model. The suture increases the amount of strain energy in the shell for a given displacement. The increase in strain energy is experienced primarily in the left bone, not in the suture region. In fact, the suture region contains less strain energy in the suture-containing model than the suture-excluding model.

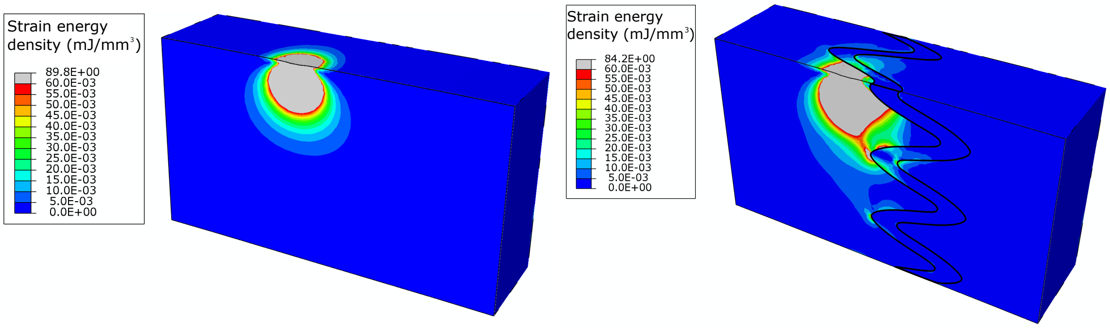

(a)

(b)

Figure 7.9: Strain energy density contours for (a) the suture-excluding model and (b) the suture-containing model at a midway cross-section. The suture-containing model exhibits a lager dispersion of strain energy density in the left and right bones than the suture-excluding model. The dispersion of strain energy increases the total strain energy whilst decreasing the maximum strain energy density from 89.8 J/m^3 in the suture-excluding model to 84.2 J/m^3 in the suture-containing model.

which is evident from Figure 7.10. Finally, the presence of a suture creates a small difference in the deformation of the top surface of the shell, shown by Figure 7.11.

Effect of fibre direction in sutures

The fibre direction has little effect on the strain energy, see Figure 7.12. However, the fibres undergo greater compression when aligned with the direction of minimum principal stretch, than their extension when aligned with the direction of maximum principal stretch (Figure

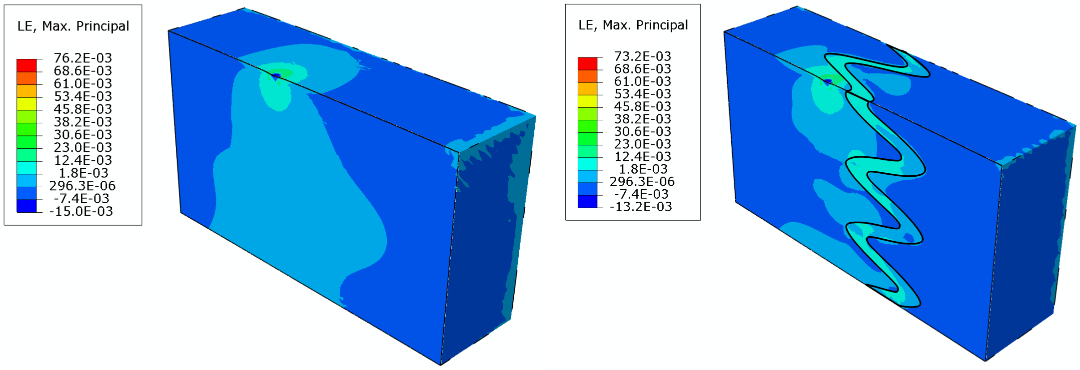

(a) (b)

Figure 7.10: Maximum principal logarithmic strain contours for (a) the suture-excluding model and (b) the suture-containing model at a midway cross-section. The suture 'absorbs' the strain of the bone - effectively cushioning it. Furthermore, the presence of the suture slightly decreases the maximum magnitude of the maximum principal strain from 76.2×10^{-3} to 73.2×10^{-3}.

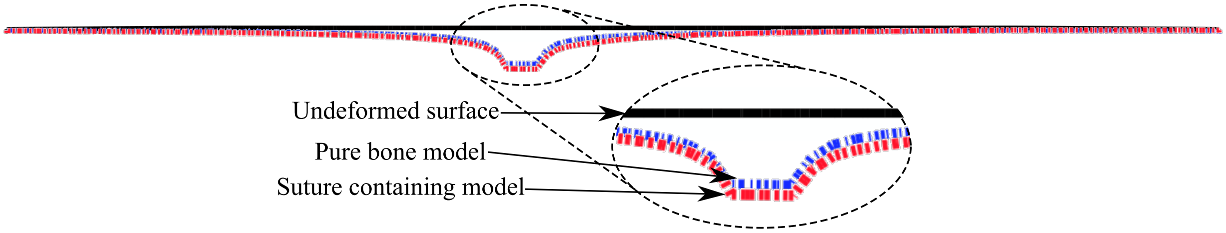

Figure 7.11: Comparison between the deformation of the top of the suture contain and suture-excluding model at a midway cross-section with a scale factor of 15. The suture-containing model deforms slightly more than the suture-excluding model.

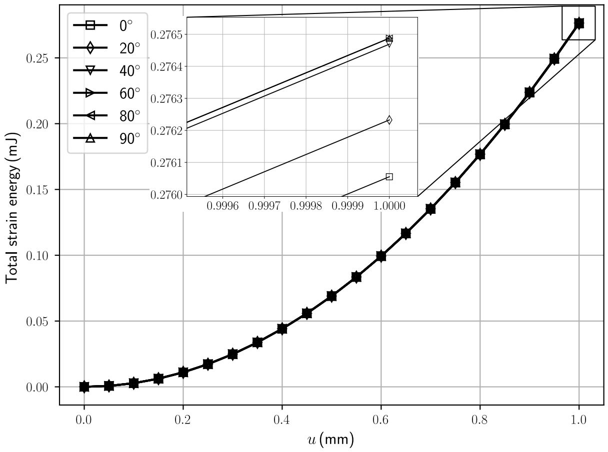

Figure 7.12: Total strain energy for different fibre directions α, see equation (7.7). The fibre direction has little effect on the strain energy. Interestingly, aligning the fibres in the direction of the maximum principal strain decreases the strain energy.

7.13).

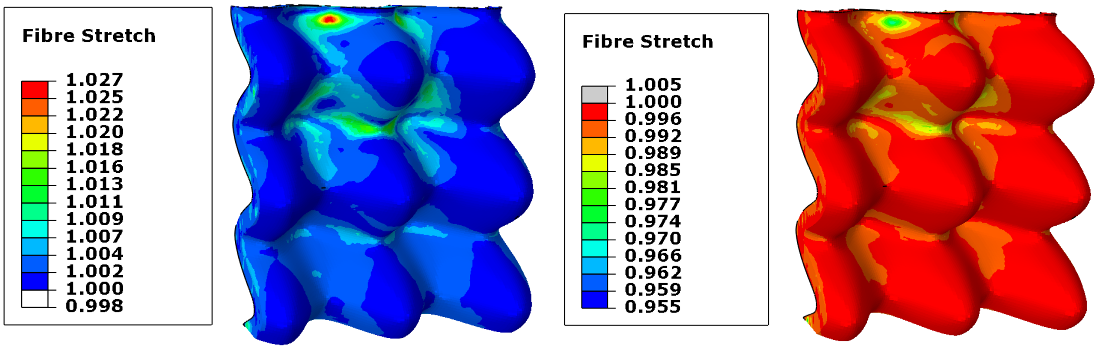

(a) (b)

Figure 7.13: Fibre stretch contour plots for fibres aligned in (a) the direction of maximum principal stretch ($\alpha = 0°$) and (b) the direction of minimum principal stretch ($\alpha = 90°$), see equation (7.7).

7.3.3 Discussion

Effect of sutures

The presence of sutures increases the amount of strain energy within the shell for a given displacement (Figure 7.8). Hence, a predator would have to exert more energy to achieve an equivalent amount of displacement of a shell that contains a suture in comparison to one that does not. By dispersing the strain energy throughout the protrusions, the suture increases the total strain energy and decreases the maximum strain energy density by 5 % from 89.8 J/m^3 to 84.2 J/m^3, as shown in Figure 7.9. This is particularly significant in the context of a brittle material, such as bone, which typically requires only a small amount of strain energy to cause fracture [110]. Furthermore, sutures have the effect of ‘absorbing’ the maximum principal strain (Figure 7.10). This decreases both the strain distribution in the bone and the maximum value of maximum principal strain. This is, again, pertinent in the context of bone fracture, as the most accurate fracture criterion for bone is based on the maximum principal strain which it experiences [111, 112].

The presence of a suture slightly increases the degree to which the shell hinges about a predator tooth when being attacked (Figure 7.11). Of course, it is preferable for the shell to deform as little as possible to protect the turtle’s internal organs. However, the difference is negligible as a scale factor of 15 was used for the deformation.

Effect of fibre direction in sutures

The fibre direction has a negligible effect on the stored energy of the shell (Figure 7.12). The difference in total strain energy between the $\alpha = 0°$ and $\alpha = 90°$ simulations was approximately 0.18 % and, interestingly, the amount of energy decreases as the fibre direction becomes more aligned with the maximum principal strain. The fibres compress more when they are aligned with the minimum principal strain (about 4.5 %) than they stretch when they are aligned with the maximum principal strain (about 2.7 %), indicating that the suture becomes stiffer when the fibres are aligned in the direction of maximum principal strain (Figure 7.13).

7.4 Effect of suture geometry

The following section presents an investigation into the influence of the suture geometry on the mechanical behaviour of the suture region.

7.4.1 Simulation setup

To determine the effect of the suture geometry, several geometric models are generated, a selection of which is shown in Figure 7.14. The models have varying values for protrusion height h, suture thickness t_s and protrusion pointiness a. In particular, seven values for h linearly spaced from 0–1.5 mm are used, five values for t_s linearly spaced from 0.15–0.3 mm are used and three values for a linearly spaced from 1–3 are used, yielding a total of 105 geometric models.

The boundary conditions applied to each model replicate the loading that the shell would experience during a predator attack, as outlined in Section 7.3.1.

7.4.2 Results

Three metrics are used to evaluate the performance of the shell as a protective structure: the stiffness of the shell, the strain energy and the maximum strain energy density at a point in the shell.

The stiffness of the shell is quantified by taking the absolute value of the difference between the maximum and the average vertical displacement. If the shell is ideally rigid, any displacement will be due to rigid body motion resulting from the spring boundary conditions and so the difference between the maximum vertical displacement and the average vertical displacement will be zero. However, as the stiffness decreases, the shell will hinge more

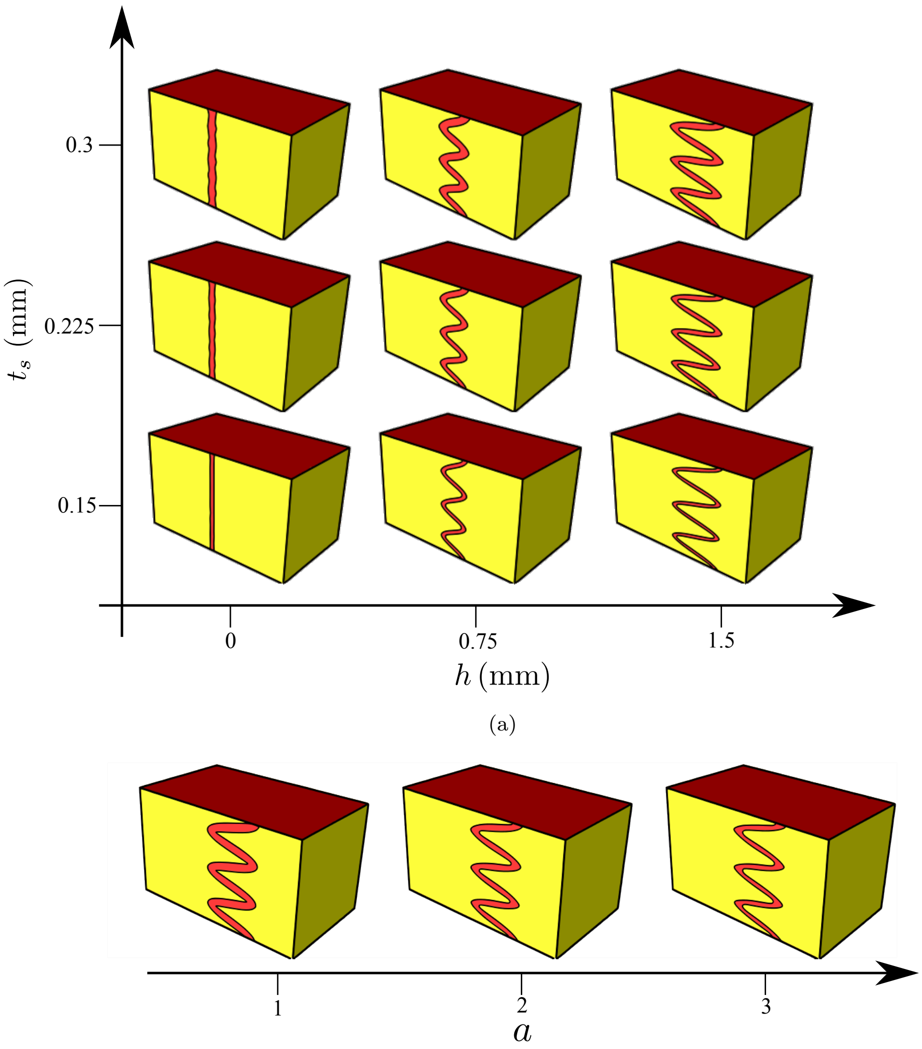

(a)

(b)

Figure 7.14: A selection of geometric models used in a parametric study. Recalling that h represents the height of the bony protrusions, t_s represents the thickness of the suture and parameter a controls the pointiness of the protrusions, the parametric study is conducted on 105 geometric models generated on a grid with the axes h, t_s and a. The grid contains seven values for h linearly spaced from 0–1.5 mm, five values for t_s linearly spaced from 0.15–0.3 mm and 3 values for a linearly spaced from 1–3. (a) Selection of models in a slice of the grid for $a = 2$. (b) Models on a line through the grid for h =1.25 mm and t_s =0.225 mm.

about the point where the loading is applied and so the difference between the maximum and average vertical displacement will increase. This value for each model is displayed in Figure 7.15.

The total strain energy indicates the amount of energy a predator would have to exert during an attack. This value for each model is shown in Figure 7.16.

The maximum strain energy density in a model indicates the likelihood of fracture occurring. This value is shown in Figure 7.17. Furthermore, the position where the maximum

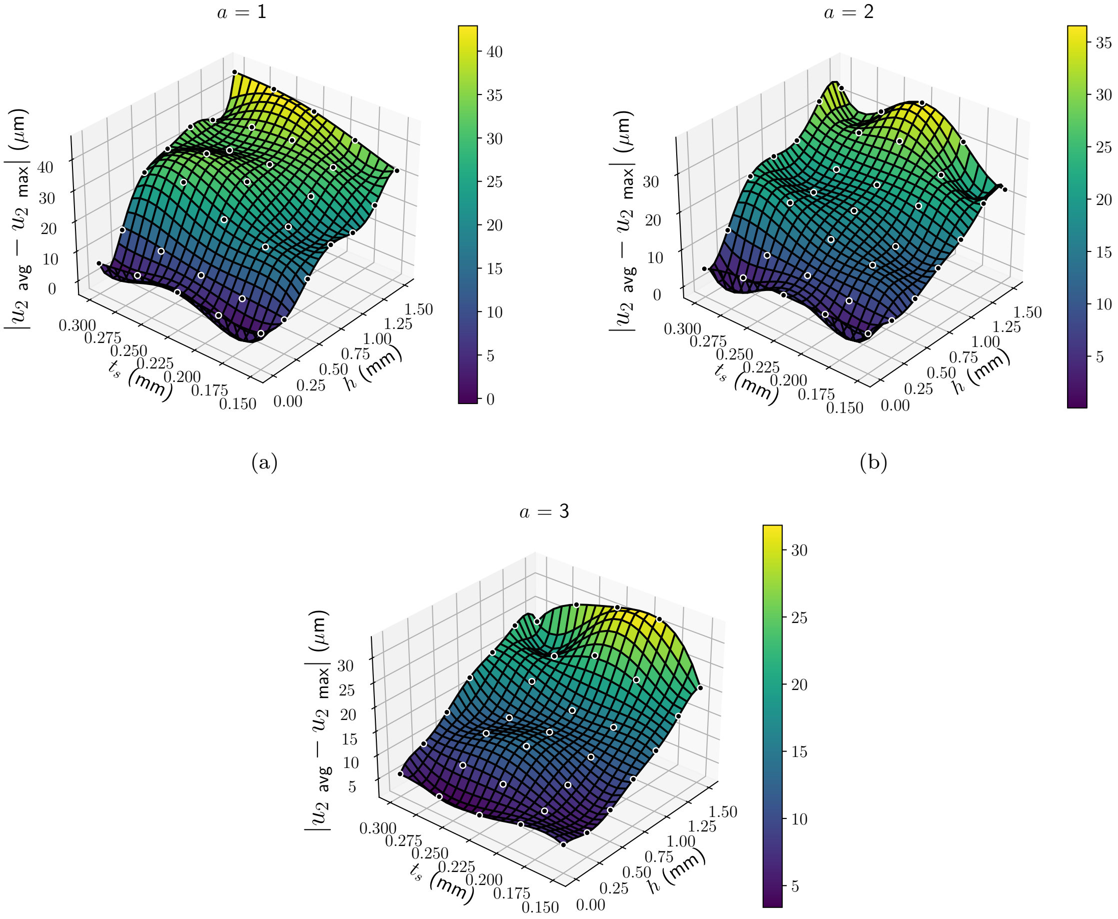

(a)

(b)

(c)

Figure 7.15: Polynomial surfaces fitted through data points for the absolute value of the difference between the average and the maximum vertical displacement in different geometric models under the prescribed loading with (a) $a = 1$, (b) $a = 2$ and (c) $a = 3$.

strain energy density occurs is where fracture is most likely to occur. Hence, a selection of strain energy density contour plots are shown in Figure 7.18 to determine which regions are at a high risk of fracture.

7.4.3 Discussion

The compliance of the region increases dramatically as a function of h while $h < 0.5\,\mathrm{mm}$ (Figure 7.15). This is likely because increasing h increases the volume of soft tissue, making the region more compliant. However, after $h = 0.5\,\mathrm{mm}$, the increase in compliance due to increasing h is greatly reduced. This is attributed to the interlocking of the bony protrusions. This feature is most pronounced when the protrusions are pointy ($a = 1$). Additionally, the

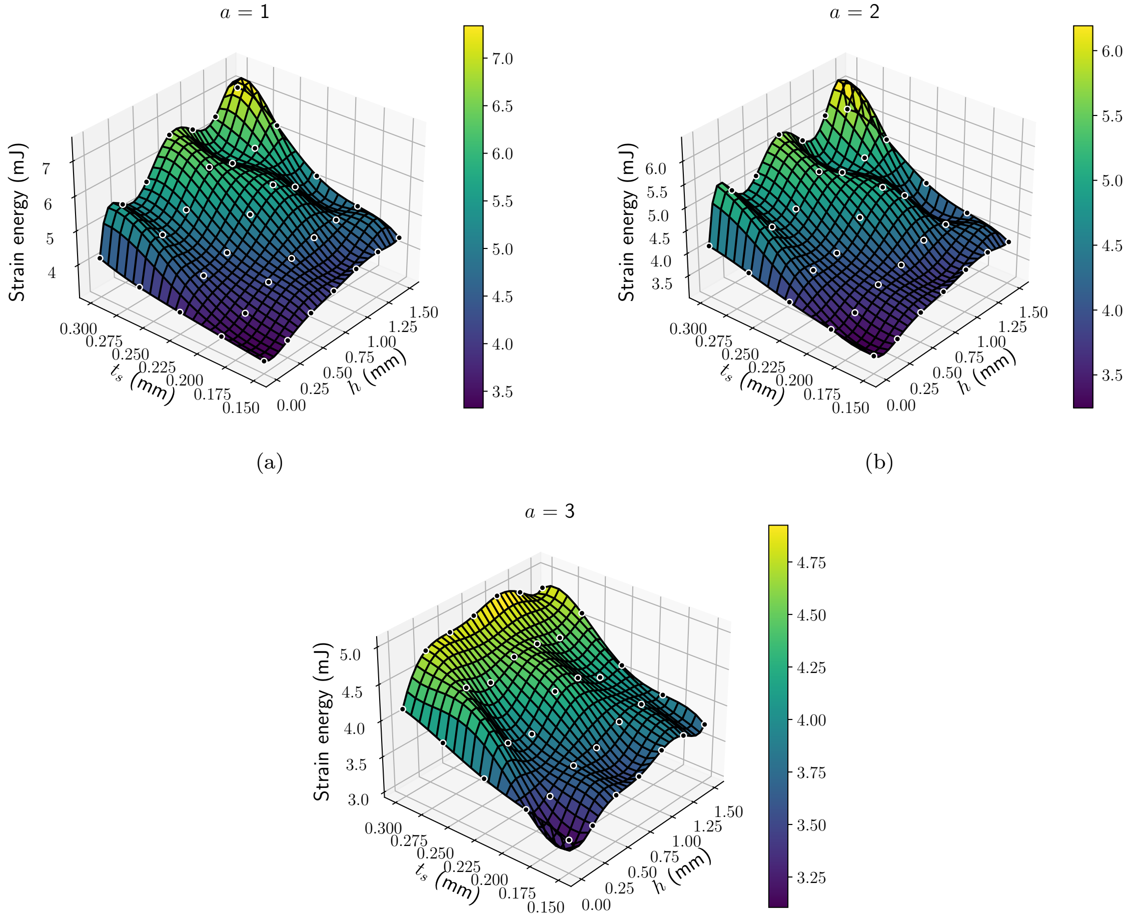

(a) (b)

(c)

Figure 7.16: Polynomial surfaces fitted through data points for total strain energy contained in different geometric models under the prescribed loading with (a) $a = 1$, (b) $a = 2$ and (c) $a = 3$.

interlocking effect occurs almost instantaneously when the suture is thinner as such shells show a more gradual and consistent increase in compliance with respect to h than the thicker suture models which have a sharp increase followed by a plateau. As it is beneficial for the shell to be relatively stiff, one might expect that it is most beneficial for h and t_s to be as small as possible; that is, for there to not be a suture.

However, while h and t_s increase the compliance of the shell, they also increase the shell's strain energy absorption (Figure 7.16). The strain energy generally increases significantly with an increase in suture thickness. However, it has an undulating response to an increase in protrusion height, although the general trend is upwards. The undulating nature of the response to an increase in h is more prominent for pointy protrusions. Additionally, pointy protrusions increase the amount of strain energy. Given the current information, it may be beneficial for the shell to have long pointy protrusions and thick sutures since it would

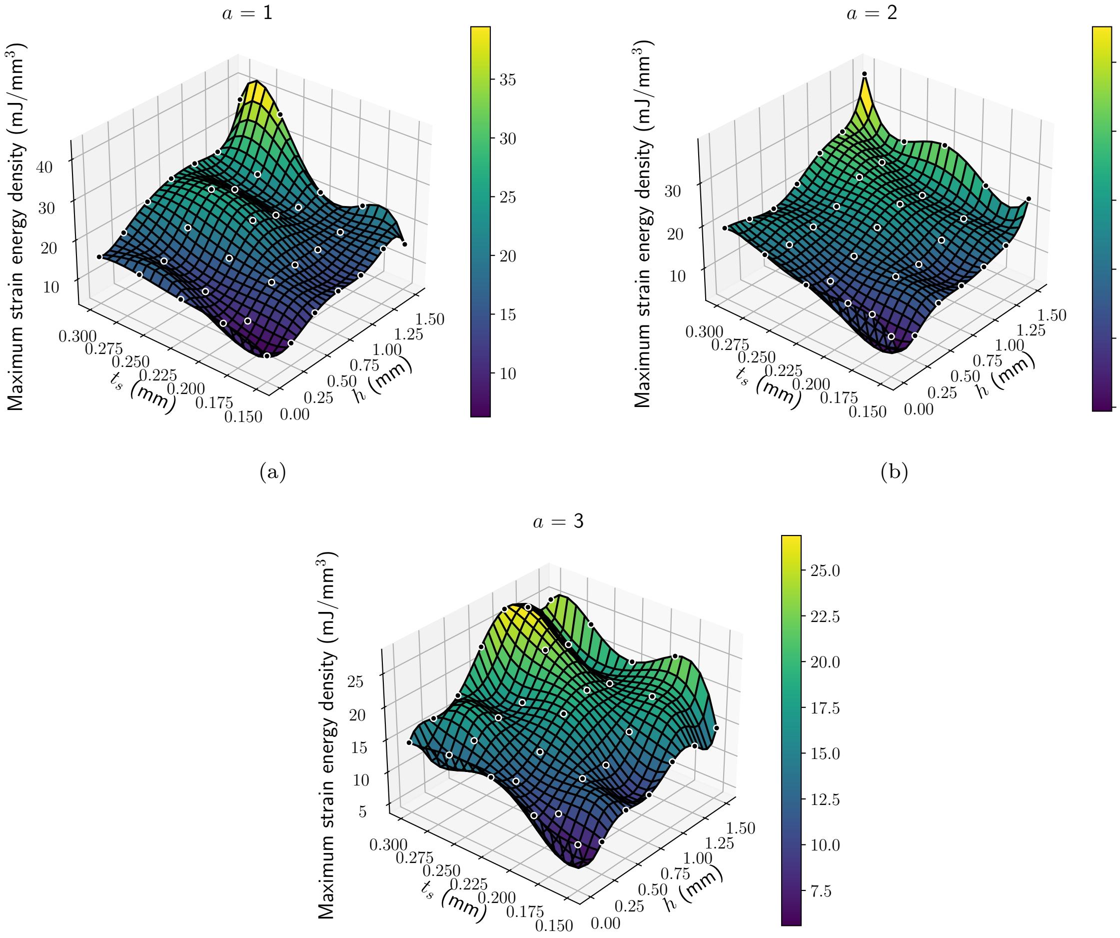

(a)

(b)

(c)

Figure 7.17: Polynomial surfaces fitted through data points for maximum strain energy density contained in different geometric models under the prescribed loading with (a) $a = 1$, (b) $a = 2$ and (c) $a = 3$.

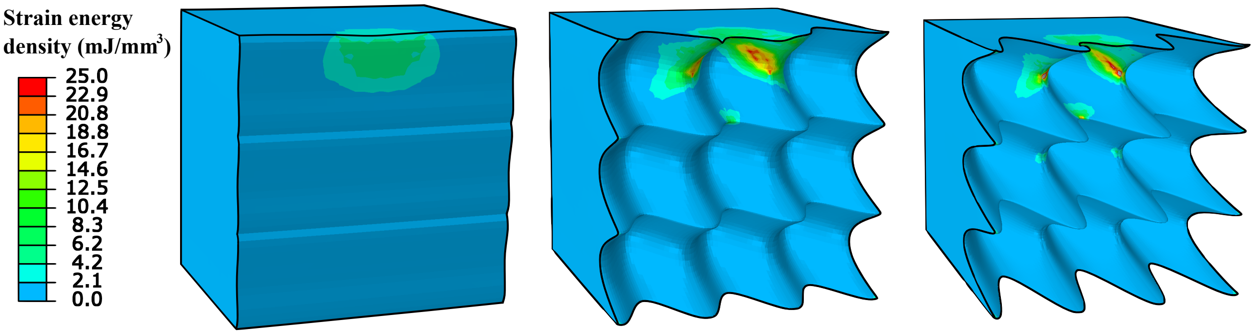

(a)

(b)

(c)

Figure 7.18: Strain energy density contour plots for the right bone of models with $a = 1$, $t = 0.225$ mm and (a) $h = 0$ mm, (b) $h = 0.75$ mm and (c) $h = 1.5$ mm.

increase the strain energy absorption capability of the suture region. Additionally, the long protrusions would increase interlocking and subdue the increased compliance due to the increase in suture volume.

However, the suture geometry is also limited by the possibility of material failure, such as fracture. A large value of strain energy density at a point indicates that there is a high likelihood of fracture at that point. Hence, the maximum strain energy density in the model, shown in Figure 7.17, illustrates the likelihood of fracture occurring somewhere in each model. The maximum strain energy density generally increases with an increase in protrusion length and pointiness and an increase in suture thickness. However, the chance of fracture increases most dramatically as the protrusion height increases from 1.25 mm to 1.5 mm. This may be why the longest bony protrusions in the real turtle shown in Figure 2.1 are in the order of 1.25 mm. Furthermore, for sutures with small protrusion heights, the strain energy density is evenly dispersed around the region where the predator's tooth or claw makes contact (Figure 7.18). However, the strain energy density becomes more concentrated in the ridges between the protrusions for sutures with longer protrusions, suggesting that this is where fracture would occur. This may offer an explanation as to why the longer protrusions shown in Figure 2.1 (c) are located closer to the ventral surface of the shell.

7.5 Conclusions

Qualitative and quantitative aspects of the mechanical behaviour of turtle shells have been investigated. The computational model replicated many aspects of the mechanical behaviour in a three-point bending test, demonstrating the validity of the model.

The application of boundary conditions representative of a predator attack to the model revealed that the presence of sutures increases the amount of energy a predator would have to expend to deform the shell. Additionally, it was found that the sutures reduced the maximum principal strain in the bone – the quantity responsible for bone fracture [111, 112]. Furthermore, although the suture is soft, the presence of a suture made little difference to the deformation of the dorsal surface of the shell.

The relationship between the suture geometry and the shell's mechanical behaviour was investigated by varying the bony protrusion height, the suture thickness and the protrusion pointiness. Increasing the protrusion height was found to increase the compliance of the shell due to the increased volume of soft tissue. However, the increase in compliance was subdued after a protrusion height of 0.5 mm due to the interlocking of the protrusions. Increasing the protrusion height, suture thickness and protrusion pointiness increases the strain energy absorption of the shell. However, it also increases the maximum strain energy density in the shell and hence the probability of fracture. The maximum strain energy density increases dramatically after a protrusion height of 1.25 mm. Furthermore, the position of maximum strain energy density occurs between the protrusions nearest to the point of loading. This is likely why the longest protrusions observed in micro-CT scans of a turtle shell displayed in Figure 2.1 are in the order of 1.25 mm and are located closer to the ventral surface of the shell – to protect them from external attacks.

In summary, the interplay between the stiff bony protrusions and the soft collagenous suture results in a protective material that is stiff due to interlocking of the bony protrusions, but also tough – that is, energy absorbent – due to the strain energy dispersion and cushioning effect of the soft suture. Furthermore, the bony protrusions are long enough to increase strain energy absorption but not so long as to dramatically increase the risk of fracture, and furthermore are located closer to the ventral surface to further reduce the risk of fracture.

Chapter 8

Dynamic suture scale simulations

This chapter presents computational investigations into the mechanical behaviour of the suture region during dynamic loading. Three loading conditions are considered: locomotion, predator attack, and stress wave transfer from one rib to the next. The same geometric model is used as in Chapter 7. However, each of the three loading cases is applied to a range of models with varying suture geometries to elucidate its influence.

The chapter is arranged as follows. The relevant material models and parameters are presented in Section 8.1; as all simulations in this chapter are applied to the same set of geometric models, these models are presented once in Section 8.2. Sections 8.3–8.5 present simulations of locomotion, predator attack and stress wave transfer, respectively; and finally, Section 8.6 presents concluding remarks on the chapter's investigations.

8.1 Material models and parameters

The relevant material models for this chapter are presented here. There are three materials of interest: cortical bone, keratin and soft collagenous tissue which resides in both the suture and skin. The material models used in this chapter are largely similar to those used in Chapter 7; however, they are extended to include viscous behaviour. Additionally, as the simulations are dynamic, a value for the density of each material must be defined.

8.1.1 Cortical bone

The cortical bone density is assumed to be similar to that of bovine cortical bone, that is, 1.95×10^{-9} ton/mm^3 [113]. The bone is modelled as an isotropic linear viscoelastic material with two Maxwell branches. Hence, the stress response is composed of a long time-scale stress $\boldsymbol{\sigma}^{\infty}$ and a viscous stress $\boldsymbol{\sigma}^{v}$:

$$\boldsymbol{\sigma} = \boldsymbol{\sigma}^{\infty} + \boldsymbol{\sigma}^{v} \,. \tag{8.1}$$

The long time-scale stress is governed by Hooke's law,

$$\boldsymbol{\sigma}^{\infty} = \frac{E\nu}{[1+\nu]\,[1-2\nu]}\,[\mathrm{tr}\boldsymbol{\varepsilon}]\,\boldsymbol{I} + \frac{E}{1+\nu}\boldsymbol{\varepsilon} \tag{8.2}$$

where E is Young's modulus and ν is Poisson's ratio, and the viscous stress is given by

$$\boldsymbol{\sigma}^{v} = \sum_{\alpha=1}^{2} \beta_\alpha \int_0^t \exp\left(-\frac{t-s}{\tau_\alpha}\right) \dot{\bar{\boldsymbol{\sigma}}}^{\infty} \mathrm{d}s \,, \qquad \bar{\boldsymbol{\sigma}}^{\infty} = \boldsymbol{\sigma}^{\infty} - \frac{1}{3}\,[\mathrm{tr}\boldsymbol{\sigma}^{\infty}]\,\boldsymbol{I} \,, \tag{8.3}$$

where β_α and τ_α are material parameters (see Section 4.3.2).

The Young's modulus and Poisson's ratio are set to 12 000 MPa and 0.25, respectively, as determined by tests on turtle cortical bone [30]. The viscous material parameters are determined by fitting the model to scaled uniaxial data of bovine cortical bone. The original data is taken from [114] and scaled so that the long time-scale Young's modulus is 12 000 MPa; that is, the same as turtle cortical bone [30]. Details of the analytical solution for uniaxial loading under this material model are given in Appendix D.1.2. The material parameters for the fitted model are presented in Table 8.1. Additionally, the scaled data, fitted material model and the implementation of the model in ABAQUS[1] are shown in Figure 8.1. It is clear that the ABAQUS implementation matches the analytical solution and the model gives a sufficiently good fit to the data.

Table 8.1: Cortical bone material parameters

ρ (ton/mm^3) [113]	E (MPa) [30]	ν [30]	β_1 (s)	β_2 (s)	τ_1 (ms)	τ_2 (μs)
1.95×10^{-9}	12 000	0.25	0.3993	3.760	44.34	10.36

8.1.2 Keratin

The keratinous tissue is assumed to have a similar density to pangolin armour, another hard keratinous tissue, that is, 0.96×10^{-9} ton/mm^3 [115]. The keratin can be modelled as a linear viscoelastic material for the range of strains considered here. Additionally, the tissue is transversely isotropic, with its preferred direction pointing perpendicularly to the surface

---

[1] ABAQUS uses a different, but equivalent form of the material model presented here. The equivalent values for the material parameters in ABAQUS are $g_1 = 0.07740$ and $g_2 = 0.7288$ and the values for τ remain unchanged.

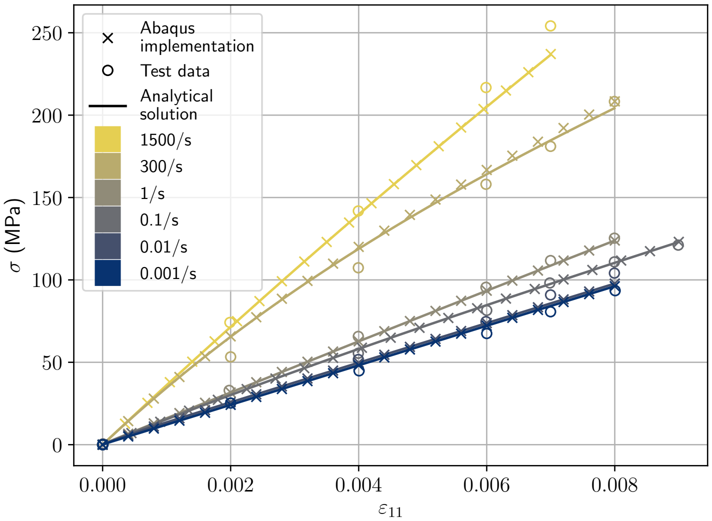

Figure 8.1: Uniaxial loading material behaviour for cortical bone at different strain rates. The model provides a sufficiently good fit to the data. Additionally, the Abaqus implementation of the model matches the analytical solution.

of the shell. However, Abaqus does not provide viscoelasticity paired with linear elastic transverse isotropy and so isotropy is used as a simplification. Hence, the keratin is modelled as a linear isotropic viscoelastic material with two Maxwell branches, similarly to the cortical bone, and so the stress response is governed by equations (8.1)–(8.3). The Young's modulus and Poisson's ratio are set to 700 MPa and 0.4, respectively, as determined by tests on turtle shell keratin [30]. As with the cortical bone, the viscous material parameters are determined by fitting the model to uniaxial test data. The test data is taken from tests on pangolin armour [116] and scaled so that the long time-scale response is equal to that of a turtle's in-plane keratinous tissue [30]. Details of the analytical solution are given in Appendix D.1.2. The material parameters for the fitted model are presented in Table 8.2. Additionally, the results of the scaled data, the fitted material model and the implementation of the model in Abaqus[2] are shown in Figure 8.2. It is clear that the Abaqus implementation matches the analytical solution and the model gives a sufficiently good fit to the data.

Table 8.2: Keratin material parameters

ρ (ton/mm^3) [115]	E (MPa) [30]	ν [30]	β_1 (s)	β_2 (s)	τ_1 (s)	τ_2 (s)
0.96×10^{-9}	700	0.4	0.8526	0.3492	0.5974	189.1

---

[2] Abaqus uses a different, but equivalent form of the material model presented here. The equivalent values for the material parameters in Abaqus are $g_1 = 0.3872$ and $g_2 = 0.1586$ and the values for τ remain unchanged.

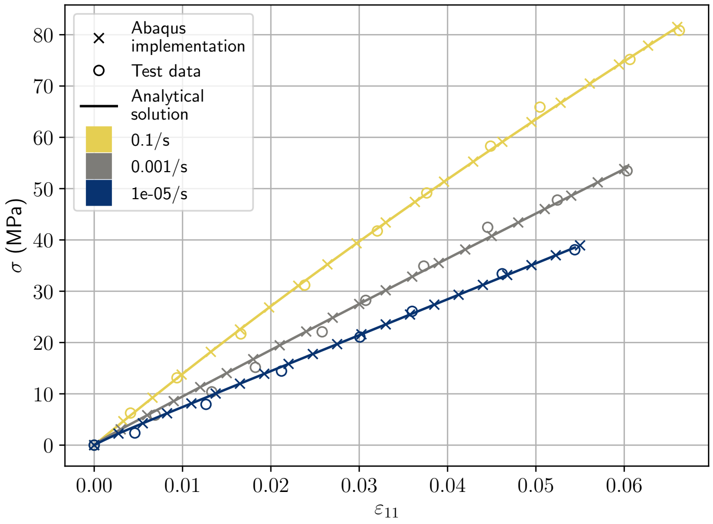

Figure 8.2: Uniaxial loading material behaviour for keratin at different strain rates. The model provides a sufficiently good fit to the data. Additionally, the Abaqus implementation of the model matches the analytical solution.

8.1.3 Soft collagenous tissue

The soft tissue contained in the suture and skin is assumed to have a similar density to that of human skin, that is, 1.25×10^{-9} ton/mm^3 [117]. It is modelled as a near-incompressible transversely isotropic viscous hyperelastic material. Hence, the stress response is composed of a long time-scale isochoric stress $\bar{\boldsymbol{\sigma}}^\infty$, a long time-scale volumetric stress $\boldsymbol{\sigma}^\infty_{vol}$ and a viscous isochoric stress $\bar{\boldsymbol{\sigma}}^v$:

$$\boldsymbol{\sigma} = \bar{\boldsymbol{\sigma}}^\infty + \boldsymbol{\sigma}^\infty_{vol} + \bar{\boldsymbol{\sigma}}^v \,. \tag{8.4}$$

The long time-scale material response is modelled using a near-incompressible Gasser-Ogden-Holzapfel model, which has been presented in Section 4.1.4. Recall that the model's strain energy function is given by

$$\Psi = \bar\Psi + \Psi_{vol}\,, \qquad \bar\Psi = G(\bar I_1 - 3) + \frac{k_1}{2k_2}\left[\exp\left(k_2\bar E^2\right) - 1\right]\,, \qquad \Psi_{vol} = \frac{1}{D}\left[\frac{J^2-1}{2} - \ln J\right]\,. \tag{8.5}$$

Here, $\bar E$ is a pseudo-invariant defined by

$$\bar E := \left\langle\!\left\langle \kappa\left[\bar I_1 - 3\right] + [1-3\kappa]\left[\bar I_4 - 1\right]\right\rangle\!\right\rangle\,, \qquad \langle\langle\bullet\rangle\rangle := \begin{cases}\bullet & \bullet \geq 0,\\ 0 & \bullet \leq 0\,,\end{cases} \tag{8.6}$$

and $G, k_1, k_2 \geq 0$, $D > 0$, $\kappa \in [0,\, 1/3]$ are material parameters. Hence, the long time-scale isochoric stress is given by

$$\begin{aligned} \bar{\boldsymbol{\sigma}}^{\infty} &= \frac{2}{J}\left[\frac{\partial\bar{\Psi}}{\partial\bar{I}_1}\left[\bar{\boldsymbol{B}} - \frac{1}{3}\bar{I}_1\boldsymbol{I}\right] + \frac{\partial\bar{\Psi}}{\partial\bar{I}_4}\left[\bar{\boldsymbol{a}}\otimes\bar{\boldsymbol{a}} - \frac{1}{3}\bar{I}_4\boldsymbol{I}\right]\right], \\ \frac{\partial\bar{\Psi}}{\partial\bar{I}_1} &= G + k_1\kappa\bar{E}\exp\left(k_2\bar{E}^2\right), \qquad \frac{\partial\bar{\Psi}}{\partial\bar{I}_4} = k_1\left[1-3\kappa\right]\bar{E}\exp\left(k_2\bar{E}^2\right), \end{aligned} \tag{8.7}$$

and the long time-scale volumetric stress is given by

$$\boldsymbol{\sigma}_{vol} = \frac{1}{D}\left[J - J^{-1}\right]\boldsymbol{I}\,. \tag{8.8}$$

The viscous part of the stress is modelled using one Maxwell branch. Hence, it is given by

$$\bar{\boldsymbol{\sigma}}^{v} = \frac{1}{J}\boldsymbol{F}\left[\beta\int_0^t \exp\left(-\frac{t-s}{\tau}\right)\dot{\bar{\boldsymbol{S}}}^{\infty}\mathrm{d}s\right]\boldsymbol{F}^T, \qquad \bar{\boldsymbol{S}}^{\infty} = J\boldsymbol{F}^{-1}\bar{\boldsymbol{\sigma}}^{\infty}\boldsymbol{F}^{-T}\,. \tag{8.9}$$

The resulting viscoelastic model is implemented in ABAQUS/Standard using a UMAT and in ABAQUS/Explicit using a VUMAT (see Sections 4.1.3 and 4.3.2 for details).

The model is fitted to biaxial test data on rabbit skin taken from [107] which is scaled so that its Young's modulus is equal to that of the suture in a turtle shell [30]. The analytical solution for the stress response of the model can be found using the procedure given in Section 4.4.2 and is presented in Appendix D.1.1. The resulting material parameters are shown in Table 8.3. Additionally, the scaled data, the analytical solution for the fitted material model and the ABAQUS implementation of the model for the biaxial loading case are shown in Figure 8.3. It is clear that the ABAQUS implementation matches the analytical solution and the model gives a sufficiently good fit to the data.

Table 8.3: Soft tissue material parameters

ρ (ton/mm^3) [117]	G (MPa)	D (MPa^{-1})	k_1 (MPa)	k_2	κ	β_1 (s)	τ (s)
1.25×10^{-9}	89.66	1×10^{-6}	10.94	74.24	1/3	1.60	0.5384

8.2 Model geometry

Each of the simulations in the following sections are run on the same set of model geometries. Hence, the set of geometries is displayed once here. A typical model geometry is displayed in Figure 8.4 (a) with annotations to be referred to when describing the prescribed boundary conditions. Each geometry in the set has a different combination of values for protrusion height h and suture thickness t_s, as illustrated in Figure 8.4 (b). This allows us to determine

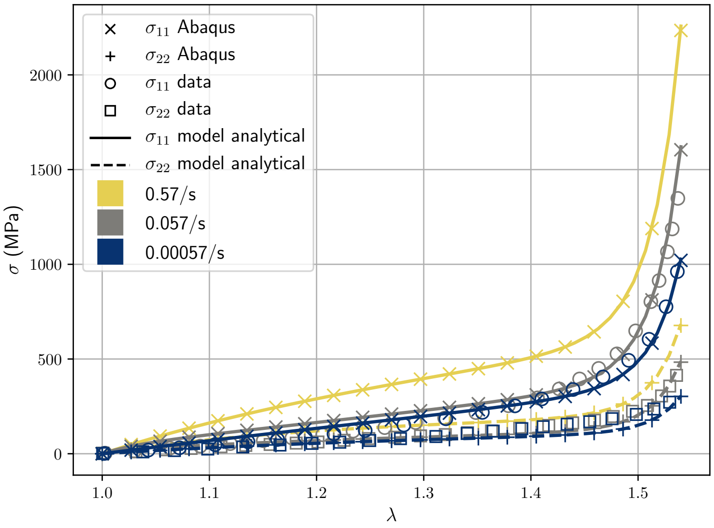

Figure 8.3: Biaxial loading material behaviour for soft tissue at different strain rates. It is clear that the analytical solution of the fitted model gives a sufficiently good fit to the data. Additionally, the ABAQUS implementation of the model matches the analytical solution.

the influence of the suture geometry on the mechanical behaviour of the suture region. In particular, a set of 5×5 models is used, as shown in Figure 8.5, with 5 linearly spaced values for h from 0–0.9 mm and 5 linearly spaced values for t_s from 0.15–0.3 mm. The internal geometry of the suture is displayed in Figure 8.5 (c) by cutting away a quarter of geometry displayed in Figure 8.5 (b). Although, from Figure 8.5 (b), it may seem that the position of the suture is not centred, Figure 8.5 (c) shows that the suture is centred in the model when the internal portion of the suture is considered.

8.3 Locomotion simulations

It is expected that there is a trade-off between the shell's performance as a protective structure and the amount by which it restricts the turtle's ability to move and breathe. Additionally, the suture geometry likely has some influence on this trade-off. That influence is investigated here by simulating the suture region during breathing and locomotion for a range of geometries. It is assumed that the loading applied to the shell during breathing and general locomotion is similar. Hence, only one set of simulations is conducted to elucidate the behaviour in both scenarios.

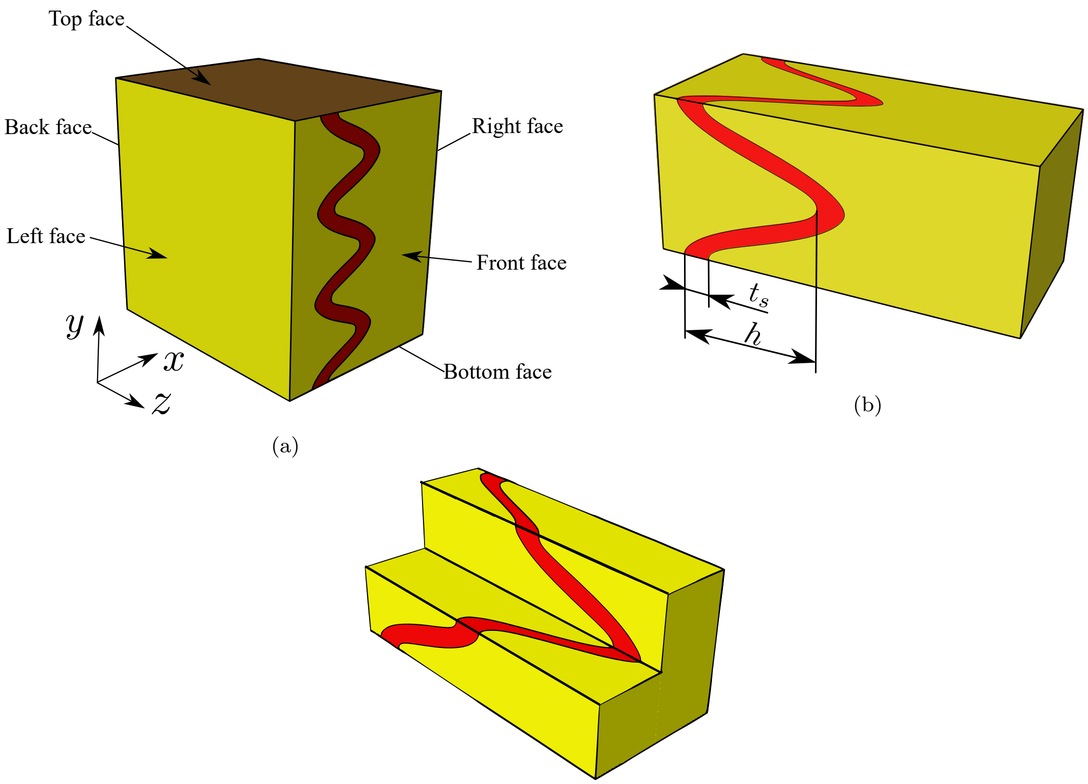

(a)

(b)

(c)

Figure 8.4: Illustration of (a) an entire geometric model with various boundaries annotated, (b) a pair of interlocking protrusions annotated with the key dimensions of the protrusion height h and suture thickness t_s, and (c) a pair of interlocking protrusions with a quarter of the geometry cut away to illustrate the internal suture geometry. The brown surface in (a) depicts the keratinous and skin layers.

8.3.1 Boundary conditions

The displacement of the front, back, left and right faces (see Figure 8.4 (a)) is constrained so that they can only move in what would be the radial direction if the entire shell were modelled, see Figure 8.6. The bottom face is prescribed a pressure load of

$$\bar{\boldsymbol{t}} = -p\boldsymbol{n}\,, \qquad p = 5 \times t/2\,\text{kPa}\,, \tag{8.10}$$

where $\boldsymbol{n}$ is the outward facing unit normal, p is pressure and t is time in seconds. The loading is applied over a time of 2 seconds, as this is the length of one inhalation for a turtle [118]. The maximum pressure applied is 5 kPa which is the lung pressure of a human [119]. The top face is traction free. A summary of the boundary conditions is presented in Table 8.4.

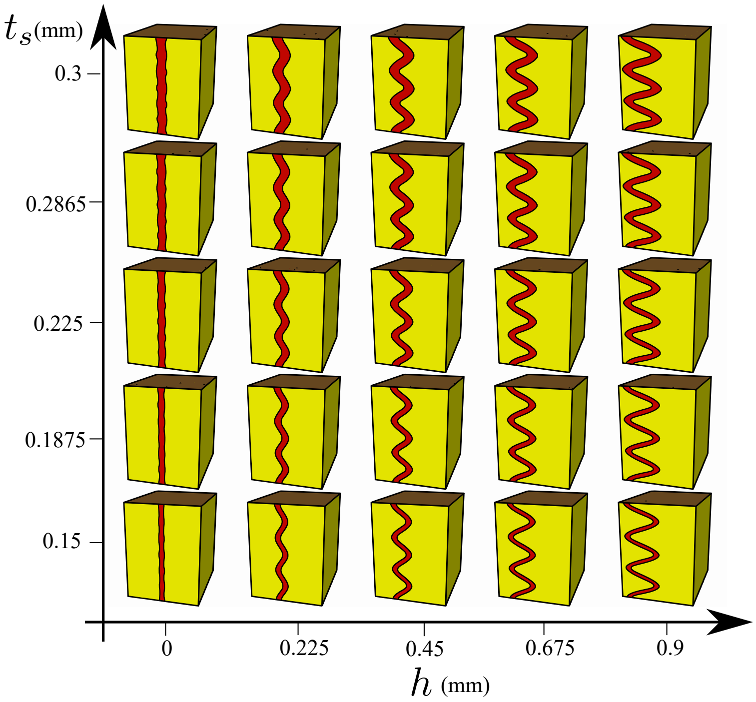

Figure 8.5: Set of geometric models used to investigate the effect of the bony protrusion height h and suture thickness t_s on the dynamic mechanical behaviour of the shell.

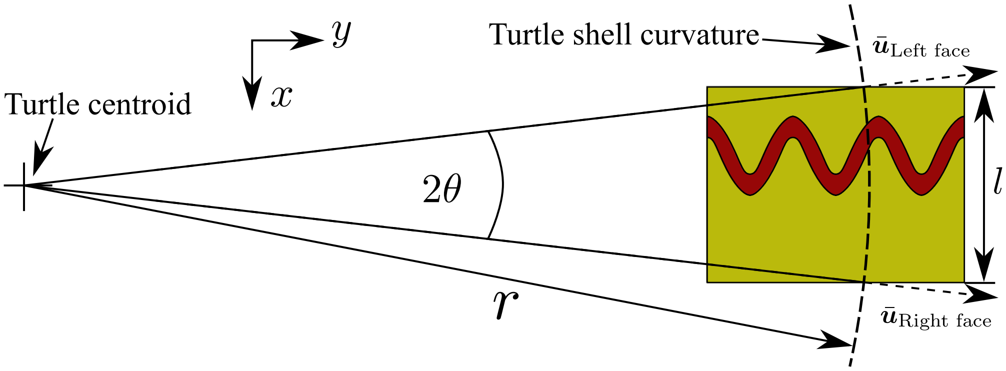

Figure 8.6: Illustration of the displacement constraint on the front, back, left and right faces of the model. Here, $\theta = \arcsin(l/2r) = 1.09°$, where $l = 2.28\,\text{mm}$ is the chosen length of the simulated model and $r = 60\,\text{mm}$ is the radius of a real turtle shell with dimensions similar to that of geometric models used here, determined via micro-CT scans.

8.3.2 Results

To determine how the suture geometry affects the compliance of the shell, the average vertical displacement of the bottom face at time $t = 2\,\text{s}$ is plotted as a function of h and t_s in Figure 8.7. It is also interesting to observe the significance of the viscous part of the material behaviour in relation to the elastic part. Hence, the long time-scale elastic strain energy is compared to the non-equilibrium energy in Figure 8.8.

Table 8.4: Boundary conditions for locomotion simulation, $c_i \in \mathbb{R}\,, i = 1, \ldots, 4$

Front face	Back face	Left face	Right face	Bottom face	Top face
$\bar{t}_1 = 0$ $\bar{u}_2 = c_1 \cos\theta$ $\bar{u}_3 = c_1 \sin\theta$	$\bar{t}_1 = 0$ $\bar{u}_2 = c_2 \cos\theta$ $\bar{u}_3 = -c_2 \sin\theta$	$\bar{u}_1 = -c_3 \sin\theta$ $\bar{u}_2 = c_3 \cos\theta$ $\bar{t}_3 = 0$	$\bar{u}_1 = c_4 \sin\theta$ $\bar{u}_2 = c_4 \cos\theta$ $\bar{t}_3 = 0$	$\bar{\boldsymbol{t}} = p\boldsymbol{n}$	$\bar{\boldsymbol{t}} = \boldsymbol{0}$

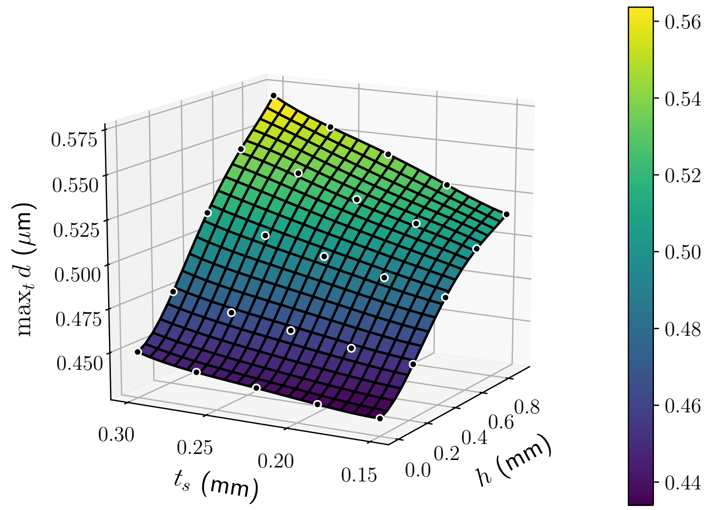

Figure 8.7: Surface plot of vertical displacement of the bottom face of each model at $p = 5\,$kPa as a function of bony protrusion height h and suture thickness t_s.

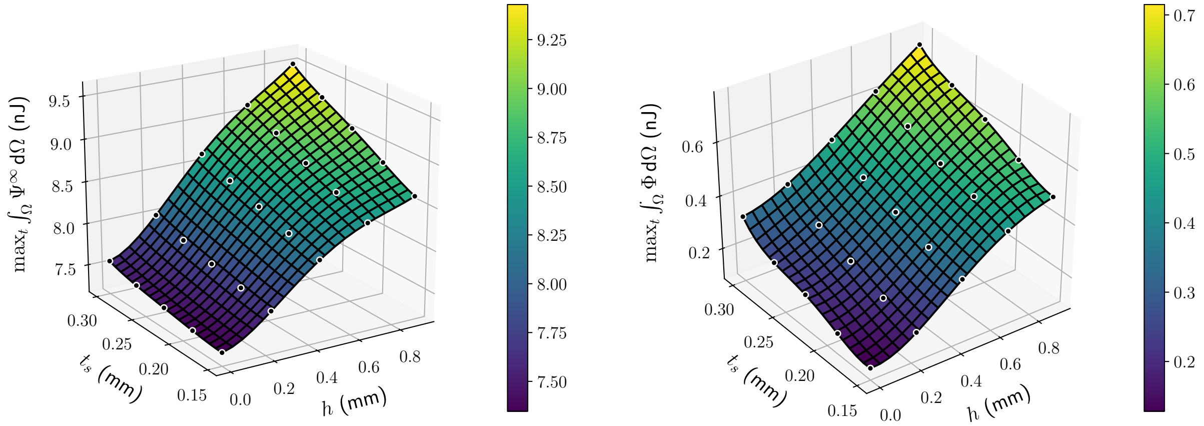

(a) (b)

Figure 8.8: Comparison of (a) the long time-scale strain energy and (b) the non-equilibrium energy in the model at the time of maximum inhalation ($t = 2\,$seconds).

8.3.3 Discussion

The shell becomes more compliant as the suture thickness t_s and the bony protrusion height h increase (Figure 8.7). This is attributed to the increase in soft tissue volume that occurs along with an increase in t_s and h. The increase in compliance is fairly significant, approximately 27 %. An increase in compliance due to increasing t_s and h has also been observed in quasistatic simulations of a predator attack [1]. However, in the predator attack simulations an interlocking effect was observed whereby the increase in compliance plateaus once h is sufficiently large. Here, the increase in compliance decreases slightly while $h > 0.4\,\mathrm{mm}$ (particularly for smaller t_s). However, the interlocking effect is far less pronounced than that observed in [1]. This is likely because interlocking only occurs during sufficiently large deformation. As the displacement in [1] (in the order of millimetres) was far larger than the displacement observed here (in the order of micrometers), the interlocking effect was more prominent. This indicates that the suture geometry allows it to interlock – stiffening the shell – in the case of a predator attack, but does not interlock during everyday locomotion.

Both the long time-scale strain energy, Figure 8.8 (a), and the non-equilibrium energy, Figure 8.8 (b), show a consistent increase with an increase in h and t_s. However, the responses are quantitatively quite different. The non-equilibrium energy increases by about 250 % whereas the long time-scale strain energy increases by about 27 %. Additionally, the strain energy is in the order of 13.5-37.5 times greater than the non-equilibrium energy. Hence, the viscous behaviour of the shell does not significantly increase the work required to move when compared to that for its elastic behaviour. This is likely because of the slow rate at which a turtle moves, particularly in comparison to the rate of displacement experienced during an attack.

However, although the suture geometry affects the compliance of the shell, it should be noted that the deformations are still very small – less than a micrometer. When a turtle of the length modelled here (about 150 mm) locomotes, its movements are in the order of tens of millimetres. Hence, for all intents and purposes, the shell may be considered rigid in relation to the force that a turtle applies to it during locomotion. So, even if one suture geometry is twice as compliant as another, it is immaterial in the context of turtle locomotion.

8.4 Predator attack simulations

Investigations of the influence of suture geometry on the behaviour of the suture region during a predator attack are presented here. The loading during a predator attack is expected to be similar to that during some other event that might injure the turtle – a rockfall, for instance.

These events are typically quite dynamic, and so the viscous behaviour of the material is expected to play a significant role.

8.4.1 Boundary conditions

Spring boundary conditions are assigned on the front, back, left and right faces, to approximate the behaviour of the remainder of the shell as in Chapter 7. This approach has been used and shown to be valid in [1]. The bottom and top faces are traction free. However, the top face experiences contact with a rigid sphere of 1 mm radius representing the tooth or claw of a predator [120] (or tip of a rock), see Figure 8.9. It is assumed that there are 4 pairs of teeth in contact during the bite, and only one of them is modelled here. Hence, the sphere is assigned a mass of $m = 3\,\mathrm{kg}$, being one fourth of the mass of a lion's head [121]. Additionally, a downwards force of $F = 442\,\mathrm{N}$ is applied to the sphere as one fourth of a lion's bite strength [121]. The sphere is also assigned an initial velocity of $v_i = 2\,\mathrm{m/s}$. The details of the boundary conditions are summarised in Table 8.5.

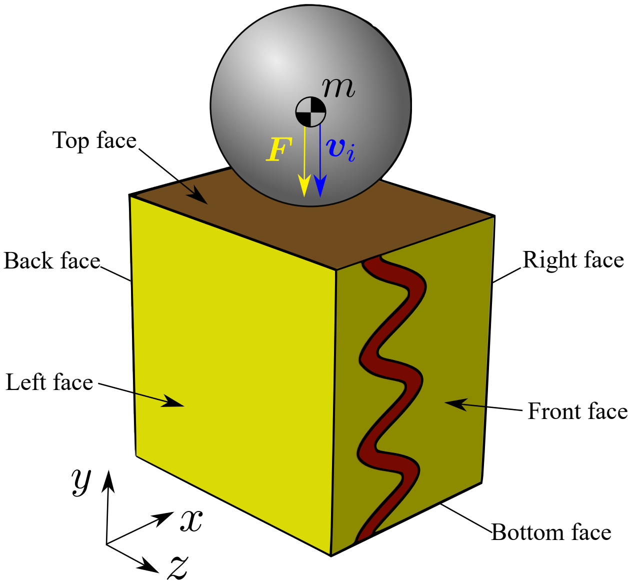

Figure 8.9: Illustration of the predator attack simulation setup in which the shell comes into contact with a rigid sphere of 1 mm radius representing the claw or tooth of a predator. The front, back, left and right faces are assigned spring boundary conditions and the bottom face is traction free.

Table 8.5: Boundary and initial conditions for predator attack simulation

Front face	Back face	Left face	Right face	Bottom face	Top face	Rigid sphere
$\bar{\boldsymbol{t}} = -k\boldsymbol{u}$	$\bar{\boldsymbol{t}} = -k\boldsymbol{u}$	$\bar{\boldsymbol{t}} = -k\boldsymbol{u}$	$\bar{\boldsymbol{t}} = -k\boldsymbol{u}$	$\bar{\boldsymbol{t}} = \boldsymbol{0}$	Contact with rigid sphere $\bar{\boldsymbol{t}} = \boldsymbol{0}$	Contact with top face $\boldsymbol{F} = [0 \quad -442 \quad 0]^T$ $\boldsymbol{v}_i = [0 \quad -2 \quad 0]^T$

8.4.2 Results

To compare the compliance of the suture region for various geometries, one requires a suitable metric to quantify compliance. This metric is chosen to be

$$\tilde{u}_2 = \max_{\boldsymbol{x}} u_2 - \min_{\boldsymbol{x}} u_2 \,. \tag{8.11}$$

If the shell is rigid, then any vertical displacement u_2 will be due to the spring boundary conditions and so $\max_{\boldsymbol{x}} u_2 = \min_{\boldsymbol{x}} u_2$ and $\tilde{u}_2 = 0$. However, as the compliance of the shell increases, the shell will hinge more about the rigid sphere and so $\tilde{u}_2$ will increase. This result for each model is displayed in Figure 8.10.

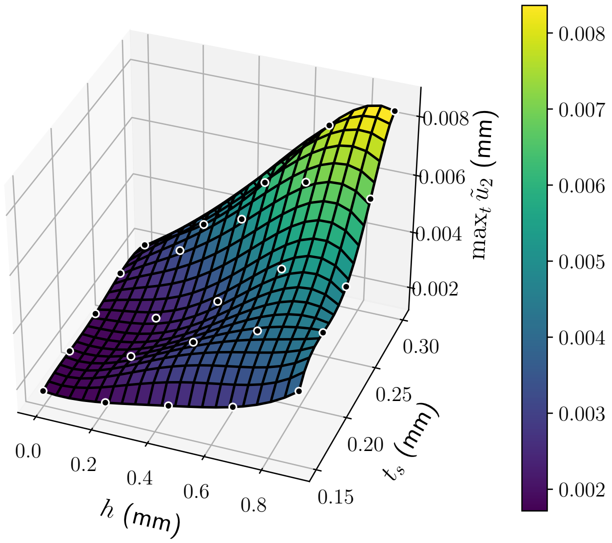

Figure 8.10: The compliance of the shell, $\tilde{u}_2 = \max_{\boldsymbol{x}} u_2 - \min_{\boldsymbol{x}} u_2$, plotted as a function of protrusion height h and suture thickness t_s. The compliance increases steadily with both h and t_s while h is in the domain of $[0, 0.6]$ mm. For $h > 0.6$ mm, however, the compliance plateaus. This is attributed to an interlocking effect which occurs for a sufficiently large protrusion height.

The long time-scale strain energy and non-equilibrium energy indicate the amount of work required from the predator to deform the shell. These quantities are presented as a function of time for a selection of models in Figure 8.11 and the maxima of these quantities in time are presented as a function of protrusion height and suture thickness in Figure 8.13. Additionally, strain energy density contour plots for two key moments in time are displayed in Figure 8.12.

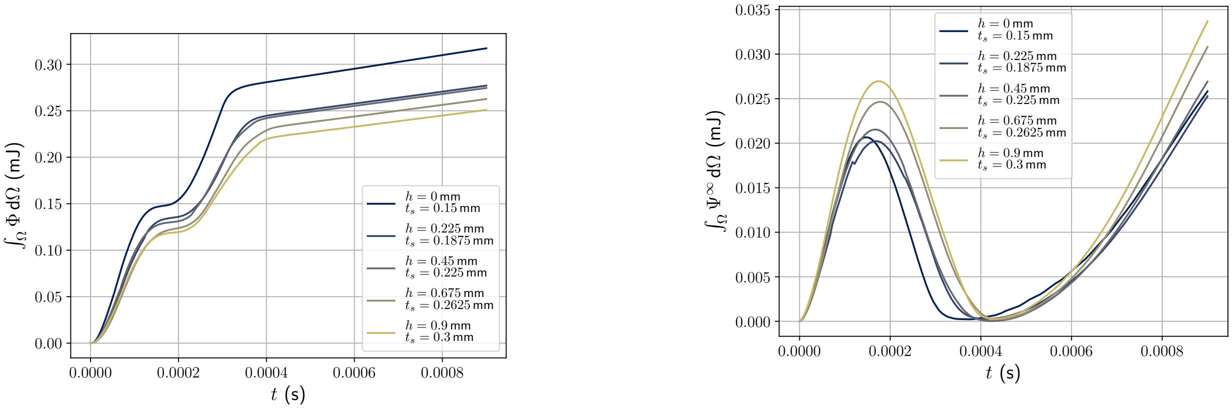

(a) (b)

Figure 8.11: Comparison of how (a) energy that is viscously dissipated and (b) energy that is stored as potential strain energy progress in time t.

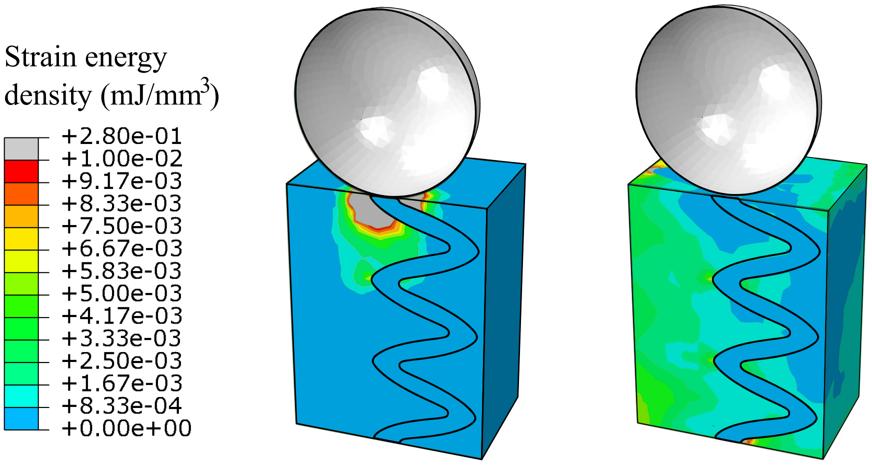

(a) (b)

Figure 8.12: Strain energy density contour plots at time (a) $t = 1.8 \times 10^{-4}$ and (b) $t = 9 \times 10^{-4}$. The peak indentation is shown in (a) and so the strain energy density is localized around the predator's tooth. In (b), however, the indentation has relaxed and dispersed deformation has ensued.

The maximum strain energy density in the shell indicates the likelihood of fracture at some position in the shell. This quantity is displayed in Figure 8.14.

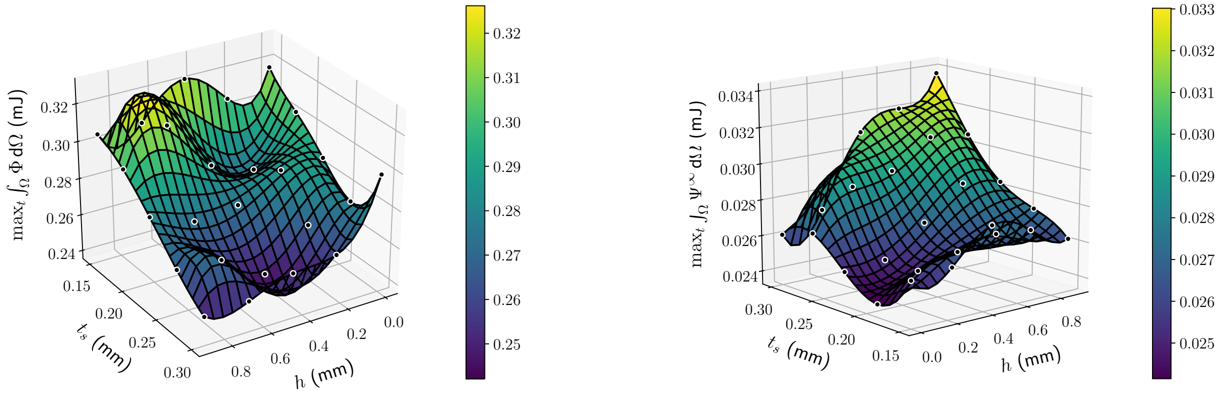

(a) (b)

Figure 8.13: Comparison of (a) energy that is viscously dissipated with (b) energy that is stored as potential strain energy, both as a function of protrusion height h and suture thickness t_s.

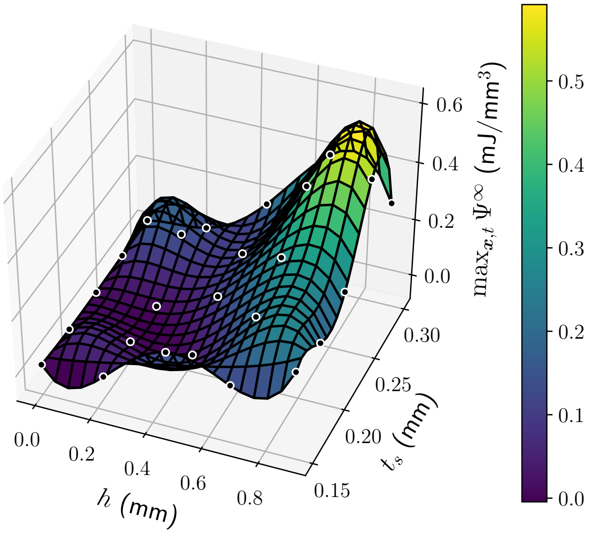

Figure 8.14: The maximum strain energy density in the suture region as a function of the protrusion height h and suture thickness t_s. The maximum strain energy density increases significantly with an increase in h. The response to an increase in t_s is less significant for smaller h than for larger h.

8.4.3 Discussion

The interlocking effect, whereby the compliance of the shell plateaus after sufficiently large protrusion height h, is observed in the dynamic simulation of a predator attack as it was in the quasistatic equivalent [1] (Figure 8.10). However, a general increase in compliance is observed with an increase in h and suture thickness t_s, as is observed in the loading case of locomotion. Again, this is likely due to an increase in the volume of the soft suture.

It is apparent that the shell goes through three distinct stages of deformation: initial contact ($t < 1.8 \times 10^{-4}$ s), indentation relaxation (1.8×10^{-4} s $< t < 4 \times 10^{-4}$ s), and distributed deformation (4×10^{-4} s $< t$); see Figure 8.11. In the initial contact stage, the shell's inertia causes a lag in the motion, resulting in large localised strain where the tooth makes contact. Consequently, there is a large rate of deformation at the contact site and so there is a large amount of non-equilibrium energy in this stage (Figure 8.11 (a)). Additionally, the long time-scale strain energy increases rapidly due to large localized deformation (Figure 8.11 (b) and 8.12 (a)). At $t = 1.8 \times 10^{-4}$ s the peak indentation is experienced, resulting in a local maximum in long time-scale strain energy. Additionally, the rate of deformation is low and so there is a plateau in the non-equilibrium energy. The deformation of the remainder of the shell then 'catches-up' with the indentation region in the indentation relaxation stage (1.8×10^{-4} s $< t < 4 \times 10^{-4}$ s). Hence, the deformation rate increases again, resulting in more non-equilibrium energy. However, the deformation is decreasing, causing a decrease in long time-scale strain energy. In the final stage, distributed deformation (4×10^{-4} s $< t$), the behaviour of the external portion of the shell, which is approximated with spring boundary conditions, has a significant influence on the deformation of the suture region. Consequently, the deformation is distributed throughout the suture region, see Figure 8.12 (b). Moreover, the rate of deformation is low, resulting in little increase in non-equilibrium energy.

The non-equilibrium energy decreases with an increase in h and t_s, Figure 8.13 (a), in contrast to the long time-scale strain energy which increases with an increase in h and t_s, Figure 8.13 (b). Moreover, the non-equilibrium energy is approximately 10 times larger than the long time-scale strain energy. As the attack progresses further than $t = 9 \times 10^{-4}$, it is likely that the strain energy will continue to increase more significantly than the viscous dissipation. However, it is evident that the viscous material behaviour has a significant effect in the loading case of a predator attack, as opposed to the loading of the shell during locomotion.

The maximum strain energy density in the shell indicates the likelihood of fracture occurring. The likelihood of fracture increases dramatically with an increase in h, see Figure 8.14. For $h < 0.45$ mm the suture thickness has little influence on the likelihood of fracture. However, for $h > 0.45$ mm an increase in suture thickness dramatically increases the likelihood of fracture.

8.5 Stress wave transmission simulations

Chapter 7 shows that sutures have the effect of dispersing the strain energy density distribution in the region during quasistatic loading. Hence, it stands to reason that the sutures could also disperse stress waves passing from one plate to the next. Investigations of this effect are presented here for a range of suture geometries. Two sets of stress wave transmission simulations are investigated here: for direct and transverse stress waves.

8.5.1 Boundary conditions

The boundary conditions for both sets of simulations are as follows:

- The right, bottom and top faces are traction free;
- The front and back faces are traction free in the x and y directions and are assigned a displacement of $\bar{u}_3 = 0\,\mathrm{mm}$ in the z direction; and
- The left face is prescribed a traction of $\boldsymbol{t}_w$ causing the incident wave.

The prescribed traction is given by

$$\boldsymbol{t}_w = \begin{bmatrix} -\sigma_{bc} & 0 & 0 \end{bmatrix}^T , \qquad \boldsymbol{t}_w = \begin{bmatrix} 0 & \sigma_{bc} & 0 \end{bmatrix}^T , \tag{8.12}$$

for the set of direct and transverse wave simulations, respectively, and σ_{bc} is a function of time, t, given by

$$\bar{\sigma}_{bc} = \begin{cases} 100\,\mathrm{MPa} & t < 1.25 \times 10^{-7}\,\mathrm{s}\,, \\ 0\,\mathrm{MPa} & t > 1.25 \times 10^{-7}\,\mathrm{s}\,. \end{cases} \tag{8.13}$$

The boundary conditions are summarised in Table 8.6.

Table 8.6: Boundary conditions for direct stress wave transfer simulation

Front face	Back face	Left face	Right face	Bottom face	Top face
$\bar{t}_1 = 0$ $\bar{t}_2 = 0$ $\bar{u}_3 = 0$	$\bar{t}_1 = 0$ $\bar{t}_2 = 0$ $\bar{u}_3 = 0$	$\bar{\boldsymbol{t}} = \boldsymbol{t}_w$	$\bar{\boldsymbol{t}} = \boldsymbol{0}$	$\bar{\boldsymbol{t}} = \boldsymbol{0}$	$\bar{\boldsymbol{t}} = \boldsymbol{0}$

8.5.2 Results

One effect of the sutures is that they break up the stress wave, distributing its energy between the two bone plates. This is quantified by the ‘transfer ratio’ r_t; that is,

$$r_t = \frac{\max\limits_t \displaystyle\int_{\Omega_R} \Psi \mathrm{d}\Omega}{\max\limits_t \displaystyle\int_{\Omega_L} \Psi \mathrm{d}\Omega} . \tag{8.14}$$

Here Ω_R and Ω_L are the spaces occupied by the right and left bone, respectively. The transfer ratio indicates how much of the stress wave was transferred from the left bone to the right. If the entirety of the wave is transferred, the ratio will be 1. This would be the case if there were no suture, as the stress wave would be unperturbed. As less of the wave is transferred, the ratio will become smaller. The transfer ratio for direct and shear stress waves is displayed as a function of protrusion height and suture thickness in Figure 8.15 (a) and (b), respectively.

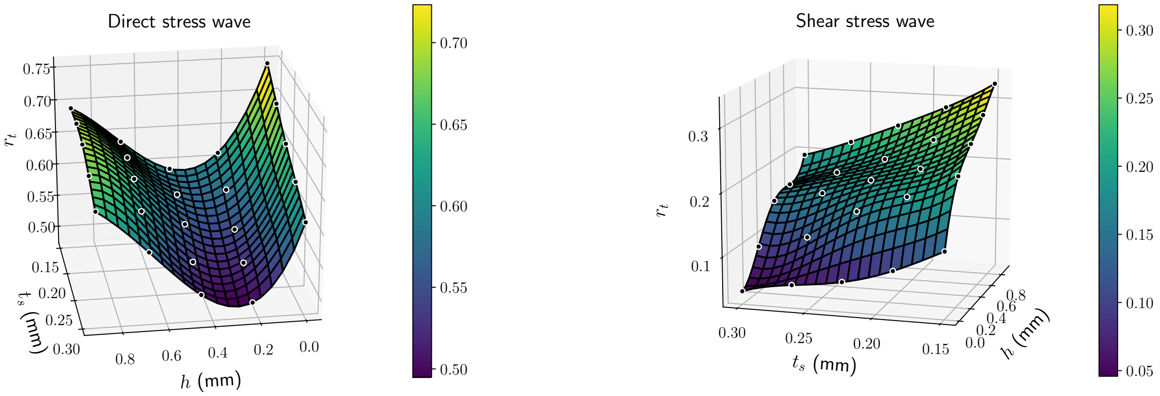

(a) (b)

Figure 8.15: The transfer ratio, $r_t = \left[\max_t \int_{\Omega_R} \Psi \mathrm{d}\Omega\right] / \left[\max_t \int_{\Omega_L} \Psi \mathrm{d}\Omega\right]$, as a function of protrusion height h and suture thickness t_s for (a) direct stress waves and (b) shear stress waves.

The maximum strain energy density in the model gives an indication of the likelihood of fracture occurring somewhere in the suture region. The effect of suture geometry on this value is displayed in Figure 8.16. Since the maximum strain energy density is a local quantity, it is interesting to observe where it occurs in the model. Hence, contour plots of maximum strain energy density when the stress wave is approximately halfway through the suture are displayed for a selection of models for the direct stress wave (Figure 8.17) and the shear stress wave (Figure 8.18).

8.5.3 Discussion

The transfer ratio r_t quantifies the percentage of the energy in the wave that is transferred from the left bone to the right bone. For both direct and shear stress waves, the transfer ratio decreases steadily with an increase in suture thickness, see Figure 8.15. This is unsurprising, as one expects that a thicker suture will provide more cushioning. The response to a change in protrusion height h, however, is varied.

For direct stress waves, the transfer ratio has a parabolic-like relationship to h with a

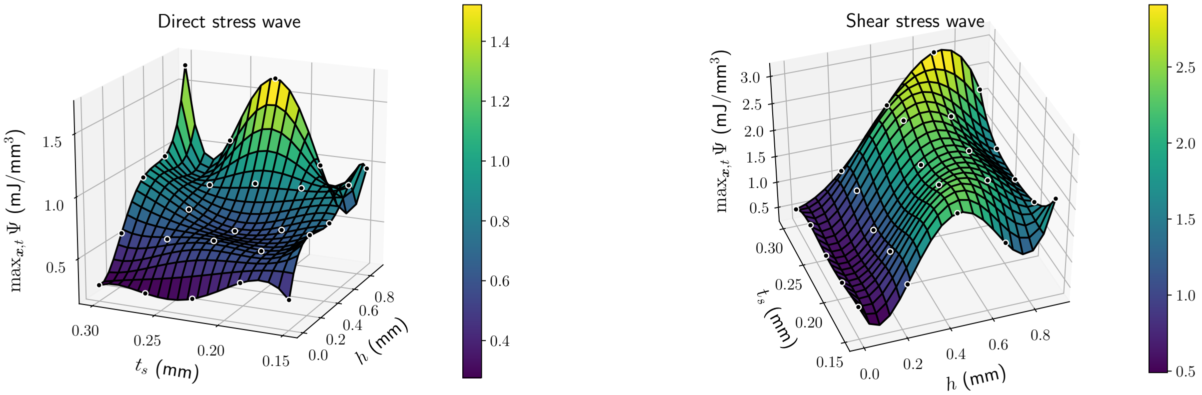

(a) (b)

Figure 8.16: Maximum strain energy density in space $\boldsymbol{x}$ and time t as a function of protrusion height h and suture thickness t_s for (a) direct stress waves and (b) shear stress waves.

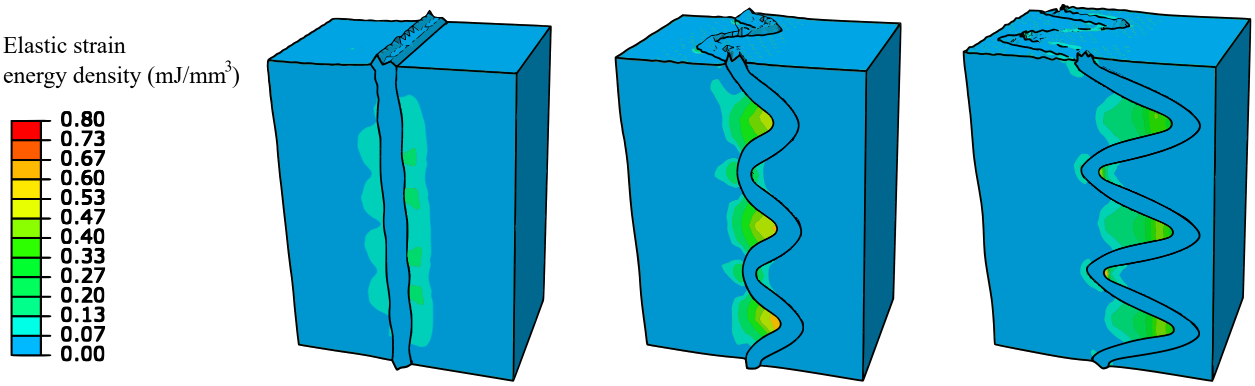

(a) (b) (c)

Figure 8.17: Comparison of strain energy density contours during direct stress wave transfer when $t_s = 0.225$ mm and (a) $h = 0$ mm, (b) $h = 0.45$ mm and (c) $h = 0.9$ mm.

minimum at approximately 0.3 mm. A possible explanation for this is that the transfer of direct stress waves is largely dependent on the volume of soft tissue that can be squeezed out of the top and bottom of the suture region; see Figure 8.17. For sutures with short protrusions (Figure 8.17 (a)) the suture contains less soft tissue and so there is less volume to be squeezed out of the suture region. Medium height protrusions (Figure 8.17 (b)) increase the volume of soft tissue in the suture region, increasing the volume of tissue to be squeezed out of the region and lowering the transfer ratio. However, although higher protrusions (Figure 8.17 (c)) increase the soft tissue volume further, the tissue becomes trapped in the suture region. Consequently, the tissue is not squeezed out of the region, and it experiences a large pressure as the direct stress wave effectively passes through the suture into the right bone. For shear stress waves, on the other hand, the transfer ratio increases steadily with

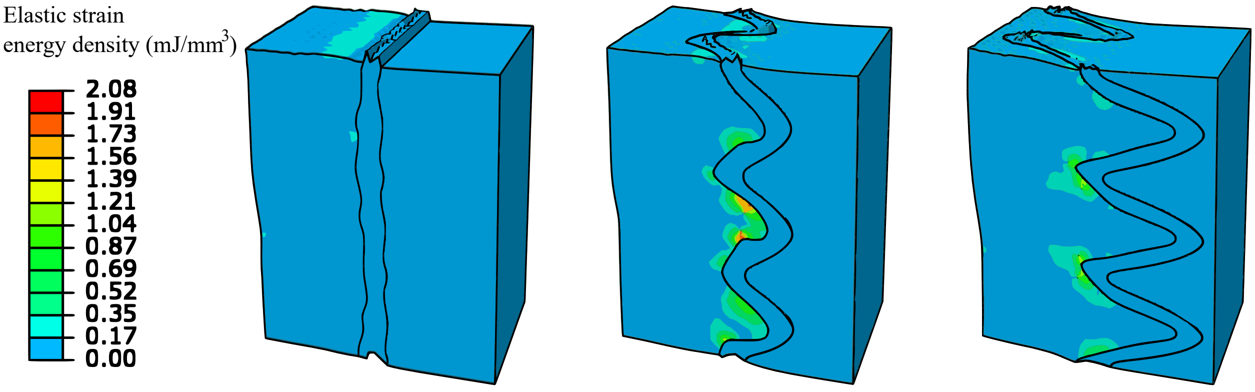

(a) (b) (c)

Figure 8.18: Comparison of strain energy density contours during shear stress wave transfer when $t_s = 0.225\,\text{mm}$ and (a) $h = 0\,\text{mm}$, (b) $h = 0.45\,\text{mm}$ and (c) $h = 0.9\,\text{mm}$.

and increase in h. This is attributed to increased degree of interlocking.

The maximum strain energy density for shear waves has a parabolic-like response to h, see Figure 8.16 (b), with a maximum at approximately $h = 0.6\,\text{mm}$. When h is small, the left bone can move vertically relative to the right bone with ease, see Figure 8.18 (a), and so the strain energy density in the bones is low. For moderately high protrusions, interlocking occurs, and large strain energy density occurs in the protrusions (Figure 8.18 (b)). However, for higher protrusions (Figure 8.18 (c)) the wave is transferred over a longer distance and time, and so the strain energy density within the protrusions is lower than for moderately high protrusions (Figure 8.18 (b)). Additionally, the influence of t_s on the maximum strain energy density is small in comparison to h.

For direct stress waves, however, the maximum strain energy density increases continually with an increase in h. This is because increasing h makes the tips of the protrusions pointer. Hence, the strain energy becomes increasingly concentrated in these regions, see Figures 8.17 (a)–(c).

8.6 Conclusions

The dynamic mechanical behaviour of turtle suture regions has been modelled. Viscoelastic models have been used for the various materials in the suture region. Each material model was fitted to physical test data and a sufficient match achieved. Additionally, the implementation of the material models in Abaqus matched the analytical solutions used to perform the fitting procedures. Hence, the material models behaved as intended in Abaqus.

The effect of suture geometry on the shell's dynamic mechanical behaviour was investigated by generating several models with varied geometric parameters. In particular, the height of the bony protrusions h and the suture thickness t_s was varied. Additionally, the shell's mechanical behaviour was investigated in a number of dynamic loading scenarios: locomotion, a predator attack and stress wave transfer.

In the case of locomotion, an increase in h and t_s both increase the compliance of the shell due to the increase in volume of the soft tissue in the suture. The interlocking effect, whereby the increase in compliance due to an increase in h plateaus for sufficiently large h, is observed to be far less prominent in this loading case than has been observed in quasistatic models of predator attacks [1]. The discrepancy is likely caused by the difference in magnitude of deformation between the two loading cases: the case of a predator attack produces sufficiently large deformations for interlocking to occur, whereas locomotion does not. Moreover, the non-equilibrium energy in the suture region is small in comparison to the long time-scale energy. Hence, for the magnitude and rate of deformation that occurs during locomotion, the bony protrusions do not cause significant interlocking and the turtle motion is not significantly further hindered by viscous overstress. However, the deformation of the shell is still small in comparison to the movements a turtle would typically make. So, even though the sutures and their geometry can increase the compliance of the shell during locomotion by a large percentage, the shell is still effectively rigid and so the suture geometry is irrelevant in this scenario.

For the dynamic loading due to predator attacks, the compliance of the shell also increases with h and t_s. However, the interlocking occurs as h becomes sufficiently large. Irrespective of the suture geometry, the dynamic loading of the shell during a predator attack has three distinct stages: initial contact, indentation relaxation, and dispersed deformation. During initial contact the indentation region near the predator's tooth has a large strain rate relative to the rest of the shell, during indentation relaxation the rest of the shell 'catches-up' to the indentation region, and during dispersed deformation the whole shell continually deforms in a distributed manner. The non-equilibrium energy, most of which occurs in the initial contact and indentation relaxation stages, is about 10 times larger than the maximum long time-scale strain energy. These observations indicate that the viscous material behaviour significantly improves the performance of the shell as a protective structure. However, the ratio of non-equilibrium energy to strain energy is likely to decrease as the loading progresses. Nevertheless, this illustrates how viscous material behaviour can serve to protect the turtle through dissipation, much as crumple zones in a car protect passengers through plastic dissipation.

For stress wave transmission, the percentage of energy in the wave that was transferred from the one plate to the next, termed the transfer ratio, was investigated. An increase in t_s decreases the transfer ratio for both shear and direct stress waves due to increased cushioning. The transfer ratio has a parabolic-like relationship to h in the case of direct stress waves, with a minimum at $h = 0.3\,\mathrm{mm}$. This is due to the interplay between an increase in soft tissue volume to be squeezed out of the region (decreasing the transfer ratio) and the soft tissue becoming increasingly trapped in the region (increasing the transfer ratio) as h increases. For shear stress waves, on the other had, the transfer ratio steadily increases with h due to the increase in interlocking, and hence, increased resistance to one bone moving vertically relative to another.

It is clear that sutures and viscoelastic behaviour improve the functionality of the shell in several loading cases. During a predator attack, sufficiently long bony protrusions cause interlocking and the viscous dissipation protects the shell and turtle. During stress wave propagation, the sutures break up the stress waves, distributing the energy among different bone plates. Moreover, these features depend significantly on the suture geometry, and hence, can be optimized by evolution.

Chapter 9

Multiscale simulations

This chapter presents an investigation into the effect of a network of sutures on the mechanical behaviour of the turtle shell. Furthermore, the influence of the suture geometry is investigated. To carry out these investigations, one must model the mechanical behaviour at the scale of the suture and the entire shell. This raises a difficulty due to the difference in length-scale between the suture and the entire shell: if one created a mesh of the entire shell that was fine enough to capture the geometry of the suture, the mesh would contain an excessive number of elements, leading to intractable computational requirements.

This issue is circumvented by using a multiscale modelling approach, FE^2. To this end, two separate geometries are generated: a macroscale geometry of the entire shell which contains regions of 'suture interfaces' and a representative volume element (RVE) which defines the constitutive relation for the suture interface. However, as outlined in chapter 6, concurrent multiscale modelling is highly computationally expensive. Hence, a simple non-concurrent approach is adopted whereby several loading cases are applied to the RVE to elucidate its mechanical behaviour. Then, a constitutive model is fitted to the resulting data and is used to model the suture interface region in the shell as outlined in Section 6.2.3.

The chapter is arranged as follows. Section 9.1 presents relevant material models along with parameters which have been determined by fitting the models to test data. Then, Section 9.2 presents the geometry at the shell scale and the suture scale models. In Section 9.3, several loading paths are applied to each RVE, thus elucidating their mechanical behaviour; Section 9.4 presents simulations of the shell's behaviour during locomotion; Section 9.5 presents simulations of the shell's behaviour during a predator attack; and finally, Section 9.6 presents conclusions based on the results presented in this chapter.

9.1 Material models and parameters

The relevant material models and parameters used in this chapter are presented here. There are three materials of interest: cortical bone, cancellous bone and soft collagenous tissue. The keratin and skin components of the shell have been excluded in this chapter since they are expected to have little influence on the mechanical behaviour of the shell.

9.1.1 Cortical bone

The cortical bone behaviour is consistent with that in Section 8.1.1. However, a hyperelastic model is used since one requires access to the deformation gradient in the UVRAM subroutine to conduct RVE simulations (see Chapter 6 for details) and this is not provided for linear elastic models. The cortical bone density is assumed to be similar to that of bovine cortical bone; that is, 1.95×10^{-9} ton/mm^3 [113]. The bone is modelled as an isotropic and viscoelastic material. The long time-scale material response is governed by a neo-Hookean strain energy function; that is,

$$\Psi^{\infty} = \bar{\Psi}^{\infty} + \Psi^{\infty}_{vol}\,, \qquad \bar{\Psi}^{\infty} = G\left[\bar{I}_1 - 3\right]\,, \qquad \Psi^{\infty}_{vol} = \frac{1}{D}\left[J^2 + \frac{1}{J^2} - 2\right]\,, \tag{9.1}$$

where G and D are material parameters. The viscous response is governed by the model presented in Section 4.3.2 with two Maxwell branches. The resulting material model is implemented in Abaqus/Standard through a UMAT (see Sections 4.1.3 and 4.3.2).

The values of G and D are determined so that the long time-scale Young's modulus and Poisson's ratio are 12 000 MPa and 0.25, respectively; these are, the Young's modulus and Poisson's ratio of turtle cortical bone [30]. The viscous material parameters are determined by fitting the model to the same scaled bovine test data as in Section 8.1.1 [114]. In this case, the analytical solution for uniaxial loading of the model is not determined. Instead, the implemented material model is used along with the procedures presented in Sections 4.4.1 and 4.4.5 to determine the stress response.

The material parameters for the fitted model are presented in Table 9.1. Additionally, the scaled data, fitted material model and the response of the model implemented in Abaqus/Standard are shown in Figure 9.1. It is clear that the Abaqus simulation matches the solution determined via the procedures outlined in Sections 4.4.1 and 4.4.5. Additionally, the model gives a sufficiently close fit to the data.

Table 9.1: Cortical bone material parameters

ρ (ton/mm^3) [113]	G (MPa)	D (MPa^{-1})	β_1 (s)	β_2 (s)	τ_1 (ms)	τ_2 (μs)
1.95×10^{-9}	2893	0.5185×10^{-3}	0.2795	2.256	133.0	10.03

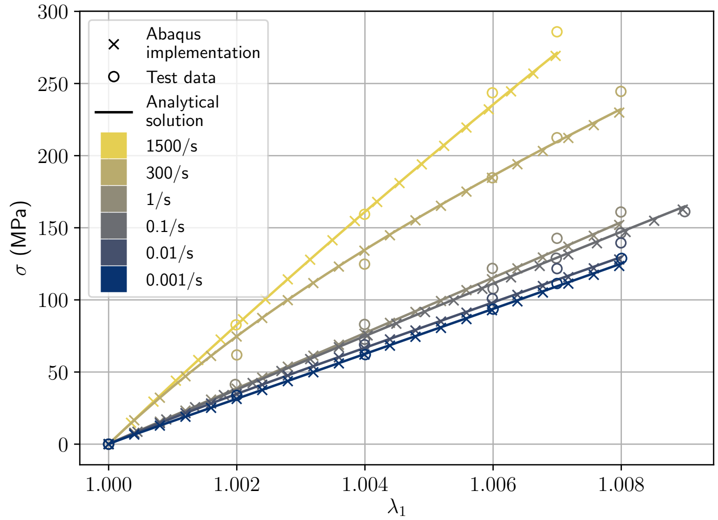

Figure 9.1: Uniaxial loading material behaviour for cortical bone at different strain rates. The model provides a close match to the data. Additionally, the Abaqus implementation of the model matches the analytical solution.

9.1.2 Cancellous bone

Turtle cancellous bone is assumed to have a density similar to human cancellous bone; that is, 0.6×10^{-9} ton/mm^3 [122]. The cancellous bone is modelled using the same material model as the cortical bone. However, only one Maxwell branch is used for the viscous material behaviour. The material parameters G and D are set so that the long time-scale Young's modulus and Poisson's ratio are 282 MPa and 0.25, respectively; these are, the Young's modulus [33] and Poisson's ratio [30] of turtle cancellous bone.

The viscous parameters are determined by fitting the model to uniaxial compression data taken from [122]. The data is scaled so that the long time-scale Young's modulus is equal to that of turtle cancellous bone. The resulting fit is displayed in Figure 9.2 along with an equivalent simulation in Abaqus. Additionally, the material parameters are presented in Table 9.2. It is apparent that the model provides a sufficiently close fit to the data, and the Abaqus simulation matches the analytical solution.

Table 9.2: Cancellous bone material parameters

ρ (ton/mm^3) [122]	G (MPa)	D (MPa^{-1})	β (s)	τ (s)
0.6×10^{-9}	56.4	4.812×10^{-3}	7.96214	2.3909e-06

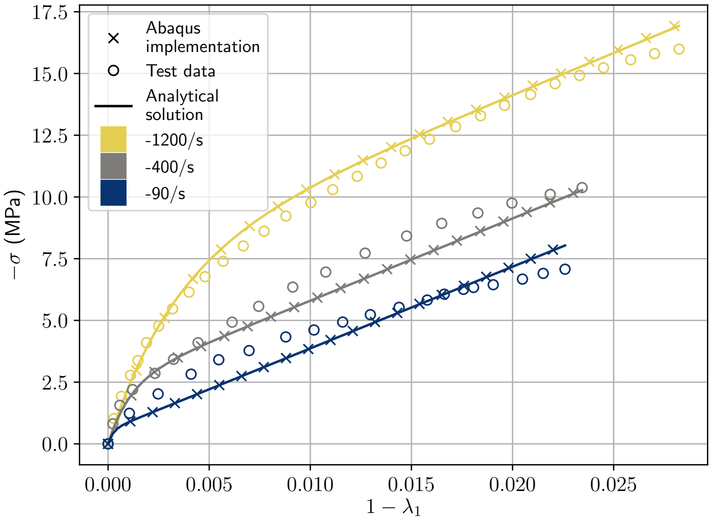

Figure 9.2: Uniaxial compression material behaviour for cancellous bone at different strain rates. The model provides a sufficient match to the data. Additionally, the ABAQUS implementation of the model matches the analytical solution.

9.1.3 Suture

The model for the suture and its material parameters are the same as in Section 8.1.3. The material parameters and biaxial loading behaviour are presented again in Table 9.3 and Figure 9.3 for convenience.

Table 9.3: Soft tissue material parameters

ρ (ton/mm^3) [117]	G (MPa)	D (MPa^{-1})	k_1 (MPa)	k_2	κ	β_1 (s)	τ (s)
1.25×10^{-9}	89.66	1×10^{-6}	10.94	74.24	1/3	1.60	0.5384

9.2 Geometric models

Two geometric models used in this chapter: one for shell-scale simulations and the other for the suture-scale (RVE) simulations. These are outlined here.

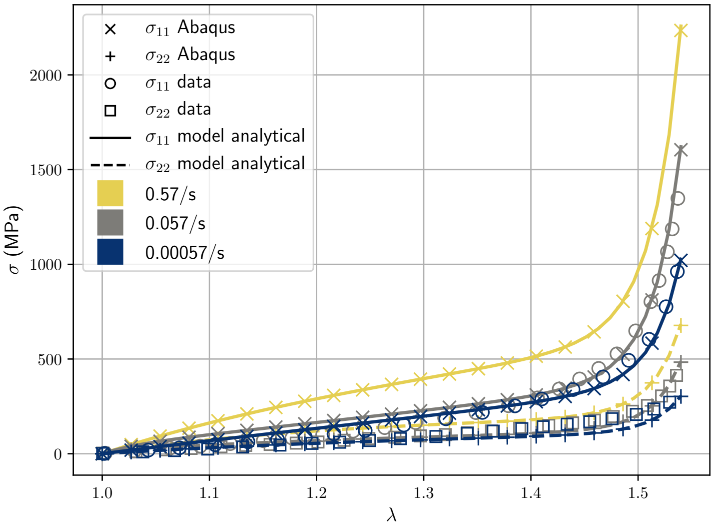

Figure 9.3: Biaxial loading material behaviour for soft tissue at different strain rates. It is clear that the analytical solution of the fitted model gives a sufficiently good fit to the data. Additionally, the ABAQUS implementation of the model matches the analytical solution.

9.2.1 Shell-scale

Due to symmetry, only a quarter of the carapace is modelled. This model is presented in Figure 9.4. The shell consists of several bone plates (illustrated in yellow and green) joined by suture interfaces (illustrated in blue). The model consists of a spinal column aligned with the x-direction and several ribs aligned with the z direction, in line with the image of a turtle shell skeleton in Figure 2.1 (a). Each bone plate has a cancellous bone core of 1 mm thickness (illustrated in white) and cortical bone plating on the dorsal and ventral surfaces

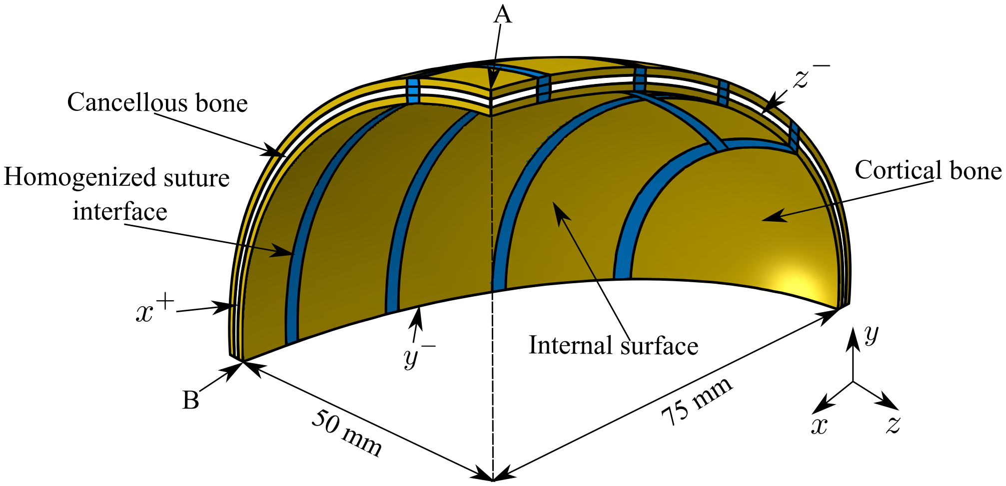

Figure 9.4: Geometric model of a turtle shell annotated with dimensions and materials regions.

of 1 mm thickness (illustrated in yellow) as per measurements of a real turtle displayed in Figure 2.1 (c). As the shell's overall length and width are 150 mm and 100 mm, respectively, the quarter of the shell modelled here has an overall length and width of 75 mm and 50 mm, respectively.

The constitutive relation for the suture interface region is determined by the RVE of the suture interface (see section 9.2.2). Since the suture is geometrically anisotropic, one must define its preferred direction in both the macro- and microscale geometries. The preferred direction of the suture interface is defined to be in the direction of the protrusions; that is, pointing transversely across the suture interface. This is illustrated on the suture interface region of the shell in Figure 9.5.

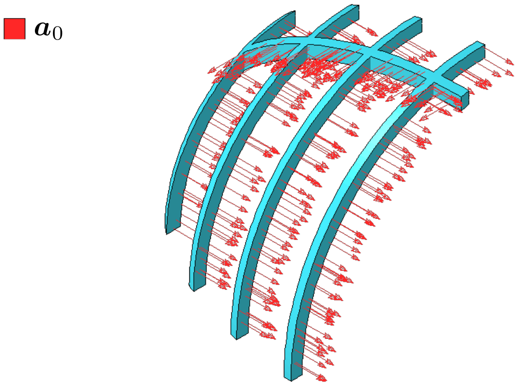

Figure 9.5: Vector field of the preferred direction in the suture interface in the initial configuration.

9.2.2 Suture-scale

Since the suture has a periodic structure, the RVE is made up of a single protrusion, as displayed in Figure 9.6. The RVE consists of two regions of cortical bone which are separated by a soft collagenous suture. From the boundary of the RVE it may seem that the suture is not centred in the RVE. However, when considering the internal geometry of the suture (see Figure 8.5 (c)), it is clear that the suture is in the centre of the RVE. The preferred direction $\boldsymbol{a}_0$ is chosen to be in the direction of the bony protrusion. The RVE's mechanical behaviour is replicated by the orthotropic material model in equation (4.92) and so one is required to define a second preferred direction $\boldsymbol{b}_0$. This is chosen to be perpendicular to $\boldsymbol{a}_0$ as illustrated in Figure 9.6. However, the behaviour of the RVE is very close to transverse isotropy due to the near rotational symmetry about the $\boldsymbol{x}_1$ axis in Figure 9.6, and so the direction of $\boldsymbol{b}_0$ is inconsequential. Hence, in the shell-scale geometry $\boldsymbol{b}_0$ is simply set to $\boldsymbol{b}_0 = \begin{bmatrix} 0 & 1 & 0 \end{bmatrix}^T$.

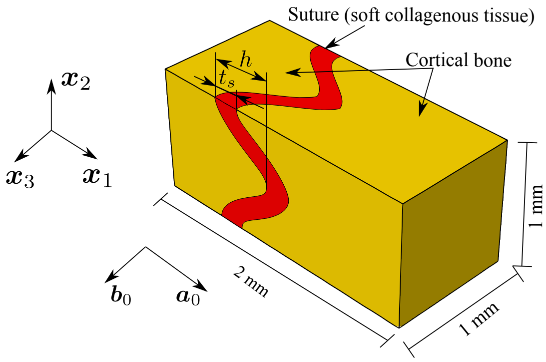

Figure 9.6: Geometry used for an RVE representing the suture interface.

The geometry of the suture depends on two parameters: protrusion height h and suture thickness t_s. To determine the effect of the suture geometry, several RVEs are generated with varying values for their geometric parameters. In particular, four values of protrusion height varying from 0-0.9 mm and four values of suture thickness varying from 0.15-0.3 mm are used, resulting in sixteen RVEs, as displayed in Figure 9.7.

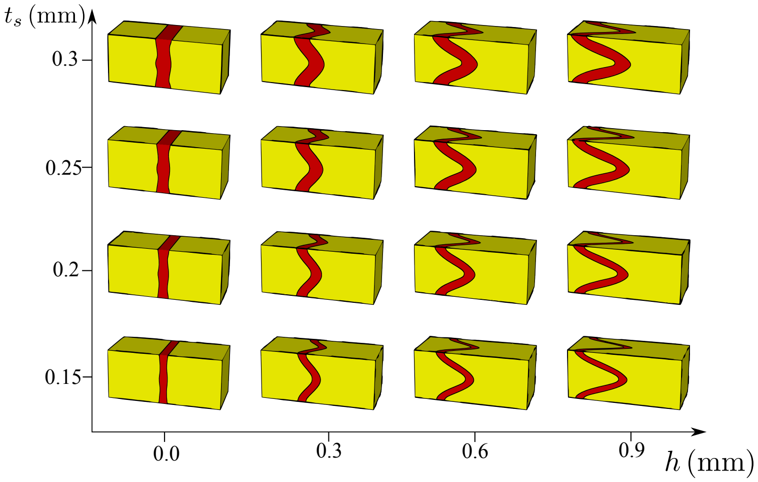

Figure 9.7: Set of RVE geometries used to elucidate the effect of suture geometry on the behaviour of the suture interface.

9.3 RVE experiments

To elucidate the mechanical behaviour of the suture interface, several loading paths are applied to each RVE. These loading paths are:

- Uniaxial loading as described in Section 4.4.1 in each direction;
- Shear loading as described in Section 4.4.4 applied in each shear direction;

- Pressure loading as described in Section 4.4.3.

Additionally, to determine the viscous behaviour of the RVE, each loading path is applied at three different loading rates: quasistatic, 7 /s and 99700 /s. Here, the loading rate refers to the rate of change of the entry in the deformation gradient, which is controlled during the loading path (see Section 6.2.3 for details). The choice of these loading rates is motivated by the relaxation times of the cortical bone presented in Table 9.1:

$$\tau_1^{-1} \approx 7\,/\mathrm{s}\,, \qquad \tau_2^{-1} \approx 99700\,/\mathrm{s}\,. \tag{9.2}$$

A separate loading rate determined by the relaxation time of the suture is not applied since it is in the same order of magnitude as τ_1 for cortical bone.

The material behaviour of the suture interface is then approximated by a surrogate model as per Section 6.2.3. The long time-scale material response is governed by the strain energy function

$$\begin{aligned}
\Psi^\infty &= \sum_{j=1}^{7} \psi_j\,, & \psi_1 &= \sum_{i=1}^{n} \kappa_{(1)i} I_1^i\,,\\
\psi_2 &= \sum_{i=1}^{n} \kappa_{(2)i} I_2^i\,, & \psi_3 &= \kappa_{(3)0} I_3^{-1} + \sum_{i=1}^{n} \kappa_{(3)i} \left[I_3 + I_3^{-1} - 2\right]^i\,,\\
\psi_4 &= \sum_{i=1}^{n} \kappa_{(4)i} I_4^i\,, & \psi_5 &= \sum_{i=1}^{n} \kappa_{(5)i} \left[I_5 - I_4 I_1 + I_2\right]^i\,,\\
\psi_6 &= \sum_{i=1}^{n} \kappa_{(6)i} I_6^i\,, & \psi_7 &= \sum_{i=1}^{n} \kappa_{(7)i} \left[I_7 - I_6 I_1 + I_2\right]^i\,.
\end{aligned} \tag{9.3}$$

Here, $\kappa_{(i)j}, \kappa_{(3)0} \geq 0\,,\ i = 1, ..., 7\,,\ j = 1, ..., n$ are material parameters. Details of this hyperelastic model are given in Section 4.1.1. The long time-scale second Piola-Kirchhoff stress is then given by

$$\boldsymbol{S}^\infty = 2\frac{\partial \Psi^\infty}{\partial \boldsymbol{C}}\,. \tag{9.4}$$

The total second Piola-Kirchhoff stress of the surrogate model is given by a superposition of the long time-scale stress and a viscous stress $\boldsymbol{S}^v$; that is,

$$\boldsymbol{S}_S = \boldsymbol{S}^\infty + \boldsymbol{S}^v\,. \tag{9.5}$$

Here the viscous stress is given by

$$\begin{aligned}
\boldsymbol{S}^v &= \sum_{\alpha=1}^{N_m} \int_0^t \beta_\alpha \exp\left(-\frac{t-s}{\tau_\alpha}\right) \dot{\bar{\boldsymbol{S}}}^\infty \,\mathrm{d}s\,,\\
\bar{\boldsymbol{S}}^\infty &= \boldsymbol{S}^\infty - \frac{1}{3}\left[\boldsymbol{S}^\infty : \boldsymbol{C}\right] \boldsymbol{C}^{-1}\,,
\end{aligned} \tag{9.6}$$

where β_α and τ_α are material parameters. The viscous material behaviour is modelled with two Maxwell branches; that is, $N_m = 2$. The Cauchy stress for the surrogate model can then be obtained by using the usual push-forward operation; that is,

$$\boldsymbol{\sigma}_S = J^{-1} \boldsymbol{F} \boldsymbol{S}_S \boldsymbol{F}^T \tag{9.7}$$

This constitutive model is implemented in a UMAT in a discretized sense; that is, discretized in time (see Section 4.3.2). Of course, the actual macroscale Cauchy stress defined by the RVE is given by

$$\boldsymbol{\sigma}_M = J^{-1} \left\langle \boldsymbol{P}_m \right\rangle_{\Omega_m} \boldsymbol{F}^T \,, \tag{9.8}$$

The material parameters for the surrogate model are obtained by fitting the model to the results of the RVE experiments.

9.3.1 Single test set

The results for the loading paths applied to a single RVE with the geometric parameters $h = 0.6\,\mathrm{mm}$ and $t_s = 0.25\,\mathrm{mm}$ are presented here. The results for the three uniaxial tests, six shear tests and pressure test are displayed in Figures 9.8–9.10, respectively. The figures also include the results of the surrogate model which is fitted to the test data. The RVE behaves close to linearly in all loading cases. Comparison of the quasistatic uniaxial loading paths shows that the RVE is approximately 65 % stiffer in the first direction than in the second and third directions. Furthermore, it is approximately 2 % stiffer in the third direction than the second direction. Hence, the RVE is approximately transversely isotropic. The transverse

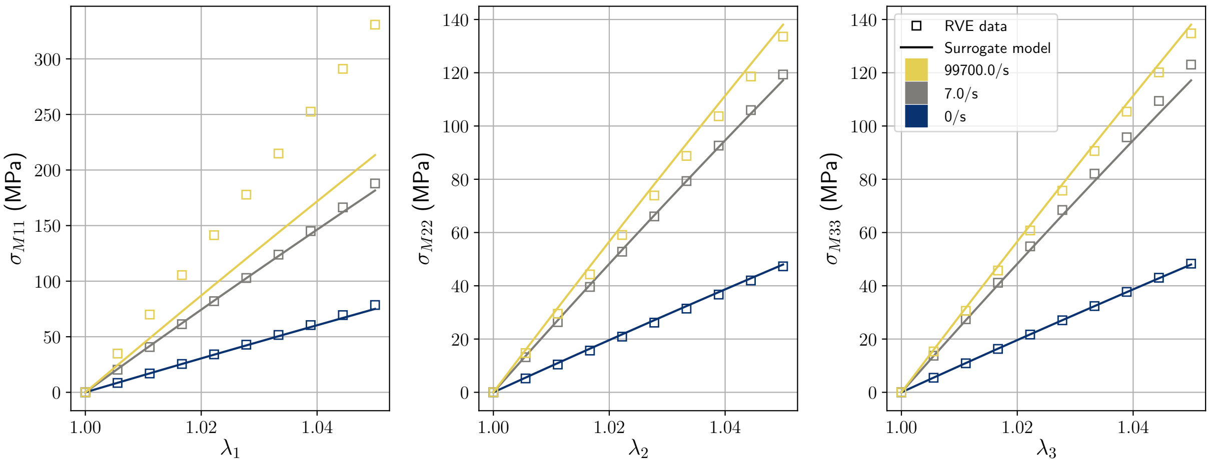

Figure 9.8: Uniaxial loading applied to an RVE with geometric parameters $h = 0.6\,\mathrm{mm}$ and $t_s = 0.25\,\mathrm{mm}$ in three different basis directions.

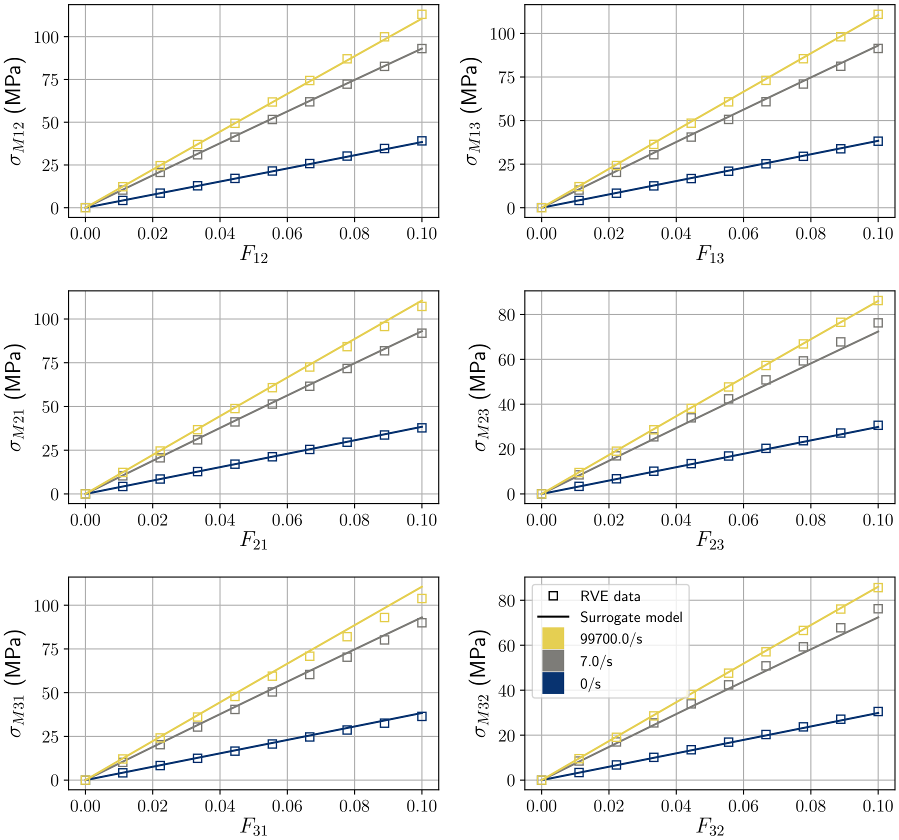

Figure 9.9: Shear loading applied to an RVE with geometric parameters $h = 0.6\,\mathrm{mm}$ and $t_s = 0.25\,\mathrm{mm}$.

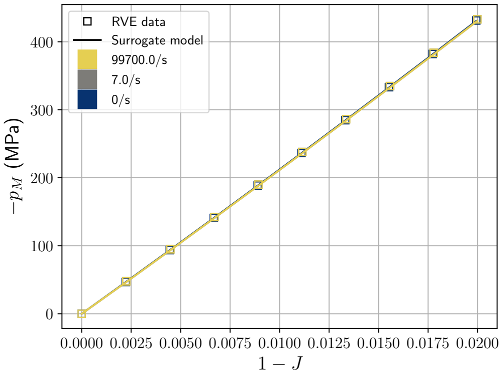

Figure 9.10: Pressure loading applied to an RVE with geometric parameters $h = 0.6\,\mathrm{mm}$ and $t_s = 0.25\,\mathrm{mm}$.

isotropy is evident in the shear behaviour as well; the results in the 1-2 and 1-3 directions are similar and stiffer than those in the 2-3 direction.

The viscous behaviour is significant in the uniaxial and shear tests. However, it is negligible in the pressure test. This is unsurprising as the viscoelastic behaviour of the bone and suture is based on shear deformation, which is small during pressure loading.

The surrogate material model can replicate the RVE's behaviour sufficiently well in all cases apart from the uniaxial loading in the first direction at a rate of 99700 /s. This is likely due to the fact that the form of the viscous contribution to the stress is defined by the long time-scale stress. Hence, at a loading rate of 99700 /s, the surrogate model is approximately 65 % stiffer in the first direction than in the other directions (the yellow line in Figure 9.8 (a) in comparison with Figures 9.8 (b) and (c)), which is in accordance with the long time-scale behaviour. However, the RVE does not behave this way; at a loading rate of 99700 /s the RVE is approximately 145 % stiffer in the first direction (the yellow squares in Figure 9.8 (a) in comparison with Figures 9.8 (b) and (c)). This shortcoming could potentially be remedied by increasing the flexibility of the viscous component of the surrogate model. In particular, it seems likely that allowing the viscous behaviour to be defined independently of the long time-scale behaviour could resolve this issue.

9.3.2 Effect of geometry

To determine how the geometry of the suture affects its mechanical behaviour, the stress at the end of each loading path is plotted as a function of protrusion height and suture thickness. The stresses at the end of the uniaxial loading in the first, second and third directions are presented in Figures 9.11 (a), (b), and (c), respectively. The stress in the first direction is consistently greater than in the second and third directions. Furthermore, the second and third directions have a similar stress response for all the geometries, again showing that the RVE behaviour is close to transverse isotropy. It is apparent that the viscous behaviour has a significant effect, approximately doubling the RVE's stiffness. In the case of loading in the first direction, an increase in suture thickness typically decreases the stiffness of the RVE. However, this is not the case when $h < 0.4\,\mathrm{mm}$ and $t_s > 0.25\,\mathrm{mm}$. Additionally, an increase in h typically increases the stiffness. In the case of uniaxial loading in the second and third directions, the stiffness also increases with an increase in h and decrease in t_s.

The stress at the end of the shear test is presented in Figures 9.12 (a), (b) and (c) for components 2-3, 1-2 and 1-3, respectively. The transverse isotropy is also apparent in this case, as the behaviour for the 1-2 and 1-3 components is similar and contrasts that of the 2-3 component. The response for the 2-3 shear component is affected by h and t_s similarly to the uniaxial loading responses in the second and third direction – it increases with an increase in h and a decrease in t_s. Additionally, the stress response is more sensitive to h than t_s. The 1-2 and 2-3 components have a sinusoidal-like response to an increase in h and, similarly to the case of uniaxial loading in the first direction, they have a parabolic-like

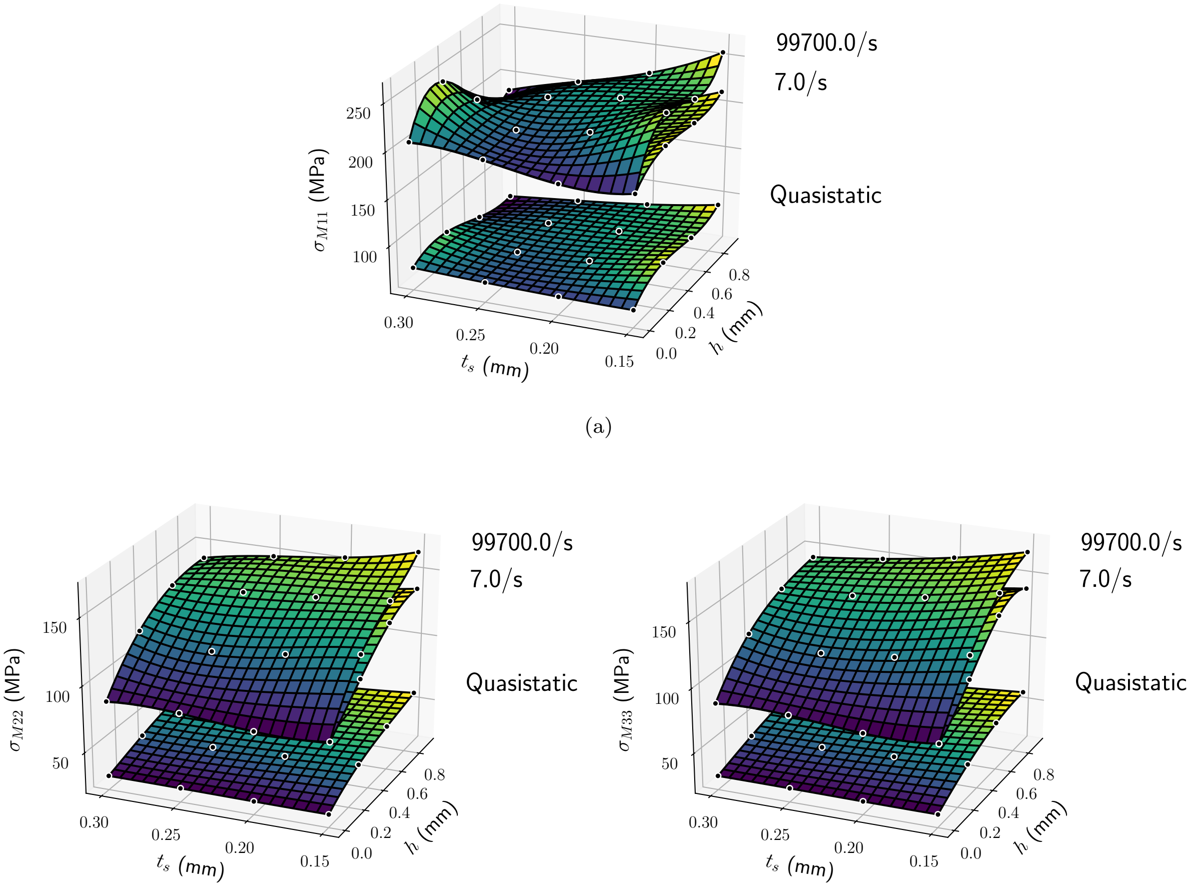

(a)

(b) (c)

Figure 9.11: Stress at $\lambda = 1.05$ during a uniaxial loading path applied at different strain rates as a function of h and t_s.

response to t_s when h is small and stiffen with a decrease in t_s for larger h.

The pressure at the end of each pressure loading path is displayed in Figure 9.13. The magnitude of pressure appears to increase significantly with an increase in h and slightly with an increase in t_s. This is likely due to the increase in volume of the near-incompressible suture. Additionally, the difference between the pressure response for different loading rates is insignificant. This is unsurprising as the viscoelasticity is based on shear deformation.

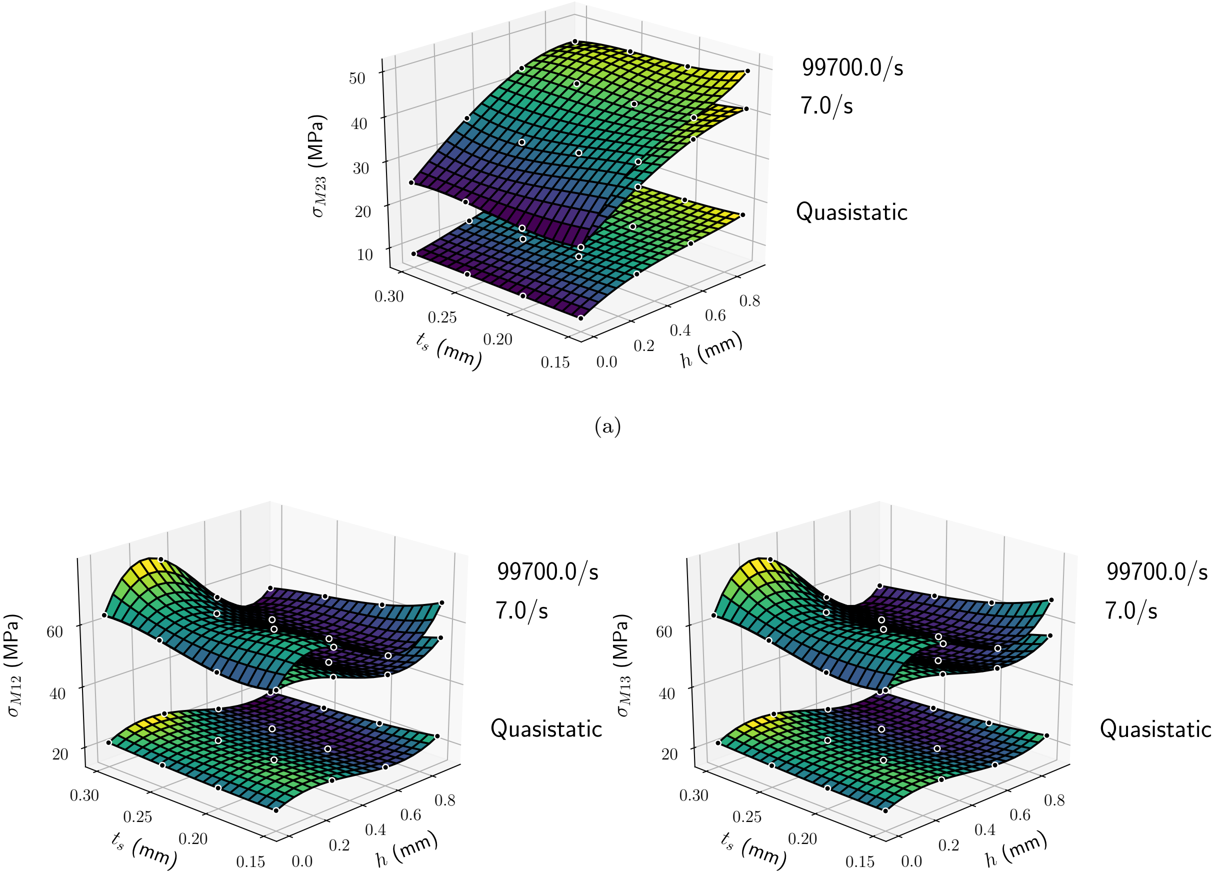

(a)

(b)

(c)

Figure 9.12: Stress component ij at $F_{ij} = 0.1$ during a shear loading path applied at different strain rates as a function of h and t_s.

9.4 Macroscale simulations: breathing and locomotion

Investigations into the restriction of the shell on the breathing and locomotion of the turtle are presented here. It is assumed that the mechanical behaviour of the shell during these two loading cases is similar. The loading is modelled by applying a pressure to the internal surface of the shell (see Figure 9.4). The loading is applied over a time of 2 seconds as this is the length of one inhalation for a turtle [118] and the maximum pressure applied is 5 kPa as this is the lung pressure of a human [119] which is expected to be in a similar range to a turtle. Hence, the boundary condition is described by

$$\bar{\boldsymbol{t}} = -p\boldsymbol{n}\,, \qquad p = \frac{5}{2}t\,\mathrm{kPa}\,. \tag{9.9}$$

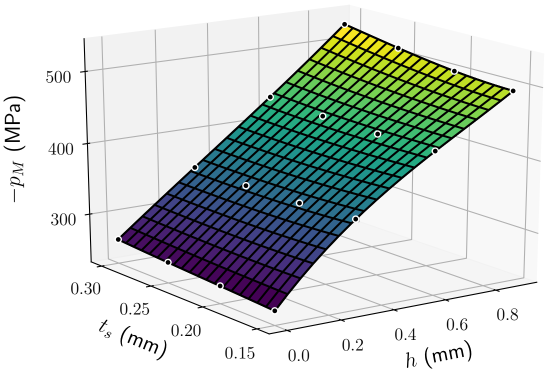

Figure 9.13: Pressure at $1 - J = 0.02$ during a pressure loading path applied at different strain rates as a function of h and t_s.

Additionally, the surfaces x^+, y^- and z^- (Figure 9.4) are prescribed roller boundary conditions. All other surfaces are traction free.

To elucidate the effect of sutures, a shell that contains sutures is compared to one that does not. The suture containing shell has geometric parameters of $h = 0.6\,\mathrm{mm}$ and $t_s = 0.25\,\mathrm{mm}$. Additionally, simulations are run for each suture geometry to elucidate its influence on the behaviour of the shell as a whole.

9.4.1 Comparing suture containing shell with suture excluding shell

Three metrics are used to evaluate the behaviour of the shell: maximum displacement in the shell, maximum strain energy and maximum non-equilibrium energy. The results of these three metrics are displayed in Table 9.4 for both the suture containing and suture excluding simulations. The maximum displacement in the suture containing shell is approximately

Table 9.4: Key metrics for comparison between suture containing ($h = 0.6\,\mathrm{mm}$ and $t_s = 0.25\,\mathrm{mm}$) and suture excluding shells during breathing and locomotion.

Shell type	Maximum displacement (μm)	Maximum strain energy (μJ)	Maximum non-equilibrium energy (μJ)
Suture containing	0.111	0.475	0.210
Suture excluding	0.248×10^{-6}	0.230×10^{-3}	0.140×10^{-9}

450×10^3 larger than that in the shell that does not contain sutures. This indicates that the sutures significantly increase the compliance of the shell. Naturally, due to the increase in deformation, the strain energy and non-equilibrium energy in the suture containing shell are far greater than the shell which does not contain sutures. However, comparison of the ratio of strain energy to non-equilibrium energy, approximately 2.3 and 1.6×10^6 for the suture containing and excluding shell, respectively, shows that the sutures make up for the vast majority of the shell's rate dependent behaviour.

9.4.2 Effect of suture geometry

To determine the effect of the suture geometry, three metrics are plotted as a function of suture thickness t_s and protrusion height h: displacement at point B (see Figure 9.4), strain energy, and non-equilibrium energy. These are plotted in Figures 9.14, 9.15 and 9.16, respectively.

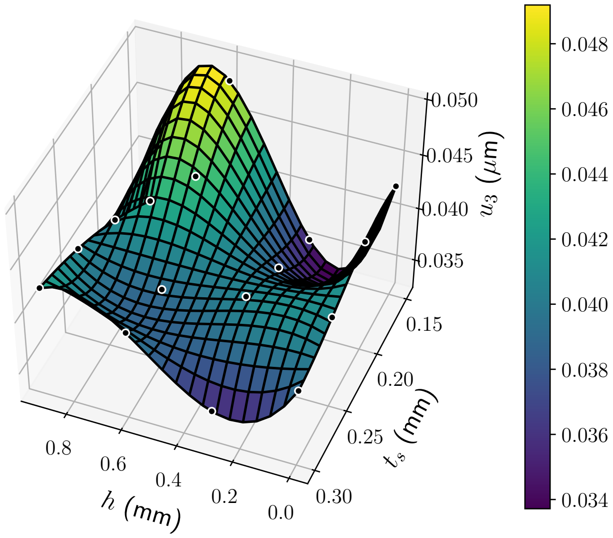

Figure 9.14: Displacement at point B (Figure 9.4) as a function of suture thickness t_s and protrusion height h.

9.4.3 Discussion

It is clear that the sutures significantly increase the compliance of the shell during breathing a locomotion. However, even though the maximum displacement in the shell is approximately 450×10^3 larger for a shell that contains sutures, it is still less that a micron. This is far smaller than the displacements of a turtle's muscles during locomotion, which is in the order

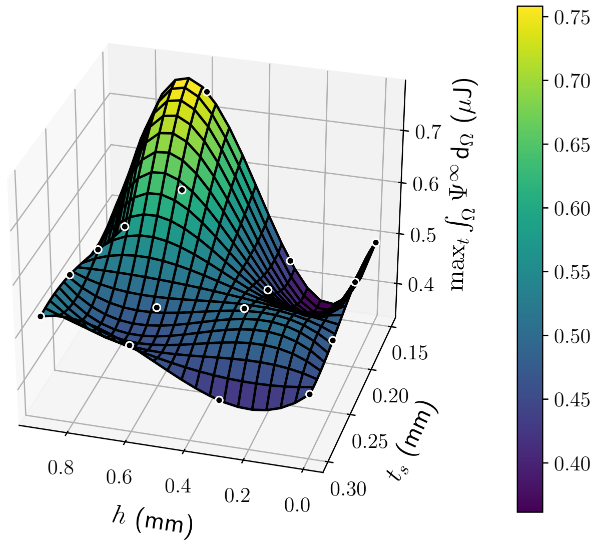

Figure 9.15: Maximum strain energy as a function of suture geometry.

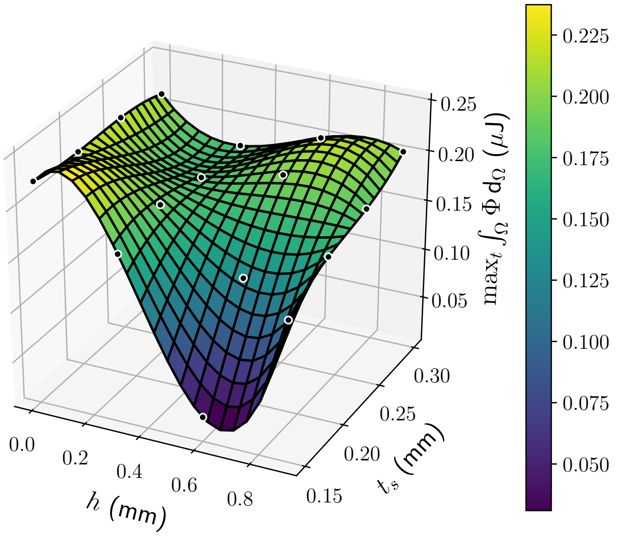

Figure 9.16: Maximum non-equilibrium energy as a function of suture geometry.

of centimetres. Hence, for all intents and purposes, the shell is rigid relative to the forces that a turtle applies to it whether it has sutures or not.

The suture geometry appears to have a significant effect on the behaviour as values range by about 20%, 100% and 400% in the distributions of displacement, strain energy and non-equilibrium energy (Figures 9.14, 9.15 and 9.16), respectively. Additionally, these values are all clearly related, as their shapes are all similar. However, there does not seem to be a sensible reason as to why the shapes of the surfaces are the way they are. This is somewhat inconsequential though since, as mentioned earlier, the shell is effectively rigid relative to a turtle whether it contains sutures or not.

9.5 Macroscale simulations: predator attack

Investigation into the effect of sutures on the performance of the shell as a protective structure during a predator attack are presented here. A point mass of 3 kg is added to the shell at point A (see figure 9.4) representing the mass of the predator's body connected to the tooth or claw which makes contact with the shell. The point mass is assigned an initial velocity of

$$\boldsymbol{v}_i = \begin{bmatrix} 0 & -2 & 0 \end{bmatrix}^T \ \mathrm{m/s}\,. \tag{9.10}$$

Additionally, a constant force of

$$\boldsymbol{f}_i = \begin{bmatrix} 0 & -442 & 0 \end{bmatrix}^T \ \mathrm{N} \tag{9.11}$$

is applied to the point mass, representing the biting strength of the predator. The surfaces x^+, y^-, and z^- are prescribed roller boundary conditions. All other surfaces are traction free. To elucidate the influence of the suture, a shell that contains sutures is compared to one that does not. The suture containing shell has geometric parameters of $h = 0.6\,\mathrm{mm}$ and $t_s = 0.25\,\mathrm{mm}$. Additionally, the effect of the suture geometry is investigated by repeating the simulations while varying suture geometry.

9.5.1 Comparing suture containing shell with suture excluding shell

Four metrics are used to determine the performance of the shell as a protective structure: the maximum displacement, maximum strain energy, maximum non-equilibrium energy and maximum strain energy density. These values are displayed in Table 9.5 for both shells. The maximum displacement in the suture containing shell is approximately 250 times greater

Table 9.5: Key metrics for comparison of suture containing ($h = 0.6\,\mathrm{mm}$ and $t_s = 0.25\,\mathrm{mm}$) and suture excluding shells during predator attack.

Shell type	Max. displacement (μm)	Max. strain energy (J)	Max. non-equilibrium energy (J)	Max. strain energy density (mJ/mm^3)
Suture containing	837	2.63	3.79	45.0
Suture excluding	3.30	3.08	3.15	1380

than in a shell without sutures. Again, this shows that sutures significantly increase the compliance of the shell. By inspecting the displacement field for the shell with sutures and shell without sutures, show in Figures 9.17 (a) and (b), respectively, one can interpret the nature of the deformation. In a shell with sutures, the majority of the deformation occurs in the suture interface regions and the bone plate which makes contact with the tooth of the predator displaces as a whole. The shell without sutures displaces much less in comparison.

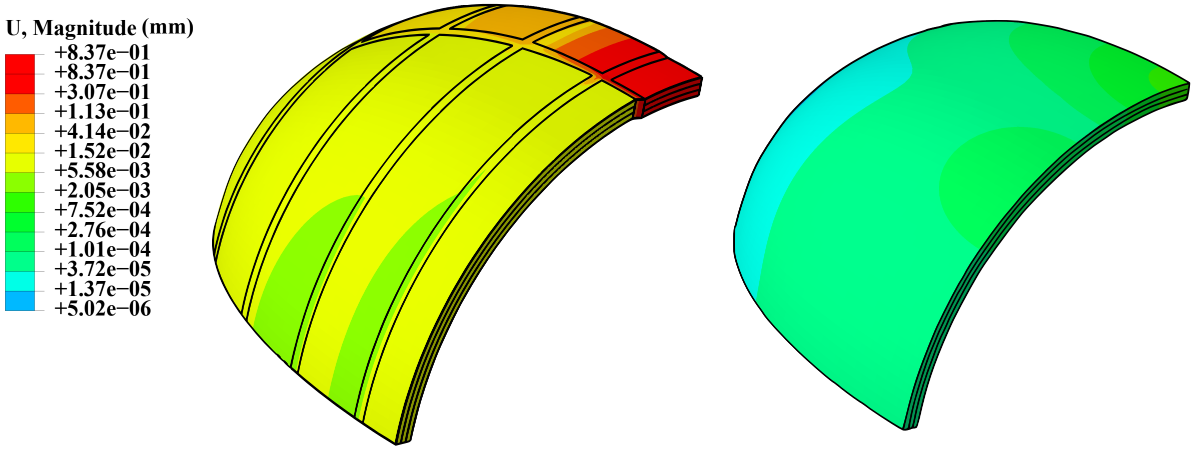

(a) (b)

Figure 9.17: Comparison of displacement field between (a) a shell which contains sutures and (b) one that does not. Note that the contours are applied on a log scale due to the large difference in magnitudes.

The maximum strain energy in a shell without sutures is about 17 % greater than the shell containing sutures. However, the maximum non-equilibrium energy is 20 % in the shell with sutures in comparison to a shell which does not contain sutures, showing how the sutures serve to dissipate energy.

It is apparent that a shell with sutures is much more resistant to failure, as the maximum strain energy density is approximately 31 times less than a shell without sutures. Inspecting the strain energy density contour plots for a shell with and without sutures, displayed in Figures 9.18 (a) and (b), respectively, provides insight as to why this is the case. The suture regions contain higher levels of strain energy density than in the bone plates. Hence, the sutures are able to distribute strain energy among the different bone plates even for a highly localised attack. On the other hand, the strain energy density in the shell without sutures is focused around the point of contact leading to a large maximum strain energy density and, hence, high likelihood of fracture. The higher levels of strain energy density in the sutures (Figures 9.18 (a)) is comparable to results of physical experiments on goat (*capra hircus*) cranial bone [123] where impact loading for specimens that contained sutures was compared with specimens that did not.

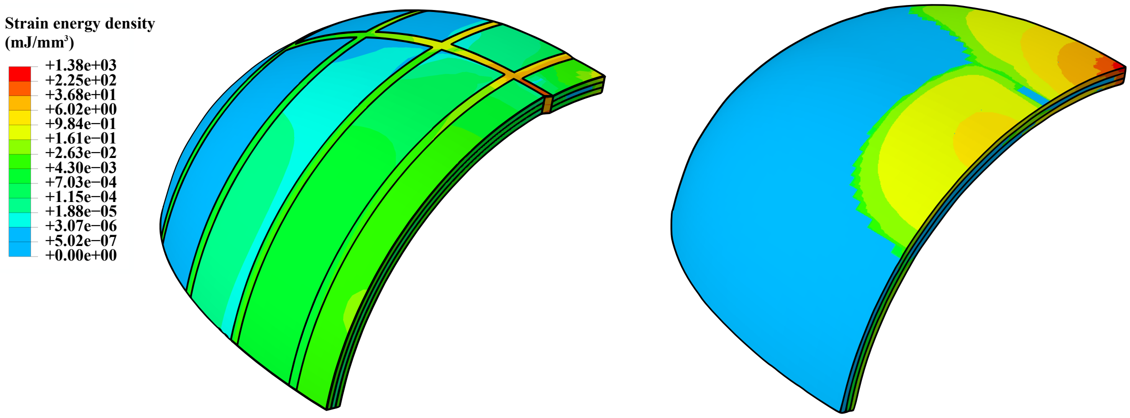

(a) (b)

Figure 9.18: Comparison of strain energy density field between (a) a shell that contains sutures and (b) one that does not.

9.5.2 Effect of suture geometry

To determine the effect of suture geometry, the attack simulation is run for the set of geometries displayed in Figure 9.7. The results for the maximum strain energy, maximum strain energy density, maximum non-equilibrium energy and vertical displacement at the point of contact are displayed in Figures 9.19 (a), (b), (c), and (d), respectively. Each of these results have a range of in the order of 10%. Hence, the suture geometry has a moderate influence on the mechanical behaviour of the shell as a whole during a predator attack.

The energy results (Figures 9.19 (a), (b) and (c)) do not seem to follow a discernible pattern. This may be because the strain energy function of the suture interface is not fitted to the strain energy resulting from the RVEs, but rather the stress determined by the strain energy is fitted to the RVEs' stress response. Hence, it may be that the strain energy function of the suture interface does not accurately reflect the strain energy in the RVE.

The magnitude of displacement increases with an increase in h and t_s. This is consistent with the results in Chapters 7 and 8 whereby an increase in the volume of the suture increases the compliance of the suture interface. However, the effect of interlocking, where the increase in compliance due to increasing h plateaus after h is sufficiently large, is not observed.

9.5.3 Discussion

The presence of sutures increases the maximum displacement of the shell from 3.30 μm to 837 μm. However, 837 μm is still small in comparison to the motion of the turtle's organs during everyday functioning. Hence, the increase in compliance is not a significant detraction from the performance of the shell as a protective structure.

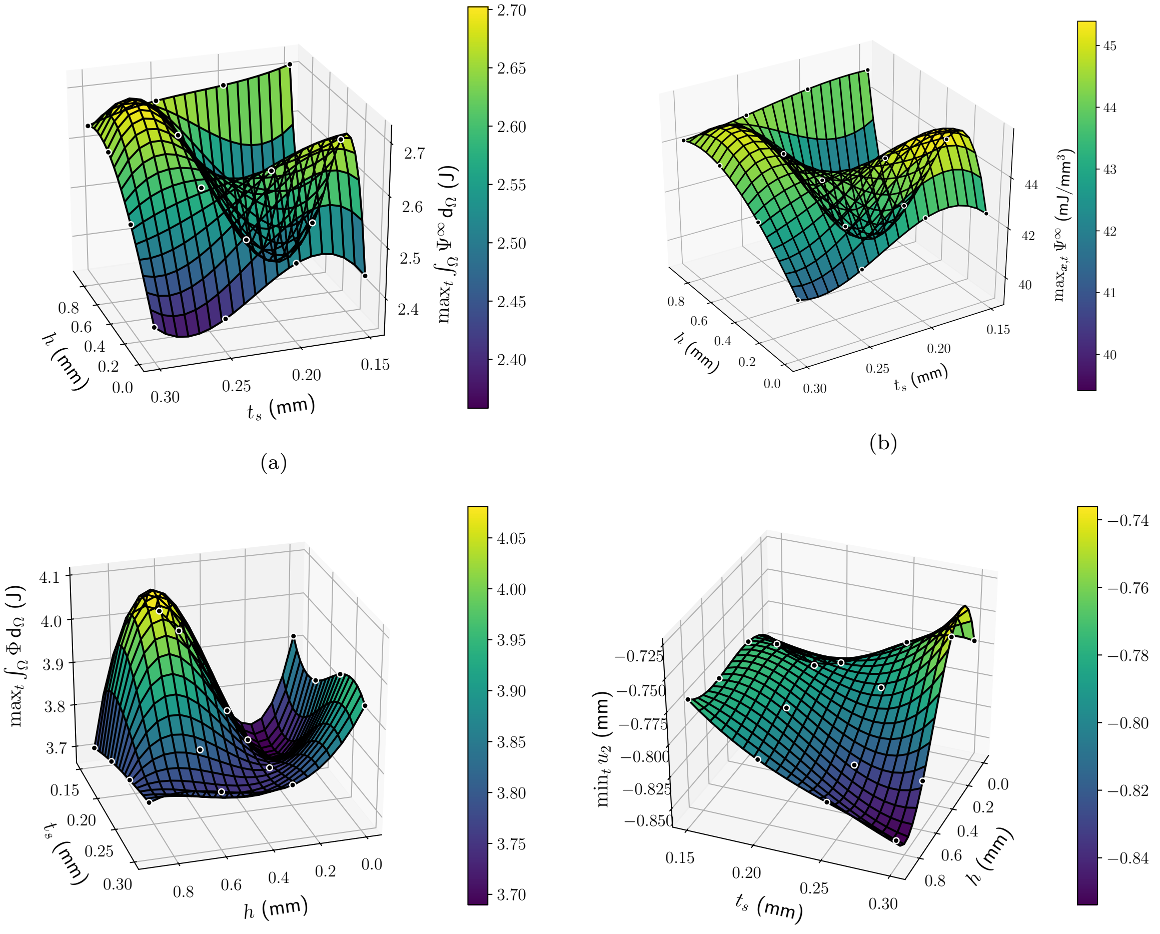

(a) (b)

(c) (d)

Figure 9.19: The effect of suture geometry on the behaviour of the shell: (a) maximum strain energy, (b) maximum strain energy density, (c) maximum non-equilibrium energy, and (d) minimum displacement at the point of contact.

However, the presence of the sutures decreases the maximum strain energy density in the shell by approximately 31 times. This is attributed to the dispersion of the strain energy caused by the sutures, which is evident when comparing Figures 9.18 (a) and (b). Hence, a shell that contains sutures is far more resistant to failure than one that does not.

Furthermore, it is evident that the sutures improve the dissipation of energy, as shells that contain sutures contain approximately 20% higher non-equilibrium energy during predator attacks than shells without sutures.

The suture geometry has some influence on the energetic behaviour of the shell, but this is limited to a range of approximately 10%. Moreover, increasing h and t_s increases the compliance of the shell, as is evident from Figure 9.19 (d). This is likely due to the corresponding increase in suture volume, and is in agreement with the results in Chapters

7 and 8. As the suture geometry does not seem to significantly improve or worsen the mechanical behaviour of the shell as a whole, the geometry may be governed by the likelihood of local fracture in the bony protrusions, as investigated in Chapters 7 and 8.

9.6 Conclusions

The presence of sutures increases the compliance of the shell, both in the case of locomotion and predator attack. However, in the case of locomotion, the shell is still stiff enough to be considered rigid even with sutures. In the case of a predator attack, a shell with sutures is still stiff enough that the displacements incurred are not problematic for the internal organs. So, in both cases, the increase in compliance is inconsequential.

However, during a predator attack the sutures disperse and dissipate energy which ultimately reduces the maximum strain energy density (and likelihood of bone fracture) by 31 times.

The suture geometry has a fairly small influence on the mechanical behaviour of the shell as a whole. Hence, the geometry may be driven by the likelihood of fracture in the bony protrusions rather than to improve the mechanical behaviour of the shell as a whole.

Chapter 10

Conclusion

Recall the research questions that are posed in the introduction:

1. Do sutures improve the protective performance of the structures in which they reside?
2. If the answer to the above question is the affirmative, what are the mechanisms by which this occurs?

The results presented in the previous chapters provide the following brief answers to these questions:

1. Yes, sutures improve the protective performance of the structures in which they reside. This is most clearly shown by the fact that, during a predator attack, a turtle shell that contains sutures experiences a maximum strain energy density of 31 times less than a shell without sutures. Hence, a shell with sutures is far less likely to experience material failure.
2. Some mechanisms by which protective performance is improved are as follows:
   (a) During a predator attack, sutures cause dispersion of deformation, and hence energy, throughout the shell, whereas for shells without sutures deformation is concentrated at the site of the attack;
   (b) Sutures increase the compliance of structures, but not so much as to allow for injury of the internal organs which the structures ought to protect;
   (c) Sutures dissipate energy due to their viscoelastic material behaviour.

These are the take-home messages of this thesis.

In addition to the research questions, two objectives are presented in the introduction:

1. Develop a framework for modelling the influence of sutures on the mechanical behaviour of structures in which they reside that could be used to aid the design of engineered structures that include sutures;
2. Determine the structure–function relationship of sutures.

Briefly, these objectives were achieved as follows:

1. The influence of sutures on the structures in which they reside was modelled using a multiscale modelling framework. A surrogate modelling approach was developed to circumvent the large computational expense of concurrent FE^2;
2. The structure–function relationship of sutures was determined through computational parametric studies whereby the suture thickness t_s and bony protrusion height h were varied.

The results of this work also allow for more detailed conclusions than those presented above. The results are compartmentalised into three chapters: quasistatic suture scale simulations, dynamic suture scale simulations, and multiscale simulations. Each chapter yields valuable conclusions, which are provided in the following sections of this chapter. The final section of this chapter presents recommendations for extensions to this work.

10.1 Quasistatic suture scale simulations

Quasistatic simulations are presented in Chapter 7. There, a computational model of a suture interface is validated by comparing the results of a bending test with that of a physical experiment. Additionally, the effect of the presence of sutures and their structure-function relationship is investigated.

10.1.1 Validation

The validation simulation replicated qualitative and quantitative aspects of the physical experiment. The findings are summarised as follows:

- The largest stresses in the simulation occurred in the regions where fracture occurred in the physical experiment;
- The maximum principal stress is aligned normal to the fracture planes in the lower portion of the model, as one would expect. However, this is not observed in the upper portion of the model;

- The load deformation curve replicates that of the physical test, not accounting for the failure of the trabeculae in the cancellous bone region.

From these findings, it is clear that the model sufficiently replicates the behaviour of the suture region, and so it is valid to use it in the computational investigations in the following sections.

10.1.2 Effect of sutures

To determine the effect of sutures, a model that contains a suture is compared to one without. The loading applied to the model replicates that applied during a predator attack. However, loading is modelled quasistatically as a simplification. Dynamic loading is considered in Chapter 8. The simulations yield the following insights:

- Inclusion of a suture increased the strain energy, and thus the work required for the predator to deform the shell, by approximately 12%;
- The suture decreased the maximum strain energy density in the bone, and thus the likelihood of fracture, by approximately 5%;
- The combination of increased strain energy with a decreased maximum strain energy density is due to a larger dispersion of strain energy density;
- The effect of the fibre direction on the mechanical behaviour of the interface is insignificant. This suggests a one-way relationship between loading and fibre direction; that is, the prevailing loading of the suture determines the fibre direction in the suture, but the fibre direction does not significantly affect the mechanical behaviour of the region.

Hence, the presence of a suture decreases the likelihood of bone fracture and increases the strain energy absorption in the suture interface region by distributing the strain energy.

10.1.3 Effect of suture geometry

The structure-function relationship of the suture is determined using a parametric study wherein the bony protrusion pointiness a, suture thickness t_s and bony protrusion height h are varied. For each geometric model the same loading conditions, that is of a predator attack, are applied. The following insights are deduced:

- Increasing bony protrusion height h and suture thickness t_s increases the compliance of the region;

- There is an interlocking effect whereby the increase in compliance plateaus once h exceeds 0.75 mm;
- Increasing h and t_s increases the strain energy in the region; that is, the amount of energy required for the predator to deform the region;
- However, increasing h and t_s also increases the maximum strain energy density, and hence the likelihood of fracture occurring;
- The maximum strain energy density increases dramatically for $h > 1.25\,\text{mm}$ which suggests an upper limit on the length on the bony protrusions.

Hence, the mechanical behaviour of the suture region can be tailored significantly by altering the suture geometry.

10.2 Dynamic suture scale simulations

Dynamic simulations of the suture region are presented in Chapter 8. There, viscoelastic material behaviour is considered for the suture, bone, and keratin. The material parameters are determined by fitting the material models to test data from the literature. Three loading cases are considered to elucidate the behaviour of the suture interface in pertinent dynamic loading scenarios it may incur: locomotion, predator attack and stress wave transfer. Additionally, a parametric study is conducted to elucidate the structure-function relationship of the interface. In particular, the effect of suture thickness t_s and protrusion height h is investigated.

10.2.1 Locomotion

It is expected that the shell restricts the turtle's ability to locomote and breathe. It is hypothesised in the literature that the presence of sutures increases the compliance of the shell to allow the turtle to locomote with greater ease [9]. These simulations provide a basis to confirm or reject this hypothesis, in addition to supplying other insights. The simulations yield the following insights:

- The viscous effects of material behaviour are negligible in comparison to the elastic effects, suggesting that the viscous effects do not inhibit the turtle from locomoting;
- The deformation is orders of magnitude smaller than the displacement of a turtle's limbs during locomotion. This suggests that the shell may be considered rigid even

with the inclusion of soft sutures. This contradicts the hypothesis presented in [9] which suggests that the function of the sutures is to allow the turtle to locomote with greater ease;

- The compliance of the suture region can be tailored by changing the suture thickness t_s and bony protrusion height h. As with the quasistatic simulations, an increase in t_s and h corresponds to an increase in compliance.

Hence, the shell may be considered rigid in the case of locomotion irrespective of the inclusion of sutures.

10.2.2 Predator attack

A key function of the shell is to protect the turtle from predator attacks, and so the behaviour of the suture region during these attacks is of interest. Simulations of a predator attack yield the following insights:

- As with the quasistatic simulations, an increase in compliance is observed with an increase in h and t_s;
- An interlocking effect is also observed where the increase in compliance plateaus for sufficiently large protrusion heights. This interlocking effect is not observed in the locomotion simulations. It is hypothesised that the interlocking effect requires sufficiently large deformations to become apparent. These large deformations occur during predator attacks but not locomotion;
- The viscous effects significantly contribute to the protection of the turtle, as the non-equilibrium energy is approximately 10 times greater than the long time-scale strain energy.

10.2.3 Stress wave transfer

In the stress wave transfer simulations, two types of waves are considered: direct and shear stress waves. The degree to which the stress waves propagate through the suture interface is quantified using a metric termed the ‘transmission ratio’; defined as the maximum strain energy in the right bone divided by the maximum strain energy in the left bone; that is,

$$r_t = \frac{\max\limits_t \int_{\Omega_R} \Psi \mathrm{d}\Omega}{\max\limits_t \int_{\Omega_L} \Psi \mathrm{d}\Omega}. \tag{10.1}$$

Hence, the transfer ratio is bounded from below by 0 (corresponding to the entirety of the wave being reflected by the suture) and from above by 1 (corresponding to the wave passing through the suture unperturbed). The simulation results provide the following insights:

- The transfer ratio is lower for shear stress waves than for direct stress waves. Values of approximately 0.05-0.31 are observed for shear stress waves in comparison to 0.50-0.75 for direct stress waves;

- The proportion of the wave that is transmitted decreases in a linear fashion in relation to suture thickness for both shear and direct stress waves;

- For direct stress waves the transfer ratio has a parabolic-like response to protrusion height h with a minimum at approximately 0.3 mm;

- For shear stress waves the transfer ratio increases linearly with protrusion height h.

10.3 Multiscale simulations

A multiscale modelling approach is used to determine the effect that a network of sutures has on the mechanical behaviour of the carapace. The multiscale approach is required, as the length scale of the sutures is far smaller than that of the carapace. Hence, an excessively fine mesh would be required if a single-scale approach is used. To this end, two separate geometric models are required: a microscale representative volume element (RVE) of the suture interface and a macroscale geometric model of the carapace which contains regions of cancellous bone, cortical bone and suture interface. The RVE is then used to define the constitutive behaviour of the suture interface region in the carapace.

A non-concurrent multiscale approach is developed to circumvent the large computational expense associated with concurrent multiscale modelling for nonlinear problems. The approach is similar to other surrogate modelling approaches presented in the literature, whereby a flexible constitutive (surrogate) model is fitted to data obtained from the RVE via several test simulations. Then, the fitted surrogate model is used in place of the RVE during the macroscale simulation. However, the approach used here differs from those found in the literature in that the surrogate model is constrained to have a polyconvex strain energy function. This ensures numerical stability in the macroscale simulation, in contrast to other surrogate modelling approaches.

With these tools in hand, several test simulations are applied to the RVE to elucidate the mechanical behaviour of the suture interface. The results of the test simulations are used to fit a surrogate model, which is in turn used in macroscale simulations. The macroscale simulations are used to elucidate the effect of a network of sutures on the behaviour of the carapace during locomotion and predator attacks. Moreover, the investigations are carried out as a parametric study, varying the bony protrusion height and suture thickness to elucidate the structure–function relationship of suture networks. Hence, the RVE test simulations are applied to several RVEs and a surrogate model is fitted to each of them.

10.3.1 RVE test simulations

To obtain data of the RVEs' behaviour, three loading paths are applied to each RVE:

- Uniaxial loading as described in Section 4.4.1, in each direction;
- Shear loading as described in Section 4.4.4, applied in each shear direction;
- Pressure loading as described in Section 4.4.3.

Furthermore, to determine the viscous behaviour of each RVE, each loading path is applied several times at different loading rates.

In addition to fitting the surrogate model, the data can be used to draw conclusions on the mechanical behaviour of the suture interface by analysing the data for a single RVE. Using a RVE with protrusion height $h = 0.6\,\mathrm{mm}$ and suture thickness $t_s = 0.25\,\mathrm{mm}$ (results in Figures 9.8–9.10), the following conclusions are made:

- The quasistatic behaviour is clearly transversely isotropic. This is best illustrated by the uniaxial loading tests which show that the RVE is approximately 64% stiffer in the first direction, that is, the direction of the bony protrusion, than the second. Additionally, the difference between the stiffness in the second and third directions is approximately 2%;
- The viscous behaviour is also transversely isotropic. Using the uniaxial loading tests for illustration again, the increase in stiffness from quasistatic loading to the largest loading rate for the first direction is about 320% whereas the increase in stiffness for the second and third directions is about 183%;
- The anisotropy of the viscous behaviour is not well captured by the surrogate model. This results in a discrepancy between the data and surrogate model for the largest loading rate in the first direction of about 56% (uniaxial loading). However, this is the only loading path where large errors are found – for all other loading paths the relative error is below 4.5%;

- The viscous material behaviour is insignificant during pressure loading. This is unsurprising as the deformation experienced during pressure loading is mostly volumetric, and the viscous stress is governed by isochoric deformation, which is small in comparison.

10.3.2 Macroscale locomotion

With the fitted surrogate models in hand, macroscale simulations of the shell's behaviour are conducted. Breathing and locomotion are simulated first by dynamically applying a pressure load to the internal surface of the shell. The effect of sutures is elucidated by comparing a simulation with sutures (protrusion height $h = 0.6\,\text{mm}$ and suture thickness $t_s = 0.25\,\text{mm}$) to one without. The following conclusions are made:

- Sutures dramatically increase the compliance of the shell. As a result, the maximum displacement experienced in a shell with sutures is six orders of magnitude greater than one without;
- Sutures also increase the significance of the viscous behaviour of the shell. This is evident from comparison between the long time-scale strain energy and the non-equilibrium energy. For a shell with sutures the strain energy is 2.3 times greater than the non-equilibrium energy, whereas the equivalent ratio for a shell without sutures is 1.6×10^6;
- Although the sutures increase the compliance of the shell, the displacement is still small (less than a micrometer) in comparison to the motion of the internal organs of the turtle during locomotion and breathing (several millimetres). Hence, the shell may be considered rigid in the case of locomotion. This contradicts a hypothesis presented in the literature that the function of sutures is to reduce the constriction caused by the shell during locomotion [9].

In addition to elucidating the effect of sutures, the structure–function relationship is investigated by repeating the breathing and locomotion simulations for various suture geometries. In this regard, the following conclusions are drawn:

- The maximum displacement, strain energy, and non-equilibrium energy have an undulating response to a change in protrusion height and suture thickness that does not reveal a clear pattern or trend. It is unclear why this is the case;

- The behaviour of the shell is significantly tailorable by altering the small-scale geometry of the sutures. This is evident as the variations in maximum displacement, strain energy, and non-equilibrium energy are 32%, 56%, and 150%, respectively.

10.3.3 Macroscale predator attack

A predator attack is simulated by applying a concentrated force to the shell. Additionally, a point mass with an initial velocity is tied to the node where the concentrated force is applied. This is intended to capture the mass of the predator's body and the initial velocity with which the predator makes contact with the shell. Again, the effect of sutures is elucidated by comparing the results of a shell with sutures to one without. The following conclusions are drawn:

- The predator attack simulations corroborate the conclusion that sutures dramatically increase the compliance of the shell as the maximum displacement is 253 times greater for a shell that contains sutures than one that does not;
- Although the sutures increase the compliance of the shell, the maximum displacement experienced during the attack is 0.837 mm – less than a millimetre. This is far less than the displacements the vital organs would experience during everyday functioning. Hence, the shell still provides the requisite protection even with the increased compliance due to the sutures;
- The maximum strain energy density, a key indicator for material failure, is 31 times larger in a shell without sutures, than one with sutures. Hence, although a shell without sutures is stiffer, it is far more likely to experience material failure than one with sutures, making it less resilient to attacks;
- Again, it is evident that the inclusion of sutures increases the ratio of non-equilibrium energy to strain energy. In the case of a predator attack, this increase is from 1.02 for a shell without sutures to 1.44 for a shell with sutures. This increase in non-equilibrium energy serves to further protect the shell and dissipate energy from the attack.

The structure–function relationship is also investigated by repeating the predator attack simulations for various suture geometries. The investigations yield similar conclusions to those obtained from the breathing and locomotion simulations:

- The strain energy, maximum strain energy density, and non-equilibrium energy have an undulating response to a change in protrusion height and suture thickness that does not reveal a clear pattern or trend;

- The magnitude of displacement increases with protrusion height and suture thickness. This corroborates the conclusion drawn from the suture scale simulations that an increase in suture volume increases the compliance of the suture region and hence the shell as a whole.

10.4 Limitation of constitutive data

For completeness, a significant limitation of the current work is discussed here. There is the lack of stress-strain data for the soft collagenous tissue of which sutures are comprised in the literature. As a result, the material model for the suture is fitted to data from another soft collagenous tissue which is scaled to have the same Young's modulus of the suture as determined by nano-indentation tests. Although this is the best one can do with the data at hand, one cannot be sure that the resulting stress-strain curve is a good representation of the suture material.

Despite this limitation, the computational models in this thesis have replicated the results of a physical three point bending test on a beam specimen extracted from a turtle shell that contains a suture, as presented in Chapter 7. Additionally, the multiscale modelling results presented in Chapter 9 are comparable to physical experiments on goat craniums [123].

10.5 Recommendations for further work

There are several ways in which this work can be extended. These are outlined here.

This work can benefit from physical experiments on test samples from turtle shells that provide accurate constitutive data for the suture. Alternatively, one could adopt different scaling strategies to the one used in this work and investigate how these influence the results. For instance, instead of using a constant scale factor, one could use a scale factor that varies linearly from κ_{scale} to 1 between $\lambda = 1$ and $\lambda = \lambda_{\text{end}}$, where λ_{end} is the maximum stretch in the data. Physical experiments could also be conducted to verify the simulations at the shell level. There currently exists 3D-printers that are able to print both hard and soft materials that are intended to replicate bone and soft biological tissue, respectively [124]. Such a printer could be used to create a synthetic shell with sutures in it. Mechanical tests could then be applied to the synthetic shell and Digital Image Correlation (DIC) [125] could be used to reconstruct a displacement, and hence, strain field. These results could be used to verify the modelling approach presented here. Additionally, such a 3D-printer could be used to construct prototypes of protective clothing that incorporates sutures.

This work investigated the behaviour of turtle shells under predator attacks prior to failure. It may also be interesting to model the effect that sutures have on the shell during failure. This may require extending the material models used here to include damage or plasticity. One could also model crack propagation through the shell.

The effect of different choices for boundary conditions can also be investigated further. For example, the placement of the predator attack for the simulations in Chapter 7 can be varied, and, in Chapter 8, the rigid sphere representing the tooth of a predator can be replaced with an elastic sphere.

Further work can also be done on the surrogate modelling approach presented here. The presented approach requires one to run several RVE simulations and then perform training of the surrogate model prior to running the macroscale simulation. Such an approach is referred to as an *offline* approach, since all RVE simulations occur independently of the macroscale simulation. It may be preferable to adopt an *online–offline* training approach instead. In such an approach, a small number of integration points in the macroscale model could be used to define the deformation gradients that are applied to the RVE concurrently with the macroscale simulation. Then, a surrogate model is trained using the resulting data. This surrogate model is then used as the constitutive model for the remaining integration points. This approach has an advantage in that the deformations applied to the RVE are guaranteed to be similar to those experienced during the macroscale simulation, since they are sampled directly from the macroscale simulation. Additionally, such an approach would not require the user to manually run test simulations on the RVE prior to the macroscale simulation.

Work can also be done to verify how well the surrogate model presented in this thesis can replicate a wider range of RVEs. One might do this by constructing several RVEs, running test simulations on them, and determining the error between the trained surrogate model and the data similarly to that in [101].

Bibliography

[1] B. Alheit, S. Bargmann, and B. D. Reddy. “Computationally modelling the mechanical behaviour of turtle shell sutures — A natural interlocking structure”. *Journal of the Mechanical Behavior of Biomedical Materials* 110 (2020), p. 103973.

[2] B. Alheit, S. Bargmann, and B. D. Reddy. “Dynamic mechanical behaviour of suture interfaces as inspiration for architectured hierarchical interlocking composites”. *Journal of the Mechanics and Physics of Solids* 157 (2021), p. 104620.

[3] B Alheit, S Bargmann, and B. Reddy. “How suture networks improve the protective function of natural structures: A multiscale investigation”. *Acta Biomaterialia* (2022).

[4] B. Alheit, S. Bargmann, and B. D. Reddy. “Computational modelling of the mechanical behaviour of turtle shells”. *25th International Congress of Theoretical and Applied Mechanics.* 2021.

[5] J. W. Dunlop, R. Weinkamer, and P. Fratzl. “Artful interfaces within biological materials”. *Materials Today* 14 (2011), pp. 70 –78.

[6] M. Grova, D. D. Lo, D. Montoro, J. S. Hyun, M. T. Chung, D. C. Wan, and M. T. Longaker. “Animal models of cranial suture biology”. *The Journal of Craniofacial Surgery* 23 (2012), p. 1954.

[7] S. Roth, J.-S. Raul, B. Ludes, and R. Willinger. “Finite element analysis of impact and shaking inflicted to a child”. *International Journal of Legal Medicine* 121 (2007), pp. 223–228.

[8] N. Lee, M. Horstemeyer, H. Rhee, B. Nabors, J. Liao, and L. N. Williams. “Hierarchical multiscale structure–property relationships of the red-bellied woodpecker (Melanerpes carolinus) beak”. *Journal of The Royal Society Interface* 11 (2014), p. 20140274.

[9] S. Krauss, E. Monsonego-Ornan, E. Zelzer, P. Fratzl, and R. Shahar. “Mechanical function of a complex three-dimensional suture joining the bony elements in the shell of the red-eared slider turtle”. *Advanced Materials* 21 (2009), pp. 407–412.

[10] C.-Y. Sun and P.-Y. Chen. “Structural design and mechanical behavior of alligator (Alligator mississippiensis) osteoderms”. *Acta Biomaterialia* 9 (2013), pp. 9049 –9064.

[11] I. H. Chen, J. H. Kiang, V. Correa, M. I. Lopez, P.-Y. Chen, J. McKittrick, and M. A. Meyers. “Armadillo armor: Mechanical testing and micro-structural evaluation”. *Journal of the Mechanical Behavior of Biomedical Materials* 4 (2011), pp. 713 –722.

[12] W. Yang, B. Gludovatz, E. A. Zimmermann, H. A. Bale, R. O. Ritchie, and M. A. Meyers. “Structure and fracture resistance of alligator gar (Atractosteus spatula) armored fish scales”. *Acta Biomaterialia* 9 (2013), pp. 5876 –5889.

[13] M. Moazen, N. Curtis, P. O’Higgins, M. E. Jones, S. E. Evans, and M. J. Fagan. “Assessment of the role of sutures in a lizard skull: A computer modelling study”. *Proceedings of the Royal Society B: Biological Sciences* 276 (2009), pp. 39–46.

[14] Q. Wang, A. L. Smith, D. S. Strait, B. W. Wright, B. G. Richmond, I. R. Grosse, C. D. Byron, and U. Zapata. “The global impact of sutures assessed in a finite element model of a macaque cranium”. *The Anatomical Record* 293 (2010), pp. 1477–1491.

[15] C. R. Jaslow. “Mechanical properties of cranial sutures”. *Journal of Biomechanics* 23 (1990), pp. 313–321.

[16] W. Saunders, D. Work, and S. Nikolaeva. “Evolution of complexity in Paleozoic ammonoid sutures”. *Science* 286 (1999), pp. 760–763.

[17] C. Darwin. *On the origin of species, 1859.* Routledge, 2016.

[18] J. T. Gulick. “Divergent Evolution through Cumulative Segregation”. *Journal of the Linnean Society of London, Zoology* 20 (1888), pp. 189–274.

[19] *The Wright Flyer’s warping wings.* URL: `https://blogs.bu.edu/biolocomotion/2011/10/18/the-wright-brothers-flyer/`.

[20] *Biomimicry – The Burr and the Invention of Velcro.* URL: `https://www.microphotonics.com/biomimicry-burr-invention-velcro/`.

[21] *Eiji Nakatsu: Lecture on Biomimicry as applied to a Japanese Train.* URL: `https://labs.blogs.com/its_alive_in_the_lab/2012/04/biomimicry-japanese-train.html`.

[22] N. M. Pugno. “The commemoration of Leonardo da Vinci”. *Meccanica* 54 (2019).

[23] *Design for a Flying Machine, c. 1488.* 1994. URL: `http://www.drawingsofleonardo.org/images/fly3.jpg`.

[24] S. C. Jasinoski and B. D. Reddy. “Mechanics of cranial sutures during simulated cyclic loading”. *Journal of Biomechanics* 45 (2012), pp. 2050–2054.

[25] L. A. Opperman. “Cranial sutures as intramembranous bone growth sites”. *Developmental Dynamics* 219 (2000), pp. 472–485.

[26] B Achrai, B Bar-On, and H. D. Wagner. “Biological armors under impact – effect of keratin coating, and synthetic bio-inspired analogues”. *Bioinspiration & Biomimetics* 10 (2015), p. 016009.

[27] M. J. Buehler. “Nanomechanics of collagen fibrils under varying cross-link densities: Atomistic and continuum studies”. *Journal of the Mechanical Behavior of Biomedical Materials* 1 (2008), pp. 59 –67.

[28] J. Parvizi and G. K. Kim. “Collagen”. *High Yield Orthopaedics*. Elsevier, 2010, pp. 107–109.

[29] J. D. Currey. *Bones: Structure and Mechanics*. 2nd ed. Princeton University Press, 2006.

[30] B. Achrai and H. D. Wagner. “Micro-structure and mechanical properties of the turtle carapace as a biological composite shield”. *Acta Biomaterialia* 9 (2013), pp. 5890 – 5902.

[31] M. Chen, N. Hu, C. Zhou, X. Lin, H. Xie, and Q. He. “The hierarchical structure and mechanical performance of a natural nanocomposite material: The turtle shell”. *Colloids and Surfaces A: Physicochemical and Engineering Aspects* 520 (2017), pp. 97 –104.

[32] K. Balani, R. R. Patel, A. K. Keshri, D. Lahiri, and A. Agarwal. “Multi-scale hierarchy of Chelydra serpentina: Microstructure and mechanical properties of turtle shell”. *Journal of the Mechanical Behavior of Biomedical Materials* 4 (2011), pp. 1440 – 1451.

[33] H. Rhee, M. Horstemeyer, Y. Hwang, H. Lim, H. E. Kadiri, and W. Trim. “A study on the structure and mechanical behavior of the Terrapene carolina carapace: A pathway to design bio-inspired synthetic composites”. *Materials Science and Engineering: C* 29 (2009), pp. 2333 –2339.

[34] R. Damiens, H. Rhee, Y. Hwang, S. Park, Y. Hammi, H. Lim, and M. Horstemeyer. “Compressive behavior of a turtle’s shell: Experiment, modeling, and simulation”. *Journal of the Mechanical Behavior of Biomedical Materials* 6 (2012), pp. 106 –112.

[35] E. Ampaw, T. A. Owoseni, F. Du, N. Pinilla, J. Obayemi, J. Hu, P.-M. Nigay, A. Nzihou, V. Uzonwanne, M. G. Zebaze-Kana, M. Dewoolkar, T. Tan, and W. Soboyejo. “Compressive deformation and failure of trabecular structures in a turtle shell”. *Acta Biomaterialia* 97 (2019), pp. 535 –543.

[36] B. Achrai, B. Bar-On, and H. D. Wagner. “Bending mechanics of the red-eared slider turtle carapace”. *Journal of the Mechanical Behavior of Biomedical Materials* 30 (2014), pp. 223 –233.

[37] N. Jongpairojcosit and P. Jearanaisilawong. “Mechanical properties and numerical simulation of sulcata tortoise carapace”. *Journal of the Mechanical Behavior of Biomedical Materials* 72 (2017), pp. 261 –267.

[38] P Jearanaisilawong, N Jongpairojcosit, and C Glunrawd. “Dynamic behaviors and protection mechanisms of Sulcata tortoise carapace”. *Computer Methods in Biomechanics and Biomedical Engineering* (2021), pp. 1–13.

[39] B. Achrai and H. Daniel Wagner. “The red-eared slider turtle carapace under fatigue loading: The effect of rib–suture arrangement”. *Materials Science and Engineering: C* 53 (2015), pp. 128 –133.

[40] G. Rivera and C. T. Stayton. “Finite element modeling of shell shape in the freshwater turtle Pseudemys concinna reveals a trade-off between mechanical strength and hydrodynamic efficiency”. *Journal of Morphology* 272 (2011), pp. 1192–1203.

[41] W. Zhang, C. Wu, C. Zhang, and Z. Chen. “Numerical study of the mechanical response of turtle shell”. *Journal of Bionic Engineering* 9 (2012), pp. 330 –335.

[42] B. An and H. D. Wagner. “Protection mechanisms of the carapace of a box turtle”. *Journal of the Mechanical Behavior of Biomedical Materials* 71 (2017), pp. 54–67.

[43] Y. Shelef and B. Bar-On. “Surface protection in bio-shields via a functional soft skin layer: Lessons from the turtle shell”. *Journal of the Mechanical Behavior of Biomedical Materials* 73 (2017), pp. 68–75.

[44] M. Xu and B. An. “Dynamic crack propagation in the turtle carapace”. *Mechanics of Materials* 151 (2020), p. 103614.

[45] Y. Li, C. Ortiz, and M. C. Boyce. “A generalized mechanical model for suture interfaces of arbitrary geometry”. *Journal of the Mechanics and Physics of Solids* 61 (2013), pp. 1144 –1167.

[46] Y. Li, C. Ortiz, and M. C. Boyce. “Bioinspired, mechanical, deterministic fractal model for hierarchical suture joints”. *Physical Review E* 85 (2012), p. 031901.

[47] Z. Yu, J. Liu, and X. Wei. “Achieving outstanding damping performance through bio-inspired sutural tessellations”. *Journal of the Mechanics and Physics of Solids* 142 (2020), p. 104010.

[48] Y. Li, C. Ortiz, and M. C. Boyce. “Stiffness and strength of suture joints in nature”. *Physical Review E* 84 (2011), p. 062904.

[49] Z. Liu, Z. Zhang, and R. O. Ritchie. “Interfacial toughening effect of suture structures”. *Acta Biomaterialia* 102 (2020), pp. 75 –82.

[50] C. Gao and Y. Li. “Mechanical model of bio-inspired composites with sutural tessellation”. *Journal of the Mechanics and Physics of Solids* 122 (2019), pp. 190–204.

[51] S. C. Jasinoski, B. D. Reddy, K. K. Louw, and A Chinsamy. “Mechanics of cranial sutures using the finite element method”. *Journal of Biomechanics* 43 (2010), pp. 3104 –3111.

[52] M. S. Hosseini, F. A. Cordisco, and P. D. Zavattieri. “Analysis of bioinspired non-interlocking geometrically patterned interfaces under predominant mode I loading”. *Journal of the Mechanical Behavior of Biomedical Materials* 96 (2019), pp. 244 –260.

[53] L. Liu, Y. Jiang, M. Boyce, C. Ortiz, J. Baur, J. Song, and Y. Li. “The effects of morphological irregularity on the mechanical behavior of interdigitated biological sutures under tension”. *Journal of Biomechanics* 58 (2017), pp. 71–78.

[54] A. G. Holzapfel. *Nonlinear Solid Mechanics: A Continuum Approach for Engineering Science*. John Wiley & Sons, Inc., 2000.

[55] I.-S. Liu. *Continuum mechanics*. Springer Science & Business Media, 2013.

[56] K. Hutter and K. Jöhnk. *Continuum Methods of Physical Modeling: Continuum Mechanics, Dimensional Analysis, Turbulence*. Springer Science & Business Media, 2013.

[57] C. Truesdell and W. Noll. *The Non-Linear Field Theories of Mechanics*. Springer, 2004, pp. 1–579.

[58] G. Hütter. “Coleman-Noll procedure for classical and generalized continuum theories”. *Encyclopedia of Continuum Mechanics* (2020), pp. 316–323.

[59] G. A. Holzapfel, T. C. Gasser, and R. W. Ogden. “A New Constitutive Framework for Arterial Wall Mechanics and a Comparative Study of Material Models”. *Journal of Elasticity* 61 (2000), pp. 1–48.

[60] J. Bonet and R. D. Wood. *Nonlinear Continuum Mechanics for Finite Element Analysis*. 2nd ed. Cambridge University Press, 2008.

[61] T. C. Gasser, R. W. Ogden, and G. A. Holzapfel. “Hyperelastic modelling of arterial layers with distributed collagen fibre orientations”. *Journal of The Royal Society Interface* 3 (2006), pp. 15–35.

[62] X. Leng, B. Zhou, X. Deng, L. Davis, S. M. Lessner, M. A. Sutton, and T. Shazly. “Experimental and numerical studies of two arterial wall delamination modes”. *Journal of the Mechanical Behavior of Biomedical Materials* 77 (2018-01), pp. 321,330.

[63] M. Latorre and F. J. Montáns. “On the tension-compression switch of the Gasser–Ogden–Holzapfel model: Analysis and a new pre-integrated proposal”. *Journal of the Mechanical Behavior of Biomedical Materials* 57 (2016), pp. 175 –189.

[64] Z.-W. Chen, P. Joli, and Z.-Q. Feng. “Anisotropic hyperelastic behavior of soft biological tissues”. *Computer Methods in Biomechanics and Biomedical Engineering* 18 (2014-08-13), pp. 1–9.

[65] D. Nolan, A. Gower, M. Destrade, R. Ogden, and J. McGarry. “A robust anisotropic hyperelastic formulation for the modelling of soft tissue”. *Journal of the Mechanical Behavior of Biomedical Materials* 39 (2014), pp. 48 –60.

[66] J. M. Ball. “Convexity conditions and existence theorems in nonlinear elasticity”. *Archive for Rational Mechanics and Analysis* 63 (1976), pp. 337–403.

[67] J. Schröder and P. Neff. “Invariant formulation of hyperelastic transverse isotropy based on polyconvex free energy functions”. *International Journal of Solids and Structures* 40 (2003), pp. 401–445.

[68] B. D. Reddy and D. van Huyssteen. “A virtual element method for transversely isotropic elasticity”. *Computational Mechanics* 64 (2019), pp. 971–988.

[69] J. Simo and T. Hughes. *Computational Inelasticity*. Springer-Verlag, 1997.

[70] T. C. Gasser and C. Forsell. “The numerical implementation of invariant-based viscoelastic formulations at finite strains. An anisotropic model for the passive myocardium”. *Computer Methods in Applied Mechanics and Engineering* 200 (2011), pp. 3637–3645.

[71] P. Wriggers. *Nonlinear Finite Element Methods*. Springer Science & Business Media, 2008.

[72] Abaqus. *Abaqus Theory Guide v6.14*. 2014.

[73] R. Hill. “On constitutive macro-variables for heterogeneous solids at finite strain”. *Proceedings of the Royal Society of London. A. Mathematical and Physical Sciences* 326 (1972), pp. 131–147.

[74] R. Hill. “Elastic properties of reinforced solids: Some theoretical principles”. *Journal of the Mechanics and Physics of Solids* 11 (1963), pp. 357–372.

[75] I. Temizer and P. Wriggers. “On the computation of the macroscopic tangent for multiscale volumetric homogenization problems”. *Computer Methods in Applied Mechanics and Engineering* 198 (2008), pp. 495–510.

[76] E. de Souza Neto, P. Blanco, P. Sánchez, and R. Feijóo. “An RVE-based multiscale theory of solids with micro-scale inertia and body force effects”. *Mechanics of Materials* 80 (2015), pp. 136–144.

[77] F. Feyel. “Multiscale FE2 elastoviscoplastic analysis of composite structures”. *Computational Materials Science* 16 (1999), pp. 344–354.

[78] F. Feyel and J.-L. Chaboche. “FE2 multiscale approach for modelling the elastoviscoplastic behaviour of long fibre SiC/Ti composite materials”. *Computer Methods in Applied Mechanics and Engineering* 183 (2000), pp. 309–330.

[79] F. Feyel. “A multilevel finite element method (FE2) to describe the response of highly non-linear structures using generalized continua”. *Computer Methods in applied Mechanics and engineering* 192 (2003), pp. 3233–3244.

[80] W. Sun, E. L. Chaikof, and M. E. Levenston. “Numerical approximation of tangent moduli for finite element implementations of nonlinear hyperelastic material models”. *Journal of Biomechanical Engineering* 130 (2008).

[81] J. Yvonnet and Q.-C. He. “The reduced model multiscale method (R3M) for the non-linear homogenization of hyperelastic media at finite strains”. *Journal of Computational Physics* 223 (2007), pp. 341–368.

[82] R. Hatano, S. Matsubara, S. Moriguchi, K. Terada, and J. Yvonnet. “FE$^{\mathrm{r}}$ method with surrogate localization model for hyperelastic composite materials”. *Advanced Modeling and Simulation in Engineering Sciences* 7 (2020), pp. 1–28.

[83] C. Farhat, P. Avery, T. Chapman, and J. Cortial. “Dimensional reduction of nonlinear finite element dynamic models with finite rotations and energy-based mesh sampling and weighting for computational efficiency”. *International Journal for Numerical Methods in Engineering* 98 (2014), pp. 625–662.

[84] C. Farhat, T. Chapman, and P. Avery. “Structure-preserving, stability, and accuracy properties of the energy-conserving sampling and weighting method for the hyper reduction of nonlinear finite element dynamic models”. *International Journal for Numerical Methods in Engineering* 102 (2015), pp. 1077–1110.

[85] M. J. Zahr, P. Avery, and C. Farhat. “A multilevel projection-based model order reduction framework for nonlinear dynamic multiscale problems in structural and solid mechanics”. *International Journal for Numerical Methods in Engineering* 112 (2017), pp. 855–881.

[86] K. Terada and N. Kikuchi. “Nonlinear homogenization method for practical applications”. *American Society of Mechanical Engineers, Applied Mechanics Division, AMD* 212 (1995), pp. 1–16.

[87] N. Takano, M. Zako, and Y. Ohnishi. “Macro-micro uncoupled homogenization procedure for microscopic nonlinear behavior analysis of composites”. *Journal of the Society of Materials Science, Japan* 45 (1996), pp. 81–86.

[88] I Temizer and T. Zohdi. “A numerical method for homogenization in non-linear elasticity”. *Computational Mechanics* 40 (2007), pp. 281–298.

[89] I Temizer and P Wriggers. “An adaptive method for homogenization in orthotropic nonlinear elasticity”. *Computer Methods in Applied Mechanics and Engineering* 196 (2007), pp. 3409–3423.

[90] J. Yvonnet, D Gonzalez, and Q.-C. He. “Numerically explicit potentials for the homogenization of nonlinear elastic heterogeneous materials”. *Computer Methods in Applied Mechanics and Engineering* 198 (2009), pp. 2723–2737.

[91] J. Yvonnet, E. Monteiro, and Q.-C. He. “Computational homogenization method and reduced database model for hyperelastic heterogeneous structures”. *International Journal for Multiscale Computational Engineering* 11 (2013).

[92] B. Le, J. Yvonnet, and Q.-C. He. “Computational homogenization of nonlinear elastic materials using neural networks”. *International Journal for Numerical Methods in Engineering* 104 (2015), pp. 1061–1084.

[93] F. Fritzen, M. Fernández, and F. Larsson. “On-the-Fly Adaptivity for Nonlinear Twoscale Simulations Using Artificial Neural Networks and Reduced Order Modeling”. *Frontiers in Materials* 6 (2019), p. 75.

[94] F. Ghavamian and A. Simone. “Accelerating multiscale finite element simulations of history-dependent materials using a recurrent neural network”. *Computer Methods in Applied Mechanics and Engineering* 357 (2019), p. 112594.

[95] Z. Liu, C. Wu, and M. Koishi. “A deep material network for multiscale topology learning and accelerated nonlinear modeling of heterogeneous materials”. *Computer Methods in Applied Mechanics and Engineering* 345 (2019), pp. 1138–1168.

[96] M. Mozaffar, R. Bostanabad, W. Chen, K. Ehmann, J. Cao, and M. A. Bessa. “Deep learning predicts path-dependent plasticity”. *Proceedings of the National Academy of Sciences* 116 (2019), pp. 26414–26420.

[97] I. Rocha, P. Kerfriden, and F. van der Meer. “Micromechanics-based surrogate models for the response of composites: A critical comparison between a classical mesoscale constitutive model, hyper-reduction and neural networks”. *European Journal of Mechanics - A/Solids* 82 (2020), p. 103995.

[98] Z. Liu and C. Wu. “Exploring the 3D architectures of deep material network in data-driven multiscale mechanics”. *Journal of the Mechanics and Physics of Solids* 127 (2019), pp. 20–46.

[99] P. Avery, D. Z. Huang, W. He, J. Ehlers, A. Derkevorkian, and C. Farhat. “A computationally tractable framework for nonlinear dynamic multiscale modeling of membrane woven fabrics”. *International Journal for Numerical Methods in Engineering* 122 (2021), pp. 2598–2625.

[100] I. Rocha, P Kerfriden, and F. van der Meer. “On-the-fly construction of surrogate constitutive models for concurrent multiscale mechanical analysis through probabilistic machine learning”. *Journal of Computational Physics: X* 9 (2021), p. 100083.

[101] J. N. Fuhg, C. Böhm, N. Bouklas, A. Fau, P. Wriggers, and M. Marino. “Model-data-driven constitutive responses: Application to a multiscale computational framework”. *International Journal of Engineering Science* 167 (2021), p. 103522.

[102] S. Budday, G. Sommer, C. Birkl, C. Langkammer, J. Haybaeck, J. Kohnert, M. Bauer, F. Paulsen, P. Steinmann, E. Kuhl, and G. Holzapfel. “Mechanical characterization of human brain tissue”. *Acta Biomaterialia* 48 (2017), pp. 319–340.

[103] R. H. Byrd, P. Lu, J. Nocedal, and C. Zhu. “A limited memory algorithm for bound constrained optimization”. *SIAM Journal on Scientific Computing* 16 (1995), pp. 1190–1208.

[104] C. Zhu, R. H. Byrd, P. Lu, and J. Nocedal. “Algorithm 778: L-BFGS-B: Fortran subroutines for large-scale bound-constrained optimization”. *ACM Transactions on Mathematical Software (TOMS)* 23 (1997), pp. 550–560.

[105] P. Virtanen, R. Gommers, T. E. Oliphant, M. Haberland, T. Reddy, D. Cournapeau, E. Burovski, P. Peterson, W. Weckesser, J. Bright, S. J. van der Walt, M. Brett, J. Wilson, K. J. Millman, N. Mayorov, A. R. J. Nelson, E. Jones, R. Kern, E. Larson, C. J. Carey, I. Polat, Y. Feng, E. W. Moore, J. VanderPlas, D. Laxalde, J. Perktold, R. Cimrman, I. Henriksen, E. A. Quintero, C. R. Harris, A. M. Archibald, A. H. Ribeiro,

F. Pedregosa, P. van Mulbregt, and SciPy 1.0 Contributors. “SciPy 1.0: Fundamental algorithms for scientific computing in python”. *Nature Methods* 17 (2020), pp. 261–272.

[106] R. Storn and K. Price. “Differential evolution–a simple and efficient heuristic for global optimization over continuous spaces”. *Journal of Global Optimization* 11 (1997), pp. 341–359.

[107] Y. Lanir and Y. Fung. “Two-dimensional mechanical properties of rabbit skin–II. Experimental results”. *Journal of Biomechanics* 7 (1974), pp. 171 –182.

[108] S. P. Timoshenko and J. N. Goodier. *Theory of Elasticity*. Mc Graw Hill, 1951.

[109] A. Phillips, P. Pankaj, C. Howie, A. Usmani, and A. Simpson. “Finite element modelling of the pelvis: Inclusion of muscular and ligamentous boundary conditions”. *Medical Engineering & Physics* 29 (2007), pp. 739 –748.

[110] J. Rösler, H. Harders, and M. Bäker. *Mechanical Behaviour of Engineering Materials: Metals, Ceramics, Polymers, and Composites*. Springer Science & Business Media, 2007.

[111] M. Doblaré, J. Garcíá, and M. Gómez. “Modelling bone tissue fracture and healing: a review”. *Engineering Fracture Mechanics* 71 (2004), pp. 1809 –1840.

[112] E. Schileo, F. Taddei, L. Cristofolini, and M. Viceconti. “Subject-specific finite element models implementing a maximum principal strain criterion are able to estimate failure risk and fracture location on human femurs tested in vitro”. *Journal of Biomechanics* 41 (2008), pp. 356 –367.

[113] T. Wright and W. Hayes. “Tensile testing of bone over a wide range of strain rates: effects of strain rate, microstructure and density”. *Medical and Biological Engineering* 14 (1976), pp. 671–680.

[114] J. H. McElhaney. “Dynamic response of bone and muscle tissue.” *Journal of Applied Physiology* 21 (1966), pp. 1231–1236.

[115] B. Wang and T. N. Sullivan. “A review of terrestrial, aerial and aquatic keratins: The structure and mechanical properties of pangolin scales, feather shafts and baleen plates”. *Journal of the Mechanical Behavior of Biomedical Materials* 76 (2017), pp. 4 –20.

[116] B. Wang, W. Yang, V. R. Sherman, and M. A. Meyers. “Pangolin armor: Overlapping, structure, and mechanical properties of the keratinous scales”. *Acta Biomaterialia* 41 (2016), pp. 60 –74.

[117] Z. Chen, Y. Lin, W. Lee, L. Ren, B. Liu, L. Liang, Z. Wang, and L. Jiang. "Additive manufacturing of honeybee-inspired microneedle for easy skin insertion and difficult removal". *ACS Applied Materials & Interfaces* 10 (2018), pp. 29338–29346.

[118] W. Milsom and P Chan. "The relationship between lung volume, respiratory drive and breathing pattern in the turtle, Chrysemys picta". *Journal of Experimental Biology* 120 (1986), pp. 233–247.

[119] C. G. Lausted, A. T. Johnson, W. H. Scott, M. M. Johnson, K. M. Coyne, and D. C. Coursey. "Maximum static inspiratory and expiratory pressures with different lung volumes". *Biomedical Engineering Online* 5 (2006), pp. 1–6.

[120] B. R. Lawn, H. Chai, A. Barani, and M. B. Bush. "Transverse fracture of canine teeth". *Journal of Biomechanics* 46 (2013), pp. 1561 –1567.

[121] S. Wroe, C. McHenry, and J. Thomason. "Bite club: Comparative bite force in big biting mammals and the prediction of predatory behaviour in fossil taxa". *Proceedings of the Royal Society B: Biological Sciences* 272 (2005), pp. 619–625.

[122] V. Shim, L. Yang, J. Liu, and V. Lee. "Characterisation of the dynamic compressive mechanical properties of cancellous bone from the human cervical spine". *International Journal of Impact Engineering* 32 (2005), pp. 525 –540.

[123] C. R. Jaslow. "Mechanical properties of cranial sutures". *Journal of Biomechanics* 23 (1990), pp. 313–321.

[124] *J750 Digital Anatomy 3D Printer.* URL: `https://www.stratasys.com/3d-printers/j750-digital-anatomy`.

[125] F. Hild and S. Roux. "Digital image correlation: from displacement measurement to identification of elastic properties–a review". *Strain* 42 (2006), pp. 69–80.

[126] W. M. Lai, D. H. Rubin, D. Rubin, and E. Krempl. *Introduction to Continuum Mechanics.* Butterworth-Heinemann, 2009.

[127] F. Rasolofoson, B. J. Grieshaber, and B. D. Reddy. "Finite element approximations for near-incompressible and near-inextensible transversely isotropic bodies". *International Journal for Numerical Methods in Engineering* 117 (2019), pp. 693–712.

Appendices

Appendix A

Mathematical preliminaries and conventions

The necessary mathematical preliminaries for the development of a continuum mechanics framework are presented here. For a more detailed presentation of these mathematical tools see [126].

A.1 Notation for vectors and tensors

Vectors are written in lower-case boldface letters, for example

$$\boldsymbol{y}\,, \tag{A.1}$$

with the exception of $\boldsymbol{X}$ which denotes position in the reference configuration (see section 3.2.1). The components of vectors exclude the boldface and include the index in the subscript, for example

$$y_i\,. \tag{A.2}$$

Basis vectors in particular are denoted by $\boldsymbol{e}$. A vector may then be written in terms of its components with respect to a prescribed basis as

$$\boldsymbol{y} = y_i \boldsymbol{e}_i\,, \tag{A.3}$$

where the Einstein summation convention for repeated indices has been adopted. An orthonormal basis is used throughout this work, typically in three dimensions.

Second order tensors, denoted by bold capital letters, describe a linear map between two vectors, for example

$$\boldsymbol{a} = \boldsymbol{B}\boldsymbol{c}\,. \tag{A.4}$$

The components of second order tensors are denoted by omitting the boldface and including the indices in the subscript. For example, the indicial notation equivalent of equation (A.4) is given by

$$a_i = B_{ij} c_j \,. \tag{A.5}$$

The tensor product $\otimes$ of two vectors $\boldsymbol{a}$ and $\boldsymbol{b}$ creates a tensor that, when operating on a third vector $\boldsymbol{c}$, follows the rule

$$[\boldsymbol{a} \otimes \boldsymbol{b}]\, \boldsymbol{c} = \boldsymbol{a}\, [\boldsymbol{b} \cdot \boldsymbol{c}] \ . \tag{A.6}$$

It follows that the components of the tensor $\boldsymbol{A} = \boldsymbol{a} \otimes \boldsymbol{b}$ are $A_{ij} = a_i b_j$. This allows one to create a basis for tensors using the tensor product of the basis vectors, for example

$$\boldsymbol{A} = A_{ij} \boldsymbol{e}_i \otimes \boldsymbol{e}_j \,. \tag{A.7}$$

The identity tensor $\boldsymbol{I}$ maps a vector to itself and its components are given by the Kronecker delta δ_{ij}. This is defined as

$$\delta_{ij} := \begin{cases} 1 & i = j, \\ 0 & i \neq j. \end{cases} \tag{A.8}$$

Fourth order tensors describe a linear map between two second order tensors. They are denoted by blackboard bold and their components are denoted by including their index in the subscript. For example,

$$\boldsymbol{A} = \mathbb{C} \boldsymbol{B} \tag{A.9}$$

is equivalent to

$$A_{ij} = \mathbb{C}_{ijkl} B_{kl} \,. \tag{A.10}$$

Similarly to second order tensors, a basis for fourth order tensors can be constructed by utilising the tensor product, for example

$$\mathbb{C} = \mathbb{C}_{ijkl} \boldsymbol{e}_i \otimes \boldsymbol{e}_j \otimes \boldsymbol{e}_k \otimes \boldsymbol{e}_l \,. \tag{A.11}$$

The permutation symbol, $\boldsymbol{\epsilon}$, is special third order tensor defined in index notation by

$$\epsilon_{ijk} := \begin{cases} +1 & \text{if } (i,j,k) = (1,2,3),\ (3,1,2), (2,3,1)\,, \\ -1 & \text{if } (i,j,k) = (3,2,1),\ (1,3,2), (2,1,3)\,, \\ 0 & \text{if } i = j, j = k, i = k\,. \end{cases} \tag{A.12}$$

Note that this is the only third order tensor that is used in this work.

A.2 Some linear algebra operations

The dot product of two vectors, $\boldsymbol{a}$ and $\boldsymbol{b}$, is defined as

$$\boldsymbol{a} \cdot \boldsymbol{b} = a_i b_i \,. \tag{A.13}$$

The inner product between two tensors is defined as

$$\boldsymbol{A} : \boldsymbol{B} = A_{ij} B_{ij} \,. \tag{A.14}$$

The trace of a second order tensor is defined as

$$\operatorname{tr} \boldsymbol{A} = A_{ii} \,. \tag{A.15}$$

The Euclidean norm is defined for vectors as

$$||\boldsymbol{a}|| = \sqrt{\boldsymbol{a} \cdot \boldsymbol{a}} \,, \tag{A.16}$$

and second order tensors as

$$||\boldsymbol{A}|| = \sqrt{\boldsymbol{A} : \boldsymbol{A}} \,. \tag{A.17}$$

The determinant of a 3 × 3 tensor is defined by

$$\det A = A_{1i} A_{2j} A_{3k} \epsilon_{ijk} \,. \tag{A.18}$$

Note that the dot product, inner product, trace, Euclidean norm and determinant are invariant to the choice of basis.

The cross product between two vectors is defined as

$$\boldsymbol{a} \times \boldsymbol{b} = a_i b_j \epsilon_{ijk} \boldsymbol{e}_k \,. \tag{A.19}$$

The symmetric tensor product is defined between two symmetric matrices as

$$\boldsymbol{A} \odot \boldsymbol{B} = [A_{ij} \boldsymbol{e}_i \otimes \boldsymbol{e}_j] \odot [B_{kl} \boldsymbol{e}_k \otimes \boldsymbol{e}_l] = \frac{1}{2} [A_{ik} B_{jl} + A_{jk} B_{il}] \, \boldsymbol{e}_i \otimes \boldsymbol{e}_j \otimes \boldsymbol{e}_k \otimes \boldsymbol{e}_l \,. \tag{A.20}$$

A.3 Tensor calculus

Differentiation with respect to a vector $\boldsymbol{b}$ is defined for scalars as

$$\frac{\partial a}{\partial \boldsymbol{b}} = \frac{\partial a}{\partial b_i} \boldsymbol{e}_i \,, \tag{A.21}$$

and vectors as

$$\frac{\partial \boldsymbol{a}}{\partial \boldsymbol{b}} = \frac{\partial a_i}{\partial b_j} \boldsymbol{e}_i \otimes \boldsymbol{e}_j \,. \tag{A.22}$$

Differentiation with respect to tensors is defined for scalars as

$$\frac{\partial a}{\partial \boldsymbol{B}} = \frac{\partial a}{\partial B_{ij}} \boldsymbol{e}_i \otimes \boldsymbol{e}_j \,, \tag{A.23}$$

and tensors as

$$\frac{\partial \boldsymbol{A}}{\partial \boldsymbol{B}} = \frac{\partial A_{ij}}{\partial B_{kl}} \boldsymbol{e}_i \otimes \boldsymbol{e}_j \otimes \boldsymbol{e}_k \otimes \boldsymbol{e}_l \,. \tag{A.24}$$

The chain rule for vectors implies

$$\frac{\partial \boldsymbol{a}(\boldsymbol{b}(\boldsymbol{c}))}{\partial \boldsymbol{c}} = \frac{\partial a_i}{\partial b_m} \frac{\partial b_m}{\partial c_j} \boldsymbol{e}_i \otimes \boldsymbol{e}_j = \frac{\partial \boldsymbol{a}}{\partial \boldsymbol{b}} \frac{\partial \boldsymbol{b}}{\partial \boldsymbol{c}} \,, \tag{A.25}$$

and for tensors it implies

$$\frac{\partial \boldsymbol{A}(\boldsymbol{B}(\boldsymbol{C}))}{\partial \boldsymbol{C}} = \frac{\partial A_{ij}}{\partial B_{mn}} \frac{\partial B_{mn}}{\partial C_{kl}} \boldsymbol{e}_i \otimes \boldsymbol{e}_j \otimes \boldsymbol{e}_k \otimes \boldsymbol{e}_l = \frac{\partial \boldsymbol{A}}{\partial \boldsymbol{B}} : \frac{\partial \boldsymbol{B}}{\partial \boldsymbol{C}} \,. \tag{A.26}$$

Partial derivatives with respect to time are denoted by $\dot{\bullet}$, which is also referred to as the material time derivative. The partial derivative of a tensor and vector with respect to time in a Cartesian basis are given, respectively, by

$$\dot{\boldsymbol{A}} = \dot{A}_{ij} \boldsymbol{e}_i \otimes \boldsymbol{e}_j \,, \qquad \dot{\boldsymbol{u}} = \dot{u}_i \boldsymbol{e}_i \,. \tag{A.27}$$

The derivative of a vector with respect to position $\boldsymbol{X}$ is defined as

$$\operatorname{Grad} \boldsymbol{v} = \frac{\partial \boldsymbol{v}}{\partial \boldsymbol{X}} \,. \tag{A.28}$$

The divergence of a vector and tensor in Cartesian coordinates are given, respectively, by

$$\operatorname{Div} \boldsymbol{a} = \frac{\partial a_i}{\partial X_i} \,, \qquad \operatorname{Div} \boldsymbol{A} = \frac{\partial A_{ij}}{\partial X_j} \boldsymbol{e}_i \,. \tag{A.29}$$

Green's theorem states that for a region $\Omega_0 \subset \mathbb{R}^3$ which is bounded by the surface Γ_0 the following holds:

$$\int_{\Omega_0} w_i \frac{\partial A_{ij}}{\partial X_j} \mathrm{d}\Omega_0 = \int_{\Gamma_0} w_i A_{ij} n_j \mathrm{d}\Gamma_0 - \int_{\Omega_0} \frac{\partial w_i}{\partial X_j} A_{ij} \mathrm{d}\Omega_0 \,, \tag{A.30}$$

where $\boldsymbol{n}$ is the outward facing unit normal to the surface Γ_0 and $\boldsymbol{X} \in \mathbb{R}^3$ denotes position. Note that this can be written equivalently as

$$\int_{\Omega_0} \boldsymbol{w} \cdot \operatorname{Div} \boldsymbol{A} \, \mathrm{d}\Omega_0 = \int_{\Gamma_0} \boldsymbol{w} \cdot \boldsymbol{A}\boldsymbol{n} \, \mathrm{d}\Gamma_0 - \int_{\Omega_0} \operatorname{Grad} (\boldsymbol{w}) : \boldsymbol{A} \, \mathrm{d}\Omega_0 \,. \tag{A.31}$$

Appendix B

Constitutive models

B.1 Schröder-Neff strain energy functions second derivatives

The second derivatives of the Schröder-Neff strain energy functions (see equation (4.92)) with respect to the invariants are as follows:

$$\begin{aligned}
\frac{\partial^2\Psi}{\partial I_1 \partial I_1} &= \sum_{i}^{n} \frac{I_4^2 \kappa_{(5)i} i^2 \left(-I_1 I_4 + I_2 + I_5\right)^i}{\left(-I_1 I_4 + I_2 + I_5\right)^2} - \frac{I_4^2 \kappa_{(5)i} i \left(-I_1 I_4 + I_2 + I_5\right)^i}{\left(-I_1 I_4 + I_2 + I_5\right)^2} \\
&+ \frac{I_6^2 \kappa_{(7)i} i^2 \left(-I_1 I_6 + I_2 + I_7\right)^i}{\left(-I_1 I_6 + I_2 + I_7\right)^2} - \frac{I_6^2 \kappa_{(7)i} i \left(-I_1 I_6 + I_2 + I_7\right)^i}{\left(-I_1 I_6 + I_2 + I_7\right)^2} + \frac{I_1^i \kappa_{(1)i} i^2}{I_1^2} - \frac{I_1^i \kappa_{(1)i} i}{I_1^2}\,, \\
\frac{\partial^2\Psi}{\partial I_1 \partial I_2} &= \sum_{i}^{n} - \frac{I_4 \kappa_{(5)i} i^2 \left(-I_1 I_4 + I_2 + I_5\right)^i}{\left(-I_1 I_4 + I_2 + I_5\right)^2} + \frac{I_4 \kappa_{(5)i} i \left(-I_1 I_4 + I_2 + I_5\right)^i}{\left(-I_1 I_4 + I_2 + I_5\right)^2} \\
&- \frac{I_6 \kappa_{(7)i} i^2 \left(-I_1 I_6 + I_2 + I_7\right)^i}{\left(-I_1 I_6 + I_2 + I_7\right)^2} + \frac{I_6 \kappa_{(7)i} i \left(-I_1 I_6 + I_2 + I_7\right)^i}{\left(-I_1 I_6 + I_2 + I_7\right)^2}\,, \\
\frac{\partial^2\Psi}{\partial I_1 \partial I_3} &= 0\,, \\
\frac{\partial^2\Psi}{\partial I_1 \partial I_4} &= \sum_{i}^{n} \frac{I_1 I_4 \kappa_{(5)i} i^2 \left(-I_1 I_4 + I_2 + I_5\right)^i}{\left(-I_1 I_4 + I_2 + I_5\right)^2} - \frac{I_1 I_4 \kappa_{(5)i} i \left(-I_1 I_4 + I_2 + I_5\right)^i}{\left(-I_1 I_4 + I_2 + I_5\right)^2} \\
&- \frac{\kappa_{(5)i} i \left(-I_1 I_4 + I_2 + I_5\right)^i}{-I_1 I_4 + I_2 + I_5}\,, \\
\frac{\partial^2\Psi}{\partial I_1 \partial I_5} &= \sum_{i}^{n} - \frac{I_4 \kappa_{(5)i} i^2 \left(-I_1 I_4 + I_2 + I_5\right)^i}{\left(-I_1 I_4 + I_2 + I_5\right)^2} + \frac{I_4 \kappa_{(5)i} i \left(-I_1 I_4 + I_2 + I_5\right)^i}{\left(-I_1 I_4 + I_2 + I_5\right)^2}\,, \\
\frac{\partial^2\Psi}{\partial I_1 \partial I_6} &= \sum_{i}^{n} \frac{I_1 I_6 \kappa_{(7)i} i^2 \left(-I_1 I_6 + I_2 + I_7\right)^i}{\left(-I_1 I_6 + I_2 + I_7\right)^2} - \frac{I_1 I_6 \kappa_{(7)i} i \left(-I_1 I_6 + I_2 + I_7\right)^i}{\left(-I_1 I_6 + I_2 + I_7\right)^2} \\
&- \frac{\kappa_{(7)i} i \left(-I_1 I_6 + I_2 + I_7\right)^i}{-I_1 I_6 + I_2 + I_7}\,,
\end{aligned}$$

$$\begin{aligned}
\frac{\partial^2\Psi}{\partial I_1\partial I_7} &= \sum_i^n -\frac{I_6\kappa_{(7)i}i^2\left(-I_1I_6+I_2+I_7\right)^i}{\left(-I_1I_6+I_2+I_7\right)^2}+\frac{I_6\kappa_{(7)i}i\left(-I_1I_6+I_2+I_7\right)^i}{\left(-I_1I_6+I_2+I_7\right)^2}\,,\\
\frac{\partial^2\Psi}{\partial I_2\partial I_2} &= \sum_i^n \frac{\kappa_{(5)i}i^2\left(-I_1I_4+I_2+I_5\right)^i}{\left(-I_1I_4+I_2+I_5\right)^2}-\frac{\kappa_{(5)i}i\left(-I_1I_4+I_2+I_5\right)^i}{\left(-I_1I_4+I_2+I_5\right)^2}\\
&\quad+\frac{\kappa_{(7)i}i^2\left(-I_1I_6+I_2+I_7\right)^i}{\left(-I_1I_6+I_2+I_7\right)^2}-\frac{\kappa_{(7)i}i\left(-I_1I_6+I_2+I_7\right)^i}{\left(-I_1I_6+I_2+I_7\right)^2}+\frac{I_2^i\kappa_{(2)i}i^2}{I_2^2}-\frac{I_2^i\kappa_{(2)i}i}{I_2^2}\,,\\
\frac{\partial^2\Psi}{\partial I_2\partial I_3} &= 0\,,\\
\frac{\partial^2\Psi}{\partial I_2\partial I_4} &= \sum_i^n -\frac{I_1\kappa_{(5)i}i^2\left(-I_1I_4+I_2+I_5\right)^i}{\left(-I_1I_4+I_2+I_5\right)^2}+\frac{I_1\kappa_{(5)i}i\left(-I_1I_4+I_2+I_5\right)^i}{\left(-I_1I_4+I_2+I_5\right)^2}\,,\\
\frac{\partial^2\Psi}{\partial I_2\partial I_5} &= \sum_i^n \frac{\kappa_{(5)i}i^2\left(-I_1I_4+I_2+I_5\right)^i}{\left(-I_1I_4+I_2+I_5\right)^2}-\frac{\kappa_{(5)i}i\left(-I_1I_4+I_2+I_5\right)^i}{\left(-I_1I_4+I_2+I_5\right)^2}\,,\\
\frac{\partial^2\Psi}{\partial I_2\partial I_6} &= \sum_i^n -\frac{I_1\kappa_{(7)i}i^2\left(-I_1I_6+I_2+I_7\right)^i}{\left(-I_1I_6+I_2+I_7\right)^2}+\frac{I_1\kappa_{(7)i}i\left(-I_1I_6+I_2+I_7\right)^i}{\left(-I_1I_6+I_2+I_7\right)^2}\,,\\
\frac{\partial^2\Psi}{\partial I_2\partial I_7} &= \sum_i^n \frac{\kappa_{(7)i}i^2\left(-I_1I_6+I_2+I_7\right)^i}{\left(-I_1I_6+I_2+I_7\right)^2}-\frac{\kappa_{(7)i}i\left(-I_1I_6+I_2+I_7\right)^i}{\left(-I_1I_6+I_2+I_7\right)^2}\,,\\
\frac{\partial^2\Psi}{\partial I_3\partial I_3} &= \sum_i^n \frac{\kappa_{(3)i}i^2\left(1-\frac{1}{I_3^2}\right)^2\left(I_3-2+\frac{1}{I_3}\right)^i}{\left(I_3-2+\frac{1}{I_3}\right)^2}\,,\\
&\quad+\frac{\kappa_{(3)i}i\left(-1+\frac{1}{I_3^2}\right)\left(1-\frac{1}{I_3^2}\right)\left(I_3-2+\frac{1}{I_3}\right)^i}{\left(I_3-2+\frac{1}{I_3}\right)^2}+\frac{2\kappa_{(3)0}}{I_3^3}+\frac{2\kappa_{(3)i}i\left(I_3-2+\frac{1}{I_3}\right)^i}{I_3^3\left(I_3-2+\frac{1}{I_3}\right)}\,,\\
\frac{\partial^2\Psi}{\partial I_3\partial I_4} &= 0\,,\\
\frac{\partial^2\Psi}{\partial I_3\partial I_5} &= 0\,,\\
\frac{\partial^2\Psi}{\partial I_3\partial I_6} &= 0\,,\\
\frac{\partial^2\Psi}{\partial I_3\partial I_7} &= 0\,,\\
\frac{\partial^2\Psi}{\partial I_4\partial I_4} &= \sum_i^n \frac{I_1^2\kappa_{(5)i}i^2\left(-I_1I_4+I_2+I_5\right)^i}{\left(-I_1I_4+I_2+I_5\right)^2}-\frac{I_1^2\kappa_{(5)i}i\left(-I_1I_4+I_2+I_5\right)^i}{\left(-I_1I_4+I_2+I_5\right)^2}\\
&\quad+\frac{I_4^i\kappa_{(4)i}i^2}{I_4^2}-\frac{I_4^i\kappa_{(4)i}i}{I_4^2}\,,\\
\frac{\partial^2\Psi}{\partial I_4\partial I_5} &= \sum_i^n -\frac{I_1\kappa_{(5)i}i^2\left(-I_1I_4+I_2+I_5\right)^i}{\left(-I_1I_4+I_2+I_5\right)^2}+\frac{I_1\kappa_{(5)i}i\left(-I_1I_4+I_2+I_5\right)^i}{\left(-I_1I_4+I_2+I_5\right)^2}\,,\\
\frac{\partial^2\Psi}{\partial I_4\partial I_6} &= 0\,,
\end{aligned}$$

$$
\begin{aligned}
\frac{\partial^2\Psi}{\partial I_4 \partial I_7} &= 0\,, \\
\frac{\partial^2\Psi}{\partial I_5 \partial I_5} &= \sum_i^n \frac{\kappa_{(5)i} i^2 \left(-I_1 I_4 + I_2 + I_5\right)^i}{\left(-I_1 I_4 + I_2 + I_5\right)^2} - \frac{\kappa_{(5)i} i \left(-I_1 I_4 + I_2 + I_5\right)^i}{\left(-I_1 I_4 + I_2 + I_5\right)^2}\,, \\
\frac{\partial^2\Psi}{\partial I_5 \partial I_6} &= 0\,, \\
\frac{\partial^2\Psi}{\partial I_5 \partial I_7} &= 0\,, \\
\frac{\partial^2\Psi}{\partial I_6 \partial I_6} &= \sum_i^n \frac{I_1^2 \kappa_{(7)i} i^2 \left(-I_1 I_6 + I_2 + I_7\right)^i}{\left(-I_1 I_6 + I_2 + I_7\right)^2} - \frac{I_1^2 \kappa_{(7)i} i \left(-I_1 I_6 + I_2 + I_7\right)^i}{\left(-I_1 I_6 + I_2 + I_7\right)^2} \\
&\quad + \frac{I_6^i \kappa_{(6)i} i^2}{I_6^2} - \frac{I_6^i \kappa_{(6)i} i}{I_6^2}\,, \\
\frac{\partial^2\Psi}{\partial I_6 \partial I_7} &= \sum_i^n - \frac{I_1 \kappa_{(7)i} i^2 \left(-I_1 I_6 + I_2 + I_7\right)^i}{\left(-I_1 I_6 + I_2 + I_7\right)^2} + \frac{I_1 \kappa_{(7)i} i \left(-I_1 I_6 + I_2 + I_7\right)^i}{\left(-I_1 I_6 + I_2 + I_7\right)^2}\,, \\
\frac{\partial^2\Psi}{\partial I_7 \partial I_7} &= \sum_i^n \frac{\kappa_{(7)i} i^2 \left(-I_1 I_6 + I_2 + I_7\right)^i}{\left(-I_1 I_6 + I_2 + I_7\right)^2} - \frac{\kappa_{(7)i} i \left(-I_1 I_6 + I_2 + I_7\right)^i}{\left(-I_1 I_6 + I_2 + I_7\right)^2}\,.
\end{aligned}
\tag{B.1}
$$

Appendix C

Quasistatic simulations

C.1 Implementation

C.1.1 Geometry generation

The generation of the geometry is automated using the ABAQUS `Python` application programming interface (API). A swept cut is used to remove the suture region from a blank, displayed in Figure C.1, leaving the left and right bone parts. The section for the swept cut, displayed as the region contained by the red curves in Figure C.1, is generated by defining the function

$$y = f(x) = \frac{h}{2} \sin\left(2\pi \frac{x}{w}\right) , \tag{C.1}$$

where h and w are the length and width of the protrusions, respectively. The left and right red curves are then generated via a transformation of the middle curve, $f(x)$, using the functions

$$\theta = \frac{\pi}{2} + \frac{\pi}{4} \cos\left(2\pi \frac{x}{w}\right) , \tag{C.2}$$

$$Y = y + n\frac{t_s}{2} \sin(\theta) \tag{C.3}$$

and

$$X = x - n\frac{t_s}{2} \mathrm{sign}(\cos(\theta)) |\cos(\theta)|^a . \tag{C.4}$$

Here, θ is the angle between the normal to the middle curve and the x-axis in radians, X and Y are the x and y positions respectively of the points on the red curves, t_s is the thickness of the suture, a controls the 'pointiness' of the protrusions and n is set to -1 for the left curve and $+1$ for the right curve. This section is then swept along a sinusoidal path extending perpendicularly to the front face. The length, thickness and depth of the region of shell are parametrized in the variables l_r, t_r and d_r, respectively.

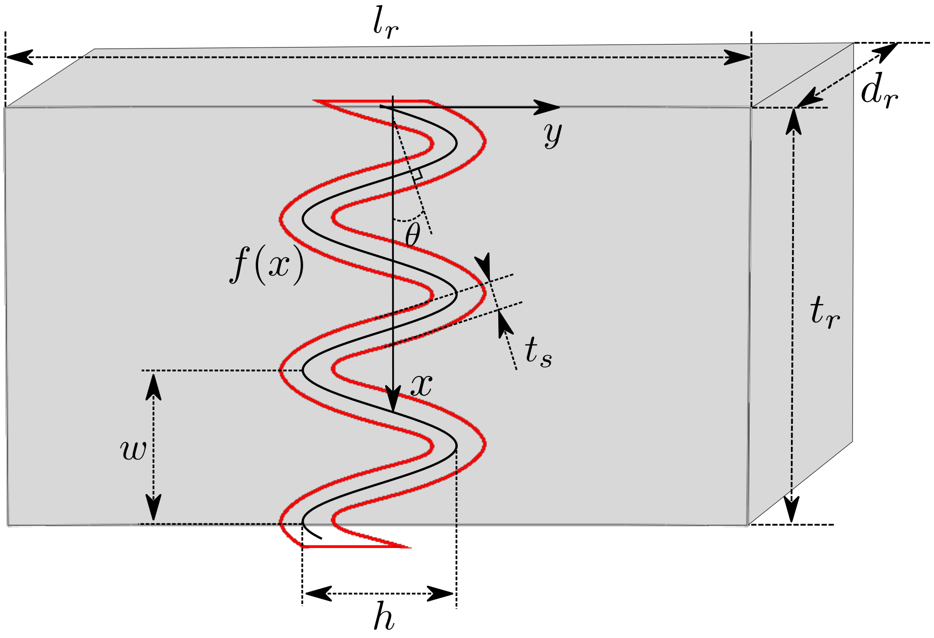

Figure C.1: Model geometry. l_r, t_r and d_r are the length, thickness and depth respectively of the section of shell to be modelled, t_s is the thickness of the suture and w and h are the width and height respectively of the bony protrusions. Geometric parameters not illustrated here include the thickness of the collagenous skin t_c and keratinous layer t_k; see Figure C.3 for interpretation. The suture geometry is generated by sweeping the region defined by the red curves along a sinusoidal path in the direction of d_r. The red curves are generated by translating the points on $f(x)$, defined in equation (C.1), perpendicularly to the curve, that is, in the direction of θ, as defined in equation (C.2).

The resulting bone parts are used with the cut feature to cut the suture region out of a second blank. The left bone, suture, and right bone parts are shown in Figure C.2. The

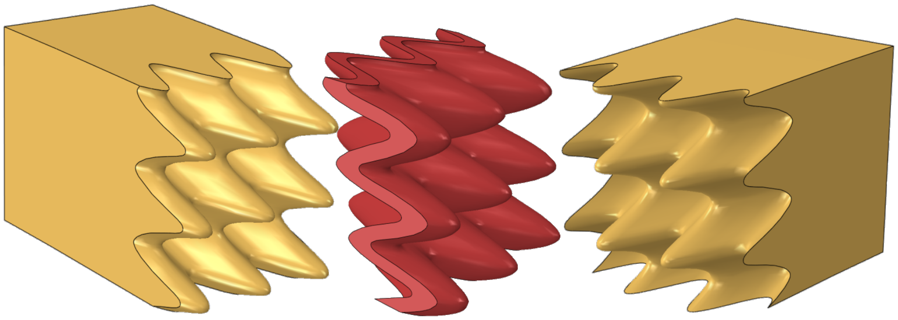

Figure C.2: Display of the model geometry: left bone part (left), suture (centre) and right bone part (right).

keratin and skin layers, having thicknesses of t_k and t_c respectively, are modelled as thin since they are approximately 100 times thinner than the bone [30]. Hence, they are generated by copying the top face of the model, as shown in Figure C.3.

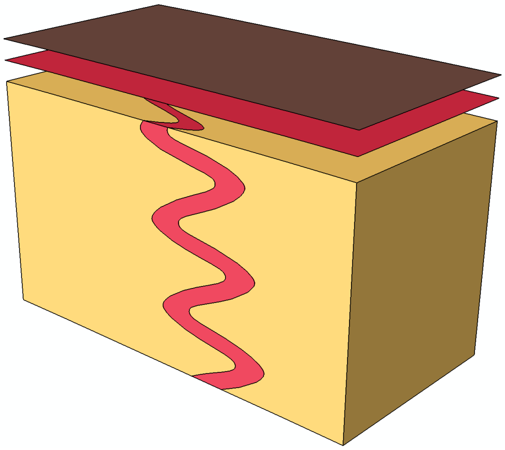

Figure C.3: Merged model geometry including the skin (red) and keratin (brown) layers. The thicknesses of the skin and keratin layers are parametrized in t_c and t_k, respectively. The layers are displayed with an offset here for visual illustration. However, they are modelled as being coincident with the top face of the model.

C.1.2 Meshing

The merged part shown in Figure C.3 is meshed with tetrahedra to generate the base mesh. The bone regions use a piecewise quadratic displacement (P2) approximation, whereas the suture region uses a mixed piecewise quadratic displacement and constant pressure (P2-P0) [71] approximation which is stable for incompressibility.

Shell-type element meshes are generated to model the skin and keratin layers by copying the element faces of the top surface of the base mesh. The skin is modelled using membrane elements, having only displacement degrees of freedom, as it is not expected to have significant shear or bending stiffness. A piecewise quadratic approximation is used. On the other hand, the keratin layer is modelled using shell elements having two rotational degrees of freedom per node in addition to displacement degrees of freedom. A piecewise quadratic approximation is used for the displacement and rotational degrees of freedom. The nodes between the skin layer, keratin layer and top surface of the base mesh are shared. Hence, the only additional degrees of freedom that the shell meshes add to the problem are rotational degrees of freedom due to the keratin layer; tie restraints are not required.

C.1.3 Keratin material model stability

Pointwise strict convexity of the material strain energy is a sufficient condition for stability of small strain material models [127]. This is equivalent to the positive definiteness of the elasticity tensor, which is equivalent to the positive definiteness of the compliance tensor.

Hence, the stability of the material model for the chosen material parameters can be verified by determining that the eigenvalues of the compliance tensor are positive. If the Poison's ratio and shear modulus are equal in all directions, then the eigenvalues are given by

$$v_1 = \frac{\nu + 1}{E_t}\,, \qquad v_2 = \frac{1}{\mu}\,, \tag{C.5}$$

$$v_3 = -\frac{E_l[\nu - 1] - E_t + \sqrt{E_l^2[\nu - 1]^2 + 2E_lE_t[\nu - 1] + E_t^2[8\nu^2 + 1]}}{2E_lE_t}\,, \tag{C.6}$$

$$v_4 = -\frac{E_l[\nu - 1] - E_t - \sqrt{E_l^2[\nu - 1]^2 + 2E_lE_t[\nu - 1] + E_t^2[8\nu^2 + 1]}}{2E_lE_t}\,. \tag{C.7}$$

Note that the second eigenvalue has a multiplicity of 3. Substitution of the chosen values for E_l, E_t and ν yields

$$v_1 = 2\,\mathrm{GPa}^{-1} > 0\,, \qquad v_2 = 2.16\,\mathrm{GPa}^{-1} > 0\,, \tag{C.8}$$

$$v_3 = 0.37\,\mathrm{GPa}^{-1} > 0\,, \qquad v_4 = 1.25\,\mathrm{GPa}^{-1} > 0\,. \tag{C.9}$$

Hence, the material model is stable.

C.1.4 Suture fibre direction

The collagenous fibres in sutures tend to align themselves so that they are loaded in tension [51, 9]. To determine the direction that this would correspond to, the system illustrated in Figure C.4 is used. First, a setup simulation with the same boundary conditions and mesh is run prior to each simulation using $\kappa = 1/3$, thus forcing the tissue to behave isotropically. In the setup simulation, the eigenvectors $\boldsymbol{N}_1$ and $\boldsymbol{N}_3$ corresponding to the maximum and minimum eigenvalues respectively of the right Cauchy-Green tensor are determined and saved in the setup output database (ODB) at each integration point. A `Python` script then uses the data from the setup simulation and a template to write the `ORIENT` subroutine for the subsequent simulation defining the fibre direction at each integration point (NPT) in each element (NOEL). The fibre direction within the suture is defined using the equation

$$\boldsymbol{a}_0(\boldsymbol{X}) = \boldsymbol{N}_1(\boldsymbol{X})\cos\alpha + \boldsymbol{N}_3(\boldsymbol{X})\sin\alpha\,, \tag{C.10}$$

where α is the angle between the fibre direction and the first eigenvector in the plane which contains both the first and third eigenvectors.

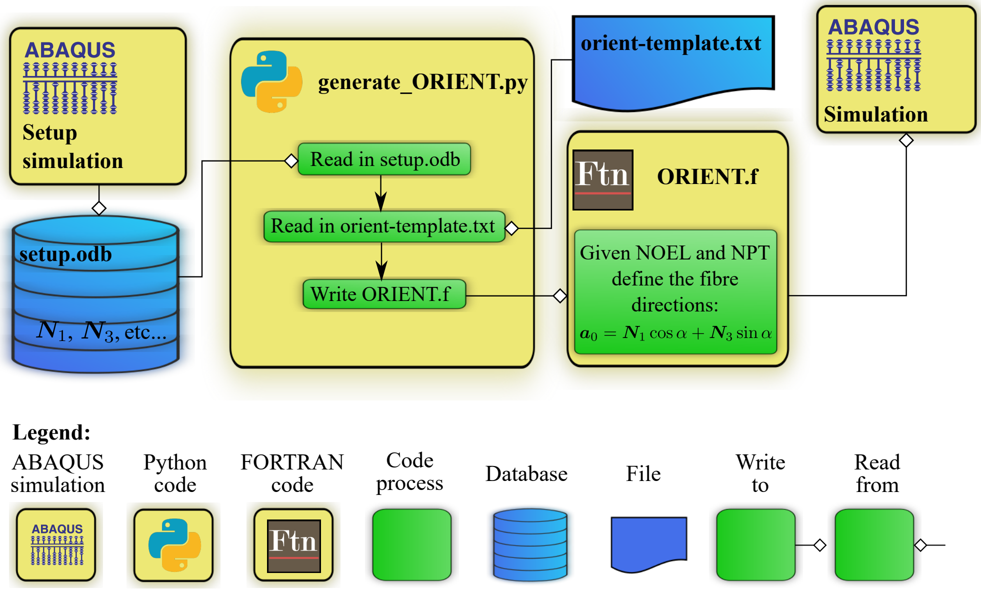

Figure C.4: System used to define fibre directions. A setup simulation is used to determine what the direction of the maximum $\boldsymbol{N}_1$ and minimum $\boldsymbol{N}_3$ principal stretches will be in the suture. A `Python` script then uses this data to define the fibre directions in the subsequent simulation.

C.1.5 Spring boundary conditions

For the spring boundary conditions to be physically realistic, the spring stiffness at each node should be dependent on the volume of external material responsible for constraining that node. Hence, the stiffness of each spring should decrease with an increase in mesh density. This is achieved by idealising the external material as a collection of cylindrical beam elements, each attached to a boundary node, as shown in Figure C.5. The radius, r, of each beam element is approximated by

$$r = \gamma \frac{d}{2}\,, \tag{C.11}$$

where d is the distance from the node to which the beam is connected, to its nearest boundary neighbour, and γ is a packing factor; in this work $\gamma = 3/2$ is used. The length of the beams, L, represents the distance from the bounding surface at which the displacement is insignificant. This value is estimated by using simulations of the mechanical behaviour of the carapace given in C.2.1, Figure C.7 (b) giving values of 14 mm for surfaces with normals in the lateral direction and 43 mm for surfaces with normals in the anterior direction. These geometric values are used to apply spring boundary conditions with representative stiffnesses in the direct, k_d, and transverse, k_t, directions using the beam stiffness equations

$$k_d = \frac{\pi r^2 E}{L} \tag{C.12}$$

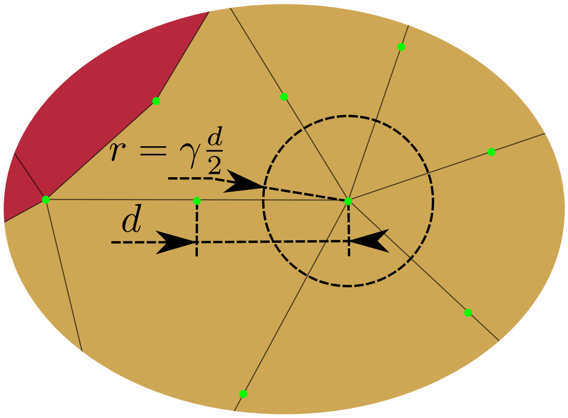

Figure C.5: Illustration of dimensions for beam element approximating external material behaviour. Here d is the distance from the node to which the spring boundary condition is being applied and its closest neighbour, γ is a packing factor and r is the radius of the beam element intended to approximate the behaviour of the external material.

and

$$k_t = \frac{3\pi E r^4}{L^3}\,, \tag{C.13}$$

where E is the Young's modulus of the beam material. This was applied in ABAQUS by utilising its `Python` API.

C.2 Validation

C.2.1 Validity of spring boundary conditions

The models used in section 7.3 and 7.4 model only a small region of the shell and use spring boundary conditions to approximate the behaviour of the rest of the shell. To determine whether this is a suitable approach, a simulation is conducted to determine the approximate behaviour of the shell as a whole, as illustrated in Figure C.6. The model makes use of symmetry and takes the cortical-cancellous-cortical sandwich nature of the shell into account. The dense cortical and spongy cancellous bone regions are modelled as linear elastic and are assigned Young's moduli of 12 GPa and 1 GPa, respectively. Both regions are assigned a Poisson's ratio of 0.25. The left surface, bottom surface and back surface are assigned boundary conditions of $u_1 = 0\,\text{mm}$, $u_2 = 0\,\text{mm}$ and $u_3 = 0\,\text{mm}$, respectively. Additionally, a force F_b with a magnitude of 295 N is applied to represent one sixth of the bite force of a lion [121] (assuming there are six pairs of teeth in contact during a bite) as shown in Figure C.6.

The high stress region in the resulting stress distribution is focused within 2 mm of the

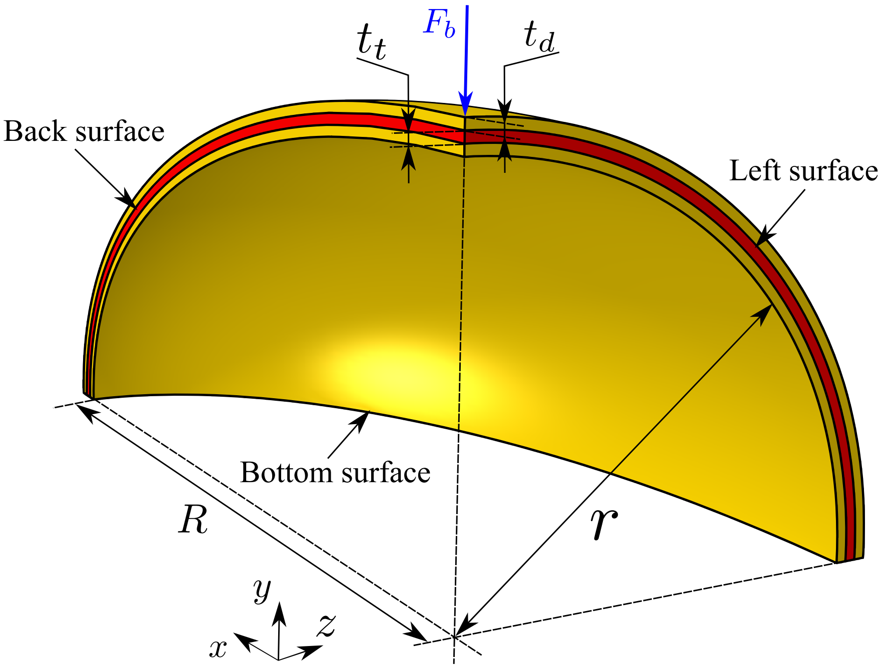

Figure C.6: Illustration of the model used to investigate the approximate response of the shell as a whole. The dimensions for the model are taken from the turtle skeleton shown in Figure 2.1. Hence, $r = 40\,\mathrm{mm}$, $R = 80\,\mathrm{mm}$, $t_t = 1\,\mathrm{mm}$, $t_d = 1\,\mathrm{mm}$. Additionally, boundary conditions of $u_1 = 0\,\mathrm{mm}$, $u_2 = 0\,\mathrm{mm}$ and $u_3 = 0\,\mathrm{mm}$ are prescribed to the left surface, bottom surface and back surface, respectively. Furthermore, a concentrated force of F_b is applied to represent the force from a predator's tooth. The magnitude of the force is set to 295 N as one sixth of the bite force of a lion [121] (assuming there are six pairs of teeth in contact during a bite).

region of loading as shown in Figure C.7 (a). Hence, modelling only a small region of the shell to determine the local behaviour in detail is deemed appropriate. Additionally, a reaction force approximately 280 N of the simulations in section 7.3 and 7.4 was observed when the displacement was equal to $-0.15\,\mathrm{mm}$. As the vertical displacement at the point of loading is $-0.16\,\mathrm{mm}$ for an applied force of 295 N, Figure C.7 (b), it is clear that the spring boundary conditions approximated the behaviour of the rest of the shell adequately.

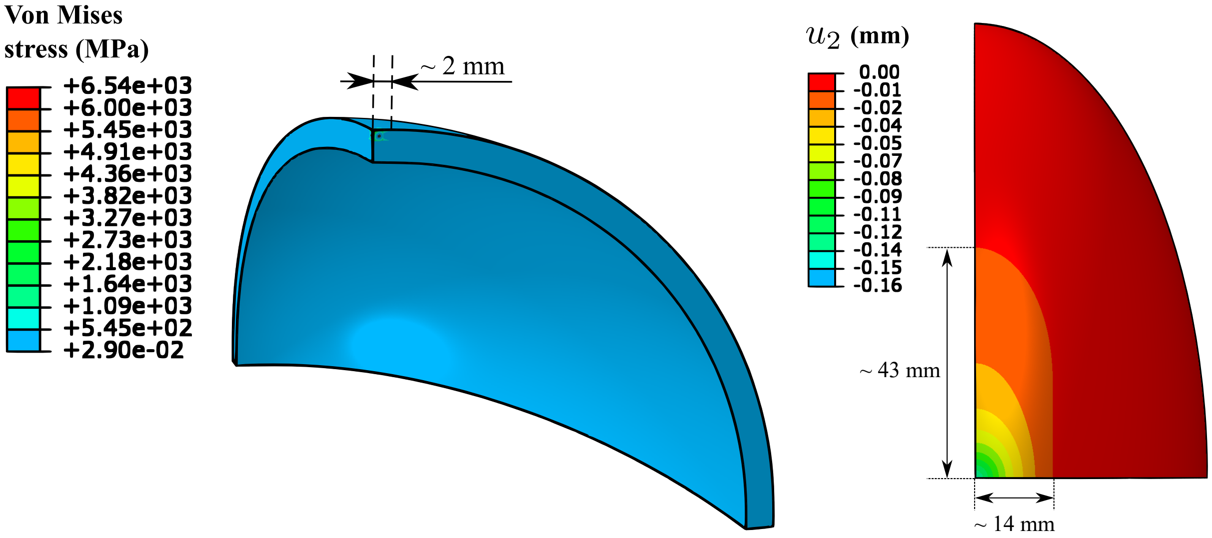

(a) (b)

Figure C.7: Contour plots of (a) von Mises stress and (b) vertical displacement. The high-stress region, that is the region of interest, is incredibly small. Hence, it is reasonable to use a detailed model to investigate the behaviour in that region. The vertical displacement becomes negligible at 43 mm from the concentrated load in the anterior direction and 14 mm in the lateral direction. Hence, these values were used for calculation of the stiffness of the spring boundary conditions as outlined in C.1.5. The reaction force for the simulations in sections 7.3 and 7.4 was approximately 280 N when the displacement was equal to −0.15 mm. Hence, it is clear that the spring boundary conditions approximated the behaviour of the rest of the shell adequately.

Appendix D

Dynamic simulations

D.1 Material test load cases analytical solutions

D.1.1 Biaxial loading of an incompressible viscohyperelastic material

For a judicious choice of basis, the deformation gradient and stress of an incompressible material during a particular class of biaxial loading is of the form

$$\boldsymbol{F} = \mathrm{Diag}\left[\lambda \quad 1 \quad \lambda^{-1}\right] , \qquad \boldsymbol{\sigma} = \mathrm{Diag}\left[\sigma_{11} \quad \sigma_{22} \quad 0\right] . \tag{D.1}$$

Hence, the right Cauchy-Green matrix and its inverse are given, respectively, by

$$\boldsymbol{C} = \mathrm{Diag}\left[\lambda^{2} \quad 1 \quad \lambda^{-2}\right], \qquad \boldsymbol{C}^{-1} = \mathrm{Diag}\left[\lambda^{-2} \quad 1 \quad \lambda^{2}\right] . \tag{D.2}$$

Given that the second Piola-Kirchhoff stress of a viscoelastic material is of the form

$$\boldsymbol{S} = \bar{\boldsymbol{S}} + \boldsymbol{S}^{\infty}_{vol} , \qquad \bar{\boldsymbol{S}} = \bar{\boldsymbol{S}}^{\infty} + \bar{\boldsymbol{S}}^{v} , \qquad \boldsymbol{S}^{\infty}_{vol} = Jp\boldsymbol{C}^{-1} , \tag{D.3}$$

and $\boldsymbol{C}$ is known, the undetermined pressure is given by

$$S_{33} = \bar{S}_{33} + pC^{-1}_{33} = 0 , \qquad \Rightarrow p = -\frac{1}{C^{-1}_{33}}\bar{S}_{33} . \tag{D.4}$$

Hence, the non-zero terms in the second Piola-Kirchhoff stress can be determined purely in terms of the isochoric stress and $\boldsymbol{C}$,

$$S_{11} = \bar{S}_{11} - \frac{C^{-1}_{11}}{C^{-1}_{33}}\bar{S}_{33} , \qquad S_{22} = \bar{S}_{22} - \frac{C^{-1}_{22}}{C^{-1}_{33}}\bar{S}_{33} . \tag{D.5}$$

If the viscoelastic model outlined in Section 4.3.2 is used then the isochoric stress is of the form

$$\bar{\boldsymbol{S}} = \bar{\boldsymbol{S}}^{\infty} + \sum_{\alpha}^{N_m} \beta_\alpha \int_0^t \exp\left(-\frac{t-s}{\tau_\alpha}\right) \dot{\bar{\boldsymbol{S}}}^{\infty} ds = \int_0^t \left[1 + \sum_{\alpha}^{N_m} \beta_\alpha \exp\left(-\frac{t-s}{\tau_\alpha}\right)\right] \dot{\bar{\boldsymbol{S}}}^{\infty} ds \,, \qquad \text{(D.6)}$$

and so only the rate of the long time-scale isochoric stress need be found. Note that to determine a closed form solution one would need to perform the required integration. However, the integrand is different for each model for the long time-scale isochoric stress. Furthermore, solving the integration is likely intractable in most cases. Hence, the integration is evaluated numerically by partitioning the time domain and applying Gaussian quadrature over each subdomain.

Holzapfel-Gasser-Ogden model

Finally to determine the analytical solution for this loading under the Holzapfel-Gasser-Ogden (HGO) model, one requires the isochoric stress rate for the model. Given that the second Piola-Kirchhoff stress for the HGO model is

$$\bar{\boldsymbol{S}}^{\infty} = 2J^{-2/3} G \left(\boldsymbol{I} - \frac{1}{3} I_1 \boldsymbol{C}^{-1}\right) + 2J^{-2/3} k_1 E e^{k_2 E^2} \left[\kappa \left(\boldsymbol{I} - \frac{1}{3} I_1 \boldsymbol{C}^{-1}\right) + (1-3\kappa)(\boldsymbol{a}_0 \otimes \boldsymbol{a}_0 - \frac{1}{3} I_4 \boldsymbol{C}^{-1})\right] \,, \qquad \text{(D.7)}$$

the isochoric stress rate is given by

$$\begin{aligned} \dot{\bar{\boldsymbol{S}}}^{\infty} = & -\frac{2}{3} G \left(\dot{I}_1 \boldsymbol{C}^{-1} + I_1 \dot{\boldsymbol{C}}^{-1}\right) - \frac{2}{3} k_1 E e^{k_2 E^2} \left[\kappa \left(\dot{I}_1 \boldsymbol{C}^{-1} + I_1 \dot{\boldsymbol{C}}^{-1}\right) + (1-3\kappa)(\dot{I}_4 \boldsymbol{C}^{-1} + I_4 \dot{\boldsymbol{C}}^{-1})\right] \\ & + 2k_1 (\dot{E} e^{k_2 E^2} + 2k_2 E^2 \dot{E} e^{k_2 E^2}) \left[\kappa \left(\boldsymbol{I} - \frac{1}{3} I_1 \boldsymbol{C}^{-1}\right) + (1-3\kappa)(\boldsymbol{a}_0 \otimes \boldsymbol{a}_0 - \frac{1}{3} I_4 \boldsymbol{C}^{-1})\right] \,. \end{aligned} \qquad \text{(D.8)}$$

D.1.2 Uniaxial loading of an isotropic linear compressible viscoelastic material

The strain and stress for uniaxial loading of a isotropic compressible linear elastic material is of the form

$$\boldsymbol{\varepsilon} = \text{Diag}\left[\varepsilon_{11} \quad \varepsilon_{22} \quad \varepsilon_{22}\right] \,, \qquad \boldsymbol{\sigma} = \text{Diag}\left[\sigma_{11} \quad 0 \quad 0\right] \,. \qquad \text{(D.9)}$$

Moreover, the stress can be decomposed into a volumetric component $\boldsymbol{\sigma}^{\infty}_{vol}$ and an isochoric component $\bar{\boldsymbol{\sigma}}$ which can be further decomposed into a long time-scale $\bar{\boldsymbol{\sigma}}^{\infty}$ and viscoelastic $\bar{\boldsymbol{\sigma}}^{v}$ component,

$$\boldsymbol{\sigma} = \bar{\boldsymbol{\sigma}} + \boldsymbol{\sigma}^{\infty}_{vol} \,, \qquad \bar{\boldsymbol{\sigma}} = \bar{\boldsymbol{\sigma}}^{\infty} + \bar{\boldsymbol{\sigma}}^{v} \,, \qquad \bar{\boldsymbol{\sigma}}^{v} = \sum_{\alpha=1}^{N_m} \beta_\alpha \int_0^t \exp\left(\frac{-[t-s]}{\tau_\alpha}\right) \dot{\bar{\boldsymbol{\sigma}}}^{\infty} \mathrm{d}s \,. \qquad \text{(D.10)}$$

The long time-scale (time independent) response $\boldsymbol{\sigma}^\infty$ can also be decomposed into a shear $\bar{\boldsymbol{\sigma}}^\infty$ and a volumetric $\boldsymbol{\sigma}^\infty_{vol}$ component,

$$\begin{aligned} \boldsymbol{\sigma}^\infty_{vol} &= \left[\lambda + \frac{2}{3}\mu\right] \mathrm{tr}\left(\boldsymbol{\varepsilon}_{vol}\right) \boldsymbol{I}\,, \qquad \bar{\boldsymbol{\sigma}}^\infty = \boldsymbol{\sigma}^\infty - \boldsymbol{\sigma}^\infty_{vol} = 2\mu\bar{\boldsymbol{\varepsilon}}\,, \\ \boldsymbol{\varepsilon}_{vol} &= \frac{1}{3}\mathrm{tr}\left(\boldsymbol{\varepsilon}\right) \boldsymbol{I}\,, \qquad \bar{\boldsymbol{\varepsilon}} = \boldsymbol{\varepsilon} - \boldsymbol{\varepsilon}_{vol}\,. \end{aligned} \tag{D.11}$$

Hence, the following relations for the stress can be determined:

$$\boldsymbol{\sigma} = 2\mu \int_0^t \left[1 + \sum_{\alpha=1}^{N_m} \beta_\alpha \exp\left(\frac{-[t-s]}{\tau_\alpha}\right)\right] \dot{\bar{\boldsymbol{\varepsilon}}} \mathrm{d}s + \left[\lambda + \frac{2}{3}\mu\right] \mathrm{tr}\left(\boldsymbol{\varepsilon}_{vol}\right) \boldsymbol{I}\,, \tag{D.12}$$

$$\sigma_{11} = \frac{4\mu}{3} \int_0^t \left[1 + \sum_{\alpha}^{N_m} \beta_\alpha \exp\left(\frac{-[t-s]}{\tau_\alpha}\right)\right] \left[\dot{\varepsilon}_{11} - \dot{\varepsilon}_{22}\right] \mathrm{d}s + \left[\lambda + \frac{2}{3}\mu\right] \left[\varepsilon_{11} + 2\varepsilon_{22}\right]\,, \tag{D.13}$$

$$\sigma_{22} = \frac{2\mu}{3} \int_0^t \left[1 + \sum_{\alpha}^{N_m} \beta_\alpha \exp\left(\frac{-[t-s]}{\tau_\alpha}\right)\right] \left[\dot{\varepsilon}_{22} - \dot{\varepsilon}_{11}\right] \mathrm{d}s + \left[\lambda + \frac{2}{3}\mu\right] \left[\varepsilon_{11} + 2\varepsilon_{22}\right] = 0\,. \tag{D.14}$$

An equation relating the known independent variables ε_{11}, $\dot{\varepsilon}_{11}$ and t to the dependent variable σ_{11} is required. This is provided by equation (D.13). However, it contains the unknown variable of ε_{22} (and its time derivative). Equation (D.14) implicitly defines ε_{22}. However, finding its closed form solution is intractable. One possible approach is to assume $\dot{\varepsilon}_{22}$ is constant. From equation (D.14) one can then obtain

$$\dot{\varepsilon}_{22} = \nu^v \dot{\varepsilon}_{11}\,, \qquad \nu^v = \frac{\frac{2}{3}\mu \sum_{\alpha}^{N_m} \beta_\alpha \tau_\alpha \left[1 - \exp\left(-t/\tau_\alpha\right)\right] - \lambda t}{\frac{2}{3}\mu \sum_{\alpha}^{N_m} \beta_\alpha \tau_\alpha \left[1 - \exp\left(-t/\tau_\alpha\right)\right] + t\left[\lambda + 2\mu\right]}\,. \tag{D.15}$$

However, this result clearly contradicts the assumption that $\dot{\varepsilon}_{22}$ is constant. Although, equation (D.15) does approximately hold for certain combinations of material parameters (details omitted). In order to determine a more robust method of determining ε_{22} one resorts to a numerical approach. The time domain is partitioned,

$$0 = t_0 < t_1 < \ldots < t_n < t_{n+1} = t\,, \tag{D.16}$$

and the following definitions are made:

$$\Delta t_{n+1} := t_{n+1} - t_n\,, \qquad t_{n+0.5} := \frac{1}{2}\left[t_{n+1} + t_n\right]\,. \tag{D.17}$$

Then, using a midpoint integration rule, that is

$$\int_{t_n}^{t_{n+1}} f(s)\mathrm{d}s \approx \int_{t_n}^{t_{n+1}} f(t_{n+0.5})\mathrm{d}s\,, \tag{D.18}$$

and equation (D.14) gives

$$\begin{aligned}\sigma_{22}^{(n+1)} =& \frac{2\mu}{3}\left[\varepsilon_{22}^{(n+1)} + \sum_{\alpha}^{N_m}\left[\beta_\alpha \exp\left(-\Delta t/2\tau_\alpha\right)\left[\varepsilon_{22}^{(n+1)} - \varepsilon_{22}^{(n)}\right] + \exp\left(-\Delta t/\tau_\alpha\right) h_\alpha^{(n)}\right]\right.\\ &\left. - \left[t + \sum_{\alpha}^{N_m}\beta_\alpha\tau_\alpha\left[1 - \exp\left(-t/\tau_\alpha\right)\right]\right]\dot{\varepsilon}_{11}\right]\\ &+ \left[\lambda + \frac{2}{3}\mu\right]\left[t\dot{\varepsilon}_{11} + 2\varepsilon_{22}^{(n+1)}\right] .\end{aligned} \tag{D.19}$$

Here, $h_\alpha^{(n)}$ is a history term for each Maxwell branch determined at the current time increment $(n+1)$ from

$$h_\alpha^{(n+1)} = \beta_\alpha \exp\left(-\Delta t/2\tau_\alpha\right)\left[\dot{\varepsilon}_{22}^{(n+1)} - \dot{\varepsilon}_{22}^{(n)}\right] + \exp\left(-\Delta t/\tau_\alpha\right) h_\alpha^{(n)} , \qquad h_\alpha^{(0)} = 0 . \tag{D.20}$$

Equation (D.19) can be used to determine $\varepsilon_{22}^{(n+1)}$ by applying a numerical root finding procedure, such as the Newton-Raphson method. The history terms at the current time increment (to be used in the proceeding time increment) can be then be determined using equation (D.20) and σ_{11} is given by

$$\begin{aligned}\sigma_{11}^{(n+1)} =& \frac{4\mu}{3}\left[\left[t + \sum_{\alpha}^{N_m}\beta_\alpha\tau_\alpha\left[1 - \exp\left(-t/\tau_\alpha\right)\right]\right]\dot{\varepsilon}_{11} - \left[\dot{\varepsilon}_{22}^{(n+1)} + \sum_{\alpha}^{N_m} h_\alpha^{(n+1)}\right]\right]\\ &+ \left[\lambda + \frac{2}{3}\mu\right]\left[t\dot{\varepsilon}_{11} + 2\varepsilon_{22}^{(n+1)}\right] .\end{aligned} \tag{D.21}$$